HIGH SPEED CHEMICAL ROTORS

by

M. P. RALLS

Thesis submitted for an
Official Degree

Department of Physics
University of Birmingham

September 1975

SYNOPSIS

This report is an account of the work carried out, mainly by the author, on the development of high speed rotors for the production of hypersonic colliding beams of molecules.

Initially a brief comparison is made between various standard techniques used for the production of molecular beams with translational energies in the range 1 to 20eV. Then consideration is given to the part that rotors, producing tip speeds of 2km/s, can play in producing colliding molecular beams with available reaction energies from 1 to 10eV.

Following this, the theoretical and practical considerations used to produce a successful high speed rotor, using carbon fibre composite arms, are discussed. A full description of the single rotor unit is given and also of the double rotor unit, which is designed to produce colliding beams. Full circuit details of the rotor suspension system, the drive unit and a semi-digital and a fully-digital unit for phase-locking two rotors for use when producing colliding beams are given.

Results of an experiment are described, using one rotor, to measure the energy-intensity characteristics of a rotor-produced beam of mercury atoms. Finally, a description of a proposed experiment to optically excite mercury atoms by collision of two rotor-produced beams is given, this to be conducted in the double unit.

ACKNOWLEDGEMENTS

I would like to express my thanks to Professor P.B. Moon for his help and guidance during the period that I have been working with him in the department. I would also like to thank Dr. J.H. Broadhurst for some of the initial work done for this project during his stay at the University, and Dr. A. Barker of the Department of Chemical Engineering for producing and testing the carbon fibre composite used for the rotor arms.

Special thanks go to B. Hail for making the intricate glassware required, and to B. Saul for making the rotors and general construction of the rotor units.

I am also grateful to Dr. Isaak for his interest and helpful discussions during the course of this project.

Finally, I would like to thank Sheila, my wife, for her help in producing the diagrams, J.E. James for the photographs, and Mrs. P.M. Courtney for her patient typing of this thesis.

CONTENTS

* This Chapter does not constitute a part of the thesis but is a supplement to conclude the work presented within it. The work was accomplished by the author in the period between the submission of the thesis and the oral examination.

CHAPTER I

INTRODUCTION TO MOLECULAR BEAM PRODUCTION USING ROTORS

Molecular beams are required by chemists and physicists to study the laws that govern the properties of molecules and atoms, just as the cyclotron is needed to study the physical realities of sub-atomic particles. In particular, molecular beams have been used to study intermolecular forces, bimolecular reactions and, now, internal energy transfer accompanying bimolecular collisions. Various techniques are used for beam production to give a fairly continuous range of energies. However, the range of energies between 1eV and 20eV is an interval which is comparatively difficult to produce, but is of great interest to chemists. It covers the energy range for the dissociation of chemical bonds and also the activation energies for most chemical reactions.

Nozzle-produced beams can cover part of this range by running them at elevated temperatures using a plasma jet technique (R. W. Kesslen and B. Koglin, 1966)[10]. In this technique an arc is struck within the nozzle raising the effective temperature to several thousand degrees Kelvin. This method produces energies of about 3eV with beam intensities of 10^{19} atoms/sr/s. General requirements for the nozzle technique are large differential pumping speeds of typically 10^{4} litres/s.

Another method which is being investigated is called Sputtering[10]. This method uses a solid target made of the material which is required for the beam and bombards this with high energy ions. The sputtered atoms are then collimated and velocity selected to form a beam. This method

appears only to produce low intensities of the order of 10^{13} atoms/sr/s. (J. Politiek et al, 1968)[10] and hence is not greatly favoured.

The seeded beam technique[11] is useful for producing beams where the carrier gas does not affect the reaction. Heavy molecules, which are required for the beam, are added to a light inert carrier gas, usually helium, in proportions ranging from 1 to 5% and then the mixture is expanded through a nozzle. The speed of the mixture is mainly determined by the carrier gas. By multiple collisions, the heavy gas molecules are accelerated to nearly the speed of the carrier gas and the emerging beam is skimmed and collimated to produce a beam of heavy molecules[12] with kinetic energies per molecule much greater than that of the carrier gas. This method has advantages over the plasma technique in that the molecules are accelerated comparatively gently and hence molecules, which would dissociate when violently heated, can be successfully formed into beams. This technique produces typical intensities of 10^{16} molecules/sr/s with a typical spread in beam velocity of 10%.

Charge exchange beam methods[10] are usually used to produce higher energy beams than 20eV but can be used to produce energies between 5eV and 10eV, but with very low intensities, typically 10^{12} atoms /sr/s. The reason why only low intensities are possible at low energies is due to mutual repulsion of ions within the ion beam, limiting the density and hence making focussing very difficult. The method relies on the fact that the cross-section for the resonant charge transfer process is very much larger than the momentum transfer cross-section. The low beam intensities make this method less attractive than the seeded nozzle method.

Now, considering the use of rotors in the production of molecular beams,[16] D.G.Marshall and P.B.Moon[13] demonstrated that rotors could be used to produce fast, molecular beams. In 1954 T.H.Bull and P.B.Moon showed that a beam of carbon tetrachloride produced using a rotor had sufficient translational energy to react chemically with caesium atoms. At this time the maximum tip speed obtainable using high tensile steel was of the order of 1km/s, which meant[17] that an atom of mercury, of atomic weight 200, would possess a kinetic energy of 1eV when travelling at this speed. This energy, however, is comparatively small and can satisfactorily be produced by many other methods. With the advent of new materials, discussed in Chapter II, a tip speed of 2km/s[15] is now possible and this leads to a four-fold increase in obtainable energy. Further to this point, if two rotors are used to produce beams of atoms with the same molecular weight, e.g. 200, and these beams are allowed to collide head-on, then the available energy for chemical reactions is doubled and hence energies of 8eV are possible.

Considering one rotor and the beam produced by it, there are various methods of transporting the beam material to the tip of the rotor, prior to the production of the beam. The method mainly considered for the rotor arm design presently used is the simple sweeping up of the molecules. The vessel can be filled with vapour of the required material and then the rotor arm collides with the molecules, which then condense and, after a time sufficient for them to come into thermal equilibrium with the rotor arm, re-evaporate with thermal velocities. Another similar method is to use a locally produced beam of slowing moving atoms travelling perpendicular to the plane of the rotor arms. This method is more

economical on gas and it reduces the frictional couple on the rotor. If a molecule collides with the rotor arm and is elastically scattered, then the translational velocity imparted to the molecule is twice the velocity of the rotor tip. These two methods have dealt with collisions between the rotor and the molecule prior to beam production. This causes heating of the rotor, which is undesirable as will be explained later. It is possible, though difficult, to feed molecules via a small tube set within the rotor arm and allow them to emerge on the leading blade of the rotor arm. The source[18] of molecules could either be a solid material set into the body of the rotor prior to the rotor being run, or molecules could be fed, via a small tube approximately on the rotational axis of the rotor body, into the body and then, by centrifugal pumping, to the tip.

The resultant velocity of a molecule observed in the laboratory frame of reference, is the vector sum of the rotor tip velocity at the moment the molecule leaves the surface, added to its thermal velocity. If the molecules are considered to come from a single point on the rotor arm with thermal velocities equivalent to energies of the order of kT, then the beam produced will have an angular spread of approximately V_t/V_r radians (half angle) where V_t is the thermal velocity and V_r is the velocity of the tip of the rotor. For rotor temperatures of 370°K and molecules of molecular weight 200, the angular spread of a 2km/s beam is of the order of 0.1 of a radian. The velocity spread of the beam is about 10%. This means that the beam will be more mono-energetic if the rotor body is as cool as possible and heavy molecules are accelerated.

Considering this rather simple view of the beam produced by the tip of the rotor, it will be apparent that molecules leaving the rotor arm

perpendicularly will have a velocity given by the algebraic sum of the rotor velocity plus the thermal velocity. However, molecules leaving the rotor arm at other angles will have an increasingly smaller speed as the angle from the normal increases. Assuming that all the molecules have a thermal velocity V_t, the lowest speed would result when a molecule had all its thermal velocity parallel to the plane of the blade. Although this would, in principle, make it impossible for the molecule to escape from the blade, a small component perpendicular to the plane would enable it to do so. This would mean that molecules leaving perpendicular to the arm would have a speed of $V_r + V_t$ and the others could have a speed as low as $(V_r^2 + V_t^2)^{\frac{1}{2}}$. If all the velocity components of the molecules leaving the rotor arm are resolved along a line perpendicular to the blade of the rotor arm, the velocity components would range from V_r to $(V_r + V_t)$.

If two collimation slits are set up in a line which forms a tangent to the locus of the rotor arm tip, the speeds of the molecules exiting from the furthest slit will show a peak when the rotor arm is perpendicular to the axis of the slits and will fall off either side of this point. This assumes the slits to be narrow and fairly close to the rotor arm, such that the differences in speed have not significantly changed the time-energy distribution of the beam. As can be seen from the previous discussion, the beam does have a velocity spread but the effectiveness of this can be reduced due to the pulsed nature of the beam. Conventional beam methods are usually continuous and this produces problems in accurate measurement of the energy of the beam. However, the energy of these beams can be measured by using choppers to make the

continuous beam pulsed, allowing time-of-flight measurements to be made. The rotor produces pulses of molecules of the order of 10^4/s at tip speeds of 2km/s and it is therefore possible to measure directly the energy spread of the beam. If the beam is allowed to travel some distance before detection, the square of the time of flight of the molecules will be inversely proportional to the translational energy of the molecules. However, the path length must not be allowed to become too long as fast molecules from the next pulse will catch up with the slow molecules from the previous pulse. If the path length is too short, the molecules with different velocities will not have time to re-position themselves in order of energy and will still possess the velocity/time function produced by the molecular emissions from the rotor arm scanning the collimation slits.

The pressure within the apparatus must be kept low, such that the mean free path of molecules within the vessel and associated areas is longer than the beam path. If this is not the case, collisions between the beam and slow background molecules will result in the broadening of the velocity spread within the beam and a reduction in the intensity.

The considerations of a beam produced by a single rotor are of interest if molecule-surface phenomena are to be considered,[19] but the main work in the following chapters will concern the apparatus required for colliding beams produced by two rotors.

The following derivation for available reaction energy, resulting from the collision of two beams of molecules with the same mass m, is a very much simplified case, but serves to highlight a useful principle connected with this type of beam production. Consider the situation

Figure 1.1

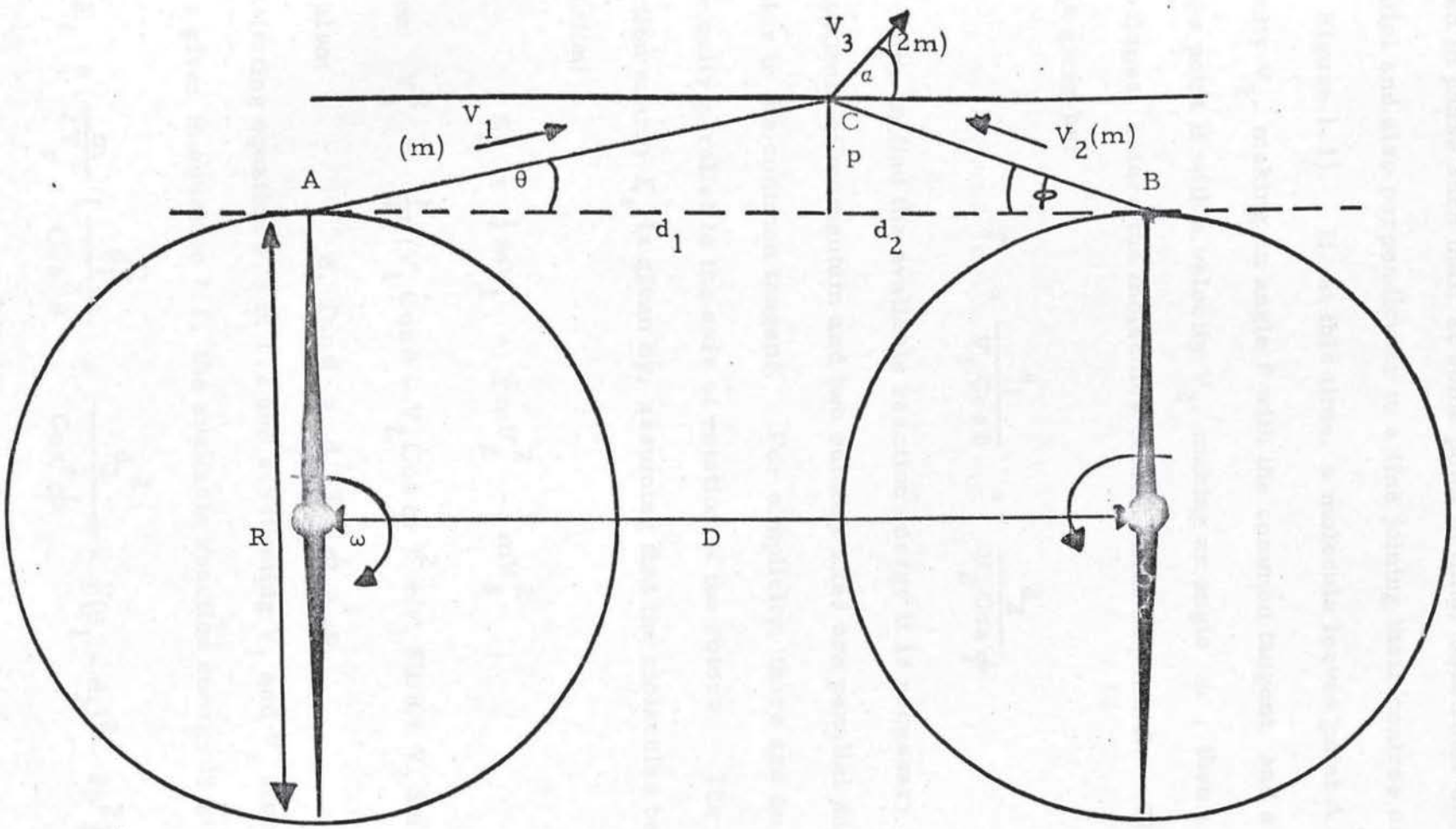

where two rotors which are counter rotating at an angular speed ω are locked in phase such that, at some point in time, both rotor blades are parallel and also perpendicular to a line joining their centres of rotation, (see Figure 1.1). If, at this time, a molecule leaves point A with a velocity V_1, making an angle θ with the common tangent, and a molecule leaves point B with a velocity V_2, making an angle ϕ, then a time T_c will elapse, before the molecules could collide at point C. The time T_c is given by:

$$T_c = \frac{d_1}{V_1 \operatorname{Cos}\theta} = \frac{d_2}{V_2 \operatorname{Cos}\phi} \qquad (1.1)$$

Now, to find the available reaction energy it is necessary to resolve components of momentum and two suitable axes are parallel and perpendicular to the common tangent. For simplicity, there are no components of velocity parallel to the axis of rotation of the rotors. The available reaction energy E_r is given by, assuming that the molecules bond after collision:

$$E_r = \tfrac{1}{2}mV_1^2 + \tfrac{1}{2}mV_2^2 - mV_3^2 \qquad (1.2)$$

where $$V_3^2 = \frac{1}{4}\left((V_1 \operatorname{Cos}\theta - V_2 \operatorname{Cos}\phi)^2 + (V_1 \operatorname{Sin}\theta + V_2 \operatorname{Sin}\phi)^2 \right) \qquad (1.3)$$

and also: $$d_1 \operatorname{Tan}\theta = d_2 \operatorname{Tan}\phi = p$$

Substituting equation 1.3 in 1.2 and substituting V_1 and V_2 from relationships given in equation 1.1, the available reaction energy is given by:

$$E_r = \frac{m}{2T_c^2}\left[\frac{d_1^2}{\operatorname{Cos}^2\theta} + \frac{d_2^2}{\operatorname{Cos}^2\phi} - \tfrac{1}{2}(d_1 - d_2)^2 - 2p^2 \right] \qquad (1.4)$$

This can be further simplified as:

$$\cos^2\theta = \frac{d_1^2}{(p^2+d_1^2)} \quad \text{and} \quad \cos^2\phi = \frac{d_2^2}{(p^2+d_2^2)}$$

to give a fairly simple equation:

$$E_r = \frac{m D^2}{4 T_c^2} \qquad (1.5)$$

T_c is the time measured from the shooting position to an observed collision. Thus, the available reaction energy is inversely proportional to the square of the time between the in-phase position of the rotors and the collision. If one of the molecules were to leave the rotor blade just prior to the in-phase position, this would not significantly change the result as the distance travelled by such a molecule would not be significantly different from the distance it would have travelled in the same time had it stayed on the blade. This assumes the thermal velocity component is much less than the tip velocity. If an imaginary plane is set up perpendicular to the common tangent, the time of arrival of molecules from either tip is mainly governed by the velocity of the molecules and not be the time at which any given molecule leaves the rotor tip. This is true for quite appreciable angles of the rotor arm from the perpendicular position of the order of $\pm 5^{o}$ and path lengths of 300mm.

In practice, the molecules do not come from a single point on the arm but from an area. This will complicate the situation but not severely change the general results.

Thus this technique lends itself to time-of-flight measurements and, with the use of laser-assisted detection, it should be possible to study molecule-molecule collisions. It is a simple unit which is cheaper

than conventional methods and can be run by a small team of one or two people. Measurements of beam intensity for mercury show intensities of the order of 5×10^{15}, atoms/sr/s. However, this can probably be increased by using differently shaped blades, discussed in Chapter II.

CHAPTER II

THEORETICAL AND PRACTICAL PROBLEMS OF PRODUCING A HIGH SPEED ROTOR

2.1 Introduction

The following discussion will concern rod-type rotors as they are one of the most useful shapes to be considered for molecular acceleration. Disc shaped rotors do have their applications, but as they can only be thinned in one dimension they have a lower peripheral speed limit than a rod spun about its short axis.

Steel rod-type rotors have been used in Birmingham previously to produce beams of molecules.[3,1] These rotors were made of high tensile strength steel and reached speed just in excess of 1km/s. The rotors were of the form of a ball-and-double-cone, which had tip-to-tip lengths of typically 5.25 ins.

2.2 Shape Considerations.

It will be clear that the limiting peripheral velocity of a rotor will depend on its shape and the material from which it is made. (Marshall et al). Considering the criterion of equal longitudinal stress, the ideal profile shape for a rotor arm follows the form of a Gaussian[2] function. Thus, the cross-sectional area of the arm A_r varies as $A_o e^{-Kr^2}$ assuming all the forces contributing to the failure of the arms to be longitudinal. This leads to infinite tip speeds as r tends to infinity, but, as the diameter of such an arm tends to zero, a truncated Gaussian is the most practical form. Unfortunately, a truncated Gaussian is also difficult to machine and hence an approximation to this shape is produced by a ball and cones, as used above. If a rotor arm has a truncated

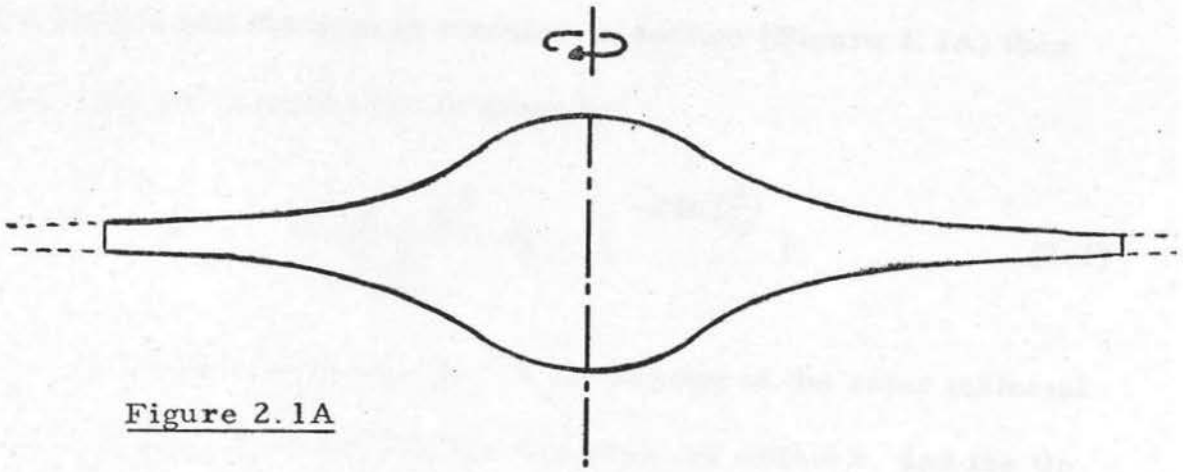

Figure 2.1A

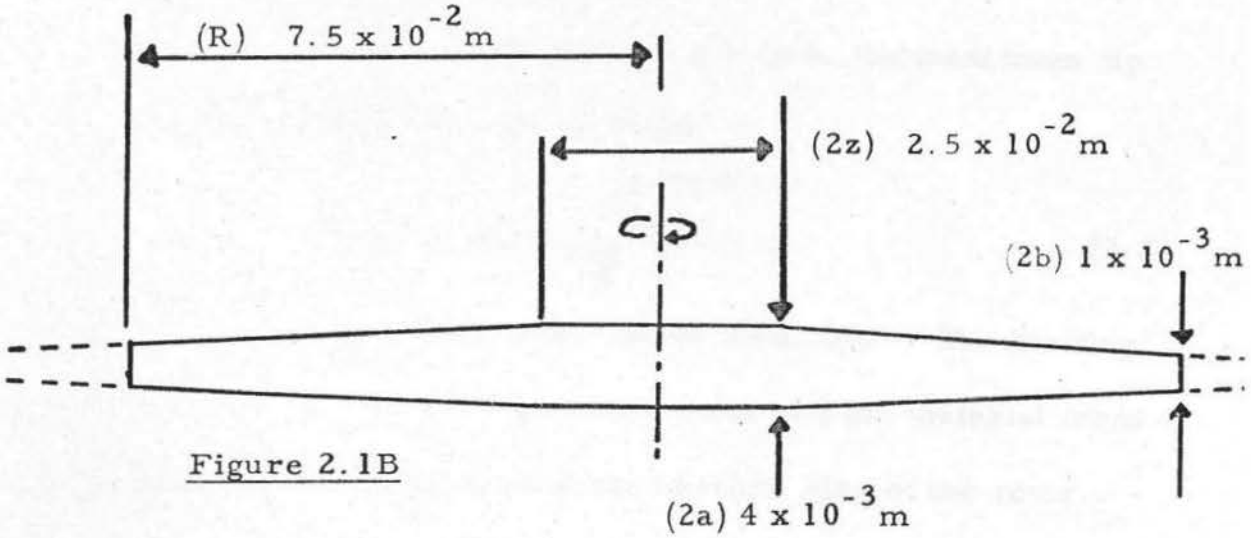

Figure 2.1B

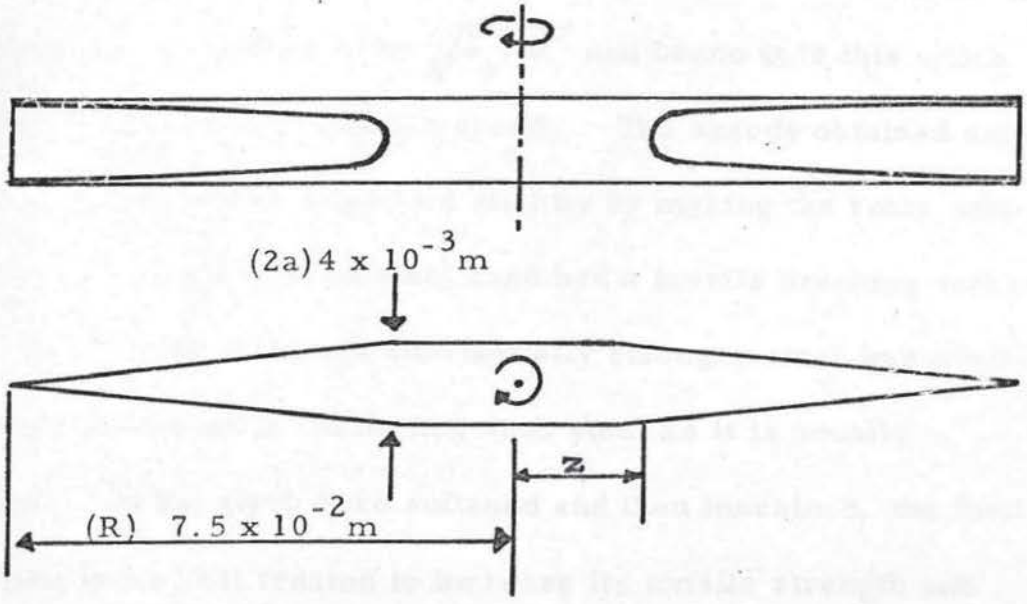

Figure 2.1C

Gaussian profile and the arm is circular in section (Figure 2.1A) then the stress S on the central area is given by:

$$S = \frac{\omega^2 \rho R^2}{4 \ln(\frac{a}{b})} [1 - e^{-2 \ln(\frac{a}{b})}] \qquad (2.1)$$

where ω is the angular velocity, ρ is the density of the rotor material and R is the distance between the central area, of radius a, and the tip area, of radius b. As the tip velocity is given by ωR then the stress at the central point of the rotor is only dependent on the square of the tip speed and the ratio of a/b. If the ratio of a/b is 4, the maximum tip speed V_m of such a shaped rotor is given by:

$$V_m = 2.432 \sqrt{\frac{S_o}{\rho}} \qquad (2.2)$$

where S_o is the tensile breaking stress of the material. The limiting speed is only dependent on the shape of the rotor and the material from which it is made and is independent of the absolute size of the rotor.

2.3 Composite Rotors.

It can generally be shown that for any shape of rotor the limiting tip speed will always be proportional to $\sqrt{S_o / \rho}$ and hence it is this which mainly limits the maximum attainable speed. The speeds obtained using all steel rotors could only be improved slightly by making the rotor arm profile a Gaussian. The type of steel used had a tensile breaking stress of $1.16 \times 10^{+9}$ N/m^2 and, although substantially stronger steel was available, there were problems in machining such steel as it is usually extremely hard. If the steel were softened and then machined, the final rotor would have to be heat treated to increase its tensile strength and this could cause deformation of the body. This means that the most

attractive way of increasing the peripheral speed of the rotor is to use material which has a considerably lower density, while still possessing a high tensile strength. This can be realised when some non-metallic substances and, in particular, carbon fibres are considered.

Carbon fibres have a typical tensile strength of 2.7 GN/m^2 and a density of 2×10^3 kg/m^3. However, the single fibres are very thin and impractical to use for the arms of a rotor, but if the fibres are combined with epoxy resin to produce a matrix of fibres and resin, the resultant carbon fibre composite substantially retains the advantageous characteristics of the fibres. The tensile strength of the composite is dependent on the volume fraction k of the fibres to resin. The tensile strength S_c of the composite is given by:

$$S_c = S_r + k(S_f - S_r) \qquad (2.3)$$

where S_f is the tensile breaking stress of the carbon fibres and S_r the tensile breaking stress of the resin. For a 60% volume fraction and S_r of the order of 6×10^7 N/m^2, the tensile strength of the composite is 1.6×10^9 N/m^2. This is slightly larger than for the machinable steel used previously. The density of the composite ρ_c is given by:

$$\rho_c = \rho_r + k(\rho_f - \rho_r) \qquad (2.4)$$

where ρ_r is the density of the resin and ρ_f is the density of the fibres. This gives a density of the order of 1.54×10^3 kg/m^3 for a 60% volume fraction. The results of the above indicate that, if carbon fibre composite is used, an increase in tip velocity of $\sqrt{\frac{\rho_s}{\rho_c}}$ times the maximum achieved using the steel of earlier rotors can be expected, assuming the

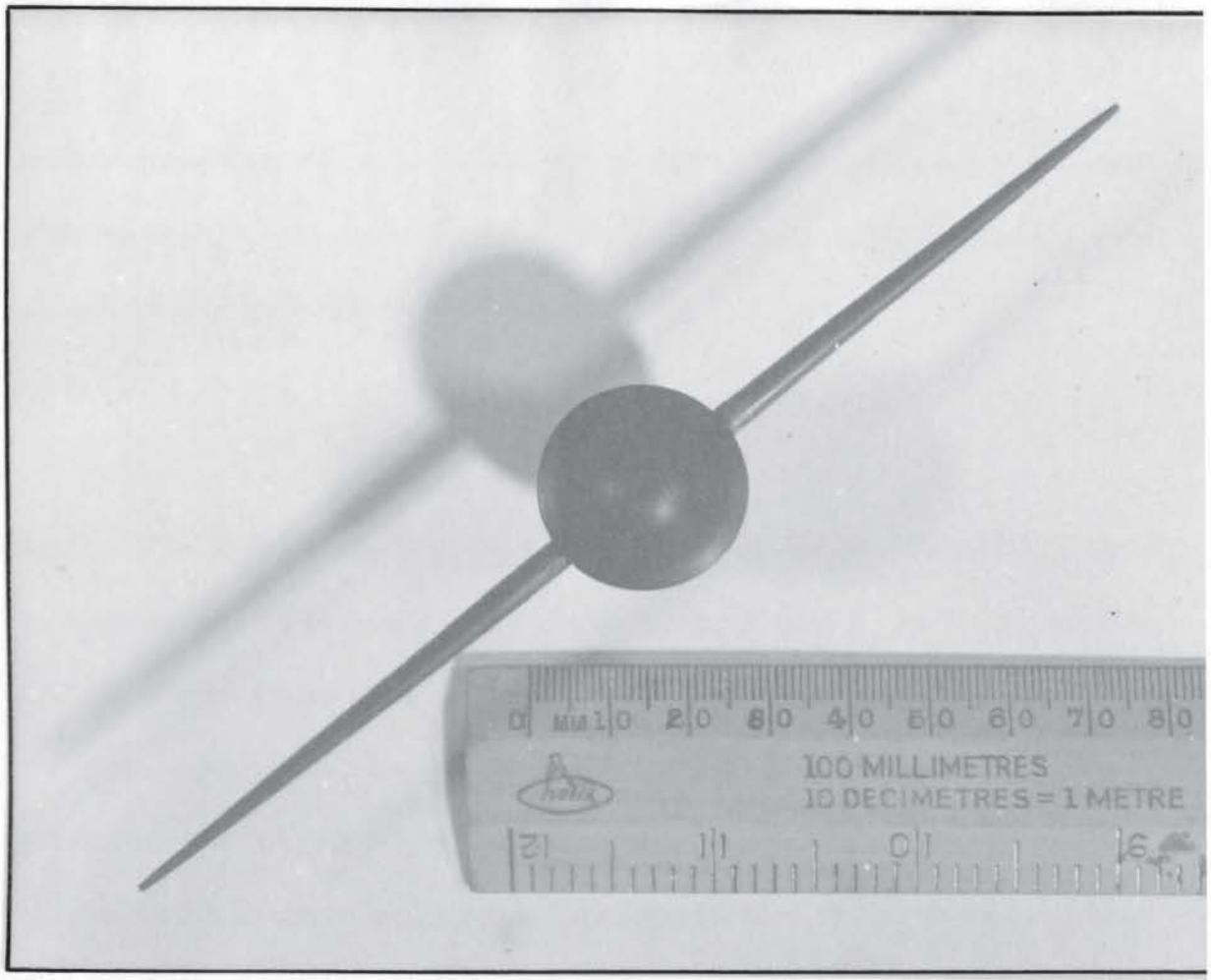

PLATE 2.1 Photograph of high speed rotor which reached tip velocity of 2km/s.

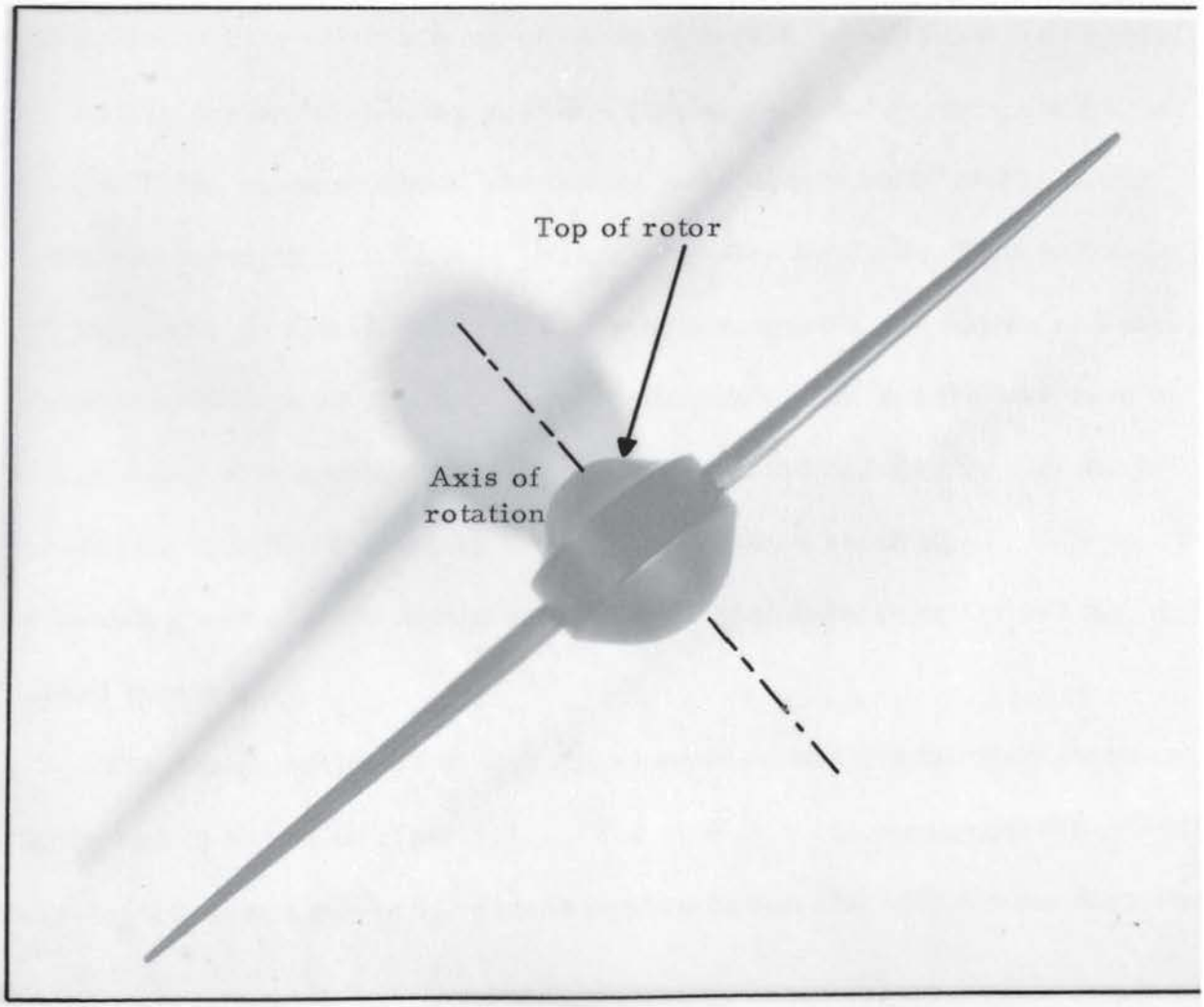

tensile breaking stresses to be comparable. Considering the density and the tensile strength of carbon fibre composite, the maximum obtainable tip velocity is given by:

$$V_m = F \sqrt{\frac{S_f + k(S_f - S_r)}{\rho_r + k(\rho_f - \rho_r)}} \qquad (2.5)$$

where F is a coefficient which is a function of the profile used. As S_f is approximately a factor of 30 times greater than S_r but ρ_f is only a factor of two greater than ρ_r, the limiting tip velocity will be improved by increasing the volume fraction k until just prior to the point when the fibres are no longer bonded together with the resin to form a composite.

As carbon fibre composite is not isotropic, it has to be carefully used so that forces perpendicular to the axis of the fibres are not allowed to pull the composite apart. The tensile strength of the material in this direction is only about a tenth of the longitudinal strength as the former is mainly due to the binding resin. As the material is not metallic, a centre boss, made of nickel chromium molybdenum steel EN24, having a tensile strength of $1.16 \times 10^9 N/m^2$, supplied by Thos. Firth and John Brown Ltd., Sheffield, was used to enable magnetic suspension and electro-magnetic drive to be applied. A $\frac{3}{4}$" diameter steel sphere was used in conjunction with a composite, tapered arm, hand finished by J.H B. to produce a rotor which ran up to 1.75km/s before breaking. This was a promising start as the design had not been particularly optimised for high speed running.

The design adopted for high speed running was produced by Professor Moon and is shown in Plate 2.1. The steel boss is machined with slowly varying curves to minimise stress concentration and with a 4mm diameter

hole drilled through the centre to hold the carbon fibre composite shaft. For the stable running of the rotor, it is necessary for the rotor body to spin on an axis, about which the moment of inertia of the rotor is a maximum. The moment of inertia of the rotor is approximately 4.4×10^{-6} Kg/m^2.

The composite shaft has a profile shown in Figure 2.1B. The width of the rotor shaft was kept as thin as possible to reduce lateral stresses within it to a minimum. These stresses are proportional to the cross-sectional area for this arm, and are at a maximum where this is largest. Calculation of the lateral stress for this shape of arm shows the lateral stress to be less than one hundredth of the longitudinal stress.

The composite shaft has a cylindrical section to allow gluing within the steel boss and two cones, which are truncated at $\pm 7.5 \times 10^{-2}$ m, as measured from the centre. Stress calculations show three points of high stress concentration. The first and maximum point of stress is at the mid-point of the arm and given by the equation:

$$S_{max} = \frac{\rho \omega^2}{a^2} \left[\frac{a^2 z^2}{2} + \frac{m}{4} [R^4 - z^4] + \frac{2cm}{3} [R^3 - z^3] + \frac{c^2}{2} [R^2 - z^2] \right] \qquad (2.6)$$

where $m = \frac{b - a}{R - z}$ and $c = \frac{Ra - zb}{R - z}$

The second and third points at which large stresses occur are at $\pm 2.87 \times 10^{-2}$ m from the centre. This corresponds to the point of maximum stress for a cone, which is a third of the height from the base. However, as the arm is a truncated cone, this moves the point of maximum

Figure 2.2

Rotor arm stress as a function of distance from centre of rotation.

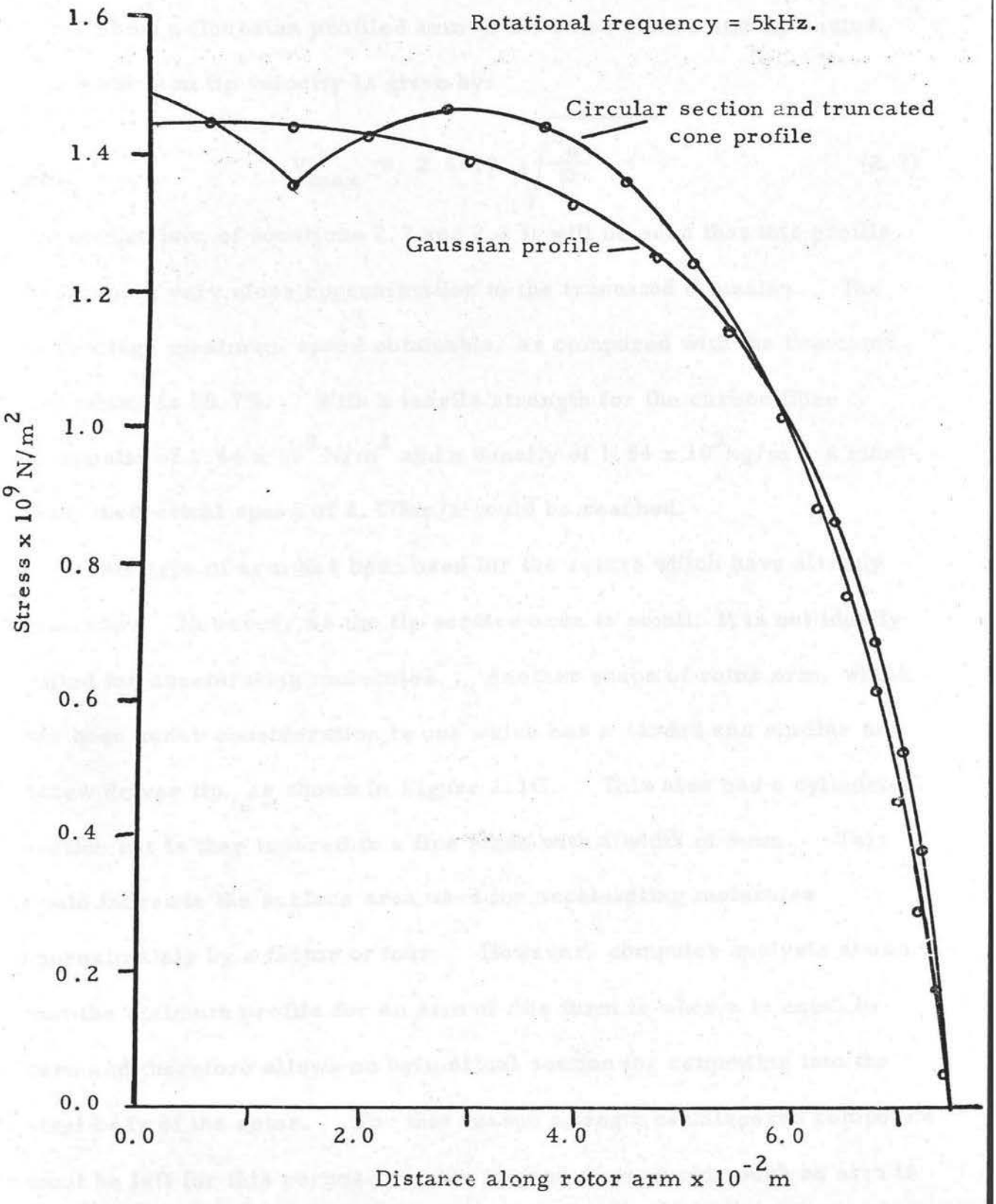

stress from 3.19×10^{-2}m to the points nearer the centre. The ratio of the stress levels gives 1.0124, thus making the centre point the most likely point for a fracture to occur. Figure 2.2 shows the curve of stress as a function of the radius from the centre of the arm. The other curve show a Gaussian profiled arm of the same centre and tip radius. The maximum tip velocity is given by:

$$V_{max} = 2.4019 \sqrt{\frac{S_o}{\rho}} \qquad (2.7)$$

By comparison of equations 2.7 and 2.2 it will be seen that this profile produces a very close approximation to the truncated Gaussian. The percentage maximum speed obtainable, as compared with the truncated Gaussian, is 98.7%. With a tensile strength for the carbon fibre composite of 1.64×10^9 N/m^2 and a density of 1.54×10^3kg/m^3, a maximum theoretical speed of 2.47km/s could be reached.

This type of arm has been used for the rotors which have already been run. However, as the tip surface area is small, it is not ideally suited for accelerating molecules. Another shape of rotor arm, which has been under consideration is one which has a bladed end similar to a screw driver tip, as shown in Figure 2.1C. This also has a cylindrical section but is then tapered to a fine blade with a width of 4mm. This would increase the surface area used for accelerating molecules approximately by a factor of four. However, computer analysis shows that the optimum profile for an arm of this form is when z is equal to zero and therefore allows no cylindrical section for cementing into the steel body of the rotor. For this reason a length of untapered composite must be left for this purpose. One method of producing such an arm is

Figure 2.3 Rotor arm stress as a function of distance from centre of rotation.

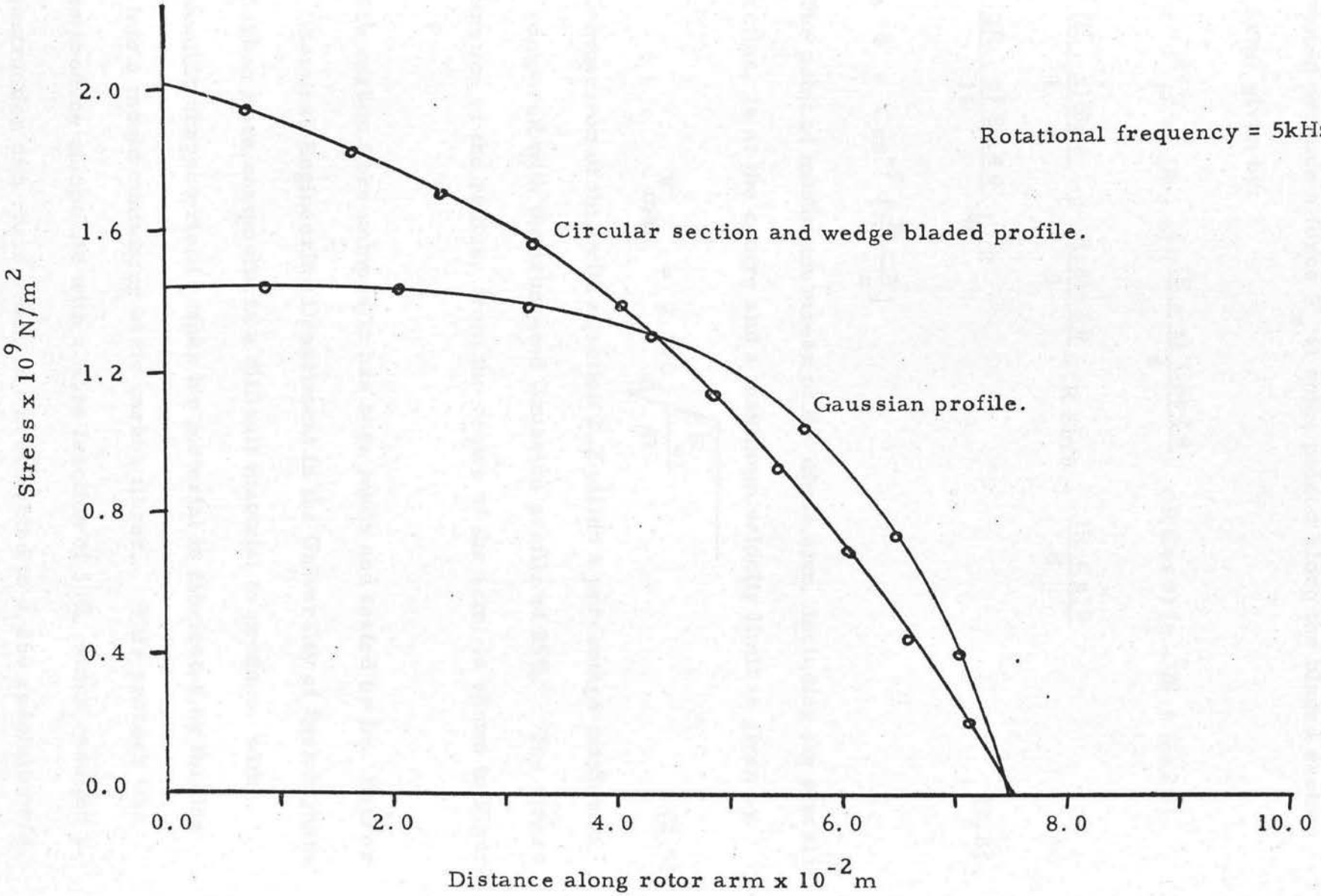

to take a length of 4mm diameter composite rod and grind a blade onto both ends. This would result in a profile which, if spun about the short axis, would produce a force F_x at some point x along the bladed section of the arm, given by:

$$F_x = \omega^2 \rho a^2 (R - z)[(\frac{(R - z)\,\mathrm{Cos}\,2\theta}{4} - R\,\mathrm{Cos}\,\theta)(\pi - 2\theta + \mathrm{Sin}\,2\theta)$$

$$+ \frac{(R - z)\,\mathrm{Sin}\,\theta}{4} + \frac{R.\,\mathrm{Sin}\,3\theta}{3} - R\,\mathrm{Sin}\,\theta - \frac{(R - z)\,\theta}{4}$$

$$- \frac{(R - z)\,\mathrm{Sin}\,4\theta}{16}\,]_\theta^{\pi/2} \qquad (2.8)$$

where $\theta = \mathrm{Cos}^{-1}\,[\frac{R - x}{R - z}]$

The point of maximum stress of the whole arm, including the circular rod section, is at the centre and a maximum velocity limit is given by:

$$V_{max} = 2.070\sqrt{\frac{S_o}{\rho}} \qquad (2.9)$$

Comparison of this with equation 2.2 yields a percentage maximum speed compared with the truncated Gaussian profile of 85%. The stress as a function of the radius, from the centre of the arm, is shown in Figure 2.3.

The carbon fibre composite has been made and tested by Dr. Barker of the Chemical Engineering Department in the University of Birmingham.

Carbon fibre composite is a difficult material to produce, with reproducible characteristics when the material is fabricated by forcing resin into a mould containing basic carbon fibres. This process was used to produce composite with a fibre fraction of 50%, which resulted in the construction of a rotor which was accelerated to 4,250 revolutions/s.

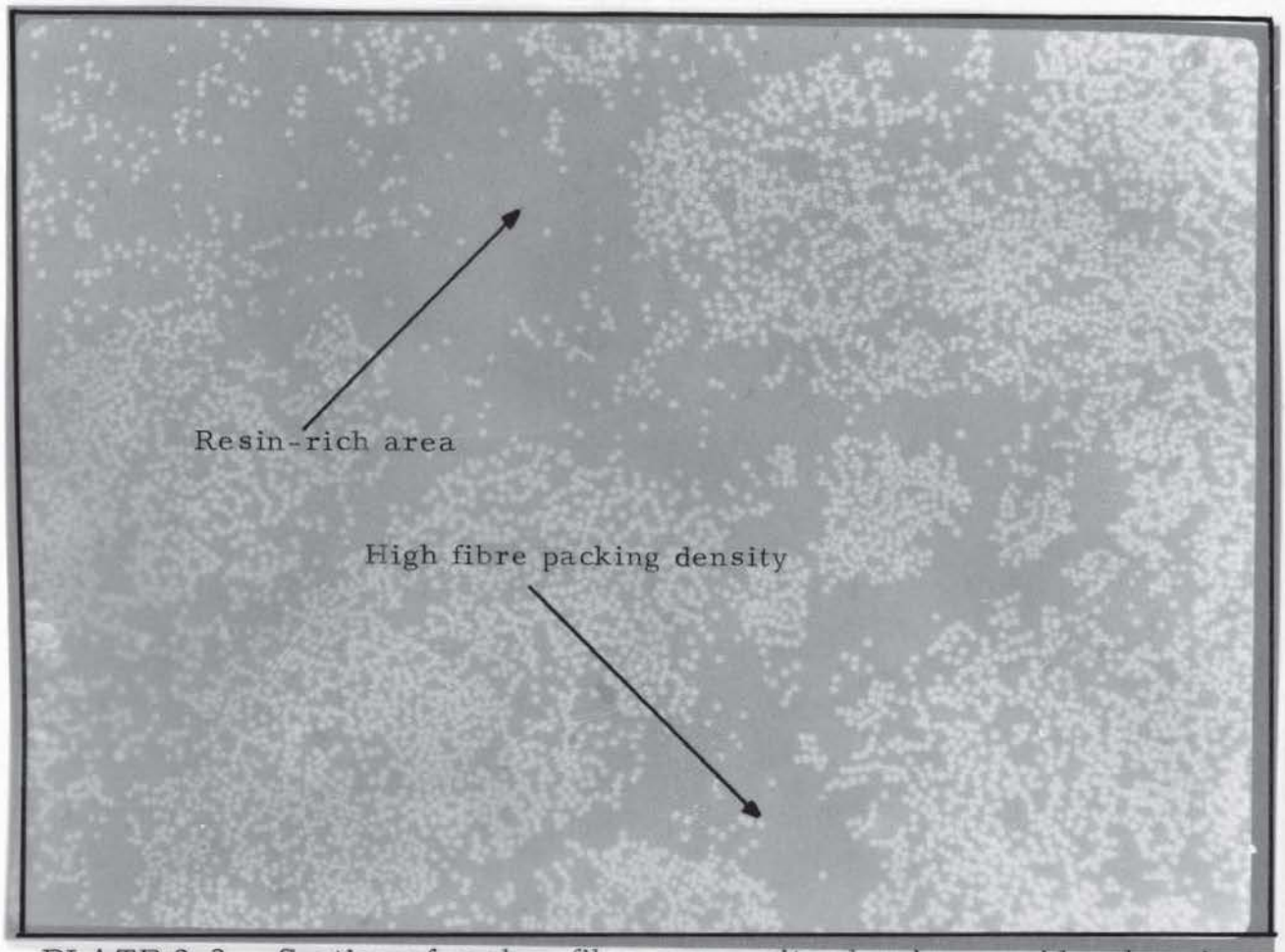

PLATE 2.2 Section of carbon fibre composite showing a void and resin-rich areas.

Courtesy of Chemical Engineering Department, University of Birmingham.

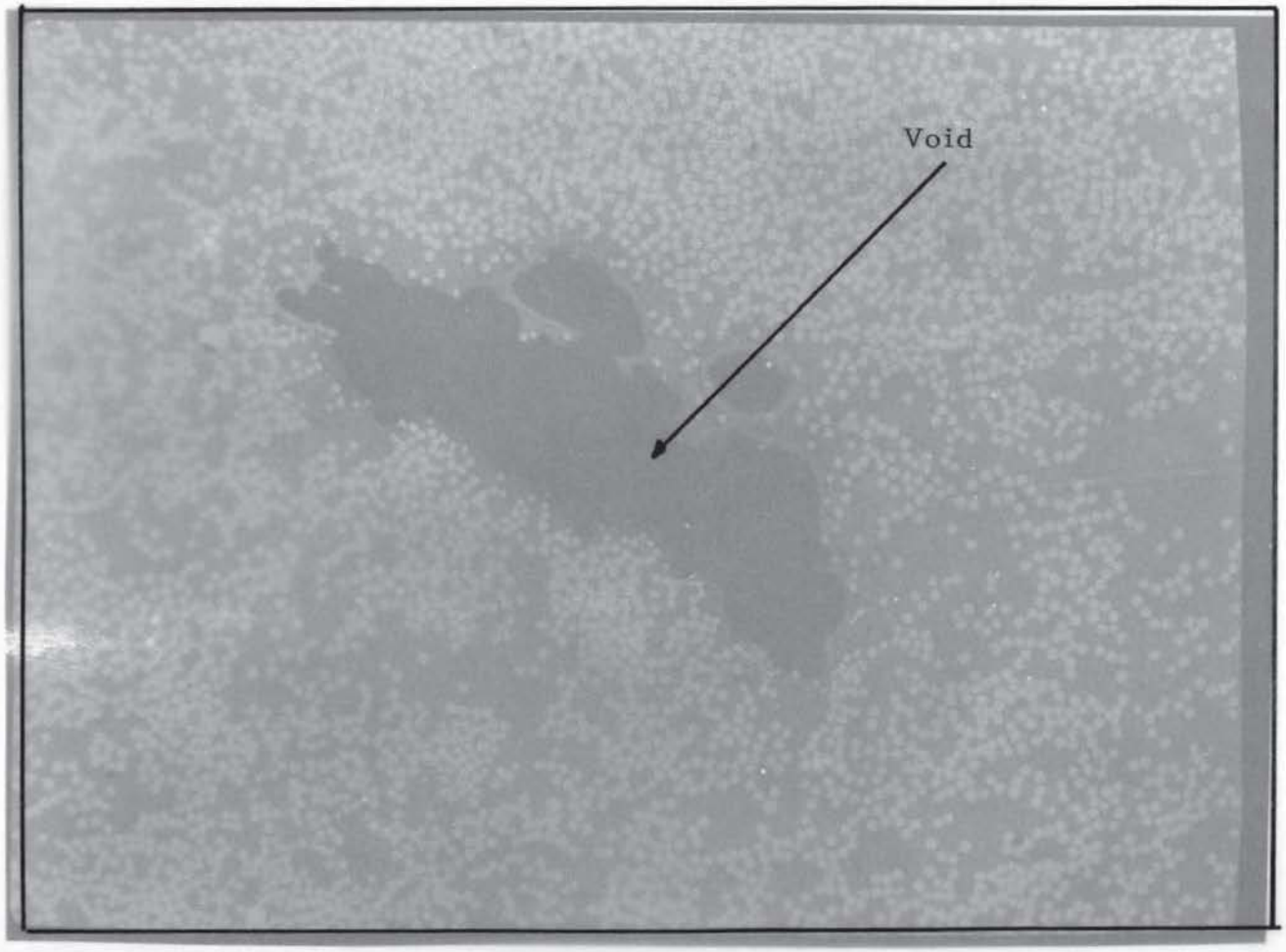

and produced a tip velocity of 2km/s. However, attempts to increase the volume fraction failed by this method, as shown in Plate 2.2. The upper plate shows a section of carbon fibre composite which has bad fibre packing and also large resin-rich areas, which would substantially reduce the strength. The lower plate shows a void in the material where there is an absence of fibre and resin. These flaws in the composite are quite typical of this type of process. Plate 2.3 shows the results of tensile fracturing of the material.

New material, called Fibredux 914C prepreg., is now being used for the manufacture of the composite. This material is in the form of sheets of carbon fibres surrounded by resin, which has not been cured. The sheets are laid one on top of the other such that all the fibres have the same orientation. An autoclave applies heat and pressure to laminate the sheets. The results have been very successful so far with fibre fractions of 60% and tensile strength of $1.5\,GN/m^2$.

2.4 Securing the Rotor Arms to the Body.

The rotor arms are held in the body of the rotor with epoxy resin glue, which is recommended for gluing metal to carbon. This joint between the rotor body and the rotor arms has produced the most problems in the production of a high speed rotor. Initially, the rotor arms were glued into the rotor body such that the geometric centre of the rotor body approximately coincided with the physical centre of the arms. However, as the composite is not isotropic, due to different fibre packing, the centre of mass of the arm is difficult to locate and place in such a way that it coincides with the axis of rotation of the boss. As the mass of the boss is much larger than that of the arms, the rotor boss can be assumed to

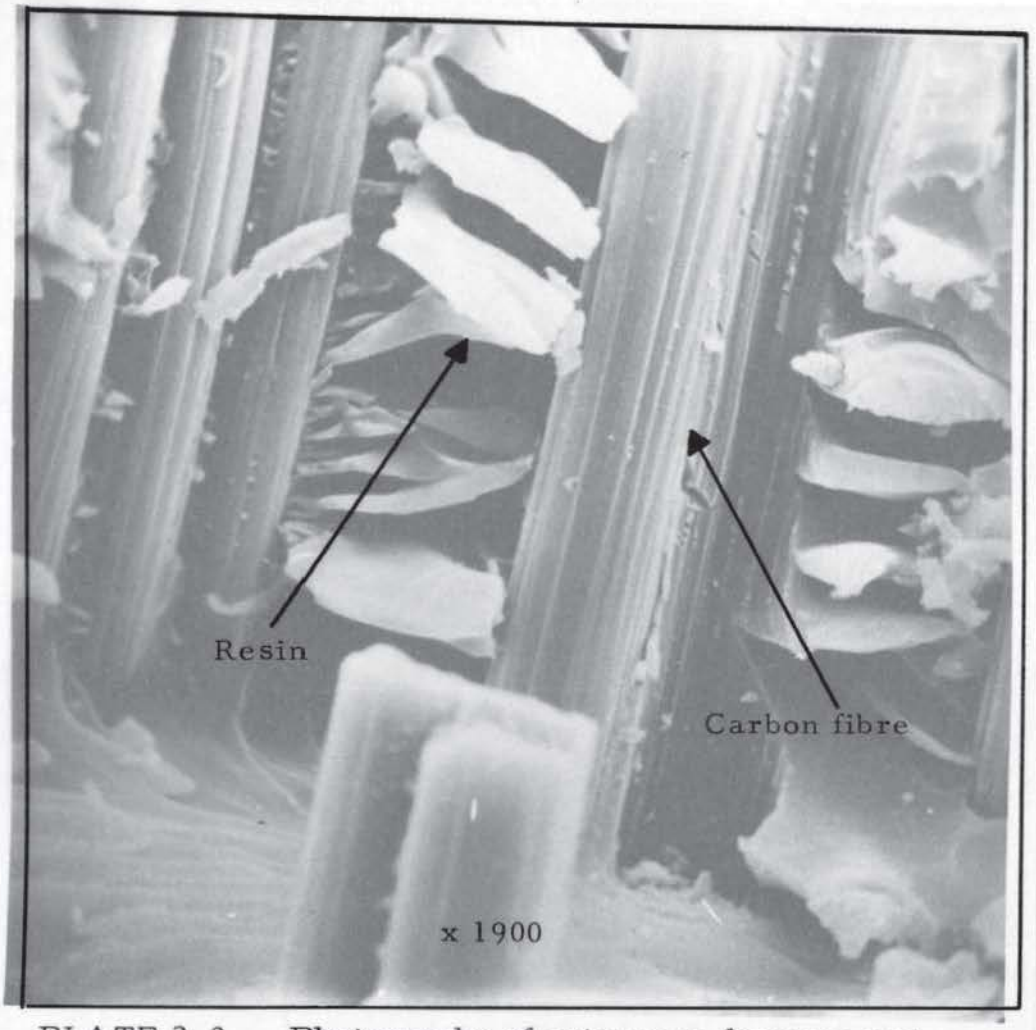

PLATE 2.3 Photographs of rotor arm fracture and general view of carbon fibre composite fracture under tensile loading.

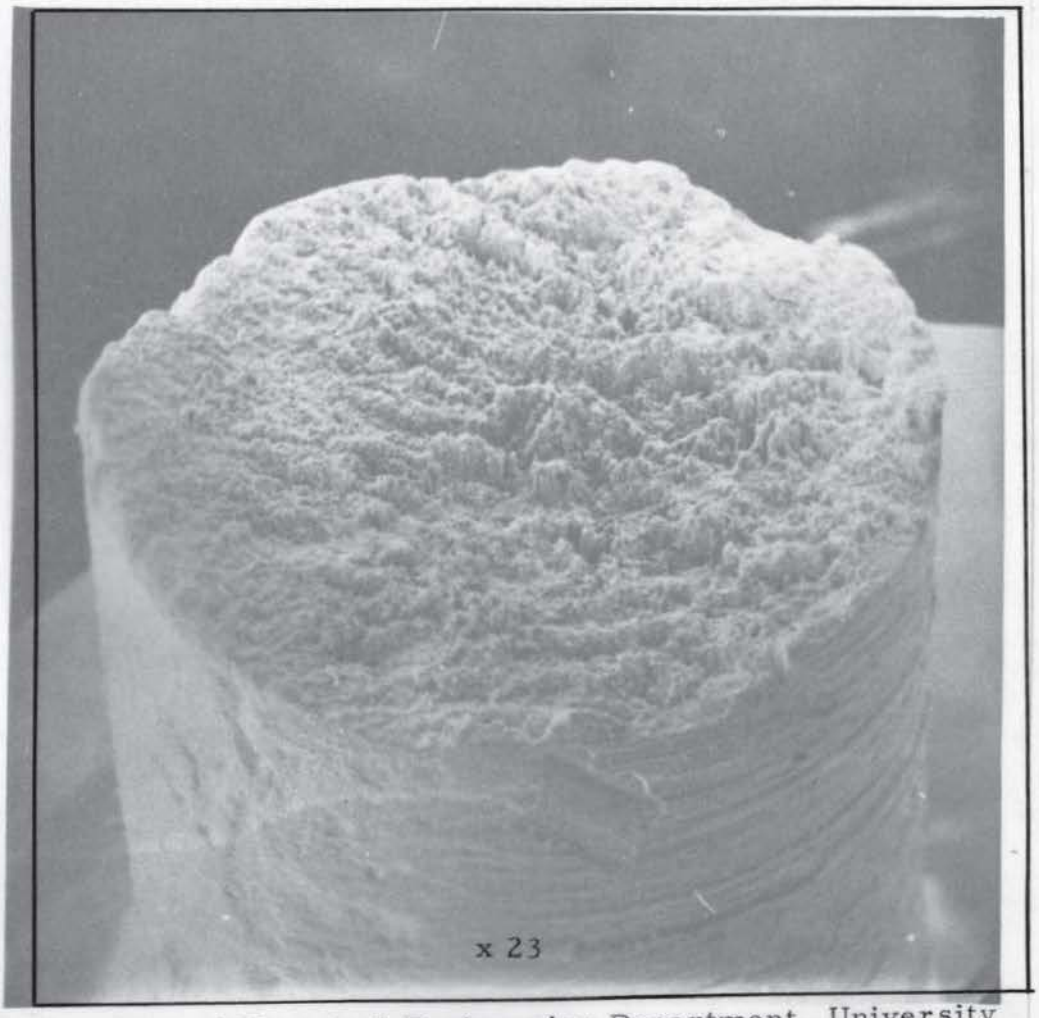

Courtesy of Chemical Engineering Department, University of Birmingham.

spin on an axis passing through its centre of mass. If the rotor arm has a mass of M_a and has a centre of mass separated by $\triangle R$ from the axis of rotation, then the force F_a required to hold the rotor arm within the rotor boss is given by:

$$F_a = \omega^2 \triangle R \cdot M_a \qquad (2.10)$$

Now, if the glued area of the arm to the boss is equal to A_g and the shear breaking stress of the glue is S_g, then the limiting linear speed of the tip of the rotor is given by:

$$V_{max} = R\sqrt{\frac{S_g \cdot A_g}{\triangle R \cdot M_a}} \qquad (2.11)$$

As the speed of the rotor arm is limited to 2.47km/s, due to longitudinal stress, this is the limit which can be used to define the maximum value of $\triangle R$. Measurement of shear glue strength for various samples gave a value for S_g of 1.16×10^7 N/m^2 compared with the manufacturer's value[4] of 1.38×10^7 N/m^2 for aluminium to carbon. The rotor arms had a mass of 1.54g with a glued area of 3.142×10^{-4} m^2 giving a maximum value for $\triangle R$ of 2mm. However, while measurements of the strength of the joint for a specimen at 20°C and 100°C showed little or no change in shear breaking stress. The effect, however, of cycling a joint under tension between these two temperature limits for six cycles showed a reduction of the breaking stress to a quarter of the un-cycled strength, this being probably due to differential thermal expansion. As this temperature cycling can take place when the rotor is in use, the balance factor of 2mm should be reduced to 0.5mm. Also the failure of the joint was not always a complete breakdown in strength, but the joint

had a tendency to slip and then lock again, this partial failure sometimes taking place at relatively low stress levels. As the increased displacement of the arm would increase the force exerted on the glued joint, the initial weakness of the joint would result in its complete failure, therefore making a good balance essential.

To achieve this degree of balance a method had to be found of dynamically balancing the rotor. One attempted method was to observe the motion of the slowly spinning rotor boss and then, by observation of the wobble when the rotor arm was in place, it could be moved until the wobble was minimised. This was detected by using the wobble to modulate the intensity of a laser beam grazing the edge of the body, but this method proved to be too insensitive. A method devised by Professor Moon and refined by the author proved most satisfactory and produced a degree of balance to less than 0.1mm. The method employed two nylon collars fitted around the rotor arms in such a way as to prevent the unglued arms from slipping out of the rotor body. The collars were set such that the rotor arms had a small amount of play within the boss and were positioned so that the physical centre of the arms roughly corresponded to the centre of the rotor boss. With one of the collars touching the rotor body, the rotor was spun to 100Hz and then brought back to rest. The collar was then observed to see if it still touched the rotor body; if it did, the shaft was pushed to put the other collar against the body and the procedure repeated. If both collars did not move from the position to which they had been set, prior to spinning the rotor, the space between the collars was reduced. If the shaft moved with one collar against the body, but not when the other collar was placed against the body, both

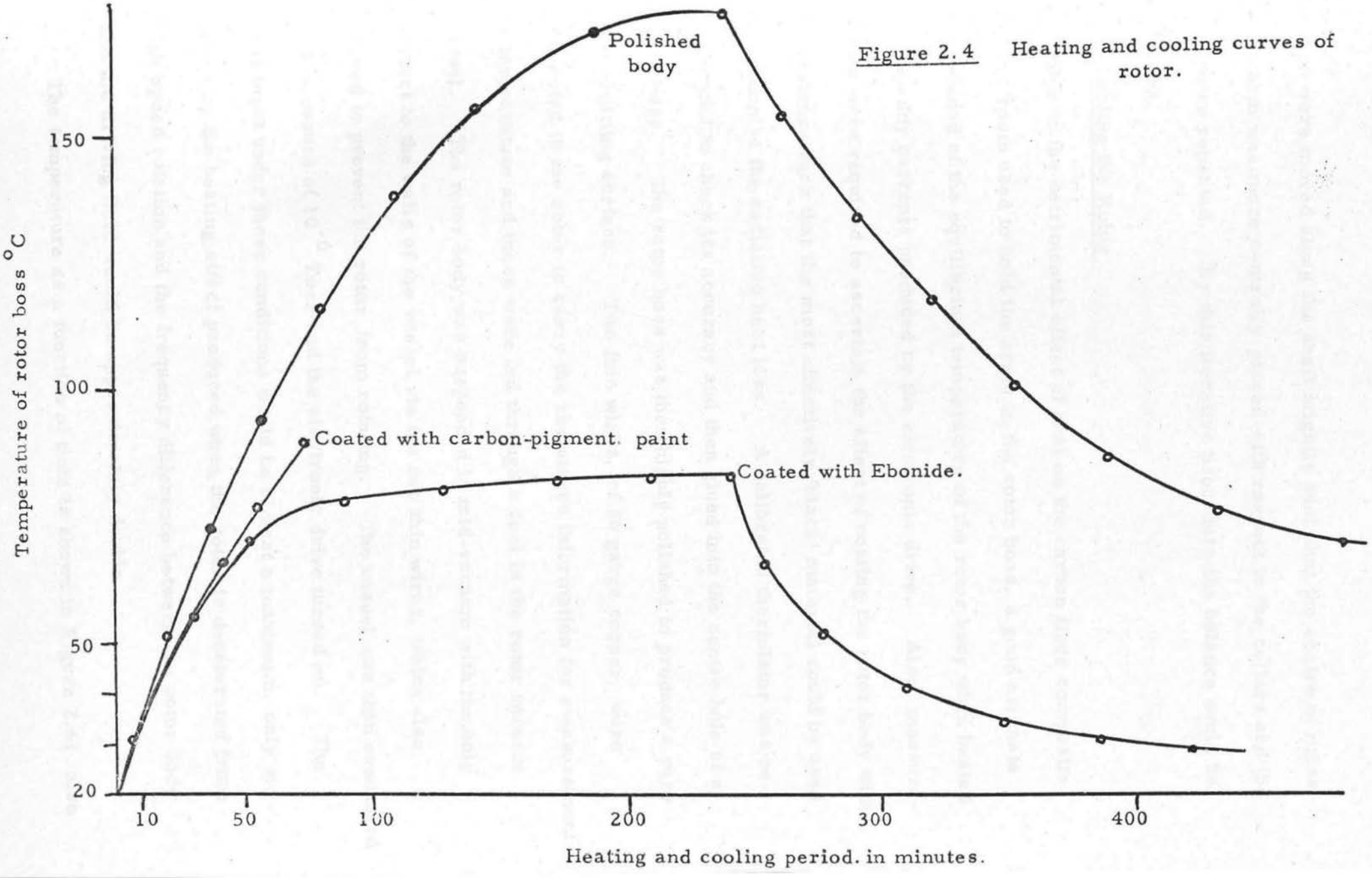

Figure 2.4 Heating and cooling curves of rotor.

collars were moved along the shaft slightly such that the centre of mass of the arm was more centrally placed with respect to the collars and the tests were repeated. By this iterative procedure the balance could be achieved.

2.5 Cooling the Rotor

Due to the detrimental effect of heat on the carbon fibre composite and the resin used to hold the arms in the rotor boss, a good estimate was needed of the equilibrium temperature of the rotor body when heated by the eddy currents produced by the electronic drive. Also, measurements were required to ascertain the effect of coating the rotor body with a substance such that the most effectively 'black' material could be used to maximise the radiative heat loss. A calibrated thermistor was re-calibrated to check its accuracy and then glued into the centre hole of a rotor boss. The rotor boss was then highly polished to produce a very poor emitting surface. Two fine wires, of 36 gauge copper, were connected to the rotor to carry the resistance information for measurement of temperature and these were fed through a seal in the rotor vacuum vessel. The rotor body was suspended in mid-vacuum with the only contact to the walls of the vessel via the two thin wires, which also served to prevent the rotor from rotating. The vessel was then evacuated to a pressure of 10^{-6} Torr and the electronic drive turned on. The heat input under these conditions would be almost a maximum, only surpassed by the heating effect produced when the rotor is decelerated from high speed rotation and the frequency difference between the rotor body and the driving field would be approximately double.

The temperature as a function of time is shown in Figure 2.4; also

the temperature/time function when the rotor body was covered with a black matt lacquer (Ebonide) and a carbon-pigmented, water-based, paint. From the curves the rotor can be seen to lose most heat by radiation when the surface is coated with Ebonide and, hence, the final rotors have the steel section coated with this lacquer.

CHAPTER III

THE PHYSICAL ARRANGEMENT OF THE SINGLE AND DOUBLE ROTOR UNITS

3.1 The Single Rotor Unit

The single rotor unit is shown in Plates 3.1 and 3.2 This unit is much simpler than the double unit as it is used for balancing and testing rotors to high speed before possible transfer into the double unit.

It consists of a glass rotor vessel which stands on top of a 2-inch diffusion pump, the vacuum seal between the two being achieved using an O-ring. The rotor vessel (Figure 3.1) is made from a two litre spherical glass flask, which has a 120mm flange moulded into the top and a 150mm flange at the bottom, on which it stands. The upper flange is used to support the lifting solenoid which is housed in a glass well filled with oil. The removal of the lifting magnet allows free access to the interior of the vessel. It is through this hole that the rotor is put into the vessel and also entry and adjustment is made of the rotor damping table. This table is supported by a T-piece, glass arrangement, which is moulded into the cylindrical sides of the port leading to the lower flange. The rotor is positioned such that the plane of rotation is approximately half way up the spherical section of the vessel, hence producing maximum clearance, this being approximately 5mm.

The description of the rotor suspension and optical arrangement is given in Chapter IV. The optical arrangement mainly comprises the prisms, lamp and detectors, which are housed inside brass shields to reduce r-f pick-up from the drive coils and also to add protection in the event of a rotor smash.

Figure 3.1 Rotor vessel assembly.

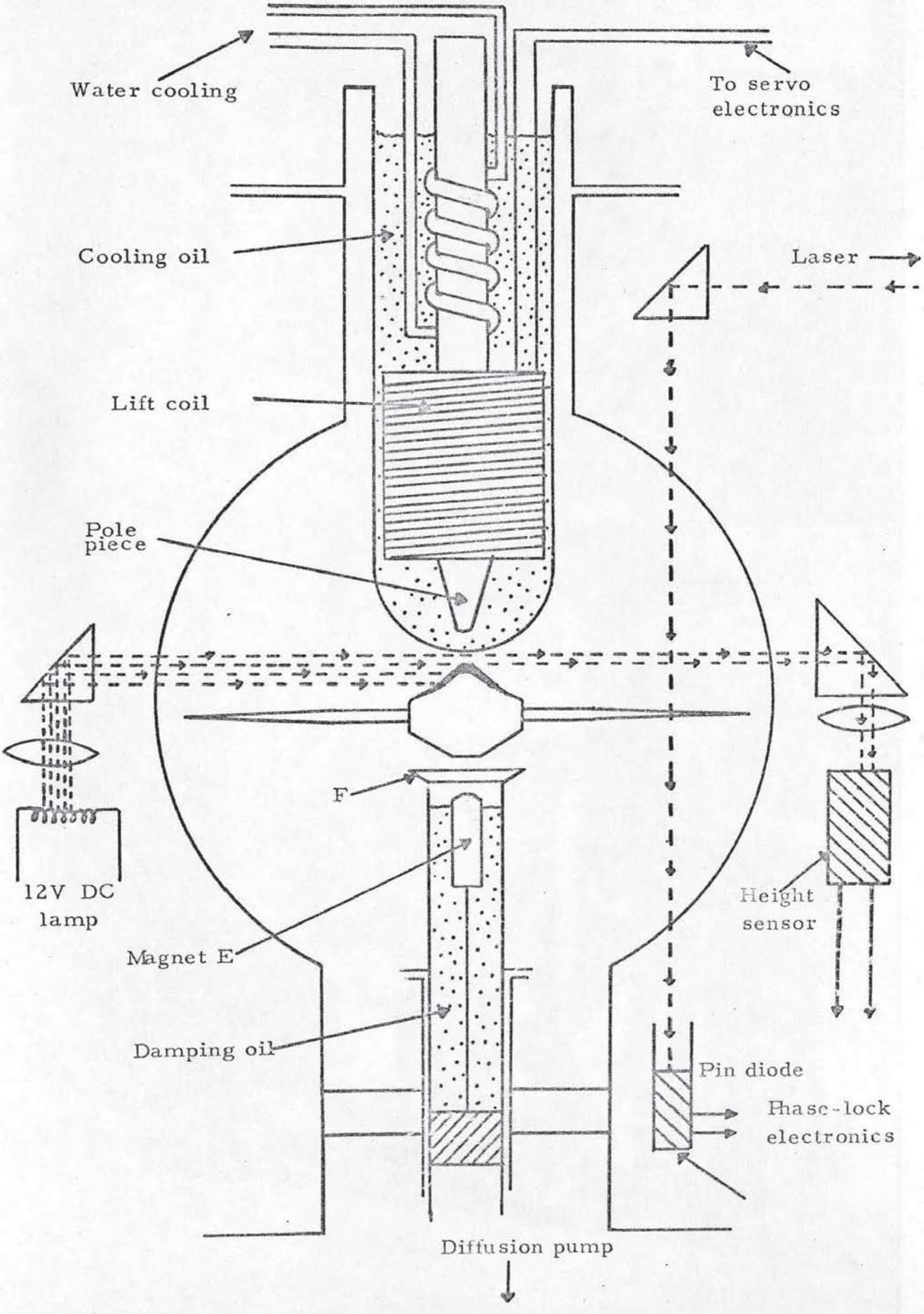

PLATE 3.3 Single rotor unit without rotor vessel.

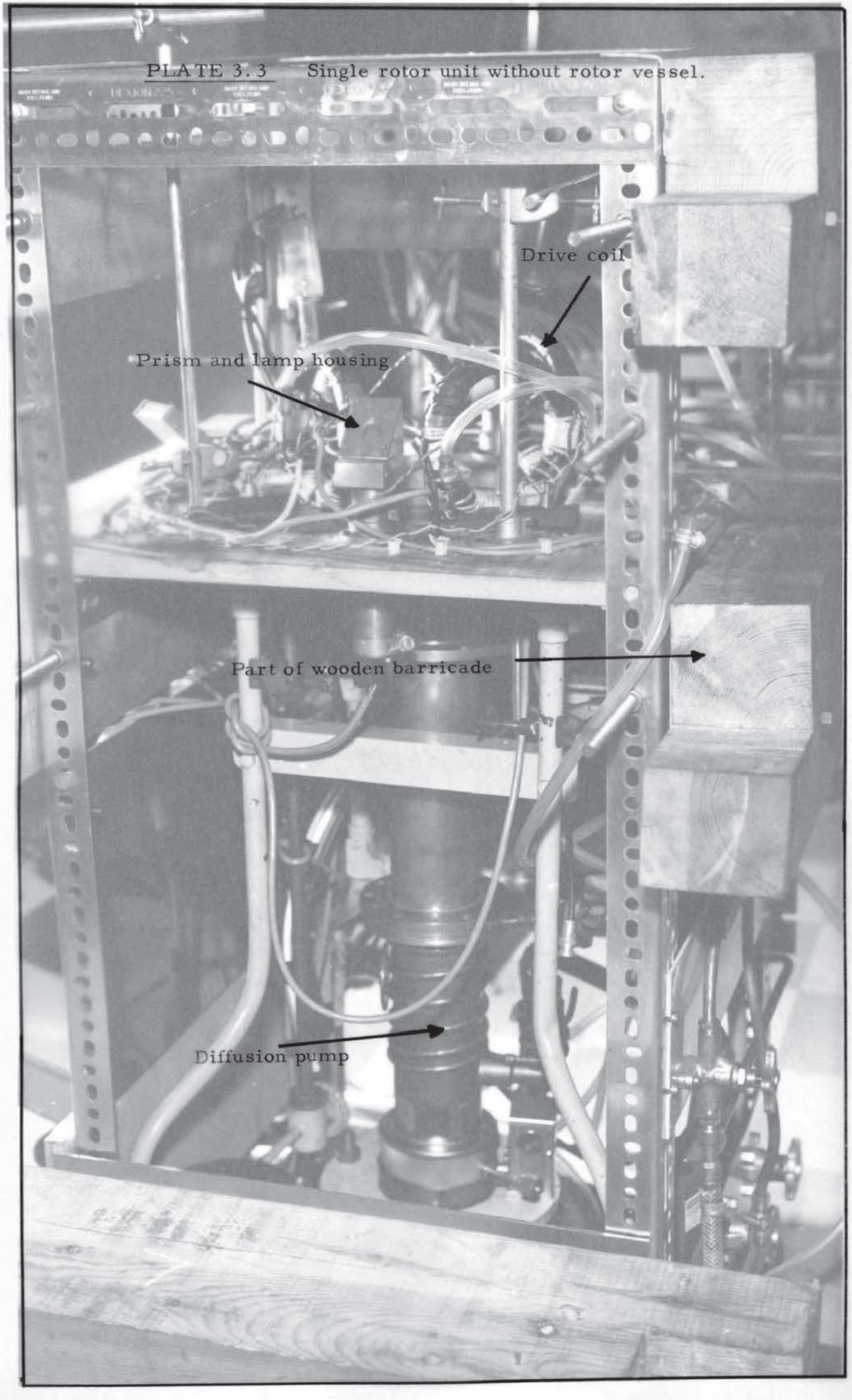

A periscope and telescope system was used to observe the rotor during high-speed running. This allowed safe observation of any low frequency oscillation of the rotor or orbital motion.

In the side of the vessel was placed a small cone joint which was used to attach an ionisation gauge to measure the vessel pressure. The typical pressure obtainable in the vessel is 5×10^{-7} Torr. The cone joint port also serves to allow positioning of the rotor arms when balancing, prior to final rotor assembly.

Surrounding the upper section of the rotor unit are 4-inch wooden blocks to provide a protective barricade in the event of a high-speed rotor smash. The barricade is necessary not only to prevent the escape of the steel rotor boss but also to stop particles of glass and carbon fibres. Wood was used as this would dissipate the energy of the particles by allowing them to penetrate or bounce inelastically. The rotor possesses approximately 3kJ of kinetic energy when running at full speed. A wooden top covers the unit and protects the laser, which is mounted above this and used for rotational speed measurement.

The backing pump is connected to the diffusion pump by means of a 1-inch copper pipe with a flexible coupling to minimise the transmission of vibration caused by the rotary pump. The ionisation gauge control unit is connected to the gauge head via a relay, which is held 'on' when there is current flowing in the heater circuit of the gauge. This relay allows power to flow into the backing pump and the diffusion pump. In the event of a rise in pressure within the vacuum chamber, the current to the gauge heater is turned off by the control unit and this releases the relay, which in turn closes the magnetic isolation valve on the backing

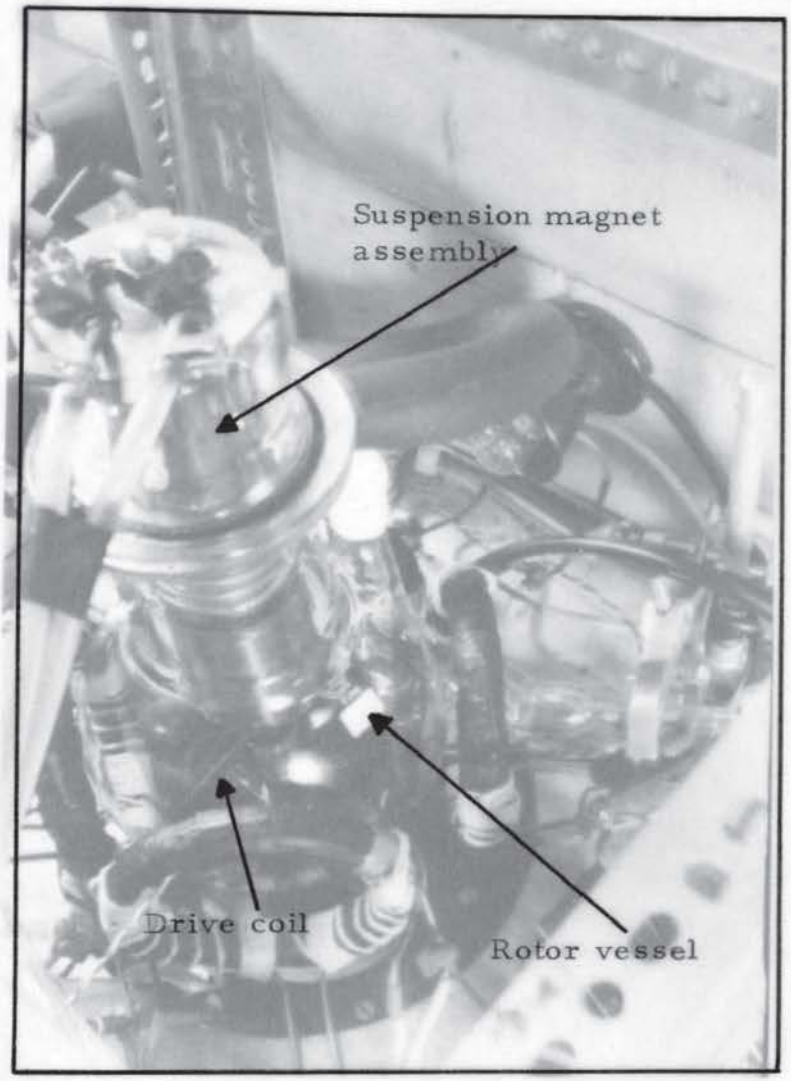

PLATE 3.2 Single rotor unit.

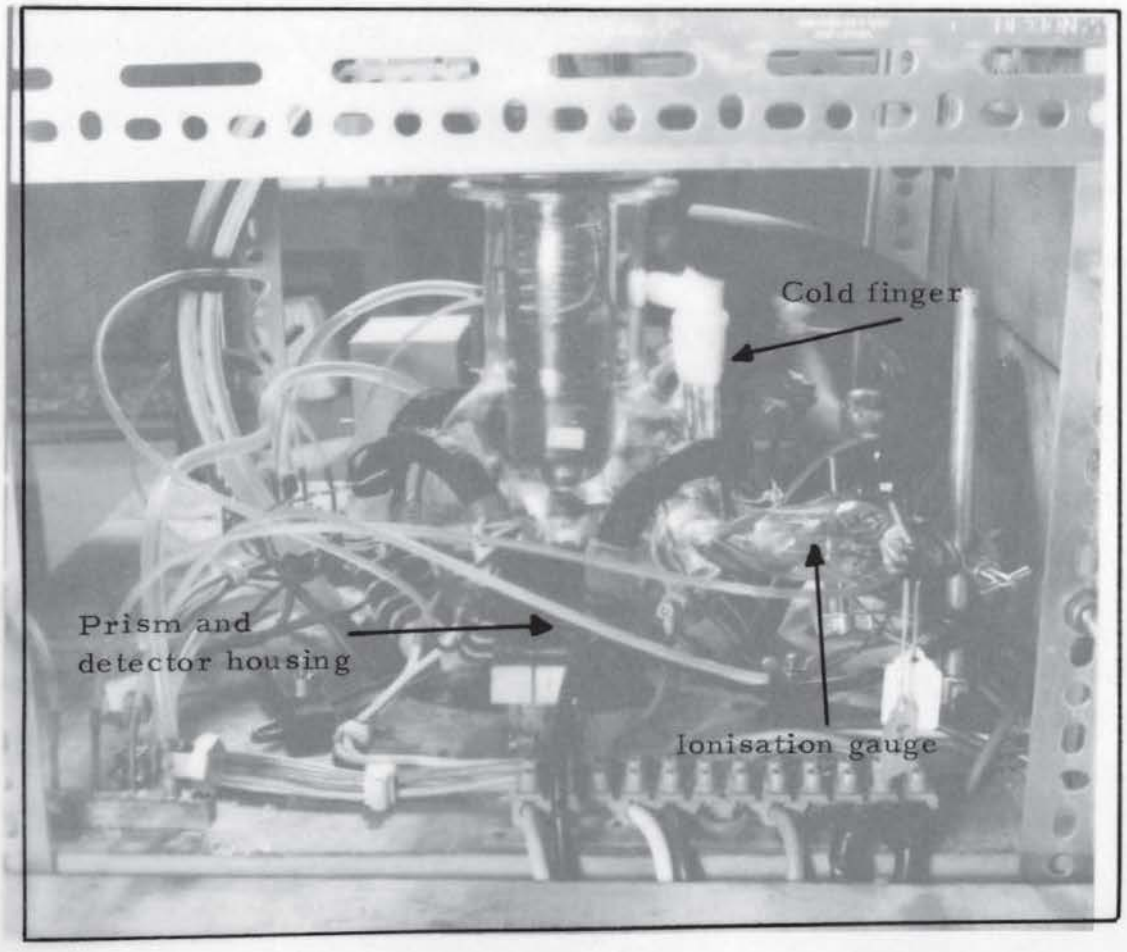

pump. A very rapid increase in pressure occurs when the rotor has crashed and so the shutting of the valve reduces the amount of damage to the backing pump. Under certain conditions it is possible for the heater in the gauge head to burn out before the control unit has turned off the current, but as this also releases the relay, it ensures that the pumps are turned off as soon as possible after the smash. A switch is used to override this arrangement when protection is not required. Unfortunately this does not protect the diffusion pump, nor the pumping line, and these are contaminated with powdered glass and carbon fibre fragments.

3.2 The Double Rotor Unit.

The double rotor unit is shown in Plate 3.3. This unit was designed to run two rotors in a vessel arrangement such that molecules, accelerated by each rotor, could be made to collide. As chemical reactions produced, using the rotors, would require much larger pumping speeds than the simple pumping system used, it was proposed to attempt an optical excitation experiment. As a photo-multiplier could be used for observing the resonance, this was much simpler than the detection of chemical reaction products, which would involve a mass spectrometer and hence an added complication to the vacuum system. A convenient resonance line exists in mercury and so it was decided to produce two colliding beams of mercury and detect the photons produced. As the resonance is in the ultra-violet part of the spectrum, the photo-multiplier, P.M., used had to have a quartz window, so it was decided to use an EMI.9558QA, specially selected for optimum quantum efficiency at 250 nm. The P.M. is optically coupled to the collision volume, using a spectrosil light pipe, 150mm long and 40mm diameter. This is

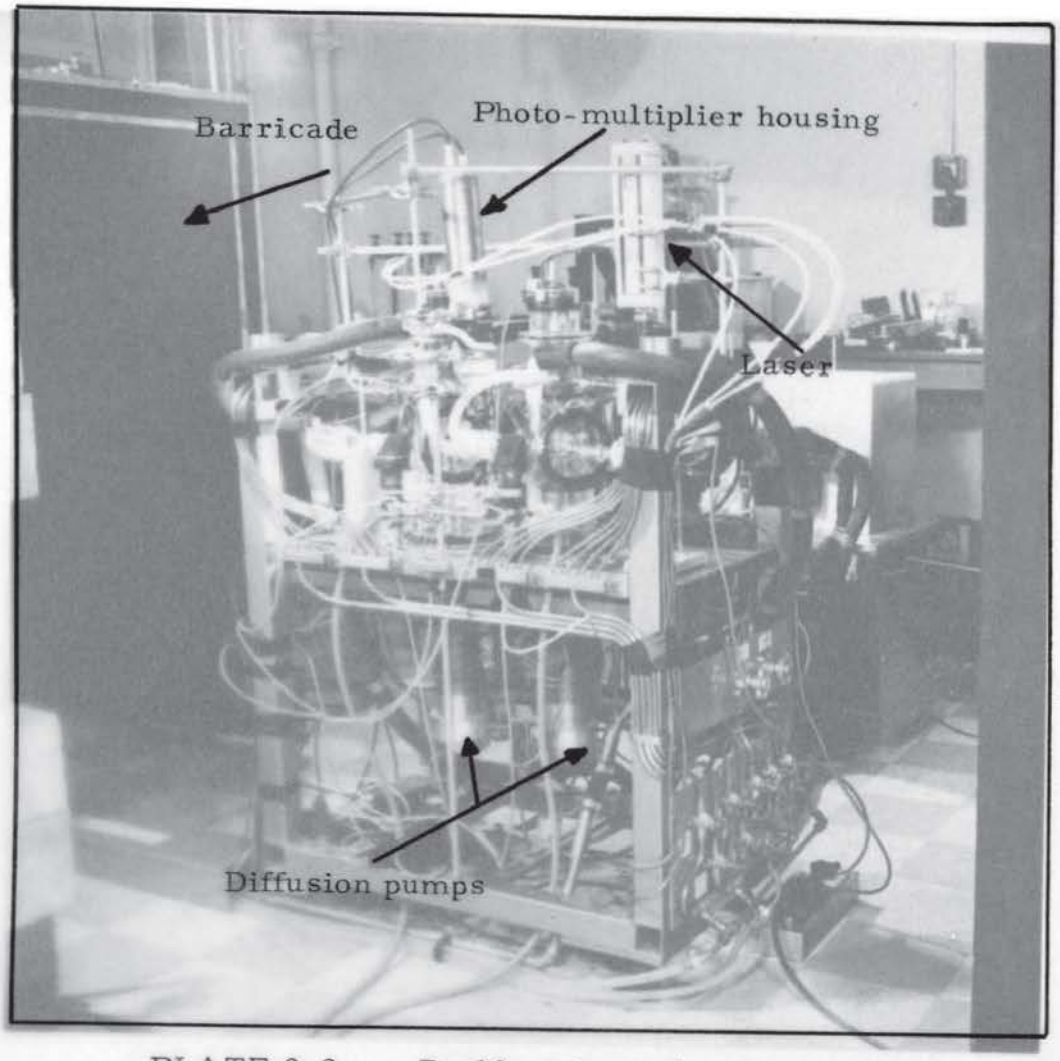

PLATE 3.3 Double rotor unit

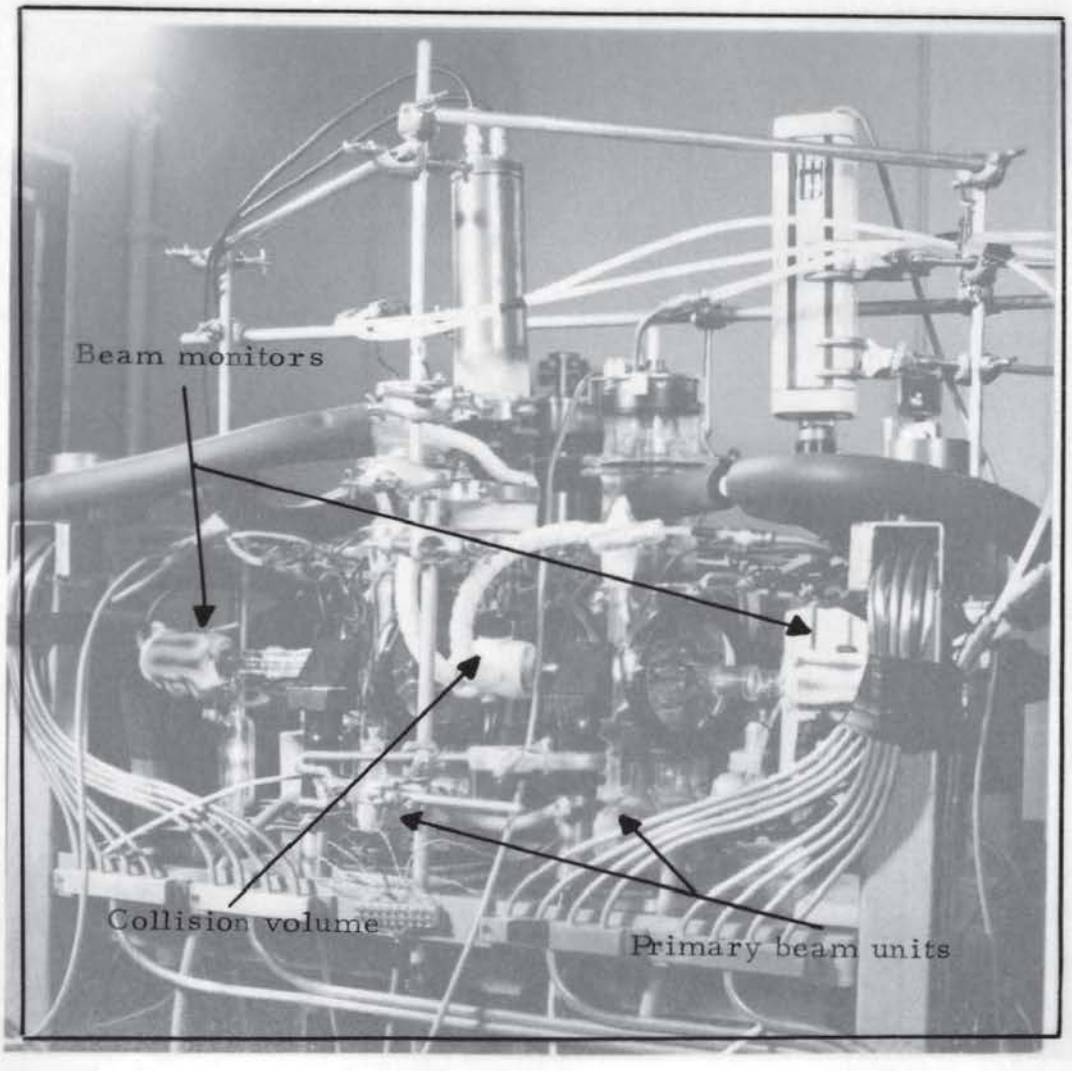

joined to the collision volume by means of an O-ring which allows a small degree of flexibility. The upper half of the light pipe and the P.M. are housed in a brass and steel unit, shown in Plate 3.3. This provides cooling for the cathode of the P.M. to reduce noise levels, and also electrostatic and magnetic screening. The cathode is also screened with mu-metal. A PTFE sleeve is used to provide protection for the light pipe within the P.M. housing and also to prevent excess water vapour from condensing inside it near the cooled cathode.

The double rotor unit is built on a steel frame, which has two two-inch oil diffusion pumps, type EO2, mounted beneath the rotor vessels and capable of providing pumping speeds of 200 litres/s. These are pumped by the rotary piston backing pump used for the single apparatus, producing a pumping speed of 170 litres/min., the combination of which produces vessel pressures of typically 10^{-6} Torr.

The two rotor vessels are basically the same as the one used in the single apparatus with the exception that there are more ports. The positioning of the ports is shown in Figure 3.2 and these are used to allow insertion of various components necessary for colliding beams experiments.

The glass tube, which constitutes the collision volume, is connected to each vessel by means of ball and socket joints, these providing some degree of flexibility. The collision volume can be seen in Plate 3.3 and is composed of a double-walled tube with a port and flange set perpendicular to the tube, on to which the light pipe connects, and opposite this a Woods horn to give a nearly black background to reduce the ambient noise level detected by the P.M. to a minimum. The cavity

Figure 3.2 Port arrangement of double rotor unit.

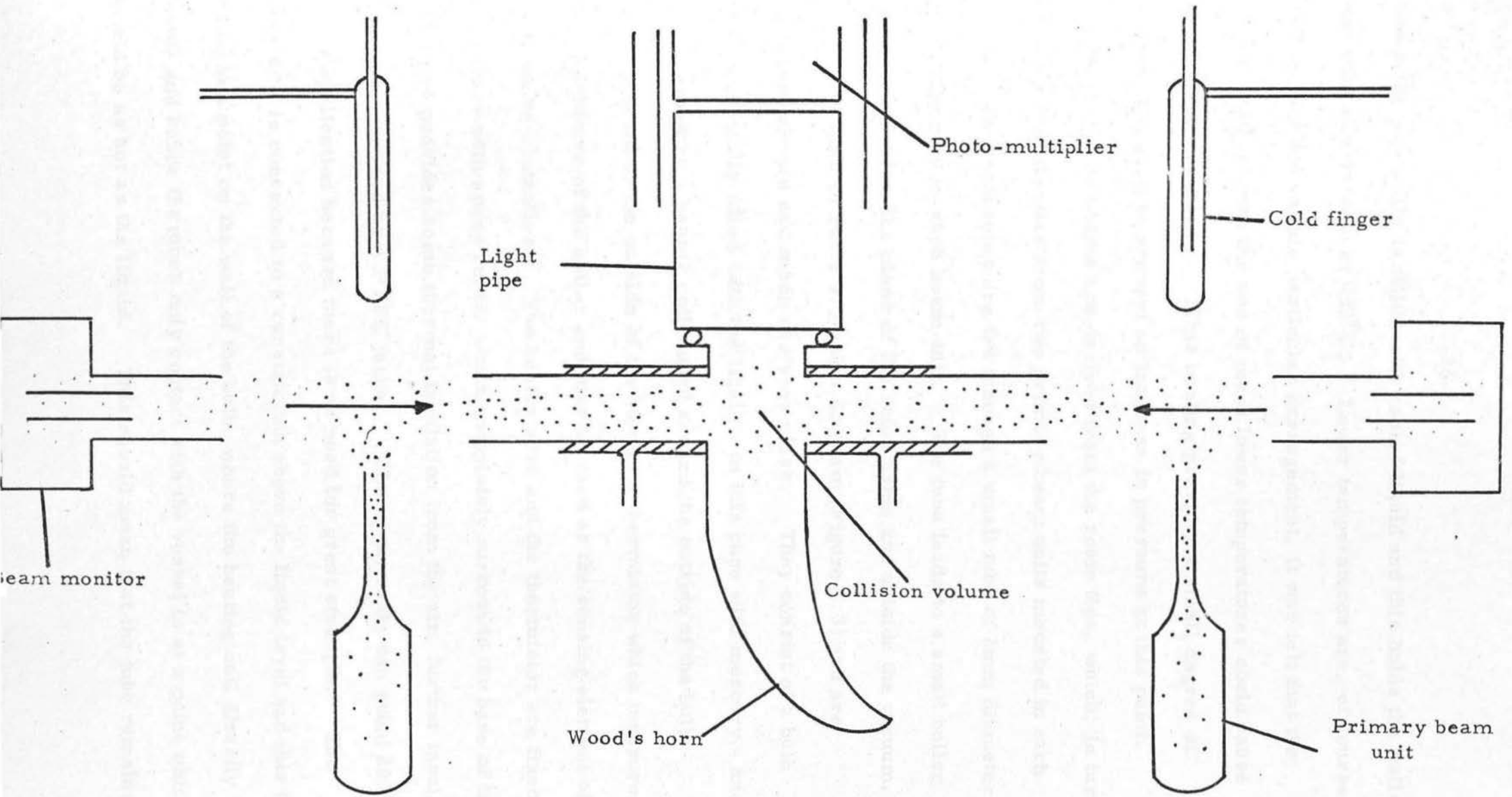

between the two walls is filled with cooled liquid and this holds the walls of the collision volume at -30°C. Lower temperatures are, of course, possible, but due to this particular arrangement, it was felt that the stress resulting from the use of much lower temperatures could cause failure of the glassware. This cooling provides a small degree of cryogenic pumping to prevent an increase in pressure at this point.

The mercury beams are derived from the rotor tips, which, in turn, collect their molecules from two primary beam units mounted in each vessel. The molecules are fed through a small tube of 2mm diameter, which originates in each beam unit. The tube leads to a small boiler, situated well below the plane of the rotor arms and outside the vacuum. These are shown in Plate 3.3 and a diagram (Figure 3.3) and are reasonably simple and made of Pyrex glass. They consist of a bulb which is partially filled with the liquid - in this case with mercury - and this is heated by a heater coil wound around the outside of the bulb. Also connected to the outside of the bulb is a thermistor which measures the temperature of the boiler and may be used as the sensing element of a temperature controller. The heater wire and the thermistor are fixed to the glass with epoxy resin, which completely surrounds the base of the boiler and provides some thermal insulation from the air, further insulation being provided by a PTFE jacket. The epoxy resin can stand 200°C in this application because there is no need for great strength. The glass tube is connected to a constriction above the liquid level and this is joined to a point on the wall of the bulb, where the heating coil directly heats, and hence the tube's only contact with the vessel is at a point which should be as hot as the liquid. This should mean that the tube remains

Figure 3.3

Primary beam unit.

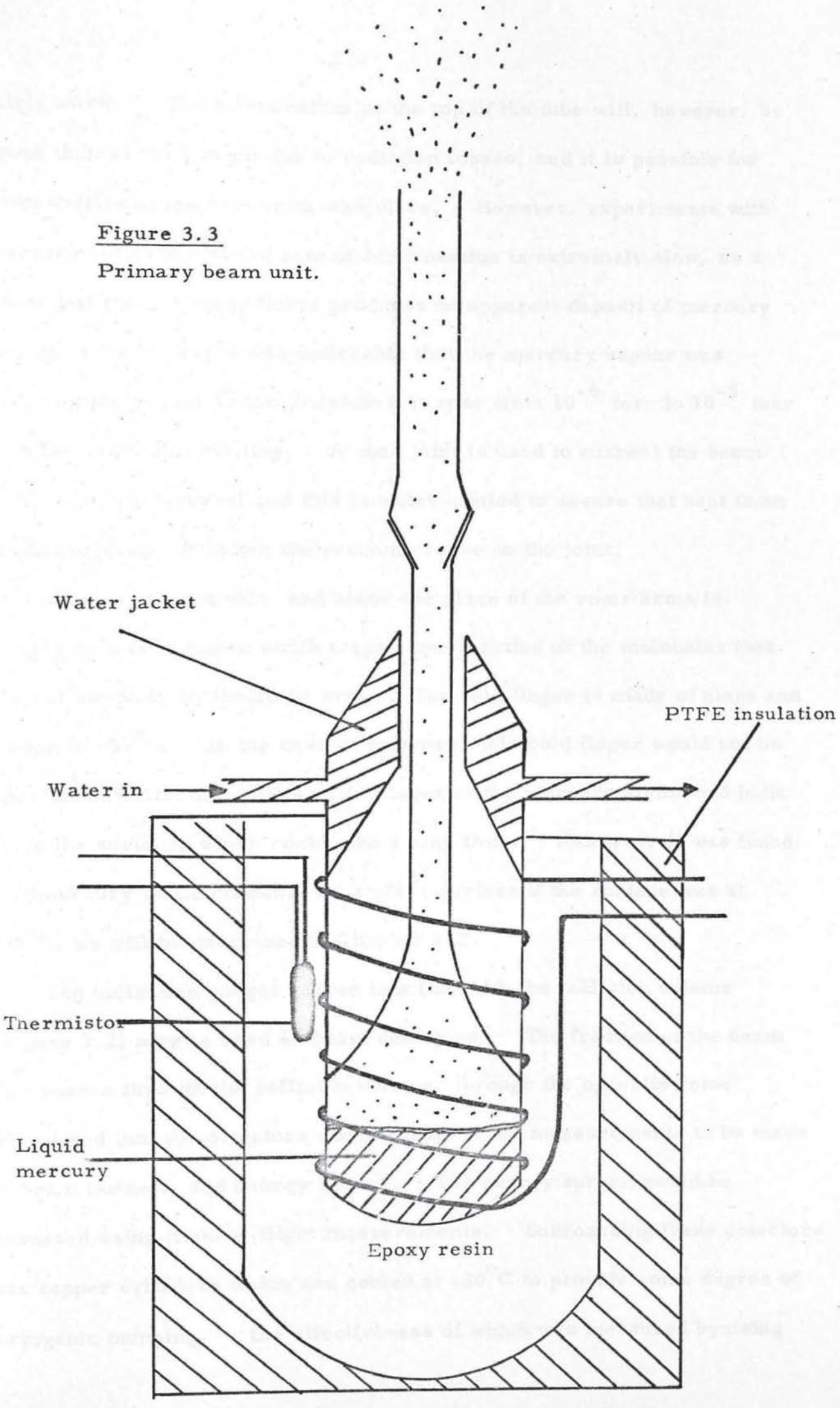

fairly warm. The temperature at the top of the tube will, however, be lower than at the bottom due to radiation losses, and it is possible for condensation of the vapour to take place. However, experiments with mercury indicate that the rate of condensation is extremely slow, as a beam unit run for many hours produces no apparent deposit of mercury onto the tube. Yet it was noticeable that the mercury vapour was reaching the vessel as the pressure in it rose from 10^{-6} torr to 10^{-5} torr with the beam unit running. A cone joint is used to connect the beam unit to the rotor vessel and this is water-cooled to ensure that heat from the boiler does not soften the vacuum grease on the joint.

Above the beam unit and above the plane of the rotor arms is positioned a cold finger which traps some fraction of the molecules that are not swept up by the rotor arm. The cold finger is made of glass and cooled to $-30^{\circ}C$. In the case of mercury, this cold finger would not be effective in collecting atoms until a layer of the mercury atoms had built up on the surface, which could take a long time. However, it was found that mercury would condense on a glass surface if the surface was at $-30^{\circ}C$, as will be described in Chapter VIII.

The ionisation gauges placed in a line with the collision volume (Figure 3.2) may be used as beam detectors. The fraction of the beam that passes through the collision volume, through the opposite rotor vessel and into the detectors would enable crude measurements to be made of beam intensity and energy spread. The energy spread would be assessed using time-of-flight measurements. Surrounding these detectors are copper cylinders which are cooled at $-30^{\circ}C$ to provide some degree of cryogenic pumping, the effectiveness of which was measured by using

the ionisation vacuum gauge unit to measure the vacuum in the detector with and without cooling. The results showed a factor of four increase in pressure when the gauge was not cooled. This metal cylinder also provides electrostatic screening, significantly reducing the noise level from the unit, when it is used with a current amplifier. The circuit used for the operation of the gauge as a beam monitor is described in Chapter VIII.

The laser beam is used, as in the single apparatus, for angular speed measurement, but the position of the beam is important in this case because the rotor's interception of the beam is used to give the in-line position of the rotor arm. In other words, the point in time when the long axis of the rotor arm is perpendicular to the axis of the collision volume. Adjustment of the position of the laser beam is achived using a beam splitter and prisms.

The cooling liquid used in the collision volume, etc., is produced by a small mobile refrigerator unit consisting of a Primary and Secondary cooling circuit. The primary cooling circuit utilises a standard compressor refrigeration unit using freon. This cools a copper coil fitted inside a 5 litre brass container used as a heat exchanger and well insulated from its surroundings by styrofoam. The secondary circuit uses ARCTON 113 as the coolant and this is pumped by a small chemical pump to the areas requiring cooling.

The temperature of the Arcton is held at $-30^{o}C$ by a thermostat fitted in the secondary circuit which controls the freon cooling circuit. The reason for using a heat exchanger instead of directly using the freon is that cooling is required within the glassware and, if a rotor smash were to break it, the freon would have to be replaced. The unit can

extract approximately 3kJ per second from the rotor vessel. The connections to the unit are made with normal rubber tubing with 'Armorflex' insulation to increase its efficiency. The drive coils are tied to the outside of the rotor vessels with nylon thread. This means that the coils are as close to the rotor body as possible and therefore the magnitude of the driving magnetic field at the centre is as large as possible. The coil separation is critical because the magnitude of the magnetic field at the centre of the vessel varies as the cube of the spacing and the drive torque is proportional to the square of the magnetic field.

The whole unit can be enclosed in a two-piece barricade, visible in the upper frame of Plate 3.3. This forms a large box in which the double rotor unit can be operated safely. The bottom of the box has a skirt, which may be lowered to form an almost light-tight box.

CHAPTER IV

ASSOCIATED CONTROL AND MONITORING ELECTRONICS.

4.1 The Rotor Suspension System.

The rotors are suspended in mid-vacuum using an electro-magnetic servo system. Complete magnetic suspension[5] is an attractive method of producing an axis about which the rotor can rotate and has been used very successfully[21] in the past. Magnetic support offers a simple method of producing a 'soft' bearing, enabling the rotor to spin about its centre of mass and alleviate the need for accurate balancing of the rotor body. The acceleration and deceleration of the rotor is accomplished using electro-magnetic induction, which produces only a small torque, but as the friction of the magnetic bearing is almost[6] non-existent, this is acceptable.

4.1A The physical arrangement of the suspension system.

The physical arrangement of the suspension system is shown in Figure 4.1. The rotor is suspended beneath an electro-magnet, the current feeding the coil being supplied by the servo electronics. The coil consists of 600 turns of 18 gauge, enamel-covered, copper wire wound on a plastic former, which is hollow and into which a soft iron core is placed. The end of the core is cone-shaped, so the magnetic field is concentrated to enable the rotor body to have point suspension. This produces the required divergent magnetic field, which provides the restoring force to centre the rotor, but in the absence of any damping, the rotor could swing or produce orbital motion. Damping for these is provided by the 'cornstalk'[7] arrangement, comprising the fixed magnet E,

Figure 4.1 Rotor vessel assembly.

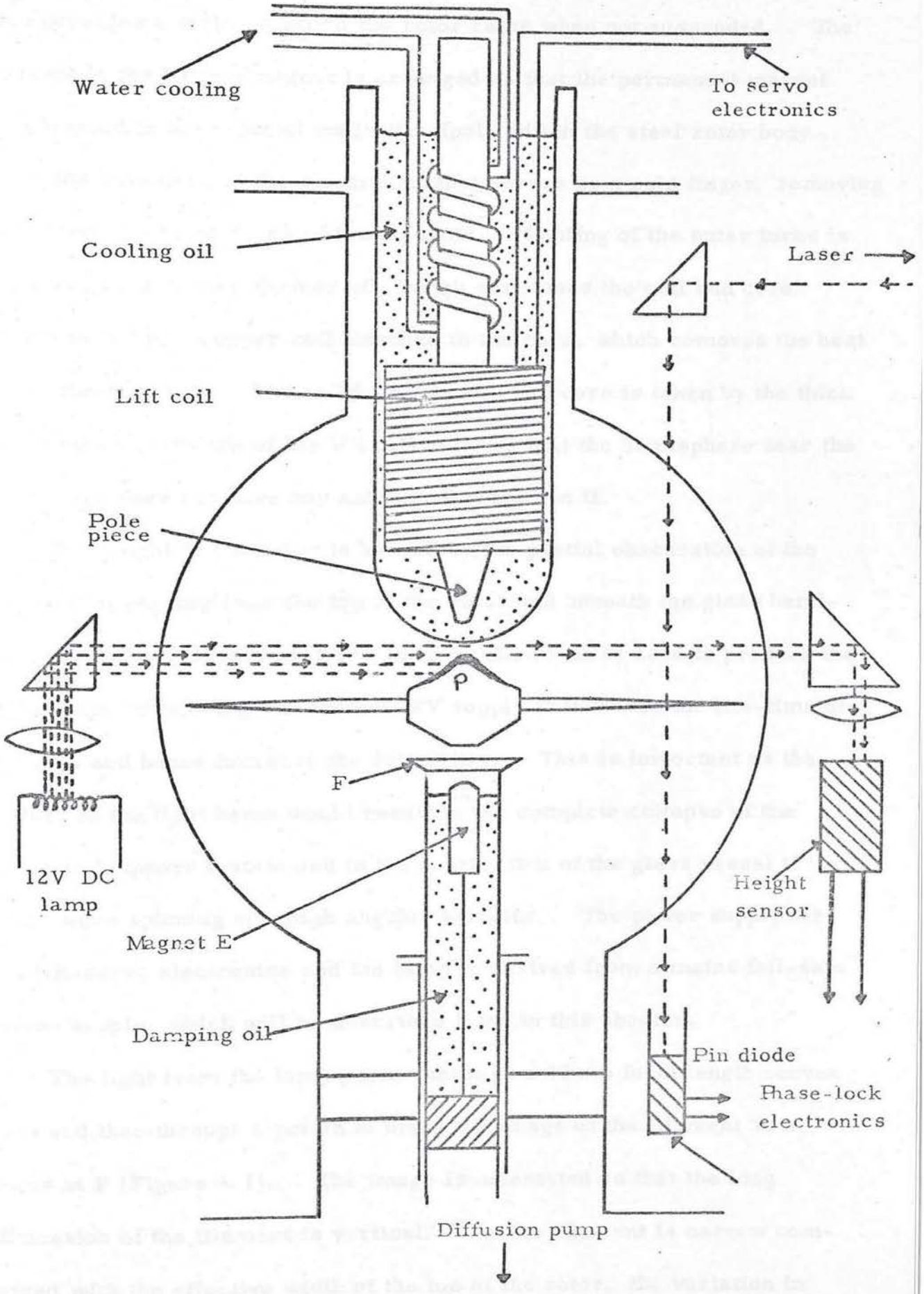

the support wire and the damping coil. The glass housing for this provides a table on which the rotor rests when not suspended. The current in the lifting-magnet is arranged so that the permanent magnet is attracted to the induced magnetic dipole within the steel rotor body.

The iron core of the electro-magnet serves as a cold finger, removing heat from the inner turns of the solenoid. Cooling of the outer turns is achieved by thin transformer oil, which surrounds the coil and core. Water is fed to a copper coil attached to the core, which removes the heat from the coil unit. The weight of the coil and core is taken by the thick glass walls at the top of the lift coil unit, so that the hemisphere near the pole piece does not have any extra load placed on it.

The height of the rotor is sensed by the partial obscuration of the light beam passing over the top of the rotor and beneath the glass hemisphere. A single filament 24V linear-coiled bulb is used to produce the light beam, this being run from a 12V supply to increase the life-time of the bulb and hence increase the reliability. This is important as the failure of the light beam would result in the complete collapse of the magnetic support system and in the destruction of the glass vessel if the rotor were spinning at a high angular velocity. The power supply for the lift-servo electronics and the lamp is derived from a mains fail-safe power supply, which will be described later in this chapter.

The light from the lamp passes through a 43mm focal length convex lens and then through a prism to bring the image of the filament to a focus at P (Figure 4.1). The image is orientated so that the long dimension of the filament is vertical. As the filament is narrow compared with the effective width of the top of the rotor, the variation in

transmitted light is approximately proportional to the change in height of the rotor. The transmitted light is fed to another prism and a 25mm focal length convex lens, to enable light to fall on the photo-voltaic cell (MS2BE, Ferranti Ltd.). The photo-voltaic cell has a sensitive area of $0.34in^2$, so that accurate focussing is not necessary.

For the stable suspension of the rotor in mid-vacuum, the servo unit must apply a current to the lifting magnet such that, if z_c is the desired height to suspend the rotor, measured from the pole piece, the direction of the resultant force on the rotor is always forcing it back to this height. However, for stable suspension, not only must the height of the rotor equal z_o but the velocity of the rotor must also be zero. This means that a net force on the rotor must also be produced proportional to the velocity of the rotor in such a way as to oppose motion, i.e. a damping term. Unfortunately, the simple solution of the transfer function of this arrangement is not possible as the very non-linear attractive force between the rotor and the lifting solenoid would produce a complex, non-linear differential equation which would be almost impossible to set up. However, the variables previously mentioned will still produce a potential well with damping of motion within it, independent of the power law, which relates the current in the lifting solenoid to the force on the rotor body and also the force on the rotor as a function of height, provided the coefficients of the height and velocity information are large enough. Therefore, if the height of the rotor is z, as measured from the pole piece, then the current I into the lift coil is given by:

[8, 9]

Figure 4.2 Rotor suspension circuit.

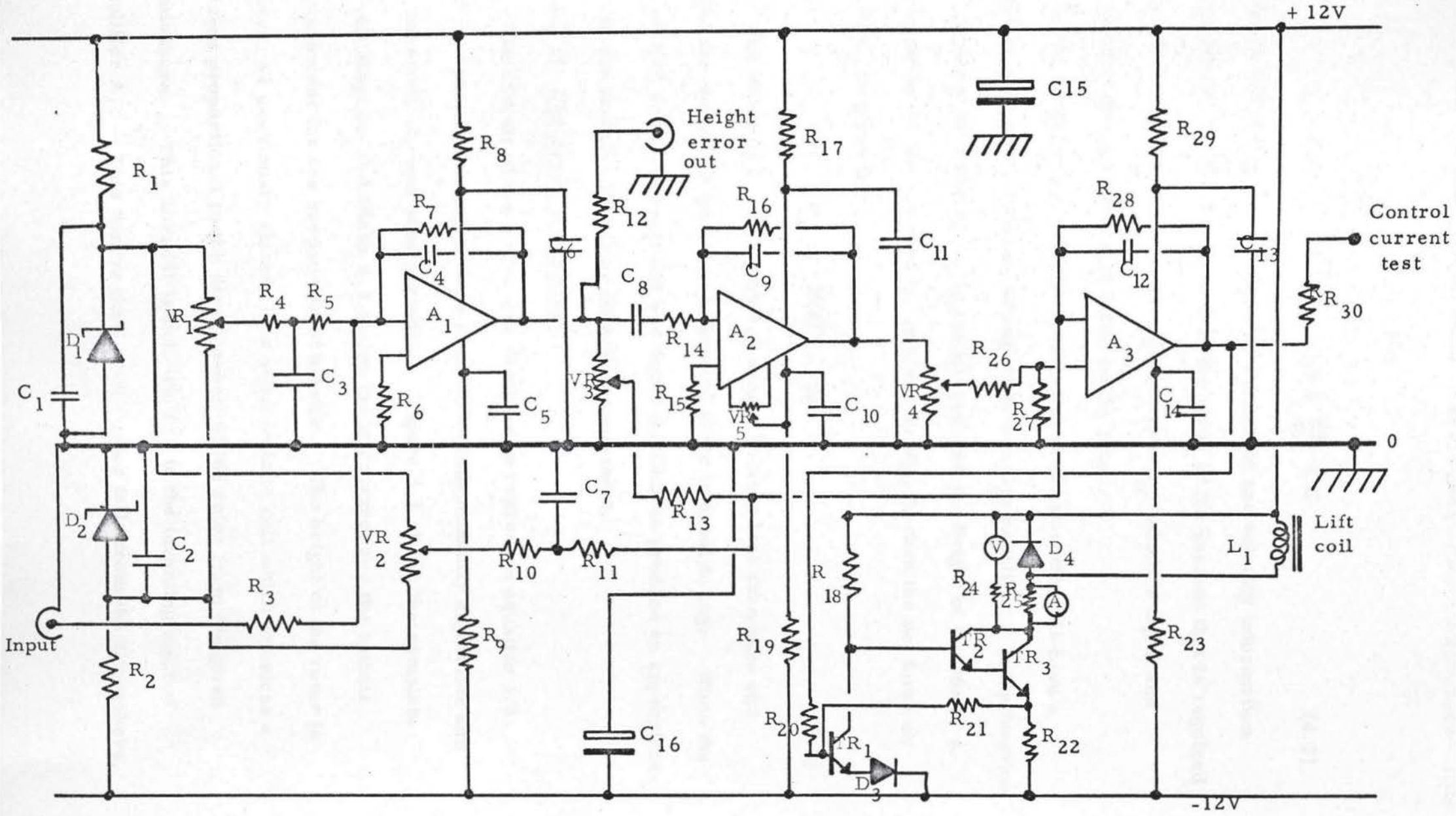

$$I = A(z_o - z) + B\frac{dz}{dt} + C \qquad (4.1)$$

where A and B are coefficients of the height and velocity information respectively. The constant C is the value of the current that is required to produce a force on the rotor at the height z_o, which is equal and opposite to the gravitational force on the rotor.

For convenience, all distances measured below the axis have a negative sign and all forces acting down are also negative. If the function that relates the current, I, in the lift coil and the height of the rotor, z, to the force on the rotor body, is given by F(z,I), then the net force on rotor F_r is given by:

$$F_r = F(z,I) - mg \qquad (4.2)$$

The value of I in equation 4.1 cannot become less than zero and hence the maximum possible downward force is equal to mg. When the servo unit was constructed it was found possible to produce an approximation to the function F(z, I) by direct measurement.

4.1.B The Servo electronics.

The circuit of the servo was designed to reproduce equation 4.1. The co-efficients A and B were made to be independently adjustable and the constant, C, was also variable. Figure 4.2 shows the complete circuit diagram and Plate 4.1 shows the lift magnet and the optical arrangement for the suspension of a rotor. The height of the rotor is sensed, as previously stated, by a photo-voltaic cell which produces a current proportional to the displacement of the rotor from the glass hemisphere. This current is fed, via R_3, to the inverting input of amplifier A_1. This means that, as the rotor falls from the hemisphere,

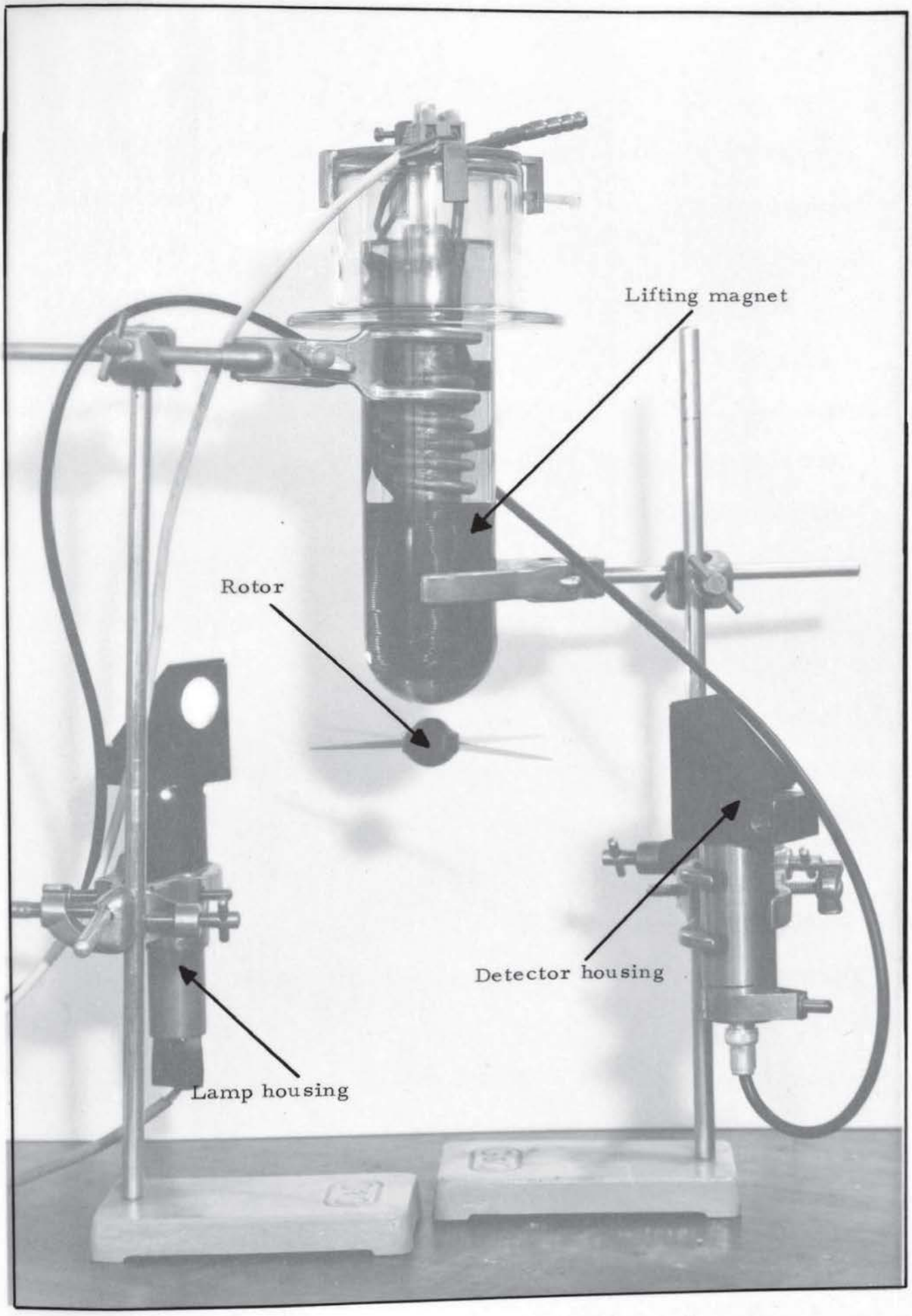

PLATE 4.1 Components of rotor suspension system.

the current through R_3 increases. The typical input current- to-displacement ratio is approximately 30μA/mm and this is converted to a voltage of 30 xR_7, V/mm on the output of A_2. As the inverting input of A_1 has negligible impedence to ground, because the amplifier is used in virtual earth mode, the photo-voltaic cell is loaded only by the resistor R_3, 68 Ω, which was included to prevent the cell driving a short circuit. It is, however, necessary to load the cell because under no-load conditions it produces a near constant voltage of about 500mV independent of the light input. Now, to reproduce equation 4.1 it is necessary to subtract the required suspension height from the actual height and, as the parameters have been converted to current, then a current equivalent to z_o must be subtracted from the input current. As A_1 has a virtual earth input, it is simple to use this as a subtracting stage. The current equivalent to z_o is produced by the variable resistor VR_1 stabilised by the zener diodes D_1 and D_2. The feedback loop of A_1 also contains a capacitor, C_4, which integrates the input current above 1kHz given by $1/(2\pi R_7 C_4)$. The integration serves to limit the unwanted band width and hence reduce the noise which would be fed into the differentiator.

The necessary response time of the system was estimated by using the time which the rotor would take to free fall 2mm, this being about 20ms resulting in an approximate band width of 100Hz. This stage, therefore, produces the height error signal and feeds to the differentiator.

The next stage produces the time derivative of the input up to a frequency of 1.6kHz given by $1/(2\pi C_8 R_{14})$ with a gain of $-10^{-3}\ dV_{max}/dt$. Above 1.6kHz the stage integrates and hence reduces the noise band

width. Variable resistor VR_5 is used to set the output to zero volts for zero input. This is necessary as a constant D.C. output would cause the control of the coefficient B, VR_4, to produce not only a voltage dependent on the velocity of the rotor but also a constant term which would be dependent on the setting of VR_4.

A_3 is a summing amplifier which produces an output voltage proportional to the height error, plus a constant and minus the time derivative of the height. The coefficient of the height error is taken from VR_3 and is variable. Stage A_3 has a voltage gain of R_{28}/R_{13} for the coefficient A. The constant is produced by VR_2, producing a variable voltage which is also stabilised by the Zener diodes D_1 and D_2. It is necessary to subtract the dz/dt information as this has been negated by the action of A_2.

The output from A_3 is now fed through R_{20} into the output stage. This is simply a voltage-to-current converter with current feedback, as the current in the coil produces the force on the rotor and not the voltage across it. The output current feeds through R_{22} which produces a voltage and so feeds current through R_{21} to the base of TR_1. The voltage-to-current conversion factor is equal to $R_{21}/(R_{20} \cdot R_{22}) = 0.5A/V$. The output current has a range of 0 to 6.25A with the supply voltage and electro-magnet used. L_1 is the lift coil and has a resistance of 3 Ω, the output transistors being protected from over-voltage due to $L \cdot \frac{di}{dt}$ by the parallel diode D_4.

Diode D_3 in the emitter of TR_1 was included to raise the voltage on the base of TR_1 relative to the -12V rail, to enable the slightly limited output swing of A_3 to completely turn off TR_1 and thereby enable all the

current flowing through R_{18} to produce maximum output current when necessary.

Outputs are available for monitoring the height error voltage and the control voltage, these being used during setting up of the servo and also during a rotor 'run' to monitor the stability of the rotor. Two servo units were constructed to support two rotors and were both supplied by a $\pm$ 12V DC supply, derived from the mains fail-safe power supply.

4.1.C Adjustment of the suspension unit.

For adjustment of the suspension unit, a rotor is placed on table F (Figure 4.1) in the vacuum vessel with a clearance of 3mm between the top of the rotor and the bottom of the glass hemisphere. The light beam is positioned such that it passes between the lowest point of the hemisphere and the heighest point of the rotor. The detector is then adjusted so that the current from the photo-voltaic cell is a maximum, measured using a sensitive ammeter. The detector is then connected to the servo electronics and an oscilloscope is connected to the height error output. With VR_3 and VR_4 set on zero, the circuit is turned on and the voltage noted on the oscilloscope for the rotor in the un-lifted state. The constant control, VR_2, is then used to lift the rotor completely up to the hemisphere and the new setting on the oscilloscope noted. By adjustment of VR_1 it is possible to set the output E so that the voltage for the lifted rotor is equal to minus the voltage for the un-lifted rotor. When this has been achieved, the servo height (z_o) of the rotor is approximately 1.5mm, therefore giving equal clearance above and below, when suspended. The control of B dz/dt is then increased to a maximum and VR_3 is increased to about half the available range. At this point the rotor is

PLATE 4.2 Various responses of lift servo.

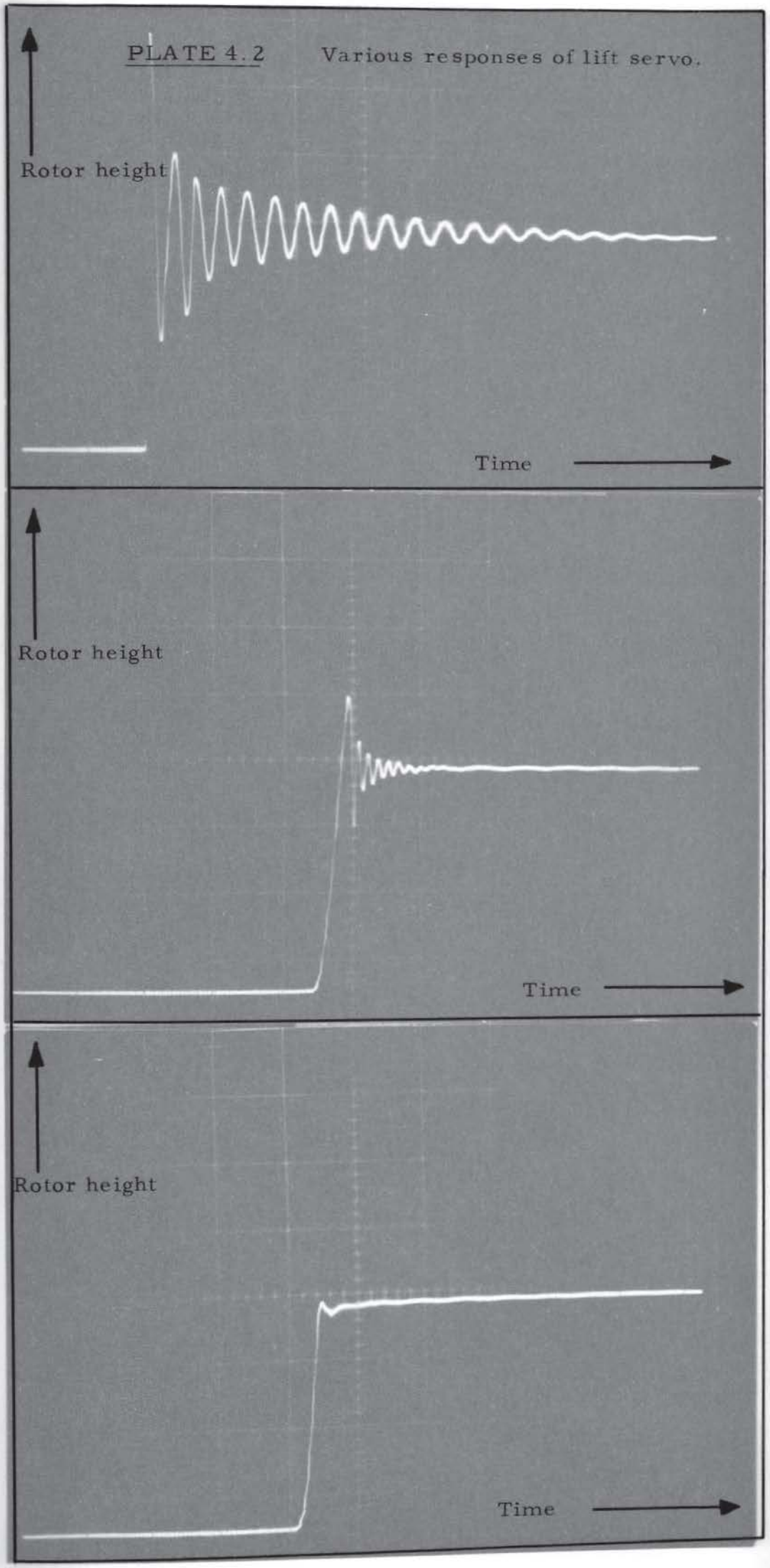

freely suspended but at the wrong height. By varying the constant, VR_2, and observing the output E, the constant should be adjusted until E equals OV. This is now the correct value of the constant for this specific suspension height.

If the light beam is obstructed and the voltage E is observed using the oscilloscope with a slow timebase, the stability of the rotor can be observed. When the obstruction is removed rapidly from the light beam, the rotor will rise to the reference height. The setting of VR_4 and VR_3 will affect the amount of 'ringing' due to insufficient damping and, with adjustment of VR_3 and VR_4 a satisfactory step-function can be produced. Plate 4.2 shows three possible responses of the rotor height to a slow step-function. The lowest trace shows the correct adjustment of the controls VR_4 and VR_3.

4.1.D Simple analysis of the lift servo.

If the suspension coil has a constant current flowing through it and the magnetic field density B varies as some function B_z on the axis of the coil, then the force on a single induced magnetic dipole $\underline{M}$ is generally:

$$F = (\underline{M} \cdot \nabla) \underline{B} \qquad (4.3)$$

and if $\underline{M}$ only has a component in the z direction, then the force in this direction is given by:

$$Fz = m \frac{\partial \underline{B}z}{\partial z} \qquad (4.4)$$

where m is the magnitude of the induced magnetic dipole.

If $m = \chi H_z$, where χ is the magnetic susceptibility and also $(1 + \chi) = \mu_r$, then

$$m = (u_r - 1)\, H_z$$

also $$B_z = \mu_o \mu_r H_z .$$

therefore $$m = (\mu_r - 1)\frac{B_z}{\mu_o \mu_r} \qquad (4.5)$$

Therefore the force in the z direction of a magnetic dipole is given by:

$$F_z = \frac{(\mu_r - 1)}{\mu_o \mu_r} B_z . \frac{\partial B_z}{\partial z} \qquad (4.6)$$

Now, if the rotor is considered to have a large number of differently orientated induced magnetic dipoles, but the resultant dipole lies on the z-axis and if the non-linear magnetization effects are small, then the attractive force on the rotor body may be approximated by:

$$F_{ROTOR} = K B_z . \frac{\partial B_z}{\partial z} \qquad (4.7)$$

where K is a constant.

If the lifting solenoid is considered to comprise a long coil with a core, which is thin, then a possible relationship for the variation of $\underline{B}$ in the z-direction can be formulated. If a current loop of radius a is considered to have a current I flowing in the loop, then the component of $\underline{B}$ on the axis of the loop at point P, a distance z from the coil, is given by:

$$B_z = \frac{\mu_r \mu_o I a^2}{2(z^2 + a^2)^{3/2}} \qquad (4.8)$$

and if $a \ll z$, then:

$$B_z \simeq \frac{\mu_o I a^2}{2 z^3} . \mu_r \qquad (4.9)$$

If a large number of these loops are used to make a solenoid of

length L, then the field at the point P on the axis is approximately equal to:

$$B_z = \frac{\mu_o \mu_r I a^2 n}{4z^2} \qquad (4.10)$$

where $L \gg z$ and n is the number of turns per unit length.

Therefore, using equation 4.7, the force on the rotor may be approximated by:

$$F_z = \frac{K.I^2}{z^5} \qquad (4.11)$$

where K is a constant. As the exact measurement of the distance z is not possible, it was made equal to (R + z), where z is now the distance from the pole tip to the top of the rotor. Therefore, the force equation becomes:

$$F_z = \frac{K.I^2}{(R+z)^5} \qquad (4.12)$$

where K and R are constants.

The rotor was stably suspended during the following measurements and these are independent of the lift servo electronics being used to stabilise the rotor. The variation of force was achieved using a weight pan attached to the rotor, such that the lift magnet only applied the force of attraction to the rotor body, but the apparent weight of the rotor could be increased and so an increase in the lift coil current required to suspend the rotor at the same height was produced. The height was measured using a travelling microscope.

The servo-controlled rotor was used to measure the variation of the attractive magnetic force on the rotor body as a function of the lift current with a constant height of 0.938 ± 0.006mm, i.e. the spacing

Figure 4.3 Graph of the force on the rotor body as a function of the lift coil current with a constant height of .938mm.

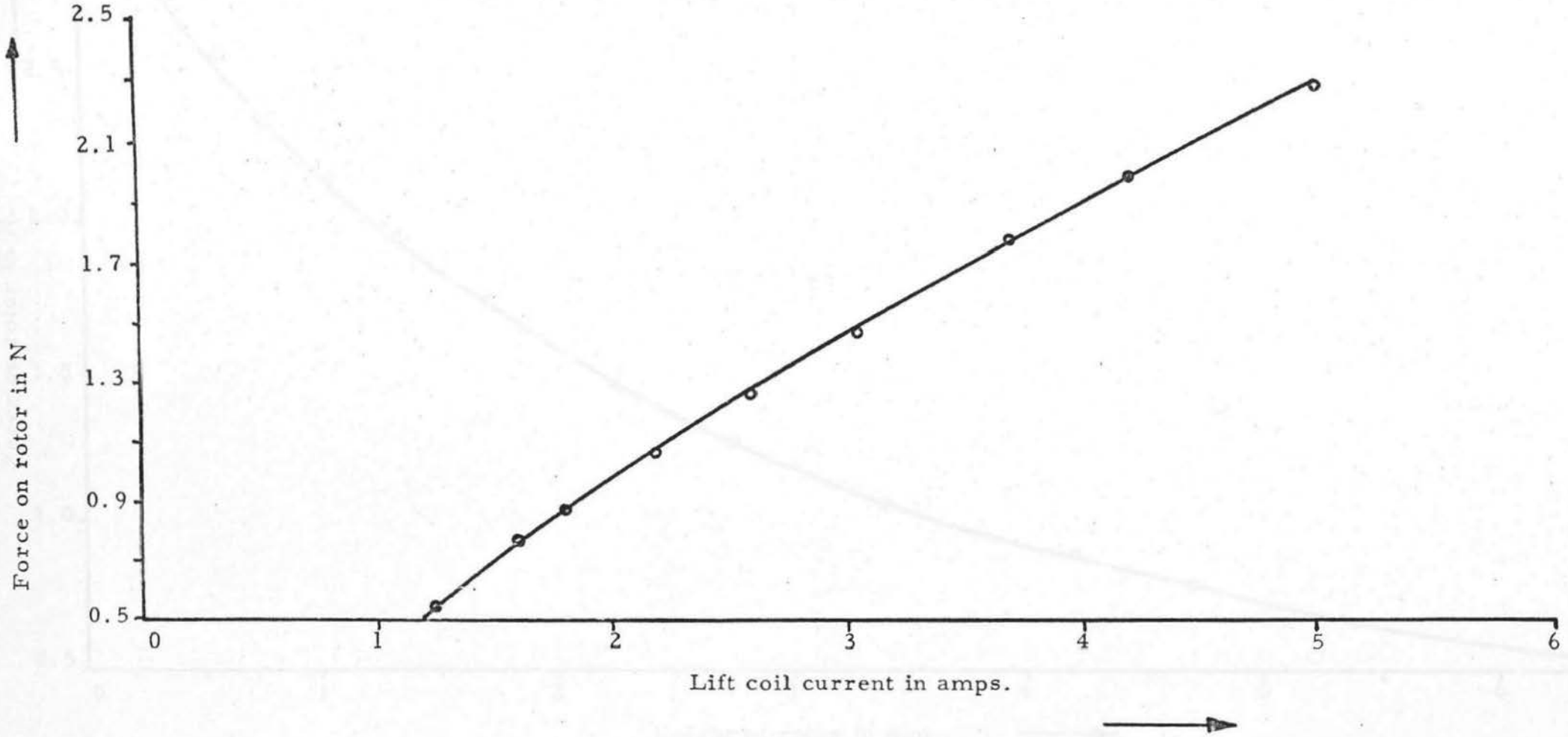

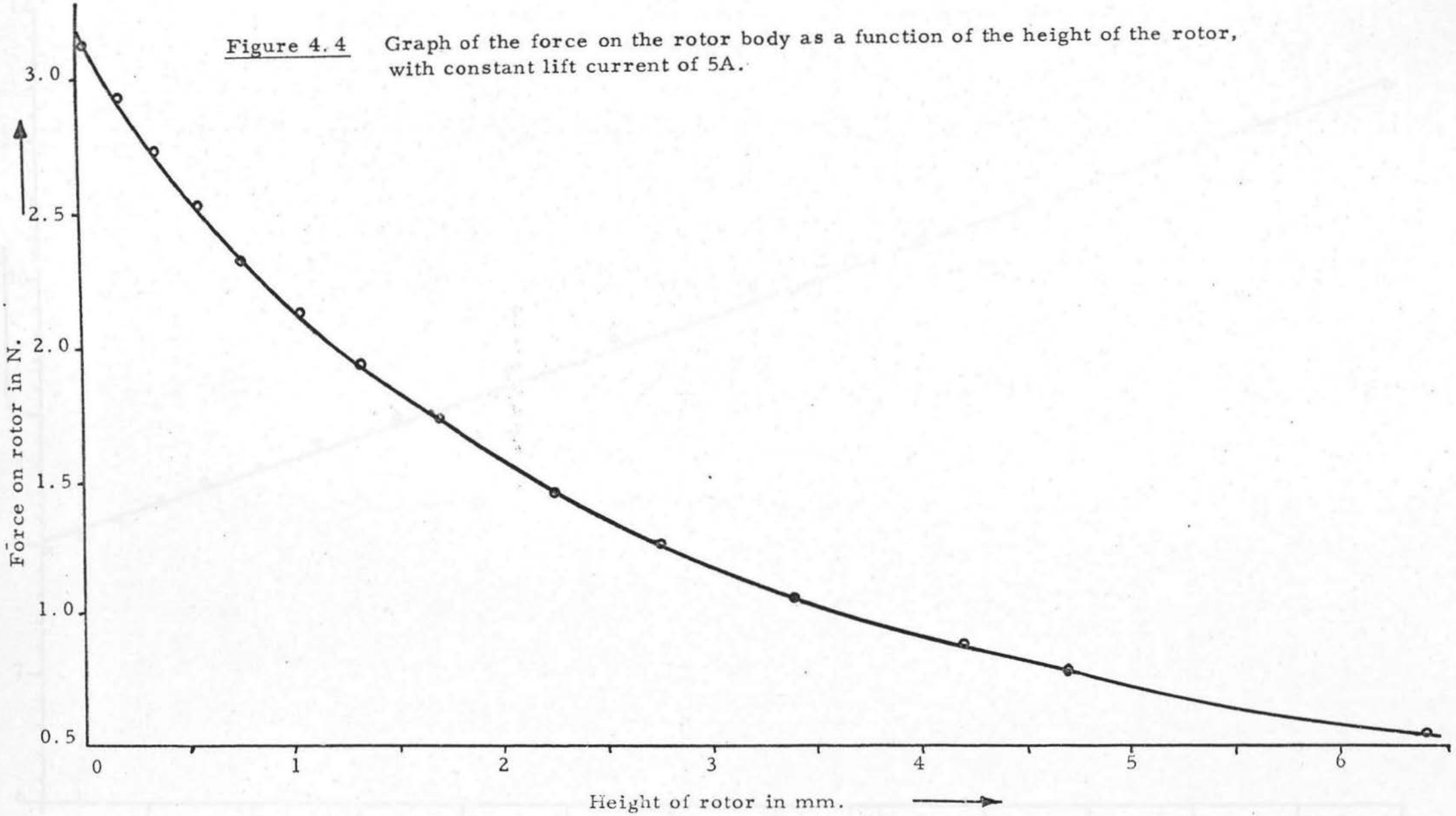

Figure 4.4 Graph of the force on the rotor body as a function of the height of the rotor, with constant lift current of 5A.

Figure 4.5 Graph of $F^{-.2}$ as a function of the height of the rotor, with a constant lift current.

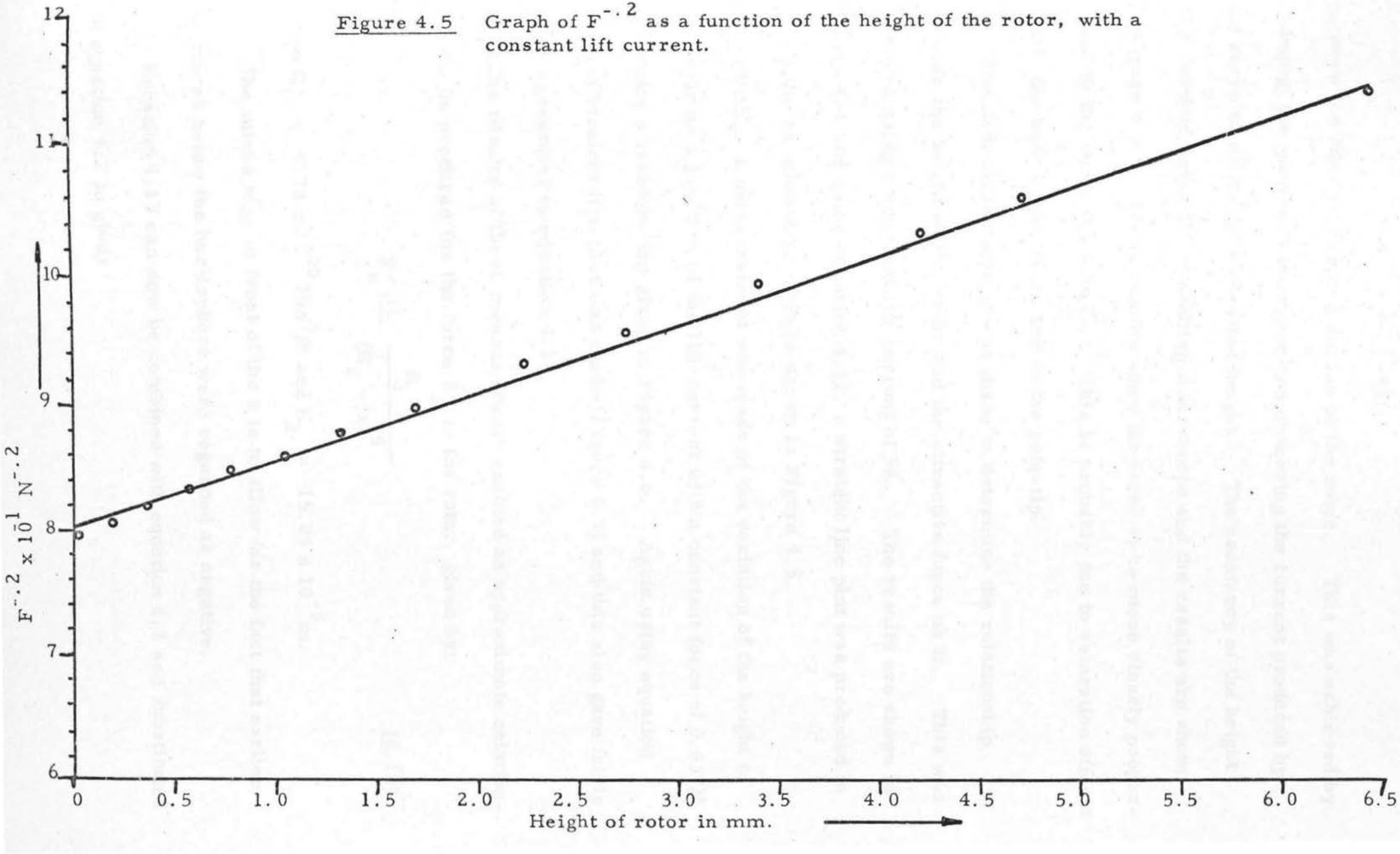

between the hemisphere and the top of the rotor. This was achieved by changing the weight of the rotor and observing the current produced by the servo to maintain a constant height. The constancy of the height was checked using the travelling microscope and the results are shown in Figure 4.3. These results show the force to be more closely proportional to the current I than I^2, This is probably due to saturation effects within the body of the rotor and in the pole-tip.

The next measurement was made to determine the relationship between the height of the rotor and the attractive force on it. This was achieved using a constant lift current of 5A. The results are shown in Figure 4.4 and using equation 4.12, a straight line plot was produced to verify the relationship; this is shown in Figure 4.5.

Finally, a measurement was made of the variation of the height of the rotor as a function of the lift current with a constant force of 0.537N producing a relationship given in Figure 4.6. Again using equation 4.12, a straight line plot was made (Figure 4.7) and this also gave fairly close agreement to equation 4.12.

The results of these measurements enabled an approximate relationship to be produced for the force F_z on the rotor, given by:

$$F_z \simeq \frac{K_1 I}{(K_2 - z)^5} \qquad (4.13)$$

when $K_1 = 4.78 \times 10^{-10}$ Nm^5/A and $K_2 = 15.05 \times 10^{-3}$m.

The minus sign in front of the z is to allow for the fact that earlier distances below the hemisphere were regarded as negative.

Equation 4.13 can now be combined with equation 4.1 and substituted in equation 4.2 to give:

Figure 4.6 Graph of the lift coil current as a function of the height of the rotor body with constant force of 0.537N.

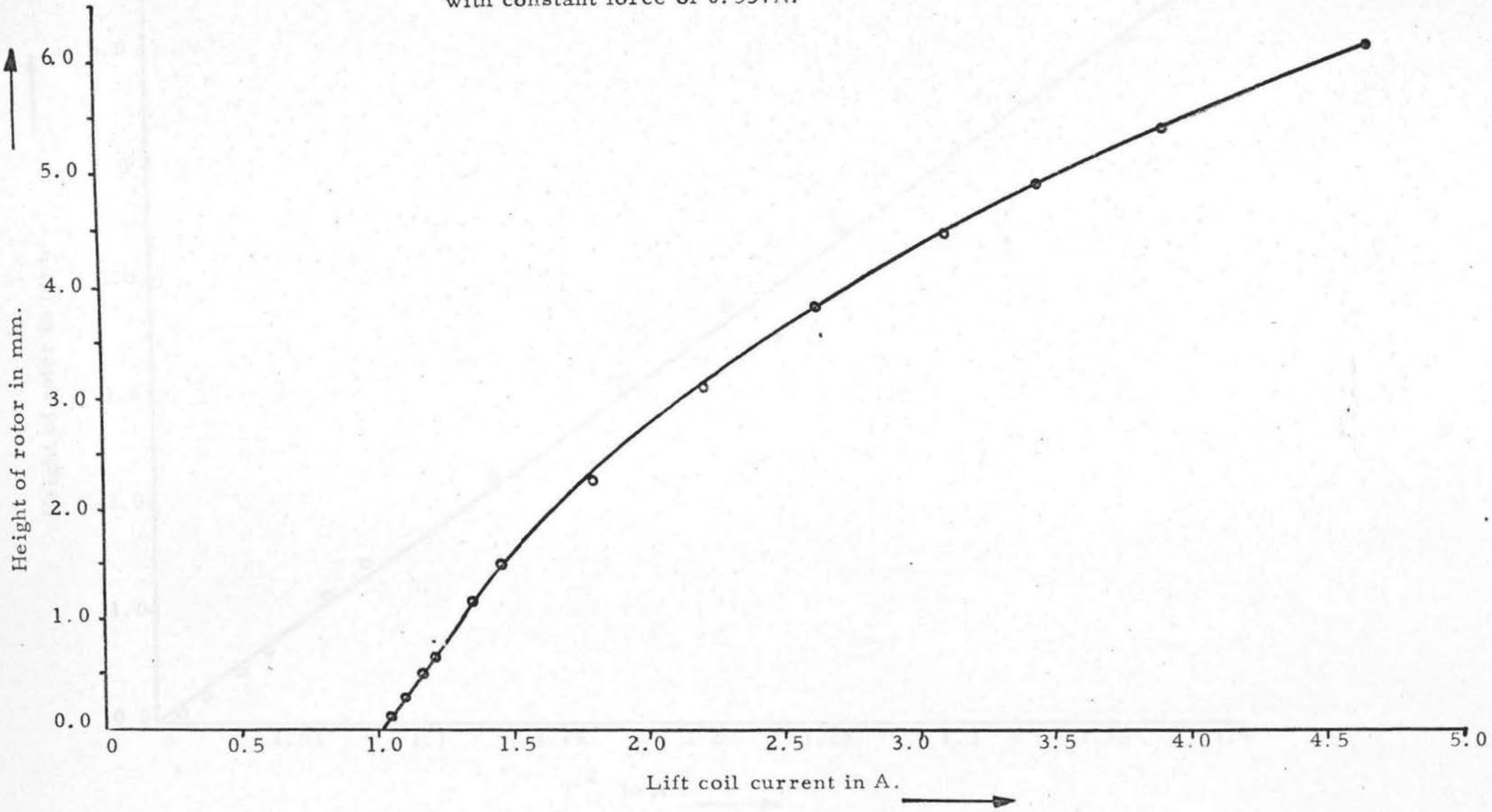

Figure 4.7 Graph of $I^{\cdot 2}$ as a function of the height of the rotor in mm. I is current in lift coil.

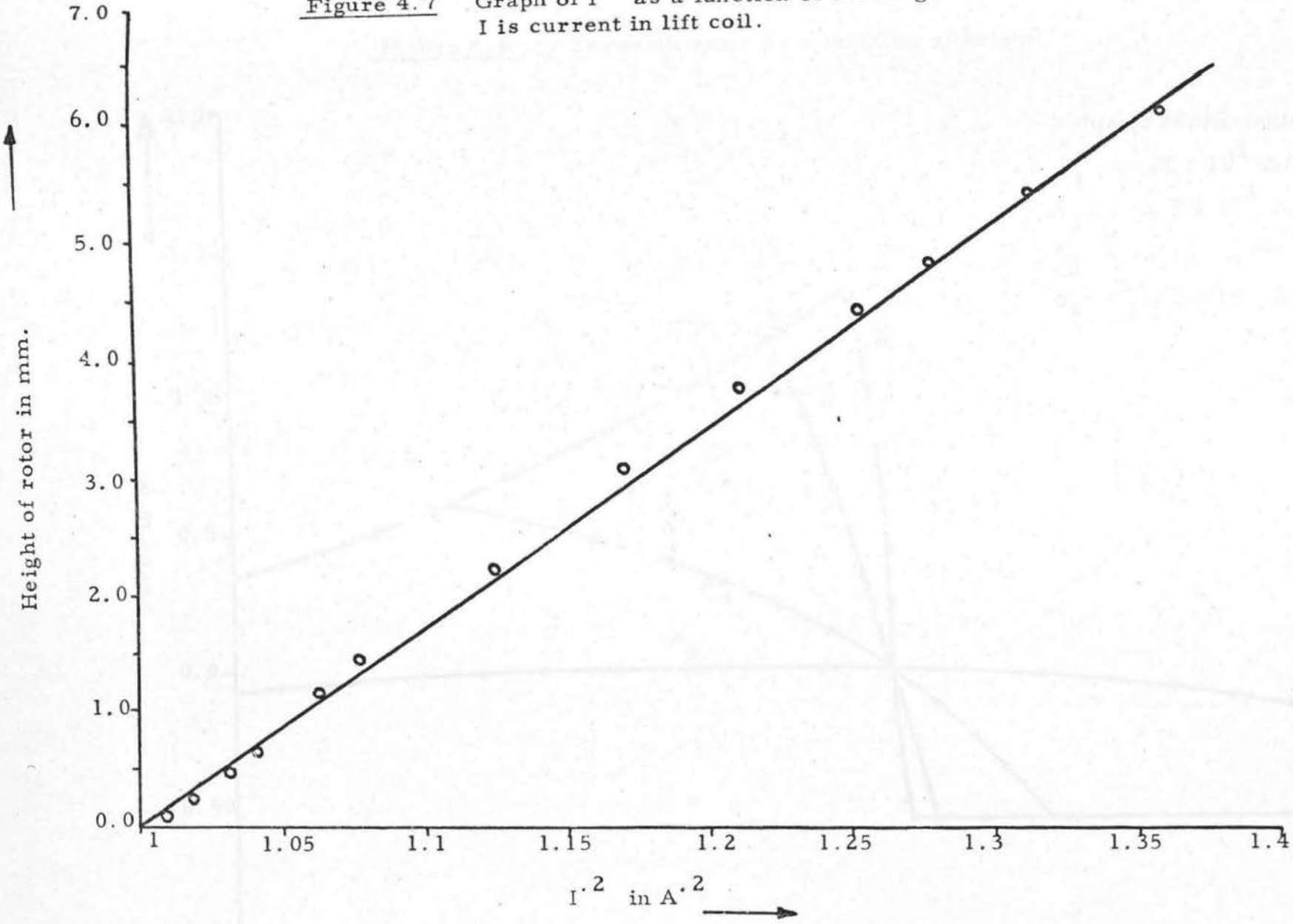

Figure 4.8 Force on rotor as a function of height.

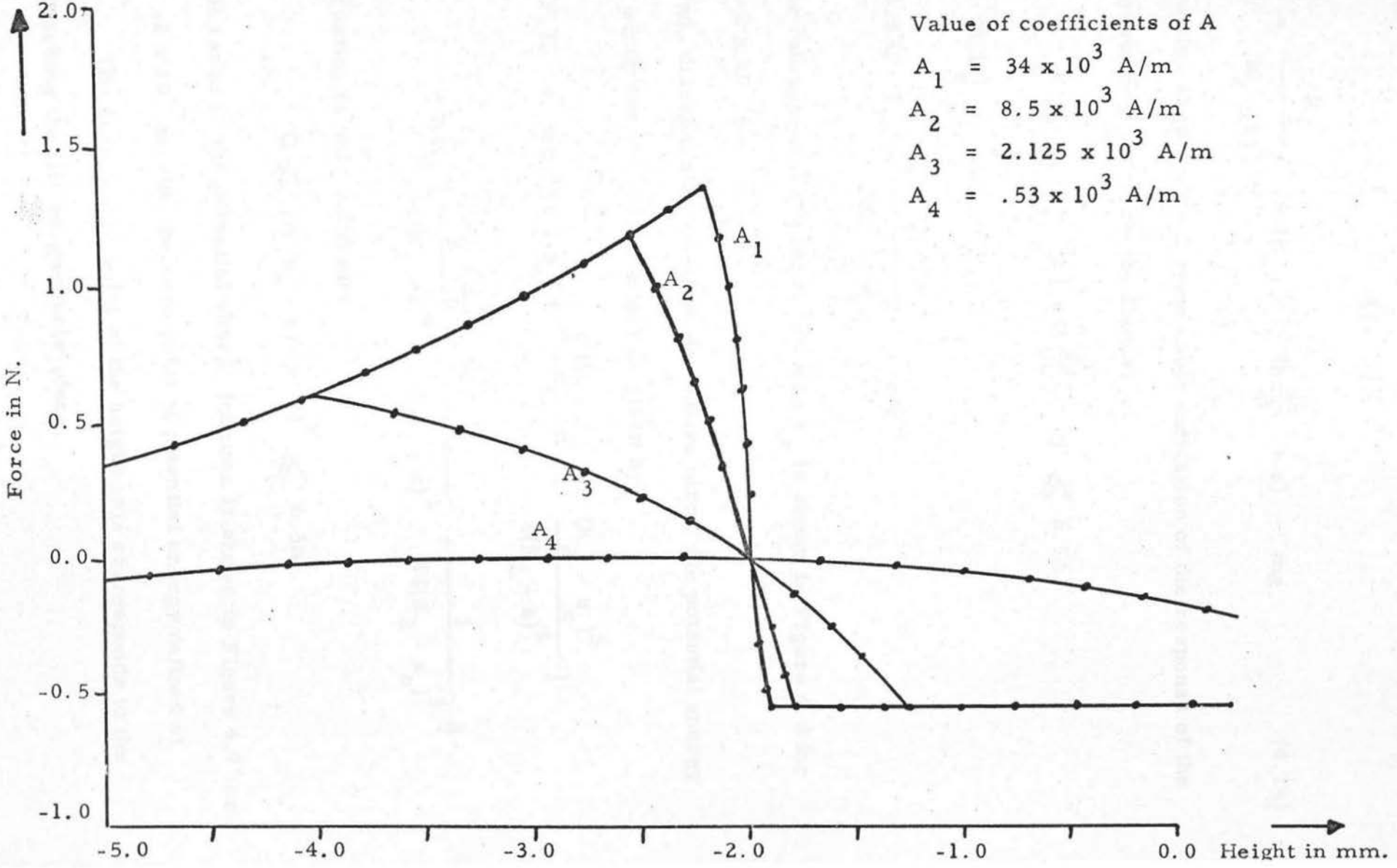

$$F_r = \frac{K_1}{(K_2 - z)^5} \left(A\,[z_o - z] + B\,\frac{dz}{dt} + c\right) - mg \qquad (4.14)$$

This equation should give a reasonable indication of the response of the whole servo loop, between the limits:

$$0 \leqslant \left(A\,[z_o - z] + B\,\frac{dz}{dt} + c\right) \leqslant 6.5A$$

Below 0.0A, $F_r = -mg$

Above 6.5A, $F_r = \frac{K_1\ 6.5}{(K_2 - z)^5} - mg$

The full range of the force function F_r is shown in Figure 4.8 for $z_o = -2 \times 10^{-3}$m.

Also, disregarding the time derivative term, the potential energy well to which the rotor is confined is given by:

$$P.E. = mg\left[(z - z_o) + \frac{(K_2 - z_o)}{4} - \frac{(K_2 - z_o)^5}{4(K_2 - z)^4}\right]$$

$$+ AK_1\left[\frac{(K_2 - z_o}{4(K_2 - z)^4} - \frac{1}{3(K_2 - z)^3} + \frac{1}{12(K_2 - z_o)^3}\right]$$

This equation is only valid for:

$$0 \leqslant (A\,(z_o - z) + c) \leqslant 6.5A$$

The full range of the potential energy function is shown in Figure 4.9 for $z_o = -2 \times 10^{-3}$m with the zero point of potential energy defined at $z = z_o$. The zero metre point of the height axis corresponds to the rotor touching the lift-magnet pole-piece.

4.2.A The mains fail-safe power supply

The mains fail-safe power supply is essential for the efficient

Figure 4.9 Rotor suspension, potential energy as a function of height.

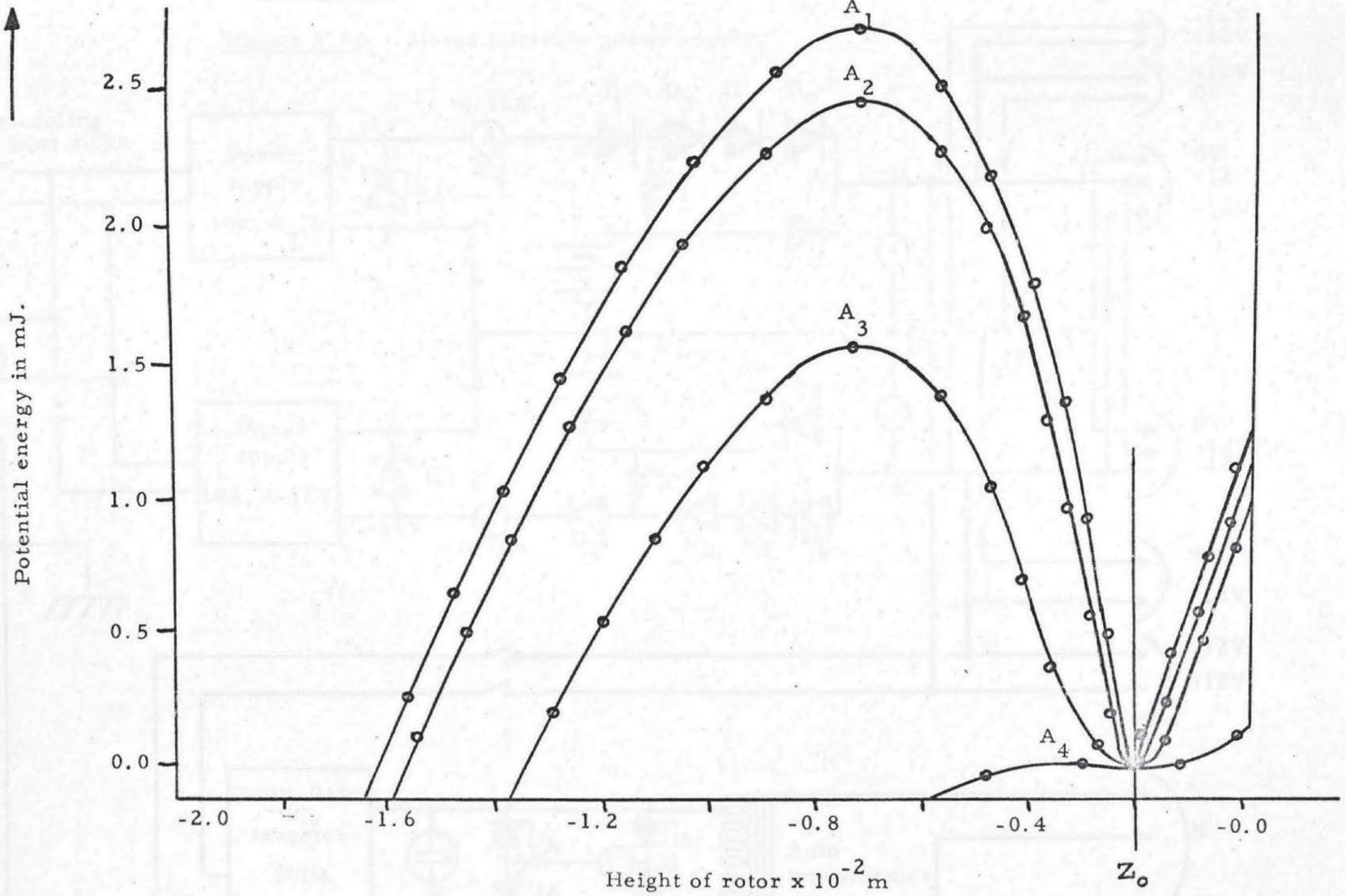

Figure 4.10 Mains fail-safe power supply.

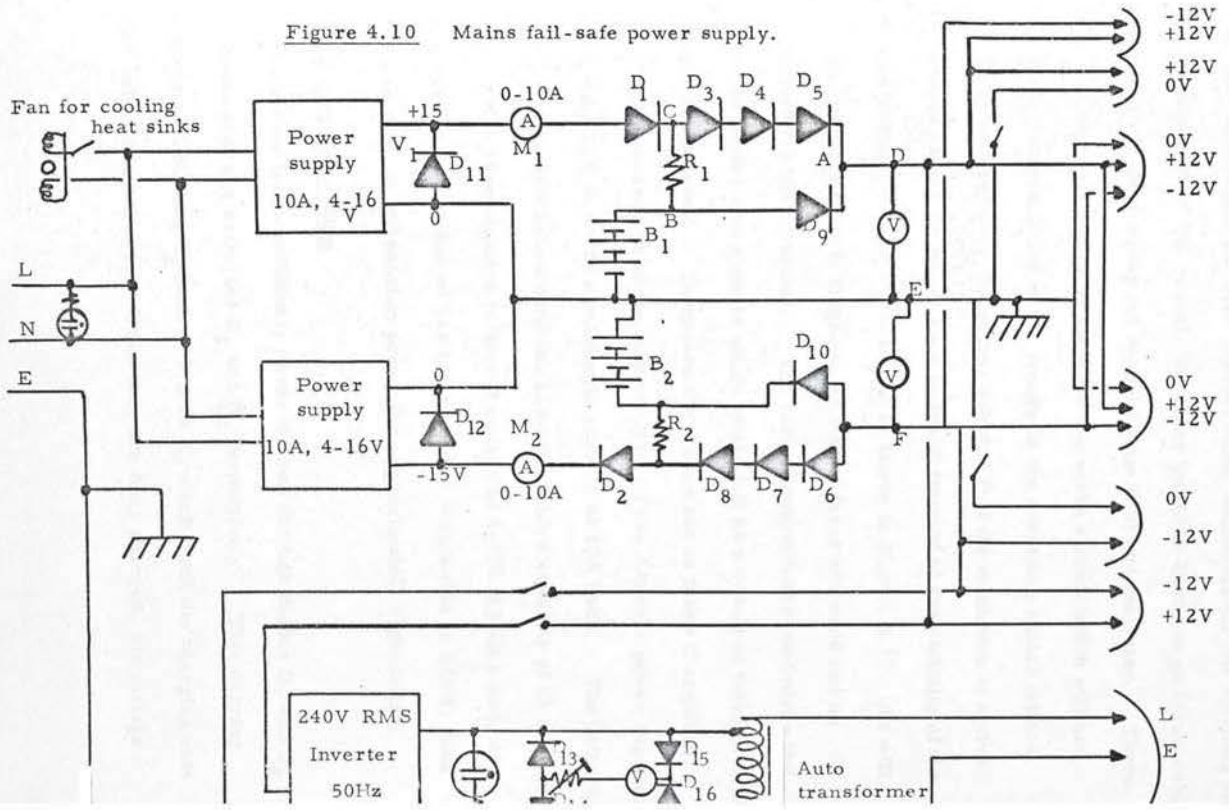

Figure 4.10 Mains fail-safe power supply.

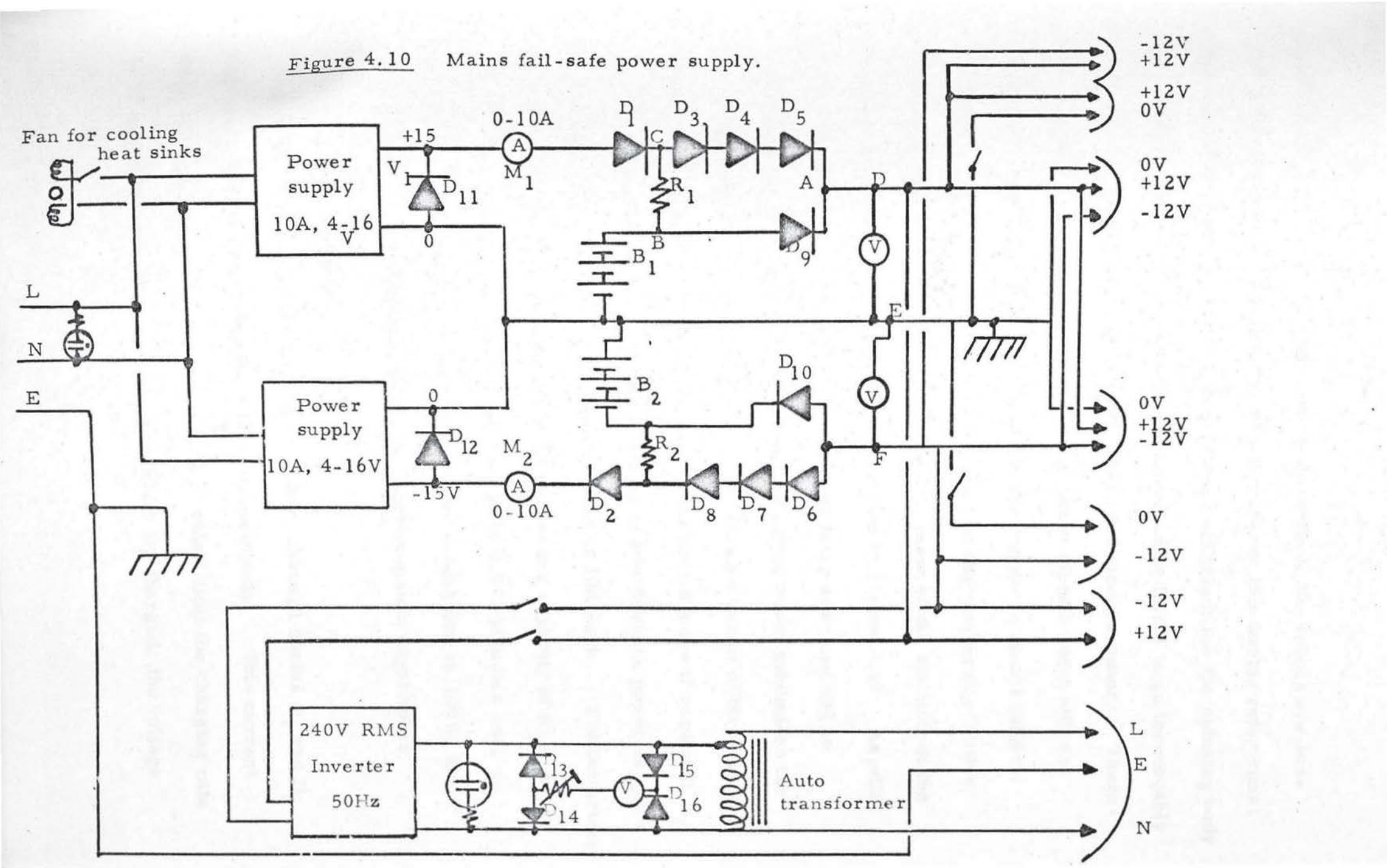

running of the rotors. As previously described, the rotors are suspended by a magnetic field servo, which must not fail during rotor runs. If the unit should fail for even a short time, sufficient for the spinning body to touch any part of the vessel, the rotor would be likely to go irrevocably out of control, destroying the vessel (Plate 4.3) and the rotor. Therefore, a power unit has to be used for the servo circuit which will not produce any interruption of the supply in the event of a mains failure.

To do this reliably the author decided that the minimum of active components should be used, even to the detriment of the stability of the supplied voltage. The circuit used is shown in Figure 4.10. As will be seen from the circuit diagram, no output fuses are used and no transistors for stabilisation. The lack of output fuses minimises the number of series components which might fail as a result of thermal and vibrational stresses. Therefore the diodes act as fuses if required.

The mains section of the unit consists of two Advance power supplies producing $\pm$ 15V D.C. at a maximum current of 10A each. The batteries, B_1 and B_2 are 12V heavy duty car batteries with a capacity of 55 A-hours each. This is equivalent to a stored energy of 4.752 M joules and, as the general consumption of two rotors under suspension is 160W, then these can provide suspension power for approximately eight hours.

4.2B Circuit Operation

Under no-load conditions, current flows through diodes D_1 and D_2 and hence charges batteries B_1 and B_2 respectively. This current flows through R_1 and R_2 both of 2.3 Ω , which limit the charging rate to 2A with a flat battery. When they are fully charged, the voltage

PLATE 4.3 Smashed roto

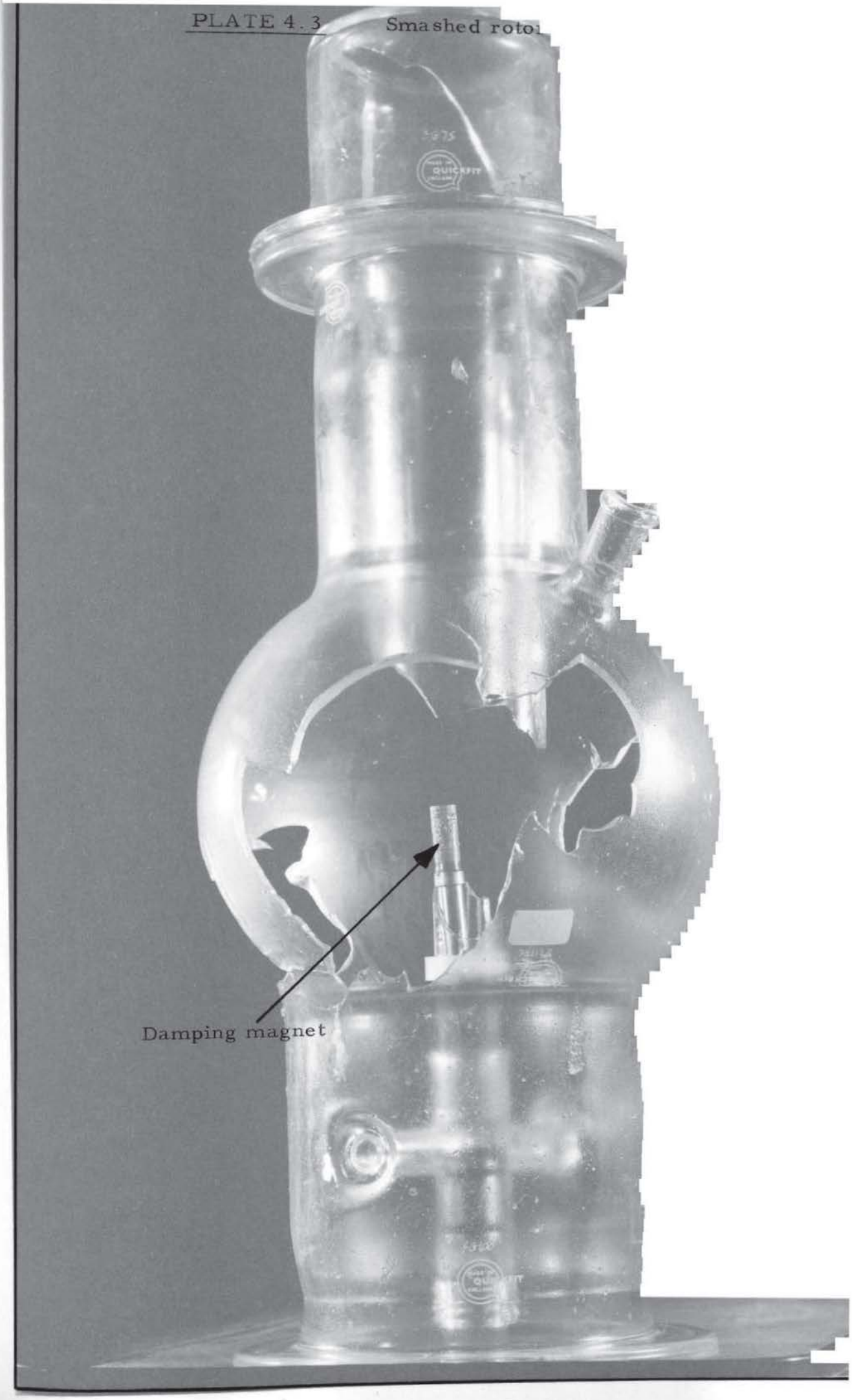

across the terminals is approximately 13.6V, which means that the charging current is less than half an amp. This enables the supply to be left on, charging continuously and so maintaining the batteries at full charge.

During normal operation, current flows to the lift circuit through diodes D_1 to D_5 for the positive supply rail, and D_6 to D_9 for the negative rail. As a result of the voltage drops across D_3 to D_5, the voltage at A is less positive than the voltage at B and hence the diode D_9 does not conduct. Therefore current is not drawn from the battery and the same process applies to the other battery. Also, point C is more positive than B; therefore a charging current is still provided for the batteries. If the mains fails, the voltage across D_{11} collapses and the voltage at C falls to that of B. Also, D_1 and D_2 prevent both batteries discharging through their respective power supplies. As there is no longer any voltage supplied from the mains to hold the potential at A above that of B, the voltage at A falls until it is held stationary by the potential of the battery. The voltage V_1 was adjusted with a load on the output of the positive supply such that a current of 10A was passed to ground. The current in the ammeter M_1 was observed and the voltage V_1 was adjusted until the meter M_1 just gave a reading of 10A. If the reading was less than 10A, the difference in the current was being met by the battery. The maximum current which can be sourced by the mains power packs is 10A and thereafter the internal current limiter comes into operation and reduces V_1 until a current of 10A is passed. This means that, if a current of greater than 10A is required, it can be provided by the battery and the mains power pack. This can be seen from the fact that, as the

current limiter reduces the voltage at C and therefore at A, a voltage will be reached which will turn on D_9. This will reduce the current from the mains supply and therefore the current limiter will raise the voltage V_1 until it just produces a current of 10A. Diodes D_{11} and D_{12} are included to protect the mains power supplies during turn-on, when a supply could be damaged by the other supply driving it. All diodes are mounted on heat-sinks and the charge-limiting resistors R_1 and R_2 are of 150W power dissipation type.

Supplied from D and F is an inverter which produces 250V R.M.S. A.C. at 50Hz with a maximum power available of 150W. This inverter is used to power a small laser, used for rotational speed sensing. It was found that while the R.M.S. voltage supplied by the unit was equivalent to the requirements of the laser, the laser's performance was impaired when using this supply. However, a study of the laser revealed that its power supply was produced by a form of voltage multiplier and therefore required a greater peak-to-peak voltage, provided by the mains but not by the square wave voltage output waveform of the inverter. This was corrected by feeding the inverter supply into an auto-transformer with a voltage step-up ratio of 1.5, which produced sufficient peak-to-peak voltage to drive the laser.

The reason for powering the laser and also other speed monitoring equipment from the mains fail-safe power supply was that, in the event of a mains failure occurring when rotors were spinning at very high speeds, there would still be power available for audible speed measurement. The diffusion pumps would slowly cease to operate and therefore the frictional torque on the rotors due to the gas load would slow down

the rotors. However, from a safety point of view it would be useful to know the approximate speed of the rotors and so the laser, PIN diode amplifier and an audio speed unit are all run from the fail-safe supply.

The supply voltage at D and F falls by 0.5V when the mains fails, but as the height servo circuit is protected against changes in the supply voltage, the height of the suspended rotors only changes by 0.025mm, which does not produce any instability. The main reason for the change in height is that the filament bulbs, used for height sensing, dim and hence this lowers the rotors fractionally.

4.3.A The P.I.N. diode amplifier.

The detection of the angular frequency of the rotor was achieved by allowing the rotor arms to intersect a laser beam which was set perpendicular to the plane of rotation. The physical arrangement of the rotor suspension magnet and the pump meant that the beam had to be set so that its interception took place near the tip of the rotor blade. At this point, the arm could be travelling at 2km/s and, as the arm is very thin at its tip (1mm) the black pulse only lasts for a short period of time, typically 500ns.

This meant that a fast detector had to be employed in conjunction with a comparatively fast amplifier. A P.I.N diode, type MRD510 (Motorola) was used, but it has a very low sensitivity of only 0.3μA/mW/cm^2 and hence large amplification was needed. Therefore, the amplifier has an input sensitive to current - as the diode is equivalent to a current source - with a D.C. voltage on the input to reverse bias the junction. The speed of the amplifier needed to be approximately 250ns

Figure 4.11 P.I.N. Diode Amplifier.

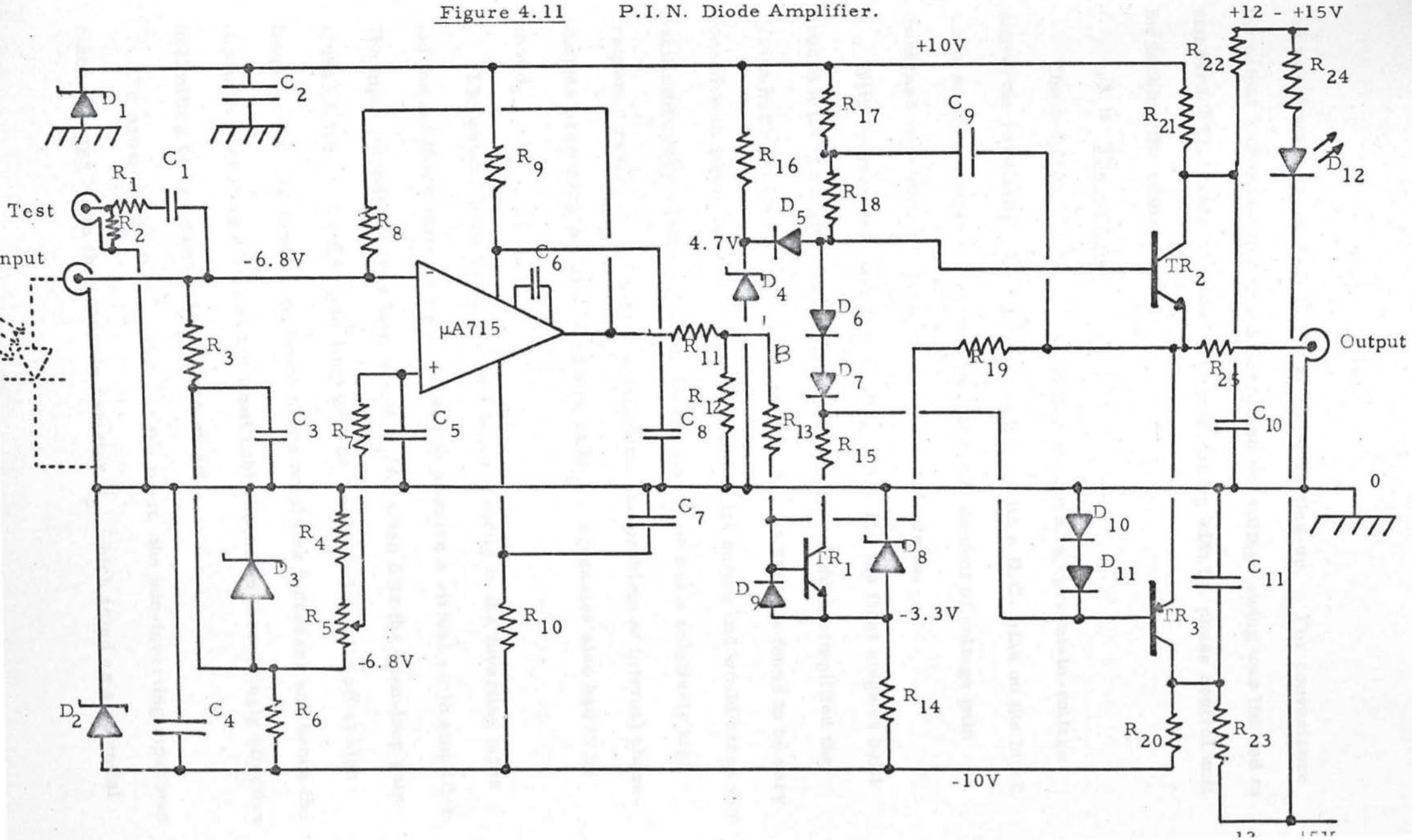

and would work down to D.C. to simplify setting-up. For convenience the output was made to drive a cable and the voltage swing was limited to standard TTL levels to allow easy interfacing with the phase control unit for locking the rotors.

4.3.B The circuit.

The amplifier is composed of two sections, a current-to-voltage converter providing a low input impedence with a D.C. bias on the input, and a second section which provides a small amount of voltage gain combined with output voltage damps and cable drive.

With reference to the circuit diagram 4.11, the first stage is built around a μA 715 high speed operational amplifier, which simplified the design but brought stability problems. The μA 715 was found to be very sensitive to phase lags or leads produced at its output and would break into oscillation very easily. Also, as the amplifier has a relatively high frequency response, of 65MHz bandwidth, the problem of internal phase-changes producing positive feedback at high frequencies also had to be solved.

The output from the diode was taken directly to the inverting input and the feedback through R_8 was used to produce a virtual earth amplifier. The input impedence was low, about R_8/A, when A is the open-loop gain of the μA 715. As the open-loop gain of the amplifier falls off at high frequencies, the input impedence of the amplifier increases and hence the capacitive shunting effect of the input cable becomes increasingly effective in limiting the response time of the stage.

To produce the D.C. offset at the input, the non-inverting input was taken through R_7 to the variable resistor R_5, which acted as a potential

divider with one end set at -6.8V and the other at-4.96V. As the non-inverting input has a high impedence, this pre-set divider could be used to set the non-inverting input at some negative potential with some adjustability. This was needed to set up the output voltage of the amplifier, as will be seen later. The output would be set by the voltage of the non-inverting input, but as a result of the current fed into the inverting input through R_3 from the -6.8V point, the output voltage is almost 0V and the input is held at -6.8V. The capacitor C_5 decouples the non-inverting input to ground. Diode D_3 produces the -6.8V point and holds it stable, so that the output voltage setting is mainly independent of supply line changes. The test input consists of a 1 M Ω resistor in series with a 10nF D.C. blocking capacitor. This enables input current pulses to be produced from a standard voltage pulse generator. The blocking capacitor is necessary to prevent the pulse generator from upsetting the D.C. conditions of the amplifier.

As this stage is a virtual earth amplifier with a current source feeding the input, then the gain, assuming sufficient open-loop gain, is dependent on the value of R_8, which is a 1 M Ω resistor and hence this gives a gain of 1V/μA.

There were various types of compensation attempted to give a stable configuration, the form of the compensation being taken from the literature supplied with the μA 715. However, various compensations were tried and all failed to give satisfactory stability and speed, so it was found necessary to produce compensation which was compatible with this circuit. Satisfactory stability was produced by a 470pF capacitor connected between pins 1 and 9 of the amplifier. The output of the μA 715, as already

stated, was very sensitive to the loading effects of subsequent stages; therefore R_{11} and R_{12} were used to produce a degree of isolation from any mildly reactive components appearing at the input of the next stage. This was found to be perfectly satisfactory and the output at point B gave a rise time of 60ns and minimal ringing.

The second stage consisted of a voltage amplifier with a gain of 4, this being defined by the ratio of R_{19}/R_{13} and a push-pull cable driver. This stage is D.C. coupled . like the first. Transistor TR_1 is used in a grounded emitter configuration, with the collector load 'bootstrapped' from the output via C_9 to give a large voltage gain. The diodes D_6 and D_7 produce the bias for TR_2 and TR_3 to prevent them both being turned off at the same time. TR_2 and TR_3 are emitter followers producing push-pull action to drive a cable. Voltage feedback is derived from their emitters through R_{19} and back to the base of TR_1. Diode D_5 prevents the positive excursion of the base of TR_2 beyond 5.3V positive, which in turn prevents the output from exceeding +4.6V. Diodes D_{10} and D_{11} prevent the negative travel of the base of TR_3 to lower than -0.5V. However, R_{15} is necessary to prevent the destruction of TR_1 by exceeding the current rating when TR_1 is fully conducting. These limits on positive and negative excursion enable TTL Schmitt trigger, SN7413, to be directly connected to the other end of the output cable without endangering the input of the TTL gate. Point B is free to swing in the positive or negative sense and, while a positive swing will only turn on TR_1, a negative swing could take the base of TR_1 more than 3V lower than the 3.3V of the emitter. This would cause breakdown of the base-emitter junction and so D_9 was included to prevent this.

The output stages of the three amplifiers built were designed to drive 50 Ω co-axial cable. All three amplifiers were found to give pulse rise times of 100ns at the other end of a 10m 50 Ω cable with correct termination. The output D.C. bias was adjusted to 0V by means of R_5. Further adjustment of R_5 has been found unnecessary as the bias is relatively insensitive to small supply rail and temperature changes.

The amplifiers were powered by the mains fail-safe power supply, which gave ±12V, but because small changes in the supply voltage were likely in the event of a mains failure, Zener diodes D_1 and D_2 were included to provide added regulation.

A 2mW HeNe laser was used to produce the light beam which was intercepted by the rotor arms. The intensity of the beam was sufficient to cause the output to be held on 4.5V unless the rotor intercepted the beam, in which case the voltage fell to -0.5V. If the voltage clamps were not present, the voltage swing would have been greater. Because the light output from the laser was sufficient to cause the output to be clamped, the large quantity of noise modulating the laser beam was not passed on to the logic units. This also made it possible for transition times of less than 40ns to be reached as the slew-rate of the amplifier was large enough to enable to output to change by 5V in a time less than 40ns, even though the rise time of the amplifier is 100ns.

One of the amplifiers was modified by the removal of diodes D_5, D_{10} and D_{11}. This increased the output range by removing the voltage clamps and made it, therefore, a useful current amplifier which was not to be used on TTL inputs.

Figure 4.12 Rotor Speed Monitor.

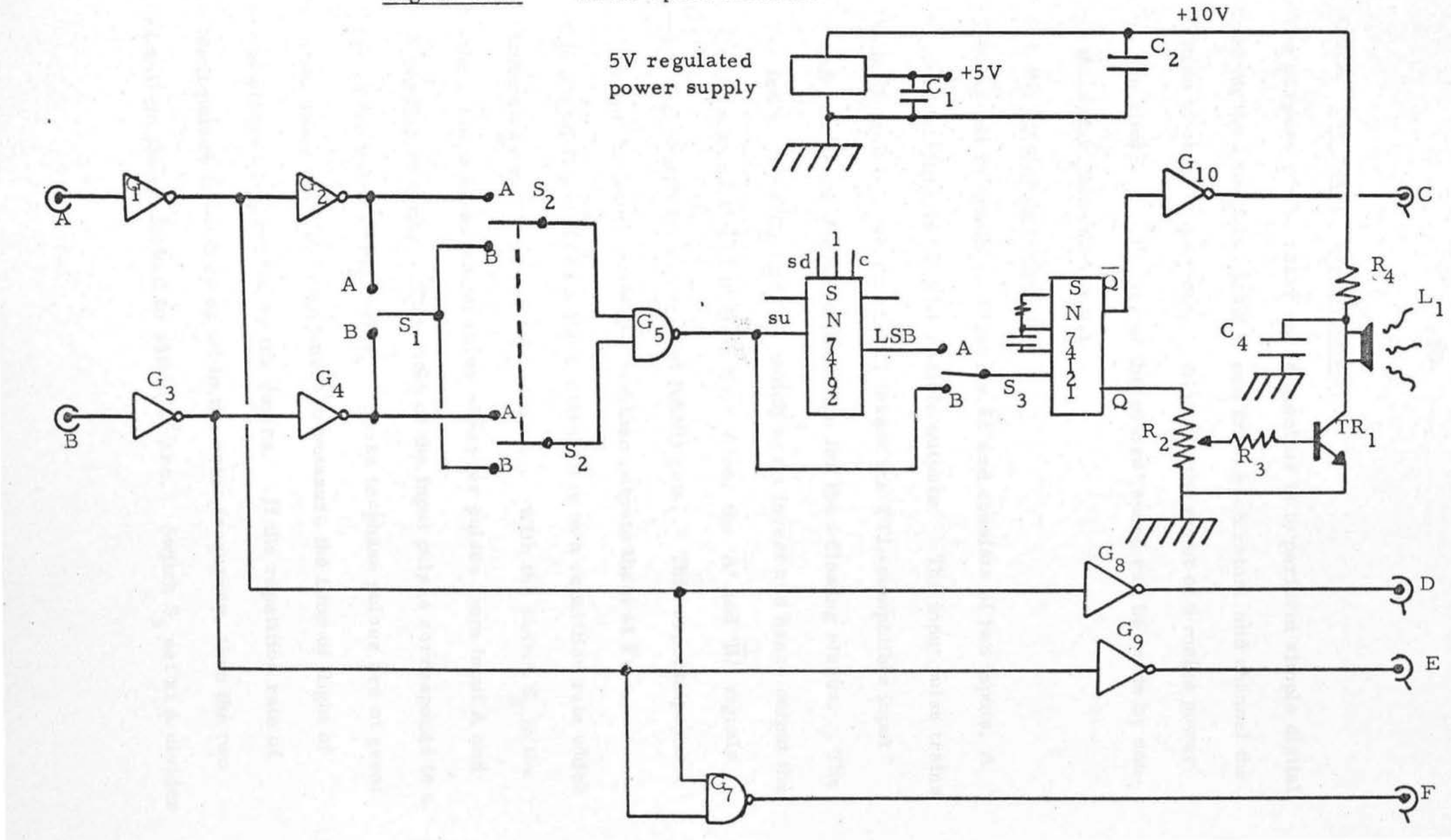

4.4.A The rotor speed monitor.

The purpose of the rotor speed monitor is to perform simple digital functions on the two-pulse trains, one from each rotor, and channel the information to other apparatus. Also, in the event of a mains power failure, the simple monitoring of the rotors' speed can be made by converting the rotor pulses to sound.

4.4.B Circuit description.

The circuit is shown in Figure 4.12 and consists of two inputs, A and B, and four outputs plus an audible outputs. The input pulse trains are fed to G_1 and G_2, which simply invert the TTL-compatible input pulses and produce a degree of isolation for the following stages. The signal is fed to gates G_8 and G_9, which again invert and hence output the input pulses of A on D and of B on E. Also, the '$\overline{A}$' and '$\overline{B}$' signals are fed to G_7, which is a two-input NAND gate. This superimposes both inputs on the same base line and then outputs them at F.

The output C produces a fixed width pulse of a repetition rate which is determined by earlier switch conditions. With the switch S_2 in the A-position, there is an output pulse whenever pulses from input A and input B overlap in time. The width of the input pulses corresponds to a 0.5^{o} arc of the rotor arms' orbit. These in-phase pulses are of great value when using counting equipment to measure the time of flight of pulses of atoms accelerated by the rotors. If the repetition rate of coincident pulses from C is equal to the rotor frequency, then the two rotors will be phase-locked to within 1^{o} arc. Switch S_3 set at A divides

the output frequency from G_5 by two and, in position B, by one. If output C is used to trigger an oscilloscope with output F on the y-axis, then the scope will be triggered whenever input pulses are in phase. If S_2 is set on B, then only one of the input pulses is fed out of C, the selection of which is made by S_1. This enables the switching of S_1 to allow the desired pulse train from output F to be selected and held stationary on the oscilloscope display. This is useful for observation of phase, as the two rotors become phase-locked. The frequency of the rotors is measured using a frequency meter, triggered by the oscilloscope time base and this makes it very convenient to trigger the oscilloscope from the output C to measure the frequency of input pulses from A or B.

The output from C is produced by using G_5, which is a two-input NAND gate which feeds a 4-bit scaler. The output from the least significant bit produces the frequency divide-by-two, which is useful as it corresponds to, in the case of a double-armed rotor, to the rotational frequency. The output from switch S_3 allows triggering of a monostable, which produces a fixed length pulse of 60μs. This was chosen so that, at maximum rotor pulse frequency, 10kHz, the period of the pulses is just greater than the pulse width. The potentiometer, R_2, controls the audible output level from the loudspeaker, which is merely fed by current pulses.

CHAPTER V

THE ELECTRONIC DRIVE FOR ACCELERATION OF THE ROTORS

5.1 Introduction.

The acceleration of the rotors is achieved using a rotating magnetic field, which drives them as an induction motor. The rotating magnetic field is produced by four coils forming the sides of a square with the axis of the coils intersecting with the rotor. Opposite coils are fed with the same sinusoidal current, forming a coil set, and the two sets are fed currents in quadrature. This produces a rotating magnetic field which accelerates the rotor by its interaction with the induced currents within the steel rotor boss. Rotors had previously been accelerated at Birmingham using ex-R.A.F. alternators which could provide rotating fields of 2,600Hz, but, because phase-lock between two rotors and, also, higher rotational speeds were required, it was necessary to produce a reliable electronic drive unit.

5.2 Rotor Drive Torque.

The torque on the rotor is produced, as previously stated, by the interaction of the induced electric currents within the rotor boss and the rotating magnetic field. If the rotor is considered as a small conducting sphere of radius R, positioned in a uniform, rotating, magnetic field, then an approximate relationship can be produced for the drive torque T_r.

If two pairs of coils are used to produce two time varying magnetic fields in quadrature, B_x and B_y, then the rotating vector $\underline{B}$ is given by

$$\underline{B} = \hat{i}B_x + \hat{j}B_y \qquad (5.1)$$

where $B_x = B \cos \omega t$ and $B_y = B \sin \omega t$,

then $\underline{B} = \hat{i} B \cos \omega t + \hat{j} B \sin \omega t$ (5.2)

At some point in time $\underline{B}$ will lie in the x-direction and, if the co-ordinate system is allowed to rotate at the same angular frequency as $\underline{B}$, then $\underline{B}$ will always lie on the x-axis.

Now, to find the torque on the steel sphere in this uniform magnetic field, it is necessary to derive the magnitude and direction of the electric field vector $\underline{E}$.[22] This can be achieved using the relationship

$$\nabla . \underline{E} = \frac{- \partial \underline{B}}{\partial t} \tag{5.3}$$

Simplifying assumptions can be made at this point due to the choice of a rotating co-ordinate system.

Generally, $\underline{E} = \hat{i} E_x + \hat{j} E_y + \hat{k} E_z$, but as the currents that produce the torque in a loop are parallel to $\underline{B}$ and $\underline{\omega}$, then $E_y = 0$ and also, from equation 5.2

$$\frac{- \partial \underline{B}}{\partial t} = \hat{j} B \omega \tag{5.4}$$

One of the solutions for $\underline{E}$, using equation 5.3, is

$$\underline{E} = \tfrac{1}{2} B \omega [- \hat{i} z + \hat{k} x] \tag{5.5}$$

The electric field vector $\underline{E}$ gives rise to circulating currents within the conducting sphere and the current flowing in a conductor of cross-sectional area ΔA is given by:

$$\underline{I} = \frac{\Delta A}{\rho} . \underline{E} \tag{5.6}$$

from $\underline{E} = \rho . \underline{J}$, where ρ is the resistivity of the material.

The force ΔF on a length of loop dl is given by:

$$\Delta F = \underline{J} \wedge \underline{B} (dl . A) \tag{5.7}$$

which generally produces a force per unit length equal to $\underline{I} \wedge \underline{B}$.

Using the above equations, the torque on a general loop in the field can be found and this can then be used to integrate over the surface of a spherical, conducting shell of thickness S, to give the total torque T_r on the shell of

$$T_r = \frac{3}{8} \frac{\pi^2 B^2 R^4 S}{\rho} (\omega_f - \omega_r) \qquad (5.8)$$

where ω_f is the angular frequency of the magnetic field and ω_r is the angular frequency of the rotor.

As the rotor boss is made of solid steel, the time varying magnetic field only penetrates a limited depth into the material and hence the circulating current only flows in a shell. The thickness of the shell is approximately equal to the skin depth S. The low frequency approximation for skin depth is given by:

$$S = \left(\frac{2 \varepsilon_o c^2}{\sigma (\omega_f - \omega_r)} \right)^{\frac{1}{2}} \qquad (5.9)$$

where σ is the conductivity of the material.

This low frequency approximation is only valid if $(\omega_f - \omega_r) \ll 1/t$ and if $(\omega_f - \omega_r) \ll \sigma/\varepsilon_o$, where t is the average time between collisions of free electrons within the metal.

As the skin depth for steel is less than the radius of the rotor, the currents should flow mainly within a shell, governed by the skin depth. This means that the torque is approximately given by, from equation 5.8:

$$T_r = \frac{3}{8} \pi^2 B^2 R^4 c \sqrt{\frac{2 \varepsilon_o}{\rho} (\omega_f - \omega_r)} \qquad (5.10)$$

As it was very difficult to measure the magnitude of the rotating magnetic field with great accuracy, it was not possible to check the

Figure 5.1

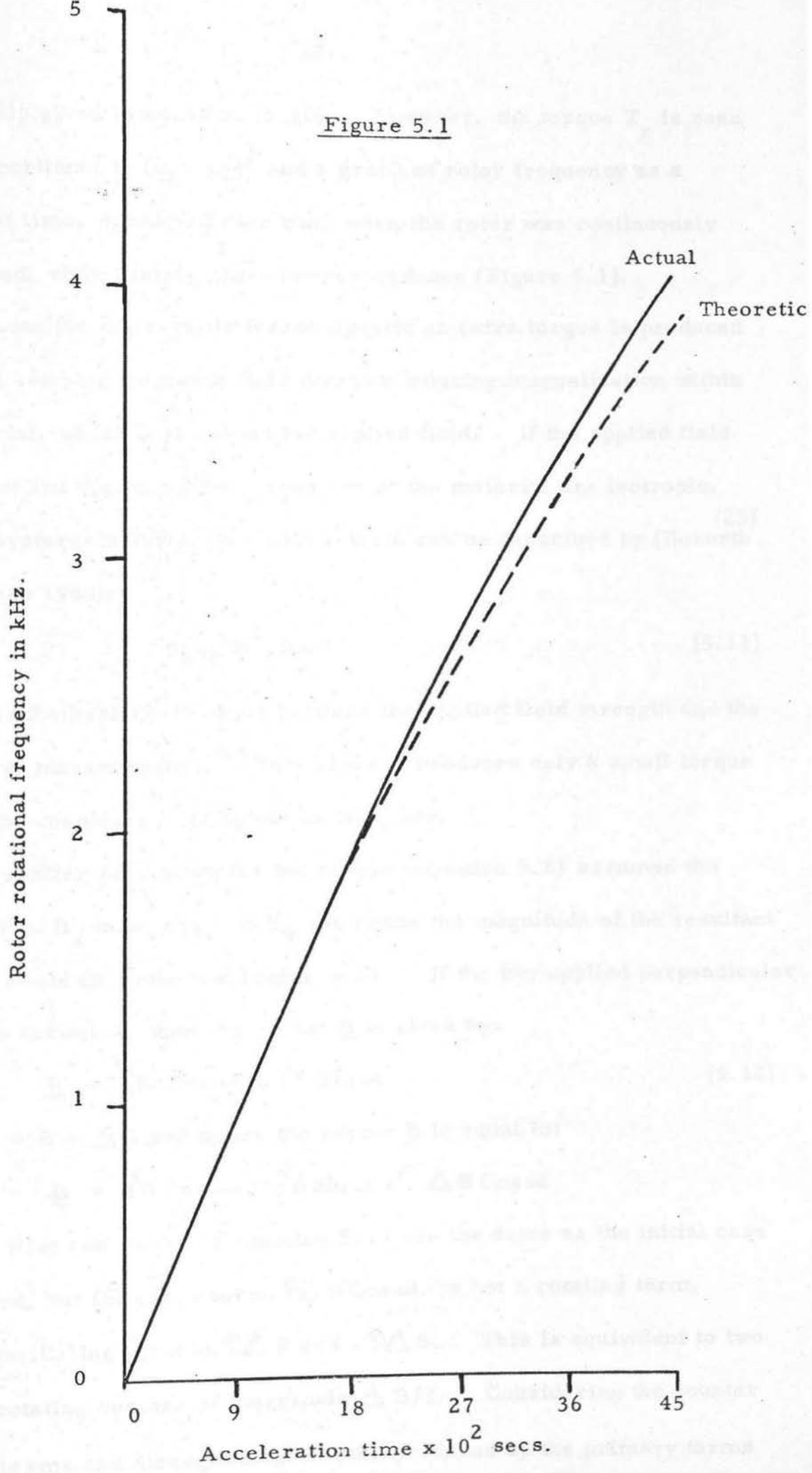
Actual
Theoretic
Rotor rotational frequency in kHz.
0
1
2
3
4
5
0
9
18
27
36
45
Acceleration time x 10^2 secs.

relationship given in equation (5.10). However, the torque T_r is seen to be proportional to $(\omega_f - \omega_r)^{\frac{1}{2}}$ and a graph of rotor frequency as a function of time, during a rotor run, when the rotor was continuously accelerated, shows fairly close correspondence (Figure 5.1).

Because the material is ferromagnetic an extra torque is produced due to the rotating magnetic field directly inducing magnetization within the material, which lags behind the applied field. If the applied field is constant and the magnetic properties of the material are isotropic, then the hysteresis-torque per unit volume can be described by (Bozorth[23] 1951, Jonas 1960):

$$T_h \propto B^2 \sin\theta \tag{5.11}$$

where θ is the hysteresis angle between the applied field strength and the intensity of magnetization. This process produces only a small torque and may be considered negligible in this case.

The earlier derivation for the torque (equation 5.8) assumed the magnitude of B_x to be equal to B_y and hence the magnitude of the resultant vector $\underline{B}$ would describe a circular orbit. If the two applied perpendicular fields are not equal, then the vector $\underline{B}$ is given by:

$$\underline{B} = \hat{i}B' \cos\omega t + \hat{j}B \sin\omega t \tag{5.12}$$

where $B' = B + \Delta B$ and hence the vector $\underline{B}$ is equal to:

$$\underline{B} = \hat{i}B \cos\omega t + \hat{j}B \sin\omega t + \hat{i}\,\Delta B \cos\omega t$$

The first two terms of equation 5.13 are the same as the initial case considered, but the extra term, $\hat{i}\Delta B \cos\omega t$, is not a rotating term, merely oscillating between $\hat{i}\Delta B$ and $-\hat{i}\Delta B$. This is equivalent to two counter rotating vectors of magnitude $\Delta B/2$. Considering the counter rotating terms and disregarding torque, produced by the primary terms

of equation 5.13, the rotor, rotating with some frequency ω_r, experiences two torques. The first is an accelerating torque proportional to $(\omega_f - \omega_r)^{\frac{1}{2}}$ and the second is a decelerating torque proportional to $(\omega_f + \omega_r)^{\frac{1}{2}}$. From this it can be seen that an imbalance in the applied magnetic fields produces a net braking torque on the rotor proportional to $[(\omega_f - \omega_r)^{\frac{1}{2}} - (\omega_f + \omega_r)^{\frac{1}{2}}]$. This can be approximated, if $\omega_r/\omega_f \ll 1$, to the retarding torque T_r being proportional to $\triangle B^2 \omega_r/(\omega_f)^{\frac{1}{2}}$. Therefore, for maximum efficiency it is necessary to adjust the field contribution from each coil set so that the fields are as equal as possible.

The uniformity of the magnetic fields is limited because of the physical layout, the coils being far from the ideal Helmholtz criterion, i.e. the radius of the coil equal to the spacing of the coils. The radius of the coils equals 55mm and the spacing is 140mm. This means that the magnitude of the magnetic field at the centre of the configuration is reduced to 0.33 of the value produced by a true Helmholtz configuration, using the same diameter coils. This also reduces the uniformity of the magnetic field within the volume occupied by the rotor boss.

5.3 Rotor Heating.

The currents that cause the acceleration also cause heating and a calculation for heat dissipation, E_h, within the rotor, assuming the heat input to be solely due to I^2R losses within the steel, yields the relationship for a spherical conducting shell:

$$E_h = \frac{3}{8} \frac{\pi^2 B^2 (\omega_f - \omega_r)^2 R^4 S}{\rho} \qquad (5.14)$$

and by comparison with equation 5.8 gives:

$$E_h = T_r (\omega_f - \omega_r) \qquad (5.15)$$

The torque T_r is related to the angular acceleration, α, by the relationship $T_r = I\alpha$, where I is the moment of inertia of the rotor. If the initial acceleration rate of the rotor is α_o and the rotor is stationary and subject to an accelerating torque, then the average temperature rise per unit time K_r is:

$$K_r = \frac{I\alpha_o \omega_f}{M_r c} \qquad (5.16)$$

where M_r is the mass of the rotor, c is the specific heat capacity and ω_f is the angular frequency of the magnetic field, in Rad/sec. The initial temperature rise of the rotor was measured as a function of time, when α_o equalled 0.8Hz/sec. This gave an initial temperature rise of 1.5K/min., which agrees closely with the initial temperature rise per unit time, given by equation 5.16, of 1.54K/min.

5.4 The Electronic Drive Unit.

The electronic drive unit was initially designed by J.H.B. and constructed by the author. This initial design was modified by the author to increase certain aspects of reliability and also to allow digital control of the direction of the rotating magnetic field.

5.4A The Basic Unmodified Circuit.

The drive unit consisted of two identical channels which provided independent drive for two rotors. Therefore only one channel will be described.

A square-wave oscillator running at 10kHz was gated and the frequency divided by two. This produced two sets of square-wave pulses at 5kHz, with a phase difference of $\pi/2$. These pulses were then fed to a switch, which was used to change the relative phase of the two pulse trains and

then to an R.T.L. gate, which had an external input, allowing the pulses to be isolated from the next section.

The next stage comprised two variable pulse length monostables which enabled the length of the pulses to be varied from 0 to 0.1mS. These were then used to pulse two banks of ten transistors each to drive the two coil sets, having a current phase relationship of $\pi/2$. The drive coils had a secondary which was tuned to 5kHz using a capacitor bank and hence the primary windings in the collectors of the transistor banks appeared to be purely resistive and therefore large currents could flow through the coils.

5.4B A detailed description of the modified electronic drive unit.

The low power section of the drive unit is supplied by a 3.6V, 10A supply and the high power stages, producing the output drive currents, are supplied by a 30V, 60A DC supply. There is also a 5V supply, which has been added to provide power for TTL, used in the modified sections.

Initially the drive oscillator at 10kHz was powered by the 3.6V supply but due to current pulses being drawn from it to provide base current for the output transistors, the oscillator frequency was 'pulled' and produced instability. When the frequency of the oscillator changed, the frequency of the current pulses did not trigger the tuned coils at the correct time and this resulted in phase shifts in current and voltage, which produced excessive dissipation in the output transistors and hence a proportional reduction of power transferred to the coils.

The drive unit was initially designed to drive the two rotors independently but with a common driving frequency of 5kHz. However, it was found that, if two rotors were set up in the double rotor vessel with their

Figure 5.2

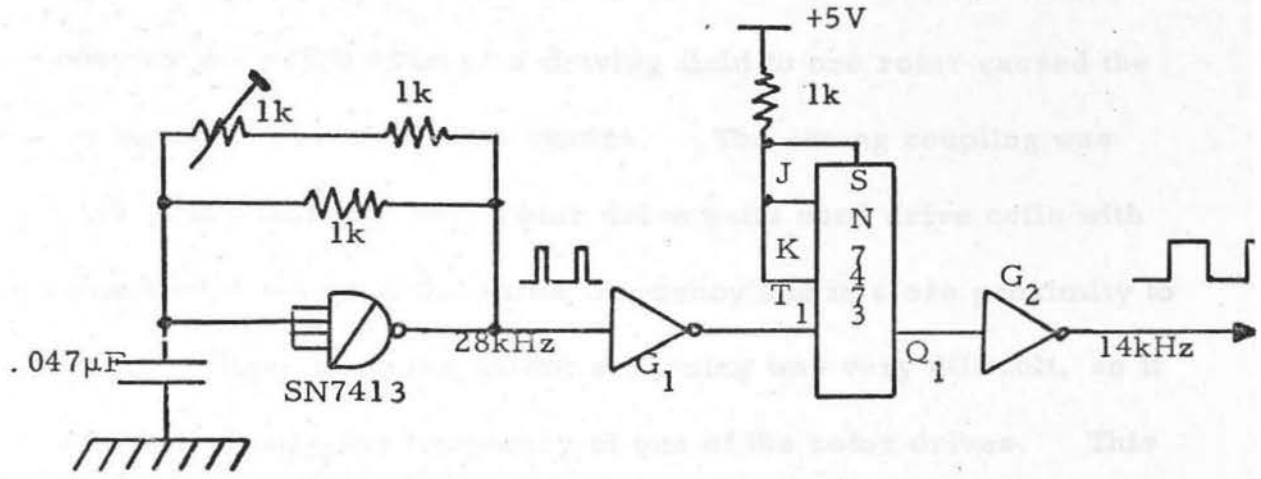
+5V
1k
1k
1k
1k
J
K
S
N
7
4
7
3
T1
G2
.047μF
SN7413
28kHz
G1
Q1
14kHz

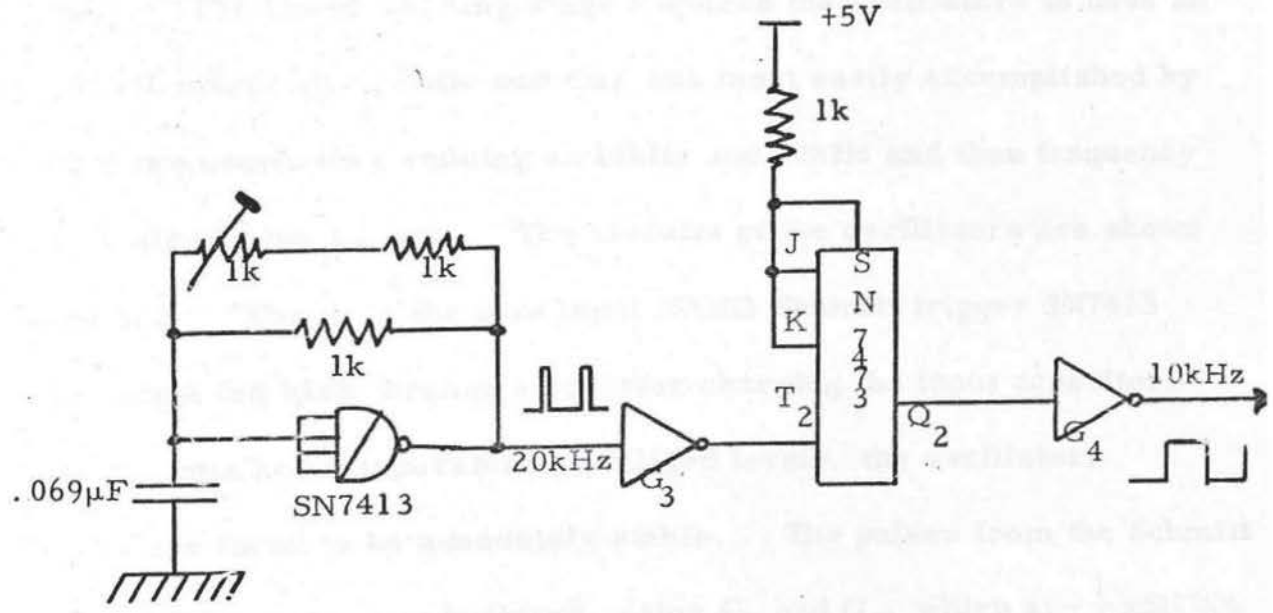
+5V
1k
1k
1k
1k
J
K
S
N
7
4
7
3
T2
10kHz
.069μF
SN7413
20kHz
G3
Q2
G4

respective drive coil sets, strong drive coupling took place between the rotors. This coupling made the independent control of the rotors impossible as the application of a driving field to one rotor caused the torque to be shared between both rotors. The strong coupling was mainly due to the fact that both rotor drive units used drive coils with their secondaries tuned to the same frequency and in close proximity to one another. Lack of space meant screening was very difficult, so it was decided to change the frequency of one of the rotor drives. This means that one rotor has a rotational field of frequency 5kHz and the other of 7kHz. Consequently the capacitor bank for tuning the 7kHz drive coil sets had to be changed and also an independent oscillator produced to run at 14kHz. Because of the frequency 'pulling' effect mentioned earlier, the 10kHz oscillator was also replaced and both were run off a stabilised 5V supply. The phase-shifting stage requires the oscillators to have an accurate 1:1 mark/space ratio and this was most easily accomplished by producing two oscillators running at 28kHz and 20kHz and then frequency dividing their outputs by two. The circuits of the oscillators are shown in figure 5.2. They use the four input NAND Schmitt trigger SN7413 with the output fed back through a resistor charging the input capacitor. Because the gate has temperature stabilised levels, the oscillators produced were found to be adequately stable. The pulses from the Schmitt trigger oscillators are then buffered, using G_1 and G_3, which are $\frac{1}{6}$ xSN7404. The pulses then feed the clock inputs of two independent J-K flip-flops. The J and K inputs are held high, which causes the outputs Q_1 and Q_2 to toggle at half the frequency applied to the clock inputs T_1 and T_2. The outputs from the JK's are then buffered by gates G_4 and G_2 and the outputs

Figure 5.3

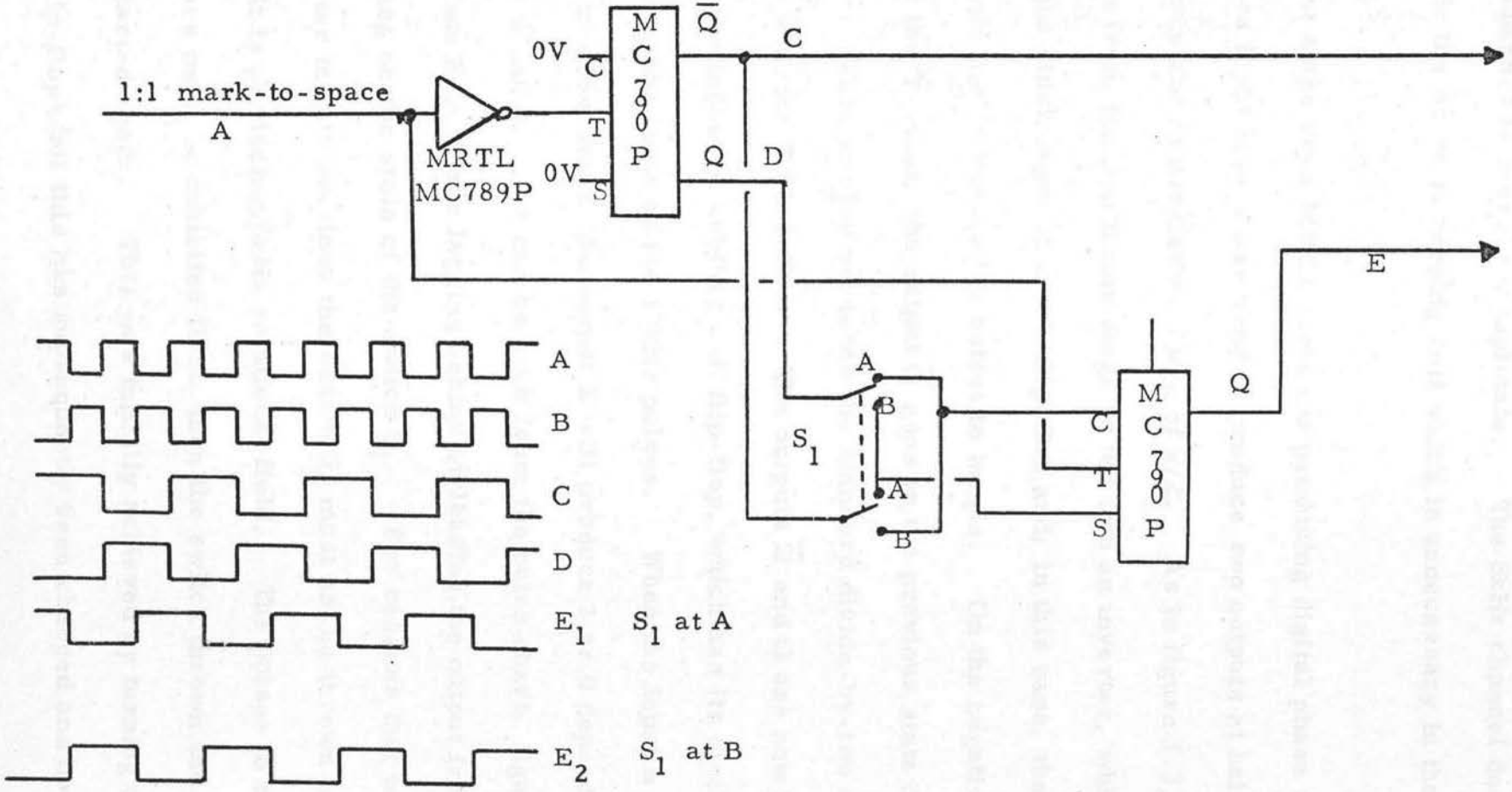
1:1 mark-to-space
A
MRTL
MC789P
0V
C
T
0V
S
MC790P
$\overline{Q}$
C
Q
D
E
A
B
S_1
A
B
C
T
S
MC790P
Q
A
B
C
D
E_1
S_1 at A
E_2
S_1 at B

fed to the next section. The frequency outputs show no 'pulling' effect when the drive unit is operational.

Only a description of the 5kHz drive channel will follow, as the 7kHz drive channel is merely a duplicate. The 5kHz channel does, however, include the drive reversing unit which is unnecessary in the other channel.

The next stage uses MRTL logic for producing digital phase shifting. In the process input pulses are used to produce two outputs at half the input frequency and at a relative phase of $\pi/2$. As in figure 5.3, the 10kHz output from the oscillator stage is fed into an inverter, which feeds pulses into the clock input of a J-K flip-flop and, in this case, the C and S inputs are held low to enable the output to toggle. On the negative transition of the T-input, the output $\overline{Q}$ goes to the previous state of Q and Q goes to $\overline{Q}$. This simply produces the standard divide-by-two action used earlier with the TTL J-K's. The outputs $\overline{Q}$ and Q are now fed via switch S_1 to the inputs of another J-K flip-flop, which has its clock connected to A, the input of the 10kHz pulses. When the input A changes from a high to a low state, the output E will produce 1 or 0 depending on the inputs of C and S. As can be seen from the pulse chart, figure 5.3, the output from E is either lagging behind or leading the output from C by $\pi/2$, depending on the state of the switch S_1. For reasons that will be described later in this section, the switch S_1 must not be thrown while the drive unit is producing a 5kHz rotational field. The pulses to the output transistors must be inhibited first, then the switch thrown and finally the pulses started again. This was initially achieved by turning off power to the J-K flip-flops, but this has subsequently been changed and now a

switch in the next stage inhibits these pulses.

The next stage is one which enables the direction of the drive torque to be reversed, using a TTL logical level input, the direction of the rotating magnetic field being defined by the logic level. It will be seen from the pulse chart, Figure 5.3, that the action of the switch S_1 is merely to negate the output E and hence reverse the direction of the driving field. However, the pulses must be isolated from the output stage during this change-over period. The first operation that must be performed by the logical reversing unit is therefore to inhibit the drive. After this has been done, the phase of the pulses can be altered and then a short period of time must elapse to allow oscillating currents in the tuned circuit to collapse before the inhibit is removed. The reason for inhibiting the pulses to the output transistors during phase-reversal is to prevent the pulsing of the output transistors at the wrong part of the oscillating current cycle, in the secondary of the drive coils. The power supply to the output transistor is derived from a 30V supply but because the collector load is a tuned circuit, it is possible for the collectors of the output transistors to reach 60V during the cycle. The voltage limit of the output transistors is 60V but if a sharp current pulse were drawn by the transistors, then this could cause secondary breakdown, resulting in the possible failure of ten transistors. The lower trace of plate 5.1 shows the decaying voltage on the collector of the drive transistors, when the drive pulses have been turned off. It can be seen that the amplitude of the oscillation has decayed to approximately $\frac{1}{5}$ of the peak amplitude after a time period of 2ms and this is then small enough to enable the output transistors to be turned on without being damaged. The oscillating

Figure 5.4

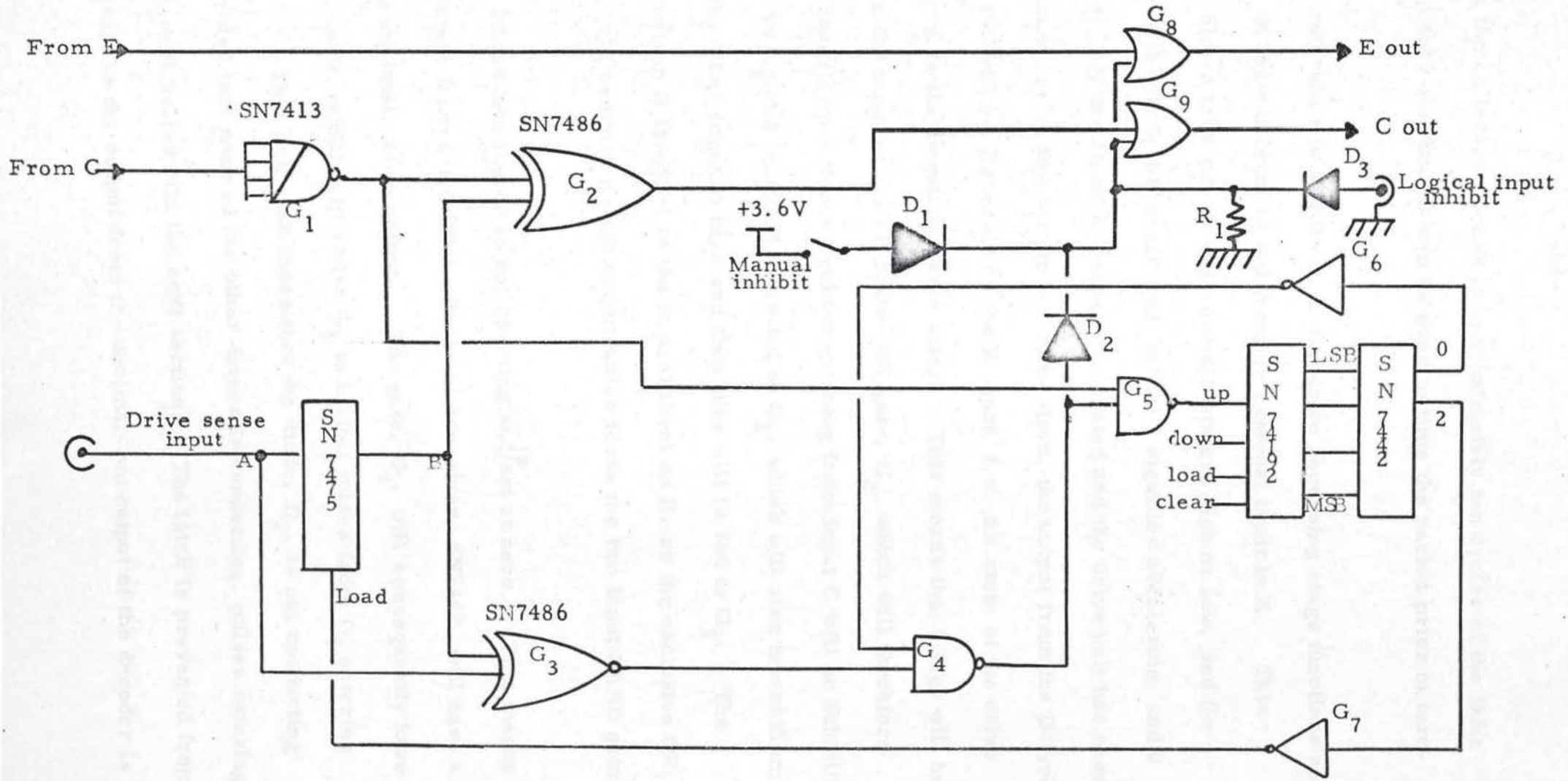
From E
E out
G8
G9
SN7413
SN7486
From C
G1
G2
C out
D3
Logical input inhibit
+3.6V
D1
R1
Manual inhibit
G6
D2
LSB
0
G5
up
down
load
clear
SN7192
SN7442
MSB
2
Drive sense input
A
B
SN7475
Load
SN7486
G3
G4
G7

voltage on the collector decays in approximately ten cycles of the 5kHz drive frequency and thus it can be used to time the period prior to turn-on.

With reference to Figure 5.4, the drive reversing stage functions as follows: A logical level is fed from an external input to A. This logical level can take one of two possible states, high or low, and for convenience it will be assumed that logical 1 signifies accelerate, and 0 decelerate. If the rotor is being accelerated and the drive unit has been applying an accelerating torque for some time, the output from the D-type latch SN7475 will be the same as the A input, i.e. the state of the drive will be equal to the required drive state. This means that a high will be present on the input of the exclusive OR gate, G_2, which will therefore act as an inverter. Hence, pulses entering from input C will be Schmitt triggered by G_1 and inverted, then fed to G_2, which will also invert them, because the other input is high and then they will be fed to G_9. The logical level on A is equal to the logical level on B, so the exclusive OR gate, G_3, will produce a high output which feeds the two input NAND gate, G_4.

The BCD 4-bit scaler is not counting and is set at zero. This means that the output from the BCD-to-Decimal converter, SN7442, will have a low on its decimal, zero output. The gate, G_4, will consequently have two high inputs, which will cause G_5 to inhibit pulses from G_1 entering the scaler. This will also mean that the diode, D_2, is not conducting and, provided that none of the other diodes is conducting, pulses entering G_9 and G_8 will be fed into the next section. The latch is prevented from loading because the output from the decimal-two output of the decoder is

high, which causes the load input to be held low. The latch will load the logic level that appears on the input A into the output at B, when the load input is high.

Now, if it is required to change the drive state to decelerate, then this will be indicated by the input of the latch becoming low. The actual drive torque now no longer agrees with the desired torque and therefore the output of G_3 goes low. This results in the output of G_4 going high and causes the diode, D_2, to conduct, inhibiting the output pulses and hence removing the torque applied by the drive unit. Also, pulses from G_1 can feed G_5, which inverts and then feeds them to the up input of the scaler. After the first pulse has entered the scaler, the decimal-zero output of the decoder goes high and this holds the output of G_4 high independent of the output from G_3. When the scaler has counted two pulses, the load on the input of the latch goes high and loads the new logic level present on input A. The output from the latch will now be low and therefore the output of G_3 will produce a high, because the two inputs are equal. This will not, however, change the output of G_4 and so the output pulses will still be inhibited. Because the output of the latch is now low, the gate G_2 no longer inverts pulses but merely feeds the input pulses to its output. Therefore, the phase reversal has been accomplished, but the output transistor cannot be turned on until the inhibit has been removed. The scaler counts up to '3' and this causes the load input on the latch to return to a low state. Counting continues up to '9' and then the scaler automatically sets itself on zero. As the scaler is once again on '0', the decoded output from the decimal-zero output goes low and this prevents subsequent pulses from entering the scaler. Also, because this is

Figure 5.5

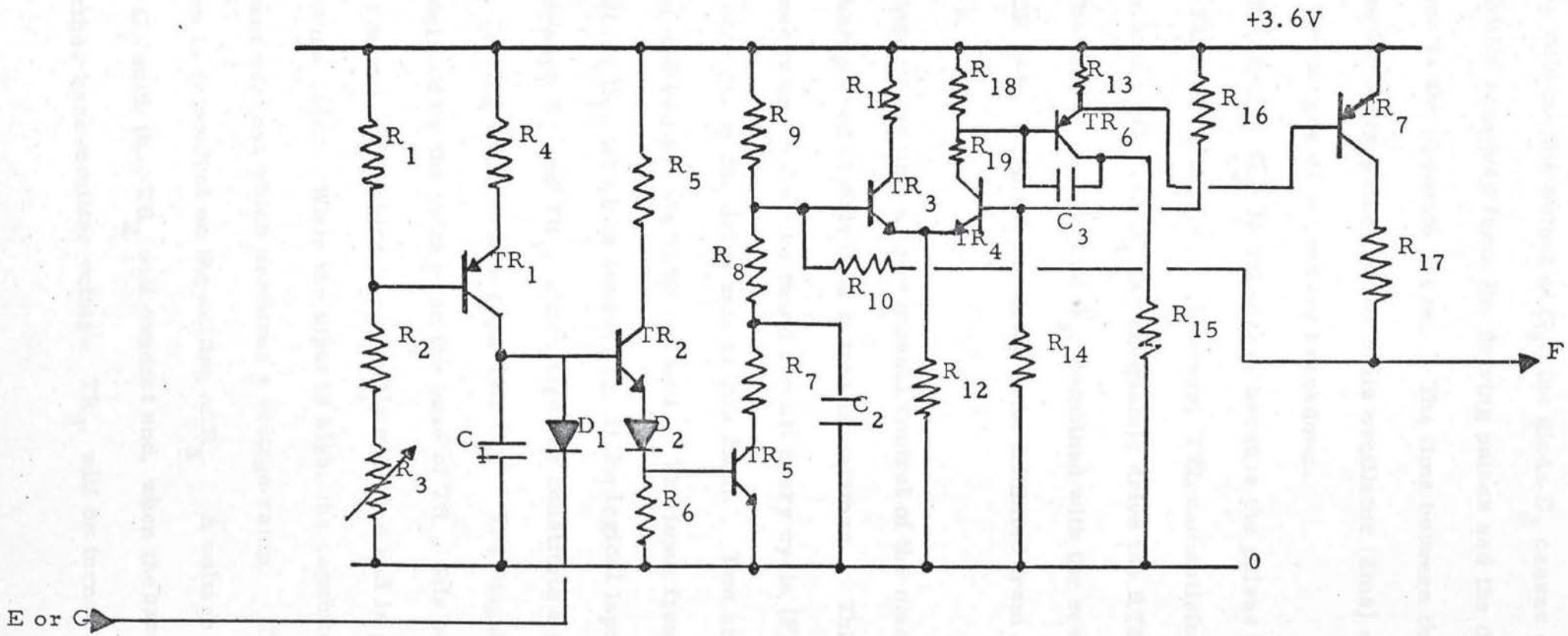
+3.6V
R1
R4
R5
R9
R11
R18
R13
R16
R19
TR6
TR7
TR3
TR4
C3
R17
TR1
R8
R10
R2
TR2
R7
C2
R12
R14
R15
F
C1
D1
D2
TR5
R3
R6
0
E or G

accompli shed by raising the output of G_4, the diode D_2 ceases conduction. Hence, the inhibit is removed from the driving pulses and the drive now produces a torque in the opposite sense. The time between the inhibit and turn-on is equal to ten pulses of the 5kHz oscillator (2ms) and hence this minimises the danger of secondary breakdown.

The Schmitt trigger, G_1, is necessary because the pulses have to be changed from RTL to TTL levels. However, TTL can satisfactorily drive RTL gates and so G_2 and G_4 can adequately drive the RTL gates, G_8 and G_9. The diodes D_1, D_2 and D_3, combined with the resistor R_1, form a type of OR gate, enabling the drive to be inhibited from one of three possible sources.

The next stage of the unit allows manual control of the mark/space ratio of pulses being used to drive the output transistors. This alters the amount of energy applied to the tuned circuit every cycle (Figure 5.5). There are four circuits in the drive unit of this form. Two are used for the 7kHz channel and two for the 5kHz channel. The input from E or C enters through diode D_1, which is conducting, if the logical input is low. Current flows through R_4 and TR_1, which together constitute a constant current source, feeding current into capacitor C_1. The magnitude of this current is defined by the voltage on the base of TR_1, this being adjusted by the variable control, R_3, which is manually operated and is accessible from the front of the unit. When the input is high, the capacitor C_1 is fed with a constant current which produces a voltage ramp. The rate of rise of this ramp is dependent on the setting of R_3. A voltage will be reached across C_1 such that TR_2 will conduct and, when the base voltage has risen, a further base-emitter voltage, TR_5, will be turned on. This

Figure 5.6

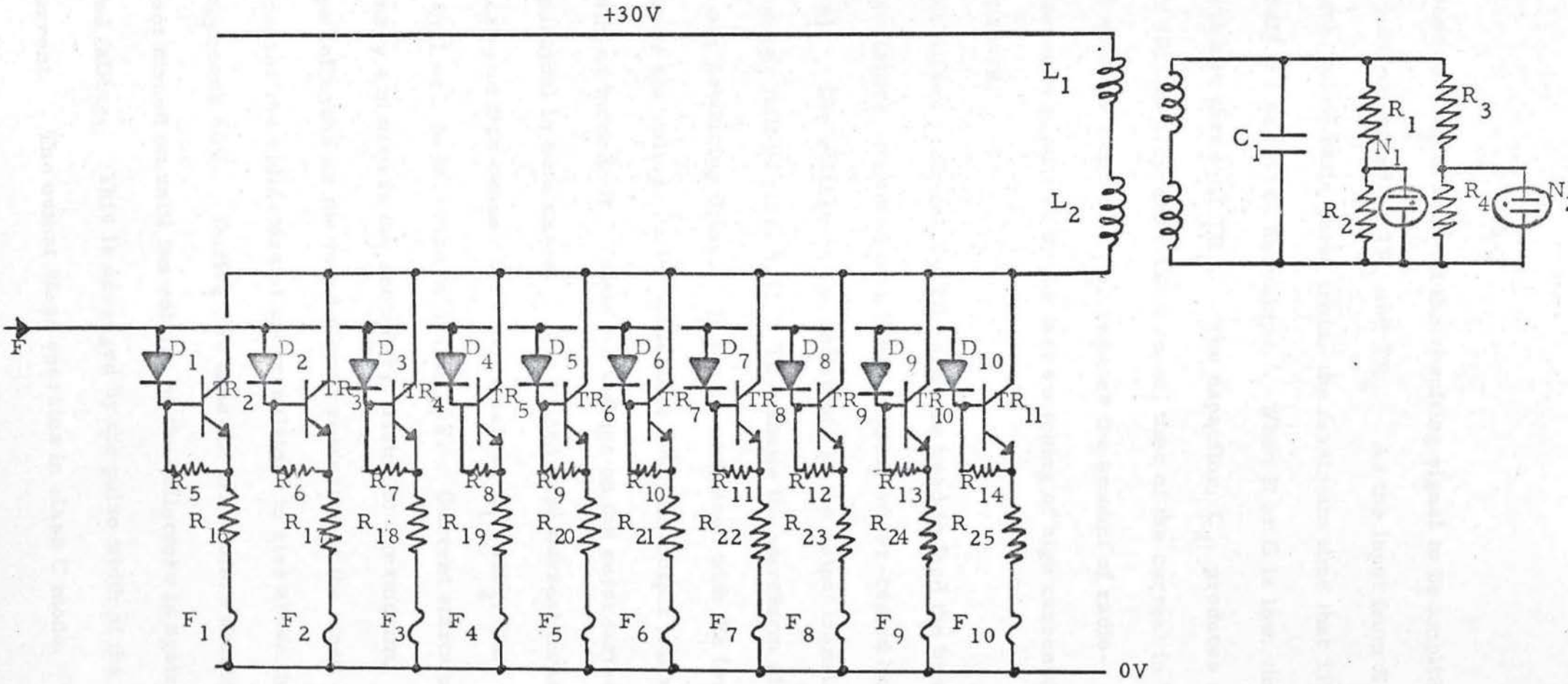
+30V
L1
L2
C1
R1
R2
R3
R4
N1
N2
F
D1
D2
D3
D4
D5
D6
D7
D8
D9
D10
TR1
TR2
TR3
TR4
TR5
TR6
TR7
TR8
TR9
TR10
TR11
R5
R6
R7
R8
R9
R10
R11
R12
R13
R14
R15
R16
R17
R18
R19
R20
R21
R22
R23
R24
R25
F1
F2
F3
F4
F5
F6
F7
F8
F9
F10
0V

will cause the base of TR_3 to fall and the resulting signal to be amplified by the long tail pair produced by TR_3 and TR_4. As the input from E or C is an even mark/space ratio pulse train, the maximum time that TR_2 can conduct is half the period of the pulses. When E or C is low, the diode D_1 conducts and turns off TR_2. The capacitor, C_2, produces a time constant of 30μs to slow down the turn-off time of the current in TR_7. This, combined with the capacitor C_3, reduces the amount of radio-frequency interference produced by the fast switching of high currents in the output transistors.

The current pulses produced by TR_7 are now used to feed the bases of ten power transistors, mounted on a large copper, water-cooled heat sink (Figure 5.6). The voltage on the collectors of the output transistors is shown in the upper half of plate 5.1. This shows the waveform when the transistors are producing drive. It can be compared with the lower trace, which shows the voltage on the collectors when the output transistors have just been turned off. Note the voltage on the secondaries of the drive is sinusoidal in both cases. The pulsed base current turns on all ten transistors and this causes the voltage across L_1 and L_2, the primaries of a coil set, to increase to nearly 30V. Current starts to flow in the primary and also in the secondary, rising to a maximum. Then the voltage collapses as the tuned circuit resonates at the tuned frequency and causes the collectors of the transistors to rise above the +30V rail and approach 60V. During this time the transistors should be turned off and not turned on until the voltage on the collectors is again +30V or less and falling. This is arranged by the pulse width of the base driving current. The output stage operates in class C mode. This

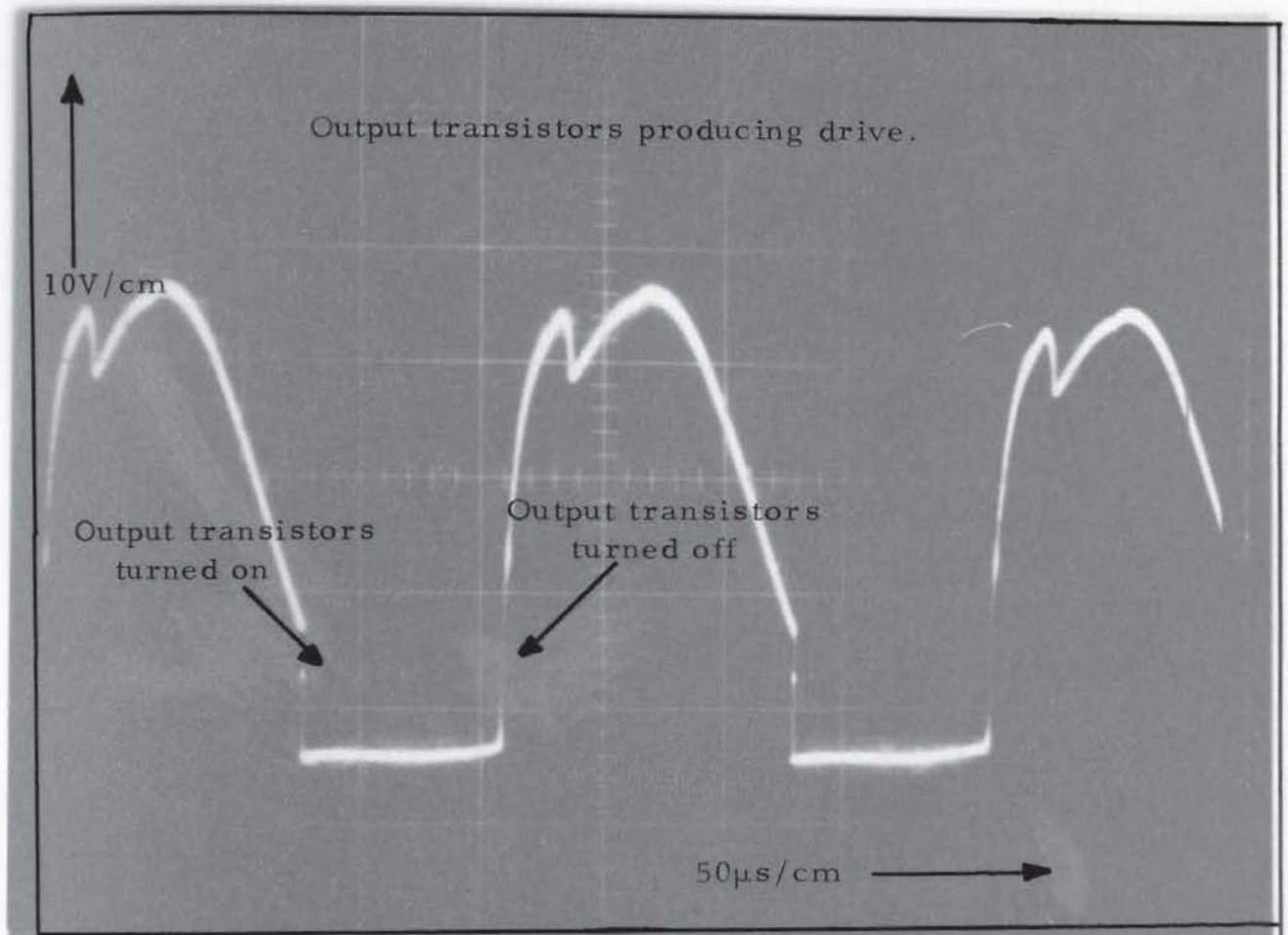

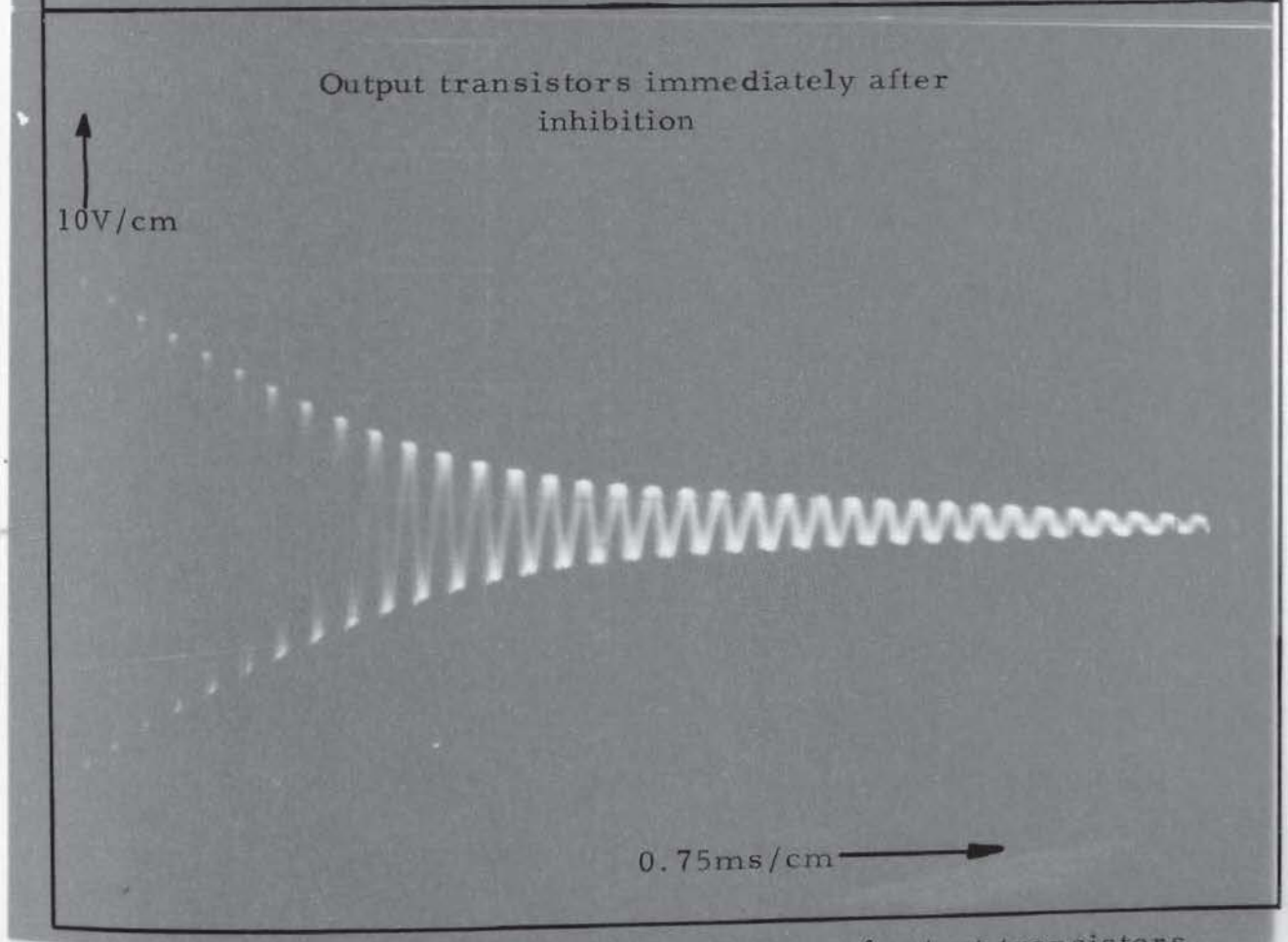

PLATE 5.1 Voltage waveform on collector of output transistors.

mode of operation is very efficient as the transistors are either turned fully on or fully off. However, the base current pulses are slowed down to prevent r.f. interference, as previously stated, and as the power transistors have a limited frequency response, there is a finite transition time between the two states. This causes dissipation within the transistors and hence a considerable heating effect.

Resistors, R_{16} to R_{25} are included in the emitters to compensate for variations in the current gain of the power transistors and also to allow for variations in base-emitter voltages. The resistors, R_5 to R_{14} are used to ensure that the output transistors are turned off when TR_7 is not conducting. Base current flows through diodes D_1 to D_{10}, which prevents all the transistors being held 'on' if a short should develop in one of the transistors between collector and base. If a short were to develop between collector and emitter, the relevant fuse would fail and the diodes would again prevent current flowing from collector to emitter and then through the base resistors, thereby turning on the transistors. This circuit is repeated for the other drive coil set, using 5kHz pulses but with a different phase.

Each drive coil consists of 2.5 turns of $\frac{1}{8}$" copper pipe, to constitute the primary, while the secondary is made up of 100 turns of 18 gauge, enamel-covered, copper wire. The primary has cold water flowing through it to provide cooling. The secondaries are potted in epoxy resin. This is necessary to provide added insulation as the voltage, on the secondary, peaks at over 1kV. This high voltage also provides problems for C_1, which has to be a high voltage type. The value of C_1 is approximately 0.29μF for the 5kHz drive and is composed of a series-parallel

Figure 5.7

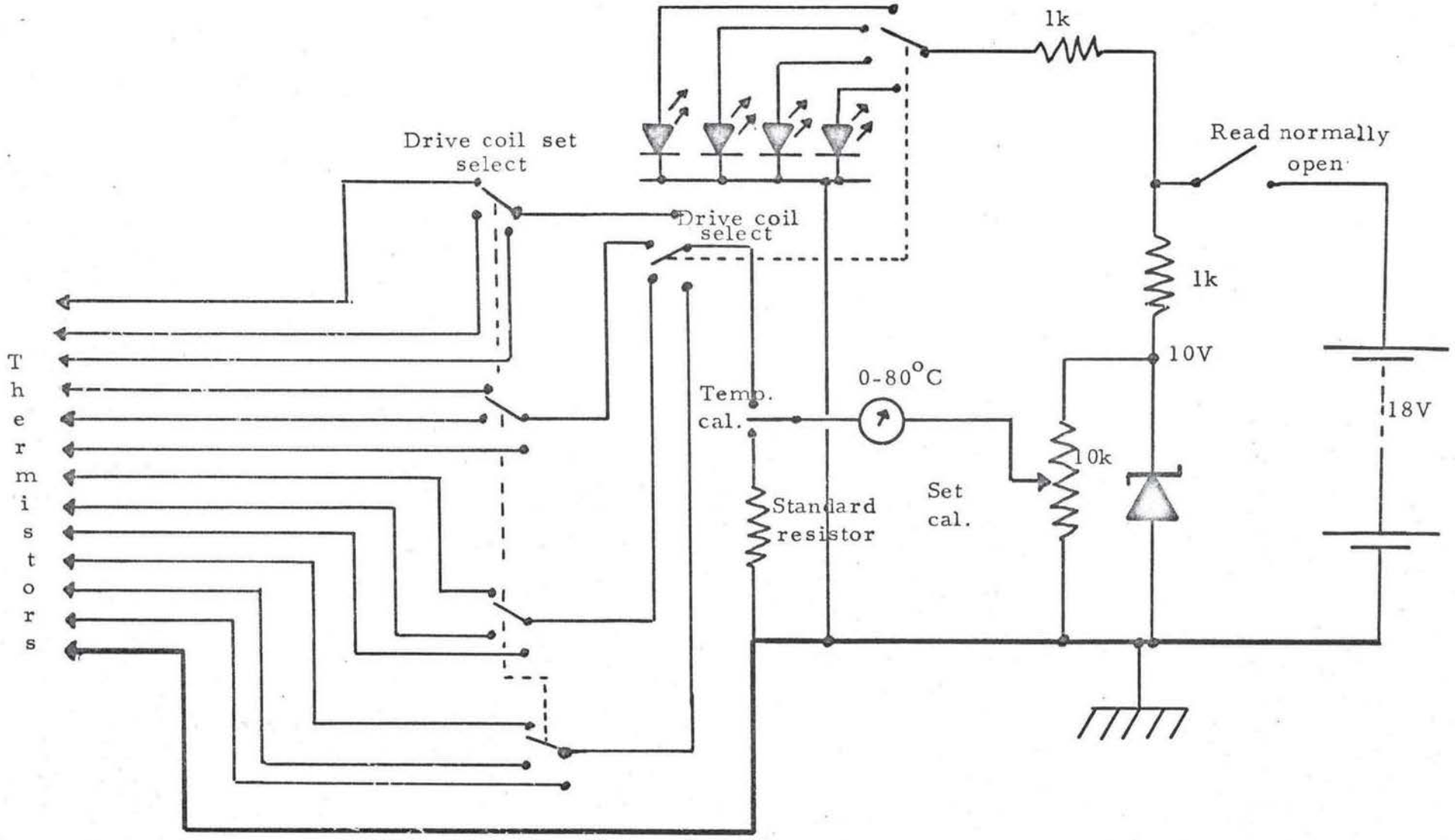
1k
Drive coil set select
Drive coil select
Read normally open
1k
10V
18V
Thermistors
Temp. cal.
0-80°C
10k
Standard resistor
Set cal.

configuration of 1000pF capacitors rated at 600V, the inductance of the coils being approximately 1.8mH each. Mica capacitors are used as the heating effect, due to the loss angle of the dieletric, at high frequencies and currents would make many other types impracticable. Neon indicators, N_1 and N_2, are set to trigger at 300V and 600V, indicating that the drive coil set is functioning correctly.

Final adjustment of each drive channel is achieved by connecting two AC volt meters to the secondary circuit of each coil set. Adjustment is then made of the relevant oscillator frequency, such that both voltages are at a maximum. This has to be done with great care as the output transistors can easily be destroyed if the oscillator frequency differs greatly from the tuned frequency of the coils.

The total RMS current flowing in the primaries of one complete drive channel operating with a fifty percent duty cycle, is 24A and if the tuning is correct, such that the load appears to be purely resistive, then the total power delivered by one rotor drive channel to the coils, is approximately 600W. Due to the currents and the powers involved, a water pressure-sensing switch was fitted to the water supply, cooling the heat sink. This ensures that the electronic drive unit cannot be used unless the water supply is cooling the transistors. The voltage rating of the transistors is reduced if their temperature rises above 25°C and hence the water-cooling is essential. Also, in consideration of the high currents flowing in the primaries and secondaries of the drive coils, causing a large heating effect, calibrated thermistors were attached to the drive coils and, with the aid of a simple circuit (Figure 5.7) the temperature of each coil can be measured during a rotor run. This is necessary as the

Figure 5.8 Acceleration of rotor as a function of time for continuous accelerating drive.

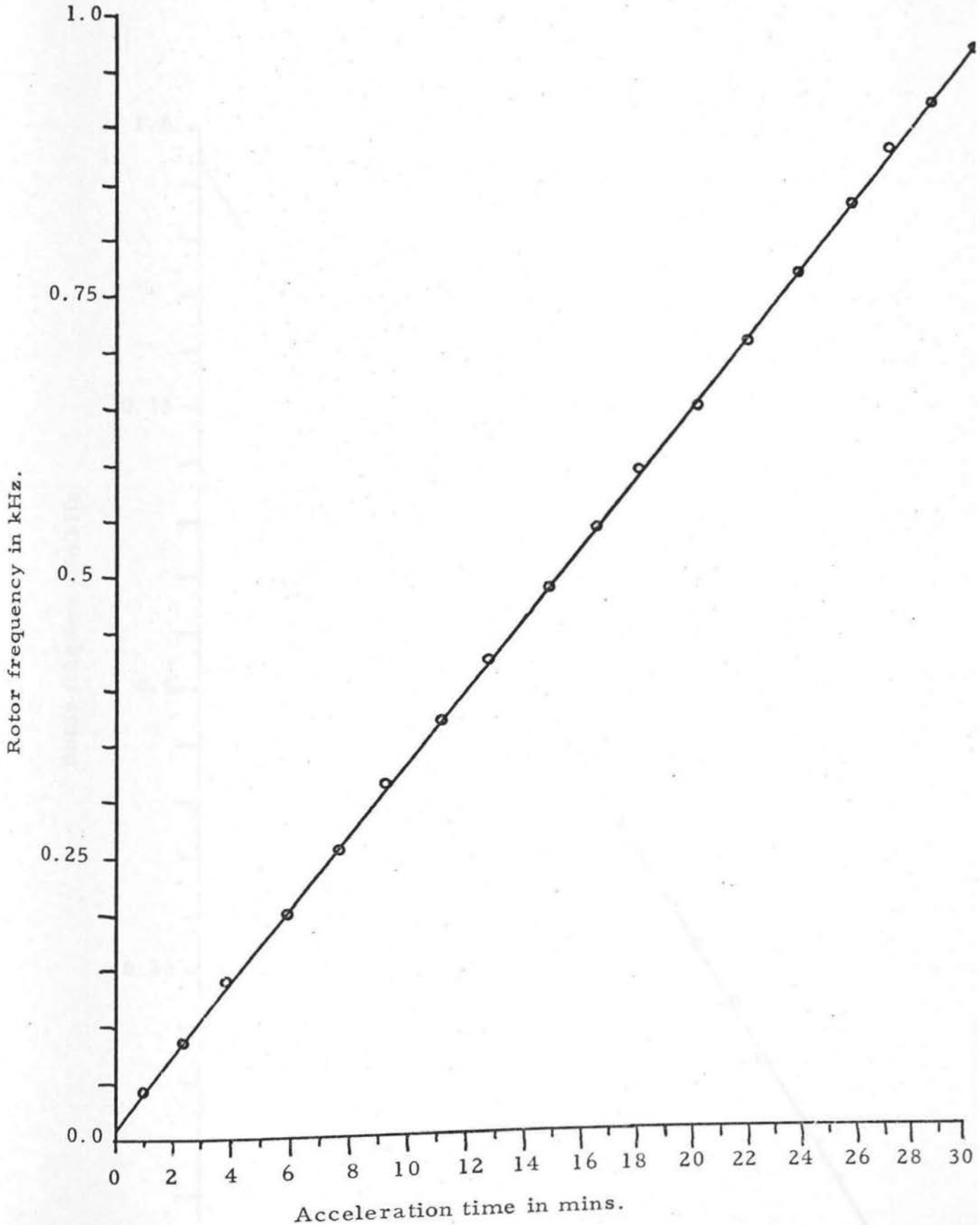

Figure 5.9 Deceleration of rotor as a function of time for continuous decelerating drive.

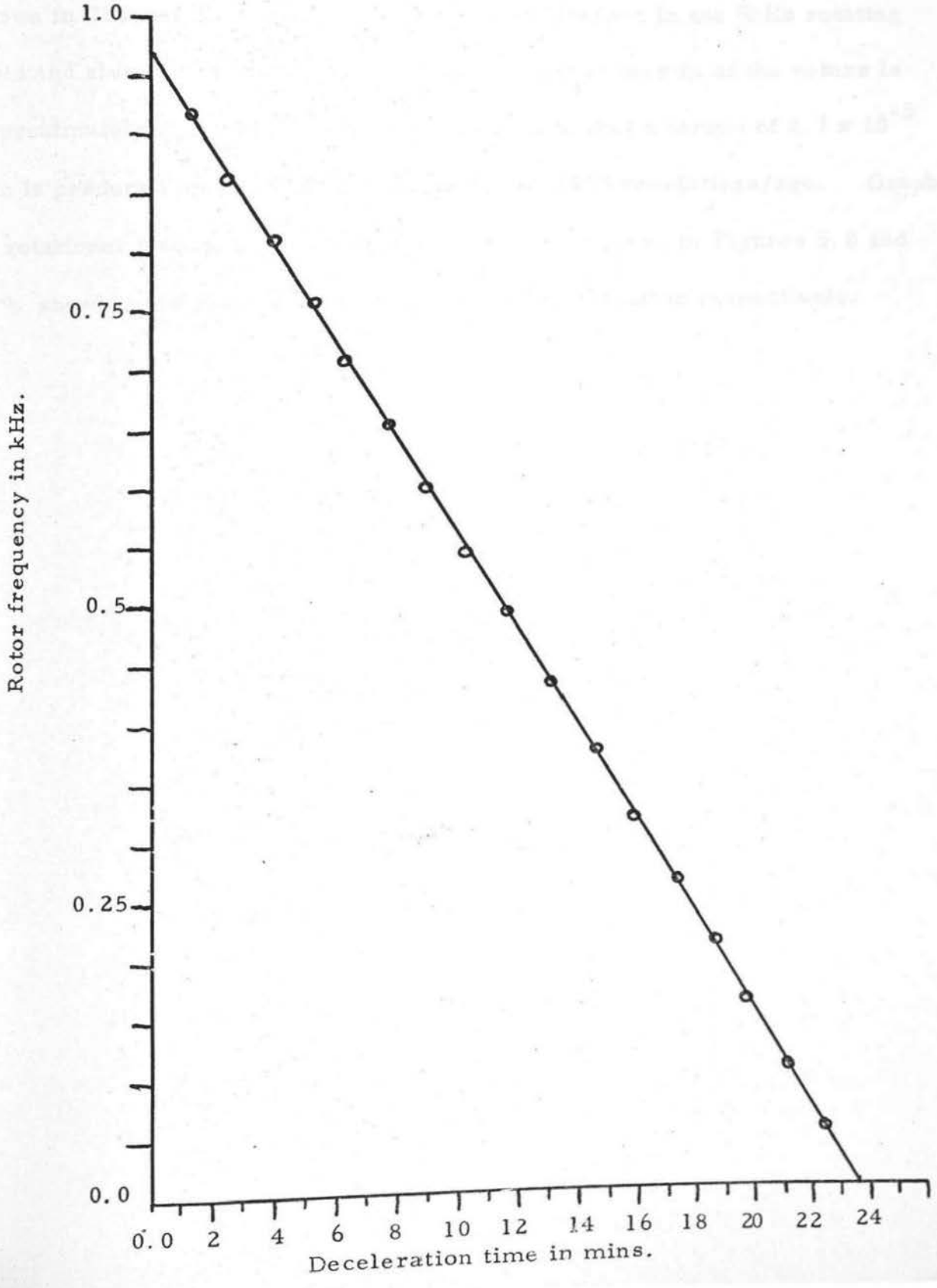

epoxy resin, in which the drive coils are potted, has a temperature limit of just over 100°C and so the temperature of the coils is not allowed to exceed 80°C, allowing some margin of safety.

5.5 General Operation of the Drive Unit.

The electronic drive unit successfully accelerates rotors of the form shown in Chapter II at acceleration rates of 1Hz/sec in the 5kHz rotating field and also in the 7kHz field. The moment of inertia of the rotors is approximately 4.3×10^{-6} Kg m^2 and this means that a torque of 2.7×10^{-5} Nm is produced up to angular frequencies of 2000 revolutions/sec. Graphs of rotational frequency as a function of time are given in Figures 5.8 and 5.9, showing the rates of acceleration and deceleration respectively.

CHAPTER VI

INITIAL PHASE LOCK SYSTEM FOR HIGH SPEED ROTORS

6.1 Introduction.

As previously stated, it is necessary to phase-lock one rotor with respect to the other to maximize the number of high velocity molecular encounters per second. This is achieved by measurement of the angular velocities of the two rotors and their respective phases, this information being used to control the applied drive torque.

A phase lock system was designed by J. H. B. and tested using one rotor, attempting to lock it in phase to a standard oscillator. This was unsuccessful owing to limitations of the rotor drive and control information used to correct the angular velocity of the rotor.

The circuitry utilized analogue sampling of the input frequencies and phase relationship between the two pulse sources and then, using only the phase error information, adjusted the applied drive torque. Unfortunately insufficient 'natural friction' of the rotor system resulted in insufficient damping and hence instability.

If the rotor drive was manually controlled it was possible to put the rotor nearly into lock with the standard; however, if the locking electronics were allowed to take over control there was a build up of oscillation about the mean phase lock point until the amplitude of the phase variations exceeded 360^{o}, after which the phase information produced positive feedback for the next period of 360^{o} and thus the system completely lost control.

The conclusions drawn from the unsuccessful attempt to phase lock

the rotor enabled a new locking system to be developed, having damping information present to control the torque in the form of frequency difference information. Also the driving system, at this stage, was only a two-state drive, either on or off. There was no provision to apply a decelerating torque controlled by an auxiliary unit; therefore it was necessary to provide some form of proportional control to prevent excessive over-shoot.

6.2 Partial Analogue Phase Lock System with Proportional Control

The following system was designed and built by the author to lock a slave rotor to a master rotor or to a standard, with a phase error of less than 3^{o} arc. The circuit diagrams are given in Figures 6.1, 6.2 and 6.3, and a block diagram in Figure 6.4.

6.2A Basic mode of operation.

Input pulses could be derived from two rotors or one rotor and a standard, and applied to inputs A and B (Figure 6.1). The input pulses could have a frequency range 500Hz to 5kHz, with standard T. T. L. logic levels. Pulses entering input A were fed into a variable time delay unit which enabled delays of up to 80% of the period of the A input pulses.

Pulses from the time delay unit and input B were then shaped (1μsec. duration) and fed to a scaler. Counting was arranged with the scaler such that additional logic, in conjunction with the scaler, could detect a frequency difference between inputs A and B, and also the sense of the difference. The frequency difference condition was sensed only after a new condition had remained constant for some short period of time, determined by the absolute frequency difference. This delay in the scaler system detecting a frequency difference crossing zero and

Figure 6.1

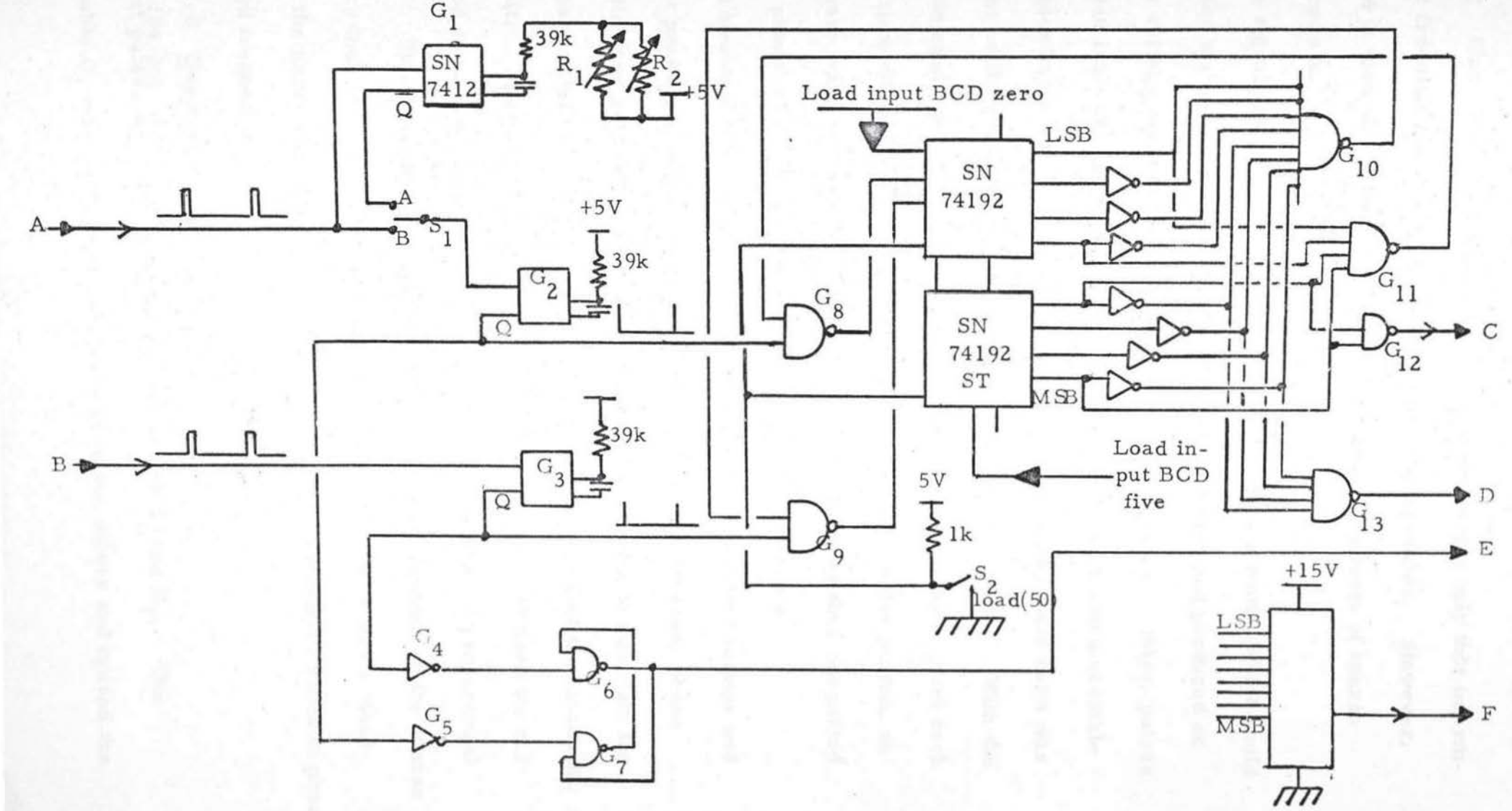
G1
SN 7412
Q
39k
R1
R2
+5V
A
B
S1
+5V
39k
G2
Q
G8
Load input BCD zero
LSB
SN 74192
SN 74192 ST
MSB
G10
G11
G12
C
Load input BCD five
G13
D
E
39k
G3
Q
5V
1k
S2
load(50)
G9
+15V
LSB
MSB
F
G4
G5
G6
G7

changing sign meant that a control arrangement using only this information for frequency lock would always produce over-shoot. However, it served to turn the drive fully on or off to produce a form of coarse frequency lock.

The signal from the scaler was used to produce a ramp, which could take either sign of gradient. This was differentiated and produced an analogue voltage proportional to the frequency difference. Also, pulses were taken from the inputs to the scaler and gated, such that a variable mark/space ratio waveform was produced. The mark/space ratio was dependent on the phase relation of the input pulses at A andB. With the two inputs equal in phase and frequency, and the time delay unit set such that the time delay equalled half the period of the input pulse period, an even square wave was produced. The square wave was then integrated and this produced a voltage proportional to phase difference.

The two variable voltages were then added to a constant voltage and an output produced which was the sum of frequency-difference, phase information and a constant. This voltage was now used to modulate the mark/space ratio of a 200Hz clock, which could then control the electronic drive unit. The mark/space ratio fed to the drive unit, defined the on/off period of the accelerating torque, giving some degree of proportional control. This control signal could, however, be overridden by the coarse frequency lock from the frequency scaler; however, there was a 'dead zone' in the coarse frequency lock which enabled proportional control of phas phase and frequency.

6.2.B Detailed circuit operation.

Input pulses[24, 25] were fed to A and then to switch S_1 and G_1. The mono-stable G_1 was fired on the rising edge of the pulses and caused the

Figure 6.2

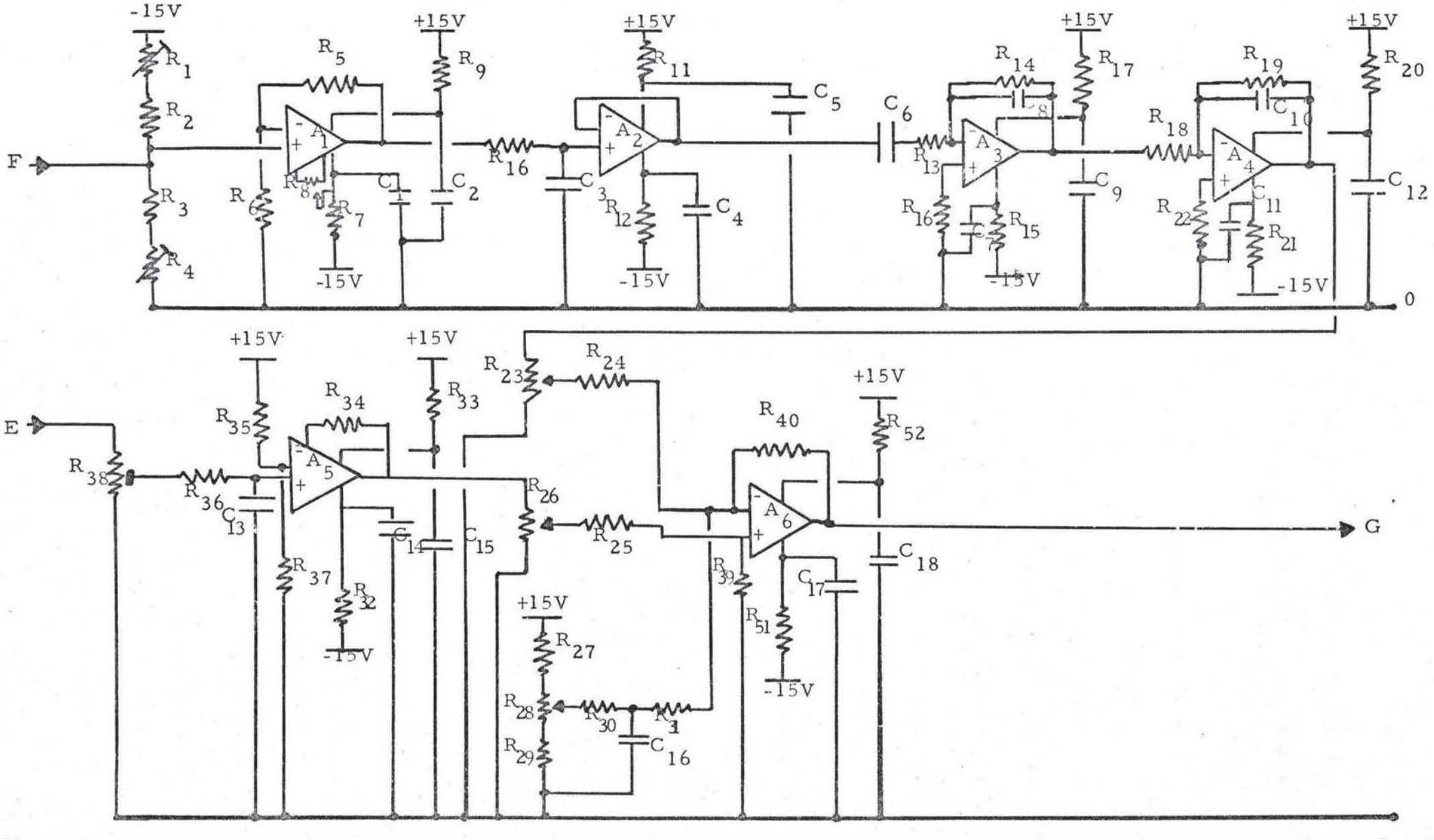
-15V
+15V
R1
R2
R3
R4
R5
R6
R7
R8
R9
C1
C2
A1
F
R16
R11
C5
C6
C3
R12
C4
A2
R14
R17
R13
R15
C7
C8
C9
A3
R18
R19
C10
R22
R21
C11
A4
R20
C12
0
E
R38
R35
R34
R33
R23
R24
R36
C13
R37
R32
C14
C15
R26
R25
A5
R40
R52
R39
R51
C17
C18
A6
G
R27
R28
R29
R30
R31
C16

output $\overline{Q}$ to go low for a period of time defined by the setting of R_1 and R_2. If S_1 was set to position A, then G_2 would fire at the end of the period and produce an output pulse of 1μsec. duration, delayed by the period of time that $\overline{Q}$ was low. If the switch S_1 was set to position B, then the input pulses were not delayed. Pulses from B were also shaped and fed to one input of the dual input NAND gate G_9 and the output from G_2 fed to G_8. These gates were used to stop scaler ST from overflowing or underflowing. The outputs from G_8 and G_9 fed into the up and down inputs respectively of the scaler ST.

The scaler was composed of two cascaded SN74192's which gave a capacity of eight Binary Coded Decimal (BCD) bits. Gates G_{10} and G_{11} were fed into the other inputs of G_9 and G_8 respectively and used to stop 'up'-counts if the scaler was set on '99' and down-counts if the scaler was set on '1'. A pre-set BCD '50' could be loaded into the scaler by means of switch S_2 and corresponded to half the scaler capacity. The scaler counted up on the rising edge of a pulse applied to the 'up' input, while the 'down' input was high, and down for rising edges applied to the 'down' input, while the 'up' input was high. For this reason the input pulses were made equally short (1μsec) compared with the input repetition rate because the shorter the period of time that the input pulses spent holding the scaler inputs down, the lower the probability of error counts due to both inputs being down simultaneously.

If the input frequency of pulses from A was less than the frequency of pulses from B, then there was an excess of down-counts resulting in the scaler counting to '1' and holding. If the two input-frequencies became equal, the scaler would remain on '1' as there would be no

Figure 6.3

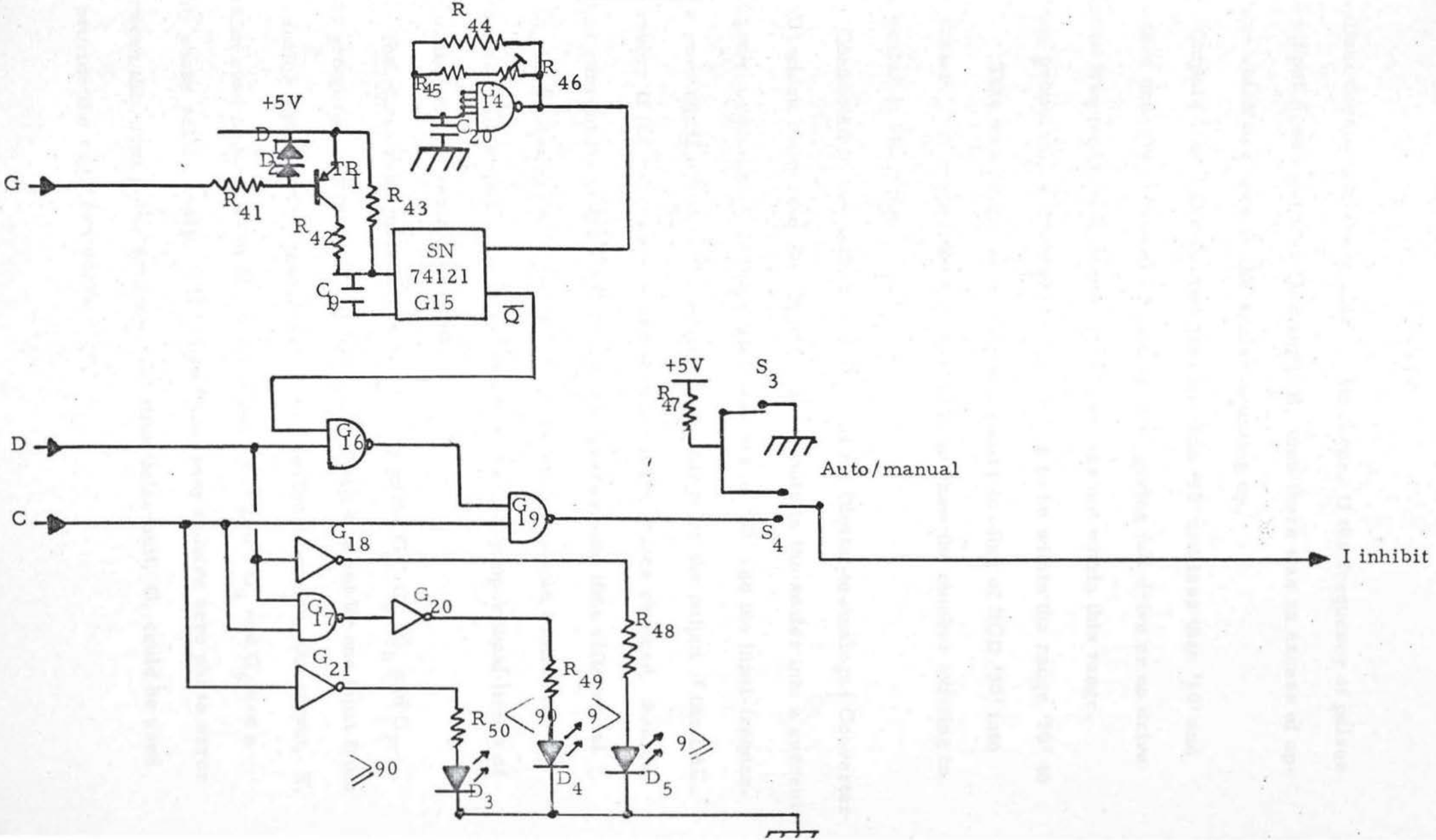
R 44
R 45
R 46
G 14
C 20
+5V
D
TR
G
R 41
R 43
R 42
C
SN
74121
G15
Q
+5V
S 3
R 47
Auto/manual
D
G 16
C
G 19
S 4
I inhibit
G 18
G 17
G 20
R 48
G 21
R 49
R 50
90
9
≥90
D 3
D 4
D 5

resultant counts into the scaler. However, if the frequency of pulses from input A was greater than input B, then there was an excess of up-counts which resulted in the scaler counting up.

Outputs C and D detected greater than '90' and less than '10' and provided non-proportional control limits, giving full drive or no drive (coarse frequency lock) when the scaler was not within this range. During proportional control the scaler had to be within the range '10' to '90'. This was achieved by the momentary loading of BCD '50' into the scaler. A digital display was used to show the number existing in the scaler at any time.

Connected to the scaler was an eight bit Digital-to-Analogue Converter (DAC) which converted the digital number held in the scaler into a current and later a voltage. If the scaler was set on '50' and the input-frequencies were equal, then there would be no change on the output of the DAC. However, if the relative frequency of the input pulses changed, then the output current from the DAC would also change, the time differential giving the frequency difference. As the system would control the frequency difference, the 'walk' towards the non-proportional limits of the scaler range would be halted.

The phase information was derived by gates G_4, G_5, G_6 and G_7. This group constituted an 'S-R flip-flop' which was set by one input from the scaler and reset by the other. As previously stated, the output, E, was an even square wave if the input pulses to gates G_4 and G_5 had a 180^{o} phase relationship. If it was necessary to have zero phase error between the input pulse sources, the time delay unit, G, could be used to provide the required correction.

Figure 6.4 Block diagram of analogue phase-lock unit.

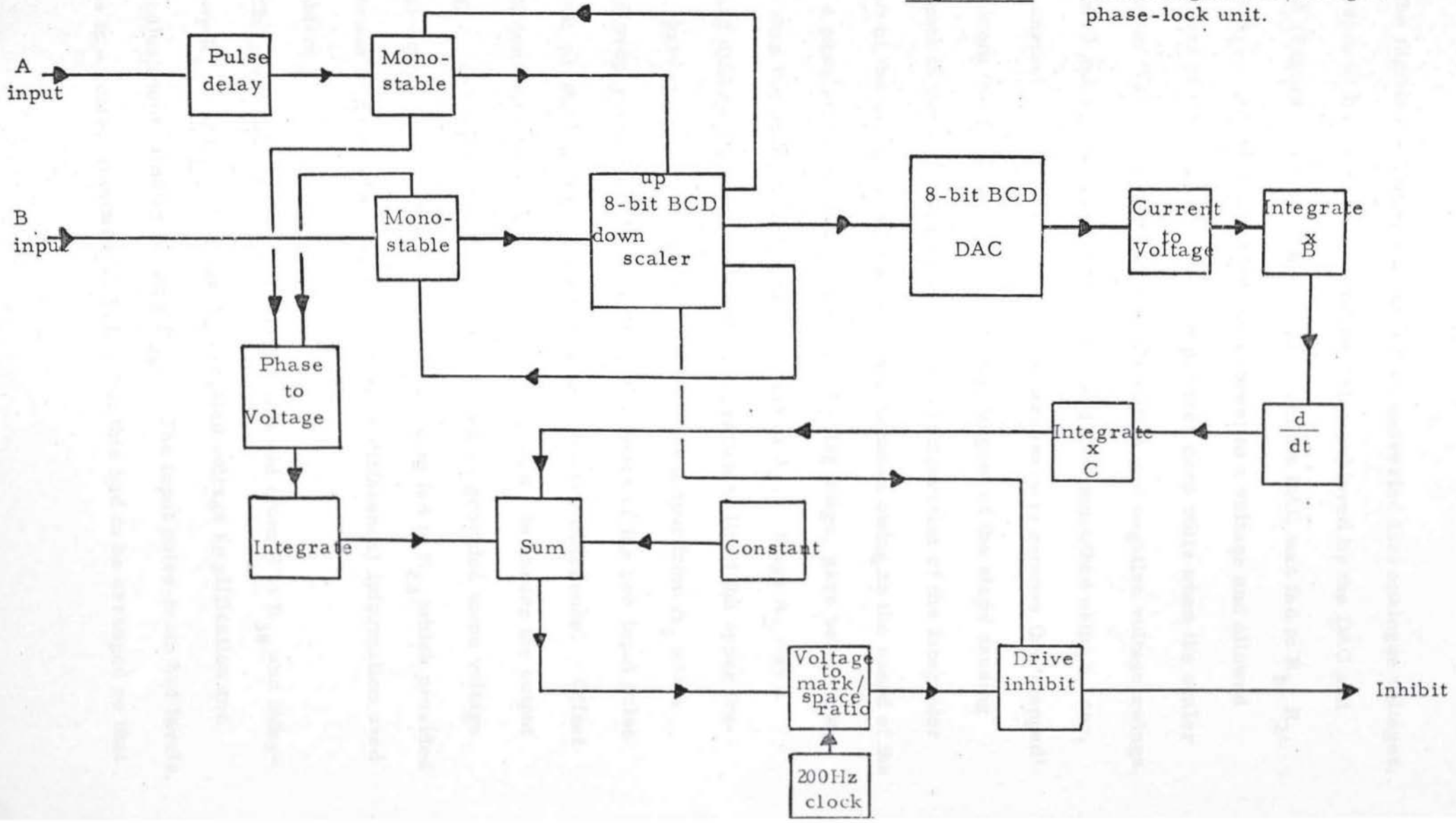

The digitized information was then converted into analogue voltages, conversion of frequency information being achieved by the DAC and stage A (Figure 6.2). The current from the DAC was fed to R_1, R_2, R_3 and R_4. These converted the current to a voltage and allowed adjustment of the output current to produce zero volts when the scaler was set on '50', thus enabling equal positive and negative voltage swings. The small voltage was amplified by A and then smoothed using a 1sec. time constant. The integration was necessary to remove the 'stepped' output from the DAC and hence stop the 'edges' of the steps causing transients in the differentiator. The configuration of the integrator was not of the usual form, using a 741, because owing to the speed of the edges a passive form, followed by a buffering stage, gave better integration than the more usual form, similar to A_4. Stage A_3 was a standard differentiator circuit with integration to limit the upper frequency gain and hence the noise level. The output from A_3 was a voltage proportional to the frequency difference of the two input pulse sources, producing zero volts for zero frequency difference. Offset null adjustment was included in the differentiator to ensure the output setting. The signal was then fed to A_4 which provided some voltage amplification and integration, the output being fed to R_{23} which provided adjustment of phase-derivative (frequency-difference) information used for control.

The phase-difference information was fed from E to R_{38} and integrated by R_{36} and C_{13}. Stage A_5 supplied voltage amplification and level adjustment, finally feeding R_{26}. The input pulse-train had levels, 0 volts tc 4 volts, standard T. T. L., but this had to be arranged so that

a 1:1 mark/space ratio would produce a d.c. voltage on C_{13}, which produced 0 volts on the output of A_5. The level change was achieved by R_{35} and the adjustment of R_{38}. The whole stage effectively produced a voltage proportional to the mark/space ratio of the input from E. R_{26}, R_{23} and R_{28} provided independent lebel adjustment for phase, phase-derivative and constant information. These three voltages were added by A_6 to produce a control voltage at G. The constant was included to provide correction for the retarding torque on the slave rotor caused by 'rotational friction'.

The signal from G (Figure 6.3) was fed to the base of TR_1 via R_{41}. This converted the voltage into a current which charged C_{19}. This charging current defined the 'on' period of pulses fed into G_{15} from the oscillator, composed of an SN7413 dual NAND Schmitt trigger, which has its output fed back to the input and used to charge C_{20}. This oscillator produces pulses at 200Hz which then had a mark/space ratio defined by the voltage from G. This gave a continuous adjustment of the time for which the accelerating torque from the drive acted. The diodes D_1 and D_2 were included to protect the base-emitter junction of TR_1 from an over positive potential appearing at the input G. This is possible as a result of the 'swing' of the output of the previous 741.

Because the power controlled by the voltage from G only had a limited range of mark/space ratios available, not extending to 1:0 or 0:1, the outputs from G_{16} and G_{19} enabled these two extremes to be realized by gating with the outputs from ST, this addition producing the coarse frequency-lock.

6.2C Phase lock tests.

The locking system was never used to lock a slave rotor to a master rotor; it was, however, used to lock a slave rotor to a standard frequency, derived by digitally dividing the 100kHz output from a Hewlett-Packard 545 frequency meter. The output frequency had a short term stability of 1 part in 10^9 and the frequency meter was used to measure the period of the slave rotor pulses when locked. The frequency-locking produced average deviations from the standard of 1 part in 10^7 sampled over 0.5 sec. at a rotational speed of 1,000 revolutions/sec. The controls were adjusted so that with zero phase and phase-derivative information the constant was adjusted to produce as near zero resultant torque on the rotor as possible. Then the phase-derivative information was increased to ensure frequency lock with the standard. Finally, phase information was increased to allow full phase lock to be established. The voltage output from A_4 was fed to the y-axis of a chart-recorder and this gave a plot of frequency-difference against time, the x-axis being driven by a voltage ramp. The manual control switch, S_4, was then used to decouple the control pulses from the rotor drive unit; this resulted in a loss of lock. Then S_4 was set to the auto position, which enabled the lock to be established again. The uncontrolled time was made short so that the rotor did not cause the frequency scaler ST to leave the proportional section. Observation of the frequency-lock recovery time enabled the best level setting of phase-derivative information. The unit produced phase-locking to the standard to better than 1^o arc, and it could maintain this under fairly constant medium vacuum (10^{-6}torr) for several hours.

6.2D Limitations.

The unit had several disadvantages, one of which was the limited torque range of the proportional section. Sudden changes in vacuum pressure or, which is more relevant, gas load variations when the rotor would have been used as a molecular accelerator, would have caused a loss of phase-lock and if the impulse was severe enough, a loss of frequency-lock. Recovery of the lock position would have taken place, provided no further impulses were applied, but if repeated impulses produced a loss of frequency lock, then the proportional section would have been unable to correct, and only coarse frequency-lock would have been possible.

The absolute phase setting tended to drift over many hours, due mainly to changes in the time delay of G_1 and drifts generally within the analogue section. Also because of the analogue nature of the unit, considerable setting up of levels was necessary and this added generally to the problems of use.

As a result of these limitations a new design of locking-unit was required. The drift problem was eliminated by using a totally digital sampling system and full drive torque capability was included over the whole control range. Modifications to the drive unit enabled a digital input signal to control acceleration or deceleration.

The author's design for the Digital Locking Unit follows in Chapter VII.

CHAPTER VII

DIGITAL PHASE-LOCK FOR HIGH SPEED ROTORS

7.1 Introduction.

The following discussion will deal mainly with the phase-lock unit designed and built by the author to supersede the locking unit described in the previous chapter. The reasons for the change to a digital system are given under the section Limitations (Figure 6.2D).

One of the main differences between this system and the partially analogue system lies in the mode of sampling. The proportional section of the previous unit had a continuous control signal, proportional to the state of the inputs at that time. This digital unit uses a sample and correct system. Two inputs are required, as in the previous unit, but there are also two outputs. These convey two sets of information to the drive unit: the sense of the driving magnetic field, and drive or inhibit information. The commands are conveyed by standard T. T. L. logical levels and enable a large degree of flexibility. The modification to the drive unit enabled the direction of the rotating magnetic field to be controlled by a single logical input, which greatly increases the control capability of any drive servo unit. Passive deceleration was the primary limitation of the previous system, this being produced by gas loads and frictional couples as a result of interaction between the steel rotor body and the suspending magnetic field.

The state of the two drive control outputs is determined by the frequency difference and phase relation of the two inputs, or by manual override.

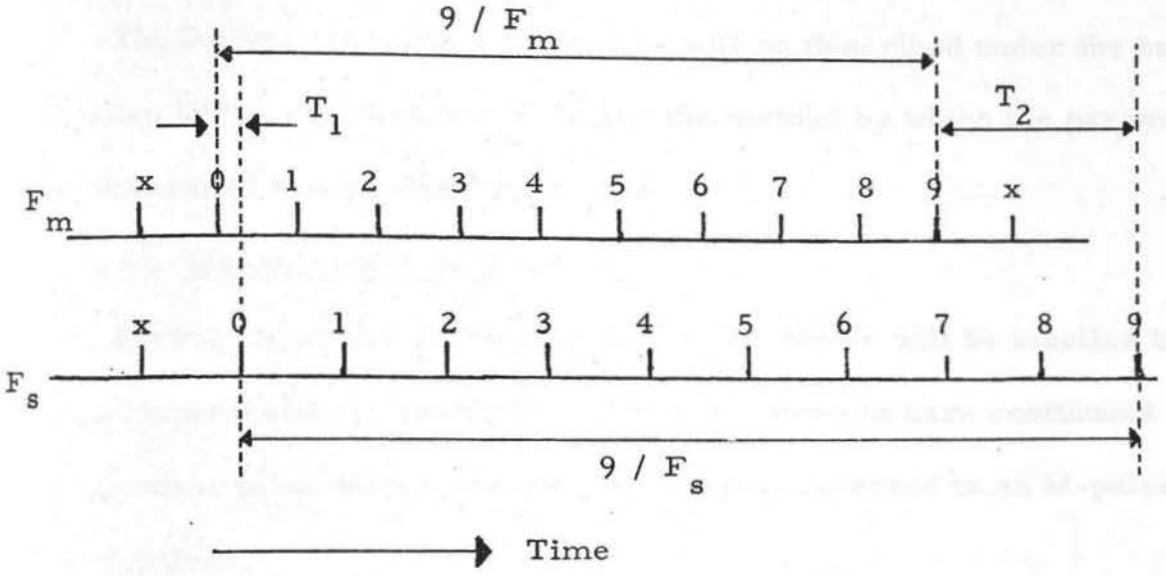

Figure 7.1

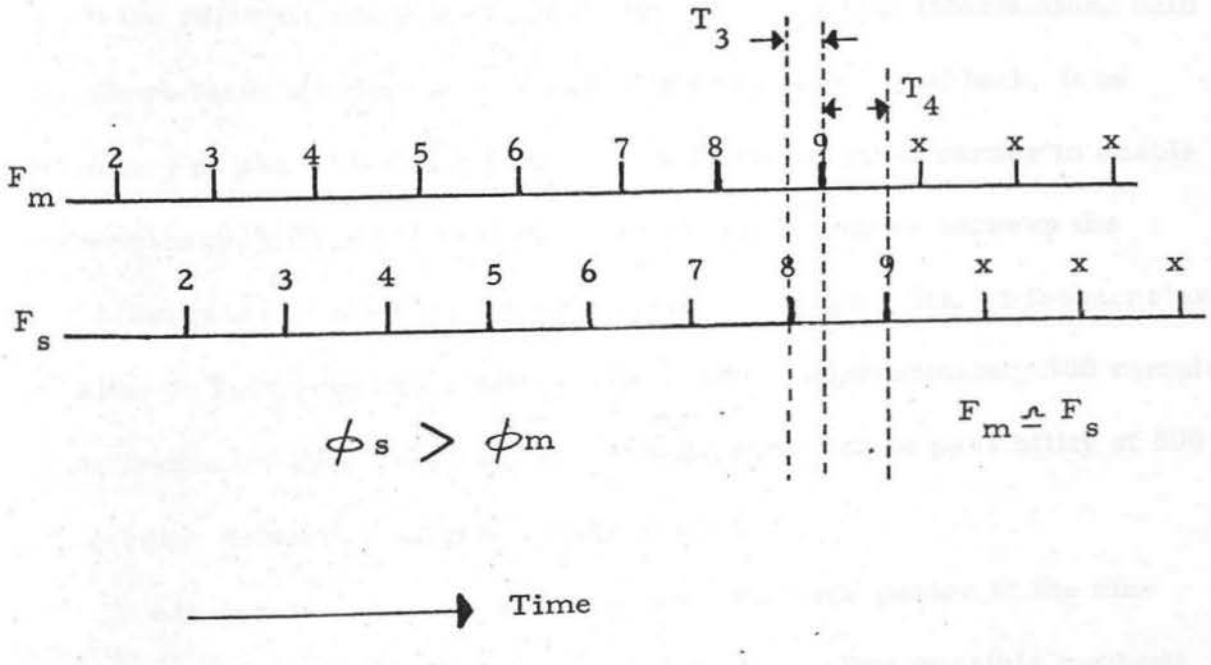

Figure 7.5

7.2 Mode of Operation.

The logical operations of the unit will be described under the heading Detailed Circuit Operations (7.3) but the method by which the parameters are measured will be described here.

7.2A Measurement of frequency.

During the following discussion the two inputs will be labelled input M and input S and the two inputs will be assumed to have continuous independent pulse trains entering each input, referred to as M-pulses and S-pulses.

With reference to Figure 7.1, the frequency difference of the two inputs is measured by subtracting the time period for nine M-pulses from the period for nine S-pulses, the time taken to perform this operation being called the sample time. At the end of each sample, a signal is fed to the relevant section to update the drive control information, held in a short-term memory. To achieve good stability of lock, it is necessary to perform the subtraction with sufficient accuracy to enable the frequency-difference unit to determine differences between the repetition rates of M-pulses and S-pulses to within 1 Hz, at frequencies of 5kHz. This repetition rate would produce approximately 500 samples of the frequency difference every second, and hence a possibility of 500 slave-rotor drive corrections every second.

To achieve the accurate subtraction, the time period of the nine pulses has to be accurately measured (.02%). Two possible methods for producing the result of the subtraction are, firstly, to simply measure the time for nine periods of pulses from each input and then subtract them. However, as one of the simplest method of measuring time, digitally is to

count the number of high frequency pulses which can be fitted into the time interval, a very large number of counts would be produced and hence this would necessitate the use of large capacity scalers. It would also require two scaler banks, because of simultaneous counting and a unit to perform the subtraction.

The second method, devised by the author, requires only one scaler bank, of modest size, 20-BCD bits, and the subtraction performed by the up/down option within it.

If the two inputs have pulse trains of repetition rates F_m and F_s and an arbitrary pulse from one of the inputs is used to start a sample - say input M - then the time between the zeroth pulse from input M and the next pulse into input S will give a time period T_1, and if this time period is subtracted from the period between the ninth pulse from input M and the ninth pulse from input S, T_2, then:

$$T_2 - T_1 = 9(1/F_s - 1/F_m) \qquad (7.1)$$

This is equivalent to nine times the average period of M-pulses subtracted from nine times the average period of S-pulses, the average being taken over the sample period (Figure 7.1). As measurements of T_1 and T_2 are made at different times one scaler can be used, and the subtraction can be accomplished using the count-up, count-down facility.

The time periods are measured using clock pulses of frequency 12MHz, which feed into a 20-bit scaler and are gated such that counting is only done during T_1 and T_2. Steering logic has to be used to define the direction of counting and to determine which pulse train starts the sample. The result of the subtraction is then compared with the value loaded in the scaler, prior to the entry to the zeroth pulse. The

absolute magnitude of the subtraction is not required, but it is necessary to know whether the result is greater than, less than or equal to zero. This information directly indicates the frequency relationship of the input pulses, $F_m > F_s$, $F_m = F_s$, $F_m < F_s$, indicating which of the three possible drive states has to be applied.

Because the frequency difference unit measures discrete intervals of time, using the high frequency pulses of period T_c, the duration of the time interval T_1 or T_2 is not an integral number of periods of T_c. Thus it is possible, depending on the phase relationship of the time period and the clock pulses, to produce one of two possible counts in the scaler. However, this does not produce any problems when the value of the subtraction $\left|T_2 - T_1\right|$ is much greater than the period T_c; but when the two input frequencies F_m and F_s are nearly equal, i.e.

$$\frac{1}{F_s} - \frac{1}{F_m} < \frac{2T_c}{9} \qquad (7.2)$$

then the results of the subtraction do not always yield the same result. The average result of the subtraction produces an automatic, proportional control section over a narrow range of frequency differences ($\pm$ .25Hz at 4kHz).

To consider this aspect further it is necessary to simplify the counting system. Assuming that the scaler does not miss counts and the oscillator clock, used to measure time, produces delta-function type pulses, and possesses a completely random phase relationship to the beginning of the period to be measured, the probability P_m of counting m counts, during the time period T_m is given by:

$$P_m = (T_m - zT_c) / T_c \qquad (7.3)$$

for $mT_c > T_m > zT_c \qquad m = 1 + z..$

Also the probability P_z of counting z counts during the time period T_m is given by:

$$P_z = (mT_c - T_m) / T_c \qquad (7.4)$$

Therefore $\qquad P_z + P_m = 1$

For any time interval T_m there are two possible results of a count, their probabilities being governed by the function P_m and P_z.

To obtain the required frequency information, two counts are required. The first to obtain T_1 and the second to remove counts governed by T_2, hence producing the subtraction. If T_1 is such that $nT_c > T_1 > (n - 1)T_c$, and T_2 such that $(n + z)\,T_c > T_2 > (n + 1)T_c$, then the measured period T_1 would yield either (n) or (n - 1) counts, and the measurement of T_2 would yield either (n + 1) or (n + 2) counts. If T_1 counts are subtracted from T_2 counts, the result must always be greater than zero. If $nT_c > T_1 > (n - 1)T_c$ and $T_2 \geqslant (n + 1)T_c$ or $T_2 \leqslant (n - 2)T_c$, then only one possible resultant drive state is possible and hence, outside of this range, the frequency difference measurement produces non-proportional control, in which the maximum drive torque is applied to accelerate or decelerate, according to the sign of the subtraction $(T_2 - T_1)$.

Within the proportional section there are three intervals, which are governed by the possible results of the subtraction. If T_1 is such that $nT_c > T_1 > (n - 1)T_c$, this being held constant for the rest of the description, then if T_2 is $(n + 1)T_c > T_2 > nT_c$, then there are two

possible results of the subtraction $(T_2 - T_1)$. The first possible result is zero, when n counts are produced by T_1, and n counts being produced by T_2. If the probabilities of T_1, producing n counts in ${}^1P_n$ and of T_2 producing n counts in ${}^2P_n$, then the probability P_o of the subtraction resulting in zero is:

$$P_o = {}^1P_n \cdot {}^2P_n \qquad (7.5)$$

and the probability P_1 of the subtraction producing a result of greater than zero is $P_1 = 1 - {}^1P_n \cdot {}^2P_n$. The values of ${}^1P_n$ and ${}^2P_n$ being given by equations 7.3 and 7.4 assuming that the probability of producing a given count for T_2 is not related to the probability produced by T_1.

A variable T_q (called the average torque fraction), can be used to express the proportion of time for which the drive would be applied as a result of the subtraction giving a result greater than zero. The value of T_q ranges from +1 to -1 to cover reverse drive, and is equal to 1 or -1 when the frequency difference is large enough to put the frequency difference sample outside the proportional range. The value of T_1 and T_2 is set by the relative phase relationship of the input pulses (Figure 7.1), but for simplicity the value of T_q given in the following relationships assumes the measurement of T_1 is always performed with the same phase relationship. For a fixed time, T_1, the value of T_q will vary as a function of T_2, which is proportional to the difference frequency ΔF of the input. When ${}^1P_n = (T_1 - (n-1)T_c)/T_c$, T_q is given by:

$$T_q = (1 - {}^2P_n \cdot {}^1P_n) \qquad (7.6)$$

for T_2 within the range $(n + 1)T_c > T_2 > nT_c$ and in terms of the frequency difference ΔF

$$T_q = {}^1P_n[{}^1P_n + \frac{9\Delta F}{F^2 T_c} - 2] + 1 \qquad {}^1P_n \neq 1 \text{ or } 0 \qquad (7.7)$$

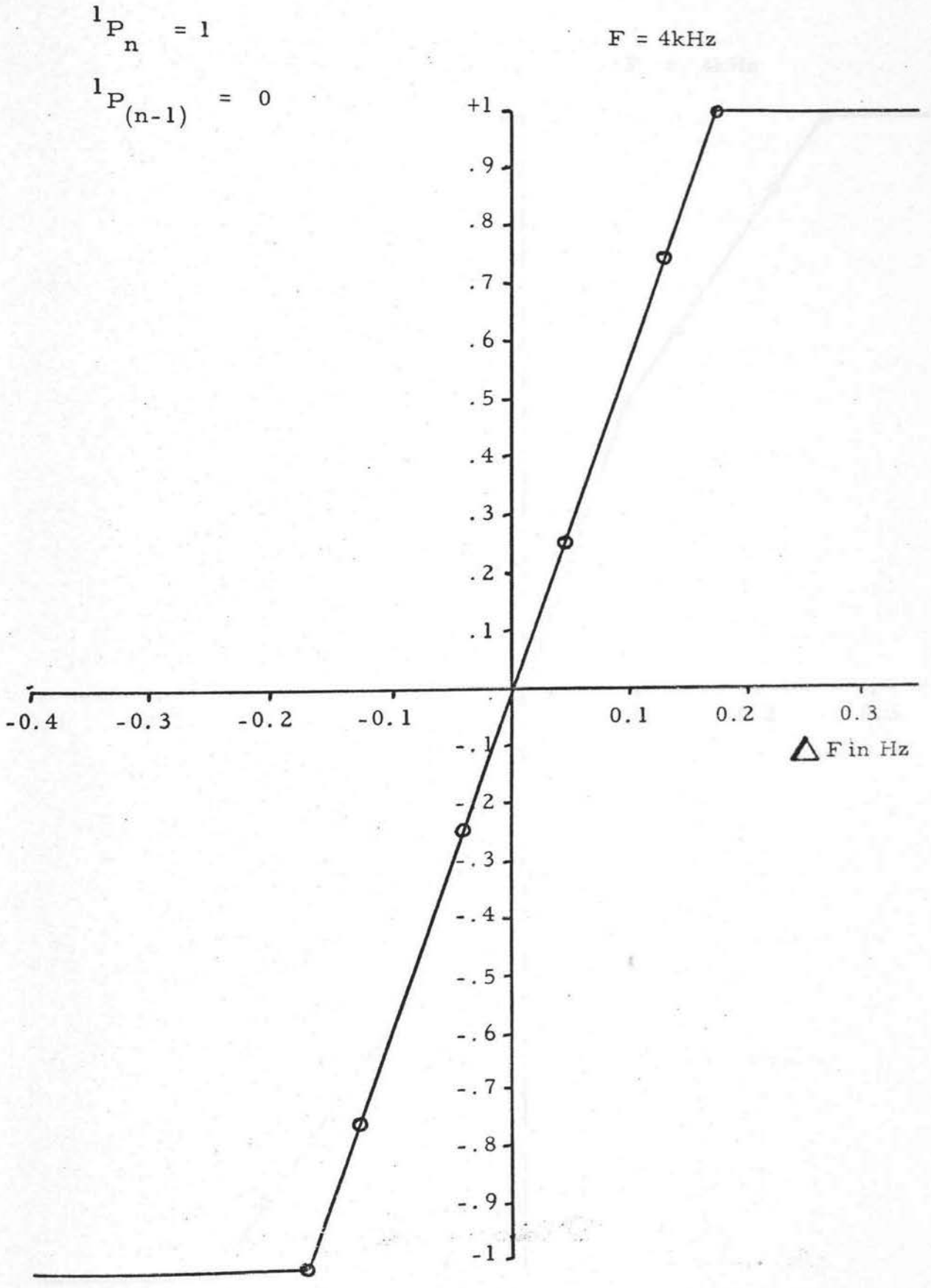
$^{1}P_{n}$ = 1
$^{1}P_{(n-1)}$ = 0
F = 4kHz
+1
.9
.8
.7
.6
.5
.4
.3
.2
.1
-0.4
-0.3
-0.2
-0.1
0.1
0.2
0.3
Δ F in Hz
-.1
-.2
-.3
-.4
-.5
-.6
-.7
-.8
-.9
-1

Figure 7.2

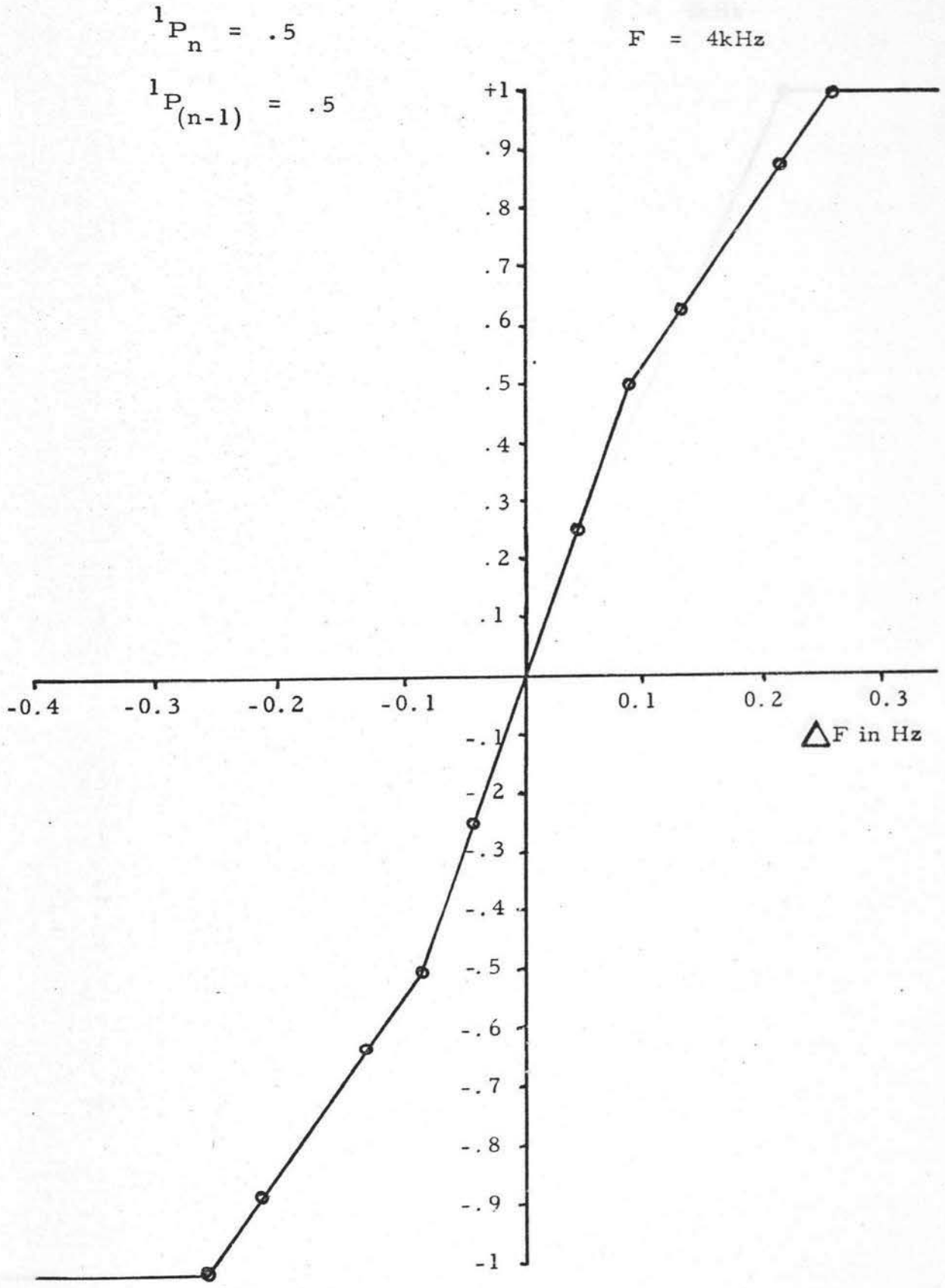
$^{1}P_{n}$ = .5
$^{1}P_{(n-1)}$ = .5
F = 4kHz
+1
.9
.8
.7
.6
.5
.4
.3
.2
.1
-.1
-.2
-.3
-.4
-.5
-.6
-.7
-.8
-.9
-1
-0.4
-0.3
-0.2
-0.1
0.1
0.2
0.3
ΔF in Hz

Figure 7.3

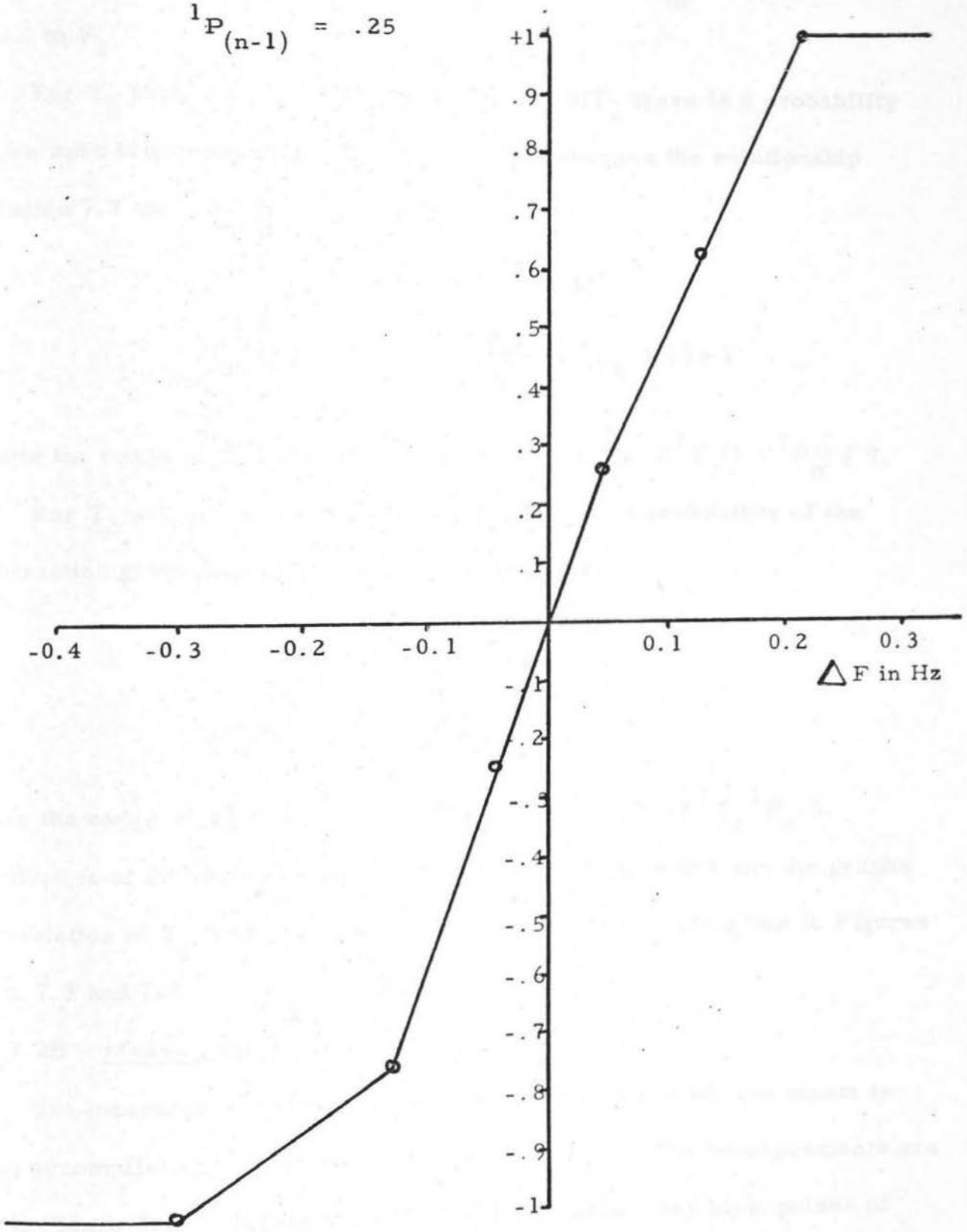
$^{1}P_{n}$ = .75
$^{1}P_{(n-1)}$ = .25
F = 4kHz
+1
.9
.8
.7
.6
.5
.4
.3
.2
.1
-0.4
-0.3
-0.2
-0.1
0.1
0.2
0.3
Δ F in Hz
-.1
-.2
-.3
-.4
-.5
-.6
-.7
-.8
-.9
-1

Figure 7.4

and the range of $\triangle F$ is $F^2T_c(2 - {}^1P_n) / 9 > \triangle F > F^2T_c(1 - {}^1P_n) / 9$. F is equal to the frequency of the input pulses when F_m is approximately equal to F_s

For T_2 such that $(n - 1)T_c > T_2 > (n - 2)T_c$ there is a probability of the subtraction producing 0 or -1. This changes the relationship equation 7.7 to:

$$T_q = (1 - {}^1P_{(n-1)} \cdot {}^2P_{(n-1)})$$

$$= ({}^1P_n - 1)[\frac{9\triangle F}{F^2T_c} + {}^1P_n + 1] + 1$$

where the range of $\triangle F$ is $F^2T_c\,{}^1P_n/9 > \triangle F > -F^2T_c(1 + {}^1P_n) / 9$.

For T_2 within the same range as T_1 there is a probability of the subtraction producing +1, 0 or -1. This gives:

$$T_q = {}^2P_n - {}^1P_n$$

$$= \frac{9\triangle F}{F^2T_c}$$

when the range of $\triangle F$ is $(1 - {}^1P_n)F^2T_c/9 > \triangle F > -F^2T_c\,{}^1P_n/9$. Derivation of the formulae for T_q are given in Appendix 1 and the graphs of variation of T_q with $\triangle F$ for various values of ${}^1P_n$ are given in Figures 7.2, 7.3 and 7.4.

7.2B Measurement of phase.

The measurement of the phase difference between the two inputs is also accomplished by two measurements of time. The measurements are as in Figure 7.5. Inputs M and S are assumed to have input pulses of the same, or very nearly the same, frequency. This is not unreasonable as the frequency difference information is dominant in the control of the

rotor, until the subtraction of $(T_2 - T_1)$ yields a zero, and for the following sample the phase information is used to control the rotor. The time periods between the eighth pulse of M-input and the ninth pulse of S-input is subtracted from the time between the ninth pulse of S-input and the ninth pulse of M-input. This subtraction produces zero when the input pulses are π out of phase. However, the rotors have two arms and it is important to phase lock the arms so the input pulses are divided by two just prior to the inputs of the locking unit. The input pulses are locked with a phase relationship of π, which results in the rotor arms being locked in phase. If $(T_3 - T_4)$ is greater than $3T_c$ then results of phase measurements will not be proportional to phase difference, but will only indicate when the relative phase of the slave rotor is lagging behind or leading the master rotor. Within time differences of $3T_c$ the phase also produces a form of probabilistic proportional control. The range of the proportional control of phase is of the order of $\pm .18^{o}$ for input pulses of 5kHz.

The next stage produces a form of integration for the frequency and phase data. This process is used to independently compare present and previous phase and frequency information. A memory stores the frequency information from the previous sample and compares it with the results of the present sample. If the two sets of results are equal, then the results of the present sample are loaded into the output memory, which is then read by the gating logic, which controls the drive. If the new data is not equal to the previous data, then the output memory is loaded with $F_m = F_s$ or in the case of phase, by phase difference = 0. This means that only consistent samples are allowed to be stored in the output

Figure 7.7

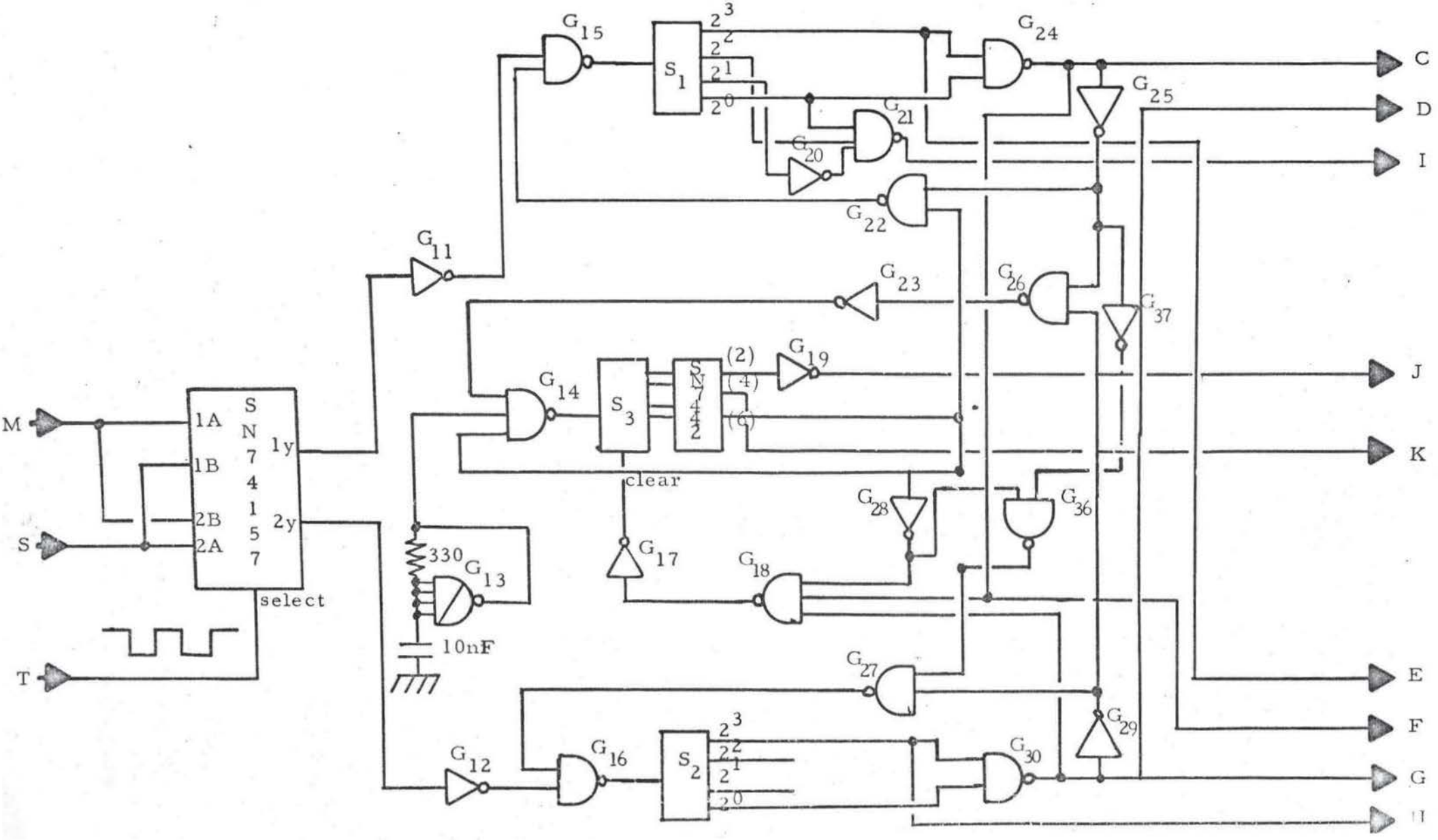
M
S
T
1A
1B
2B
2A
SN7415157
1y
2y
select
330
10nF
G11
G12
G13
G14
G15
G16
G17
G18
G19
G20
G21
G22
G23
G24
G25
G26
G27
G28
G29
G30
G36
G37
S1
S2
S3
SN7442
(2)
(4)
(6)
clear
C
D
I
J
K
E
F
G
H

memory and this reduces the effects of the proportional section of frequency and phase. As it is generally useful to have limited proportional control, the integration facility can be switched off. The way the interaction between phase and frequency information affects the control of the slave rotor drive is shown in the truth table, Figure 7.20.

Neutralisation of systematic errors was accomplished by a type of multiplexing of the inputs and the phase and frequency results every sample.

7.3 Detailed Circuit Operation.

With reference to the circuit diagrams (Figures 7.6 to 7.13), and the block diagram (Figure 7.14), the operation of the digital phase-lock unit is as follows:

Pulses from the two rotors enter inputs R_m and R_s (Figure 7.6). These pulses come from the P.I.N. diode amplifiers which amplify the pulses produced by the rotors intersecting the laser beam twice every rotation. These pulses are shaped by the DUAL NAND SCHMITT TRIGGERS, SN7413, G_1 and G_2. The pulses entering R_m come from the master rotor, with frequency F_m, and those entering R_s come from the slave-rotor, with frequency F_s.

The pulses are fed from their respective Schmitt triggers to the scalers S_A and S_B. These are synchronous 4-bit counters, the outputs from the least significant bit giving a pulse train of equal mark/space ratio and of half the input frequency. This frequency is therefore equal to the rotational frequency of the relevant rotor, as the rotors produce two pulses per revolution. These two signals are fed to the outputs M and S

which feed the next section. Other outputs are available at this point, for monitoring the rotor frequencies. The mono-stables M_1 and M_2, SN74121, with pulse lengths longer than the repetition rate of the input pulses, provides light outputs to indicate the presence of input pulses. The two input NAND gate G_3 is used to gate the two output signals from the Schmitt triggers so that an output pulse results when the two input pulses overlap in time. The signal is then fed to M_3 and the output of M_3 to an L.E.D. indicator to show when the rotors are in phase.

The outputs M and S are now fed to the multiplexing unit G_{10} (Figure 7.7) composed of a Quad 2-Line-To-1-Line Data Selector/Multiplexer, SN74157. This integrated circuit is used to switch pulses from M and S to its outputs 1y and 2y. However, the input that appears on the output is defined by the select input T. The purpose of this unit is to reverse the input to the next section after every sample, and thereby neutralise systematic errors. The select input T has a square wave applied to it, with a period equal to two sample periods. The square wave is derived in another part of the circuit and the effect of this switching will be described later.

If the input to the select input T is low it allows pulses from M to feed G_{11} and from S to feed G_{12}, these being simply inverter buffers. This section controls the sample and the use of the acquired data, having a sequence of operations which is not affected by any other part of the system except the inputs. This section has three scalers, S_1, S_2 and S_3, of which S_3 is the time sequence control scaler. The scalers are all type SN74192, synchronous BCD 4-bit up/down counters. Because this section has a closed sequence of operations it is necessary to start the description

at some arbitrary point in the cycle. For convenience, this point will be the end of a sample cycle; this means that the data has been stored and the unit is ready to begin the next sample cycle.

At this point scaler S_3 has just counted to BCD '5' and this output has been decoded into decimal by the SN7442. The other scalers, S_1 and S_2, are both on '9' which is detected by the two input NAND gate G_{24}, inverted by G_{15} and fed to one of the inputs of the two input NAND gate G_{22}. Scaler S_3 is not on '6', therefore the other input to G_{22} is high and because S_1 is on '9' then the other input is also high. This means that the output of the NAND gate G_{15} is held high and this stops the scaler S_1 counting, and hence locks it on '9'.

In connection with scaler S_2, gates G_{30} and G_{29} produce a high into G_{27}, because the scaler is set on '9'. As the output from the NAND gate G_{36} is high, the input to S_2 is also high and hence is locked on '9'. As a result of both scalers being on '9', the output from G_{23}, which is fed from G_{26} and detects that both scalers are on '9', feeds a high to G_{14} which is a three input NAND gate feeding the up input of scaler S_3. As scaler S_3 is set on '5', the decoded six output is high, so that the pulses produced by the 100 kHz oscillator G_{13} are inverted by G_{14} and fed to S_3. This results in the scaler counting to '6'. At '6' the output from the decoder goes low on the decimal six output, and this forces the output of G_{14} high, preventing further counting by S_3. However, this also means that the output from the decoder to G_{22} will force the output high and enable the next pulse coming from G_{11} to be fed into the scaler S_1. This will cause it to count to '10', which will clear the output to zero and send out a carry pulse, which is not used. S_1 is not on '9' and hence the out-

Figure 7.8

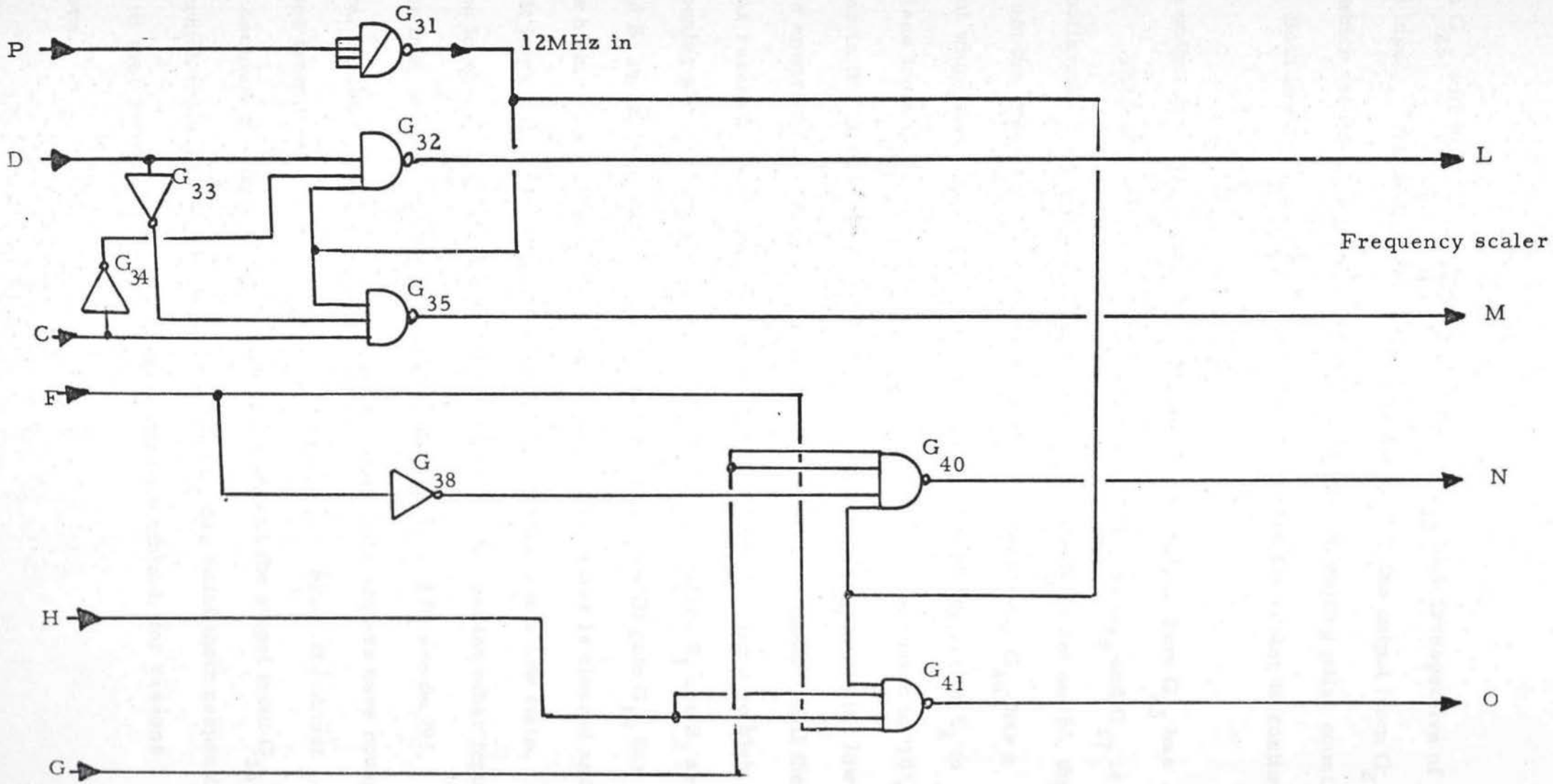
P
G31
12MHz in
D
G32
L
G33
Frequency scaler
G34
G35
C
M
F
G38
G40
N
H
G41
O
G

put from G_{25} will be low, holding the output of G_{22} high irrespective of its other input. As both scalers are not set on '9', the output from G_{23} is low, which means that gate G_{14} has two inputs inhibiting pulse counting by S_3. Both low inputs must be removed to enable the scaler to continue counting.

The output from G_{37} will be high because the output from G_{25} has gone low. The double inversion of the output of G_{24} by G_{25} and G_{37} is used to buffer the heavily loaded output of G_{24}. As S_3 is set on '6', the output from the inverter G_{28} is high and, as a consequence, G_{36} has a low output which makes the output from G_{27} high, enabling scaler S_2 to count pulses from G_{12}, inverted by G_{16}. Scaler S_2 then counts to '10', clears, as in the case of S_1, resulting in the output of G_{29} becoming low and hence ensures that the input pulses to S_2 cannot be inhibited until the scaler has reached '9'. Meanwhile, the output from G_{43} must go high, this happening almost immediately as neither of the scalers S_1 nor S_2 are on '9' and S_3 is on '6'. As a result, the three input NAND gate G_{18} has all inputs high, making the clear input high. The scaler is cleared and, because it is no longer on '6', the output of G_{17} returns to a low state. One of the inputs to G_{14} is driven high in consequence, but the other input, which was low, will not go high until both scalers S_1 and S_2 are on '9'. Therefore, S_3 cannot count pulses from G_{13} until both scalers have counted nine pulses from their respective inputs 1y and 2y. Also, the output from the decimal six digit of the decoder is high and the output from G_{36} is high, which means that both scalers S_1 and S_2 can count their respective inputs until they reach '9', and then they will be inhibited, for reasons given above.

Figure 7.9

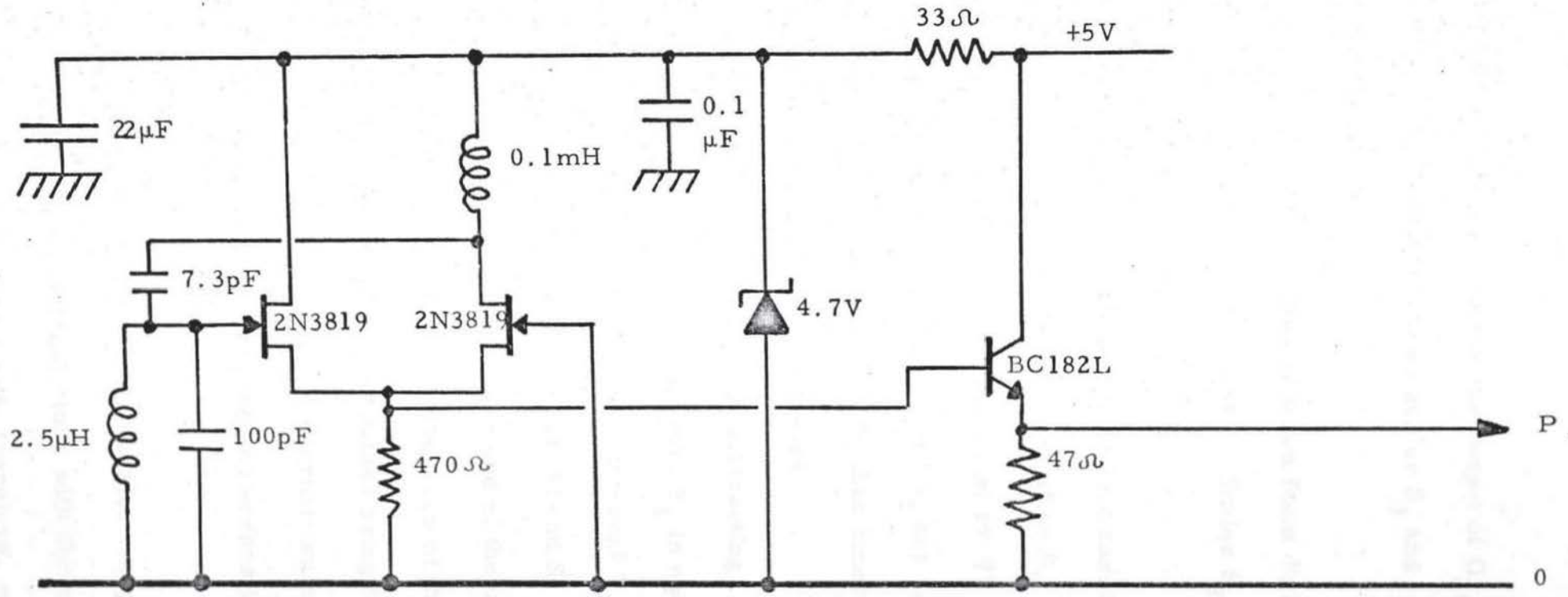
33Ω
+5V
22μF
0.1mH
0.1
μF
7.3pF
2N3819
2N3819
4.7V
BC182L
2.5μH
100pF
470Ω
47Ω
P
0

When both scalers have reached '9', they stop and the output of G_{26} which has detected this state, now lifts the inhibition on scaler S_3 and enables pulses from G_{13} to be counted by S_3.

During the count, timing and loading information is taken from digit outputs two and four of the decoder to control other stages. Scaler S_3 counts to '6' and then the whole cycle is repeated.

To simplify the cycle, S_3 counts up to '6' enabling S_1 to be cleared and begin counting pulses from G_{11}. S_2 can be cleared only after S_1 has been cleared and then counts pulses from G_{12}. Both count to '9' and stop. Meanwhile, S_3 has been cleared and, when S_1 and S_2 are both '9', begins counting pulses from the 100kHz oscillator. S_3 then counts unhindered to '6', when it is stopped and the cycle is repeated.

During the cycle other stages have been counting and subtracting. For the frequency-difference measurement, the time interval T_1 is equal to the time that scaler S_1 is not on '9' and S_2 is '9', and the interval T_2, at the end of the cycle, is equal to the time that scaler S_1 is '9' and S_2 is not '9'. It is possible for the situation to occur, at the end of the cycle, that S_2 is '9' and S_1 is not '9'. This happens when the frequency of the pulses being fed to S_1 is much less than the frequency of pulses being fed to S_2. If $F_m \gg F_s$ then this situation will occur every alternate sample governed by the multiplexing unit G_{10} but will not produce any errors in the frequency-difference measurement.

The frequency scaler S_6 (Figure 7.11) is a 20-bit BCD scaler composed of 5 x SN74192's, synchronous up/down counters (dual clock with clear) in cascade. These scalers have up/down facilities and, therefore, subtraction is accomplished by feeding pulses in the up-input and into the down-

Figure 7.10

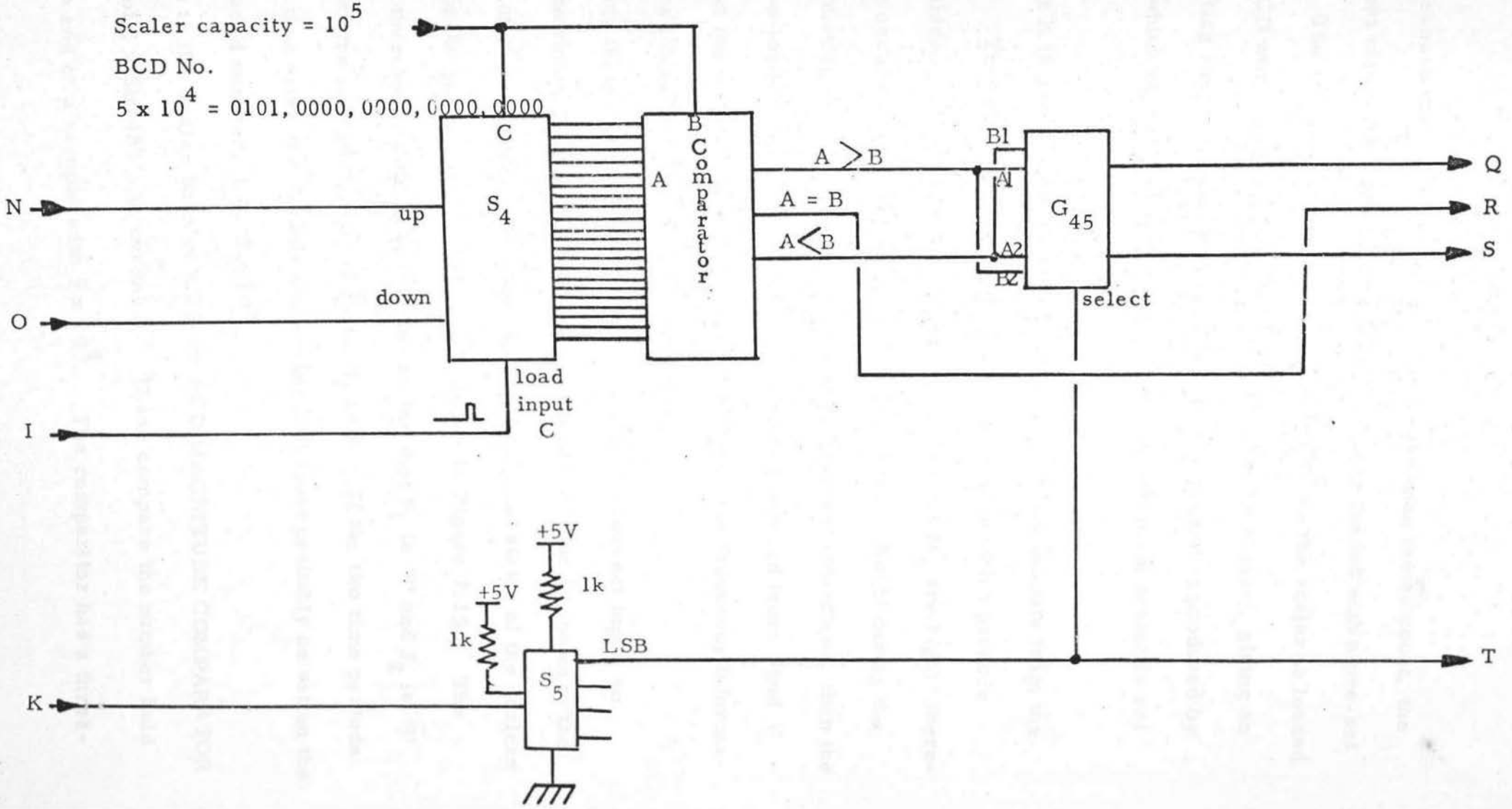
Scaler capacity = 10^5
BCD No.
5×10^4 = 0101, 0000, 0000, 0000, 0000
C
B
A
Comparator
S_4
N
up
O
down
I
load
input
C
A > B
A = B
A < B
B1
A1
A2
B2
G_{45}
select
Q
R
S
+5V
1k
+5V
1k
LSB
T
K
S_5

input. Because the down count could be larger than the up count, the scaler is not cleared before counting begins but is loaded with a pre-set number. The scaler has a decimal range of 10^5 so the scaler is loaded with the BCD word equivalent to 5×10^4 prior to the sample, giving an equal counting range up and down. The load command is produced by scaler S_3 which outputs a low state to output 'K' when the scaler is set on '4'.

Output K is gated with the underflow and overflow outputs from the scaler S_6. These outputs are fed into mono-stables which produce 500nsec pulses. Normally the outputs from M_7 and M_5 are high; therefore loading occurs only when the K output goes low. But if during the sample, counting is such that the scaler overflows or underflows, then the scaler is re-loaded with 5×10^4 and outputs are produced from U and V to show that the scaler count is in error and hence the frequency information produced during the sample is incorrect.

Steering logic is required to feed pulses to the correct input, to measure the times T_1 and T_2, and a diagram of the logic is shown in the upper half of Figure 7.8 and a truth table relating the states of the scalers S_1 and S_2 to the count up /down inputs is shown in Figure 7.15. The scaler S_6, therefore, counts up for the period that S_1 is '9' and S_2 is '$\overline{9}$' and down for the period that S_1 is $\overline{9}$ and S_2 is 9. If the two time periods are equal, then after the sample the scaler will most probably be set on the initially loaded number, i.e. 5×10^4.

Wired to the scaler bank is a 20-bit BCD MAGNITUDE COMPARATOR composed of 5 x SN7485's in cascade. These compare the number held in S_6 at the end of a sample with 5×10^4. The comparator has a three-

Figure 7.11

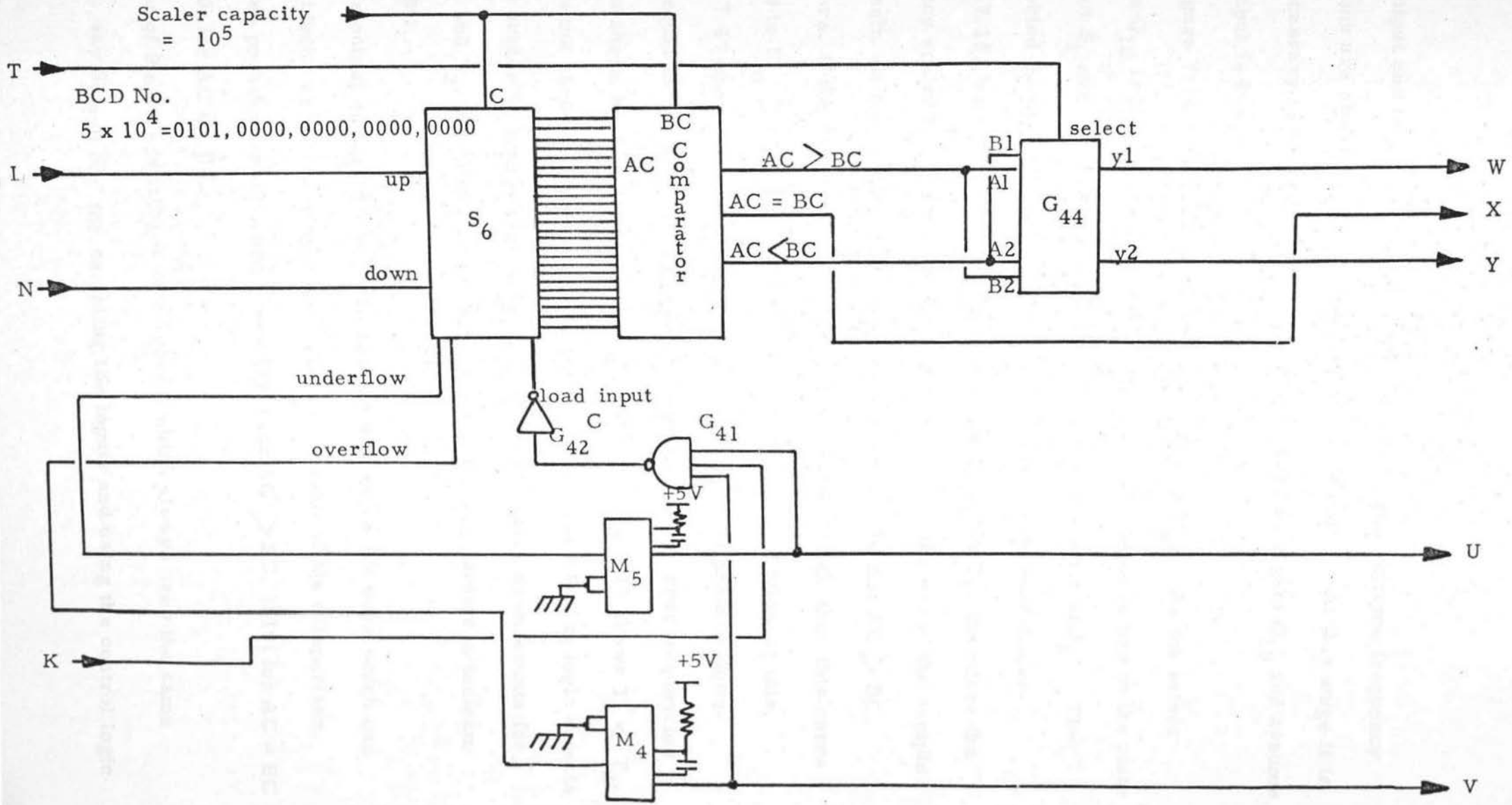
Scaler capacity
= 10^5
T
BCD No.
5×10^4=0101, 0000, 0000, 0000, 0000
C
BC
AC
Comparator
I
up
S_6
N
down
AC > BC
AC = BC
AC < BC
B1
A1
A2
B2
G_{44}
select
y1
y2
W
X
Y
underflow
overflow
load input
C
G_{42}
G_{41}
+5V
M_5
U
K
+5V
M_4
V

state output and this is shown in Figure 7.11. The extreme frequency conditions are shown in Figures 7.16, 7.17 and 7.18. At this stage it is still necessary to ignore the effect of the multiplexing gate G_{10} and assume the T input is low.

Figure 7.16 shows the input condition $F_m > F_s$. As the select input on G_{10} is low, then the number above the R_m input refers to the state of scaler S_1 and the number above the R_s input, the state of S_2. The time period T_1 corresponds to down-counts in the frequency scaler Figure 7.15, but T_2 produces a larger up count, $T_2 > T_1$, therefore the frequency scaler has a count in excess of 5×10^4 at the end of the sample. The result, as far as the comparator is concerned, is that AC > BC. Therefore, if the comparator outputs the state AC > BC, then this corresponds to $F_m > F_s$ as long as the T input is low. Following this, Figure 7.17 shows $T_2 = T_1$, and this is most likely to produce down-counts equal to up-counts, indicating an equality in the input frequencies and also shown by the comparator. Finally, Figure 7.18 shows $T_1 < T_2$, which is the same relationship as Figure 7.16 but the steering logic detects that the scaler S_2 started the period T_2 and this causes down-counts for both T_1 and T_2, thereby causing the output of the comparator to indicate AC < BC.

The output of the comparator consists of a three-bit word which can be considered as a binary code indicating the result of the comparison. The three possible results are coded (001) for AC > BC, (010) for AC = BC and (100) for AC < BC.

One of the disadvantages of a system which always uses the same scalers, say S_1 and S_2, for sampling the inputs and using the control logic

Figure 7.12

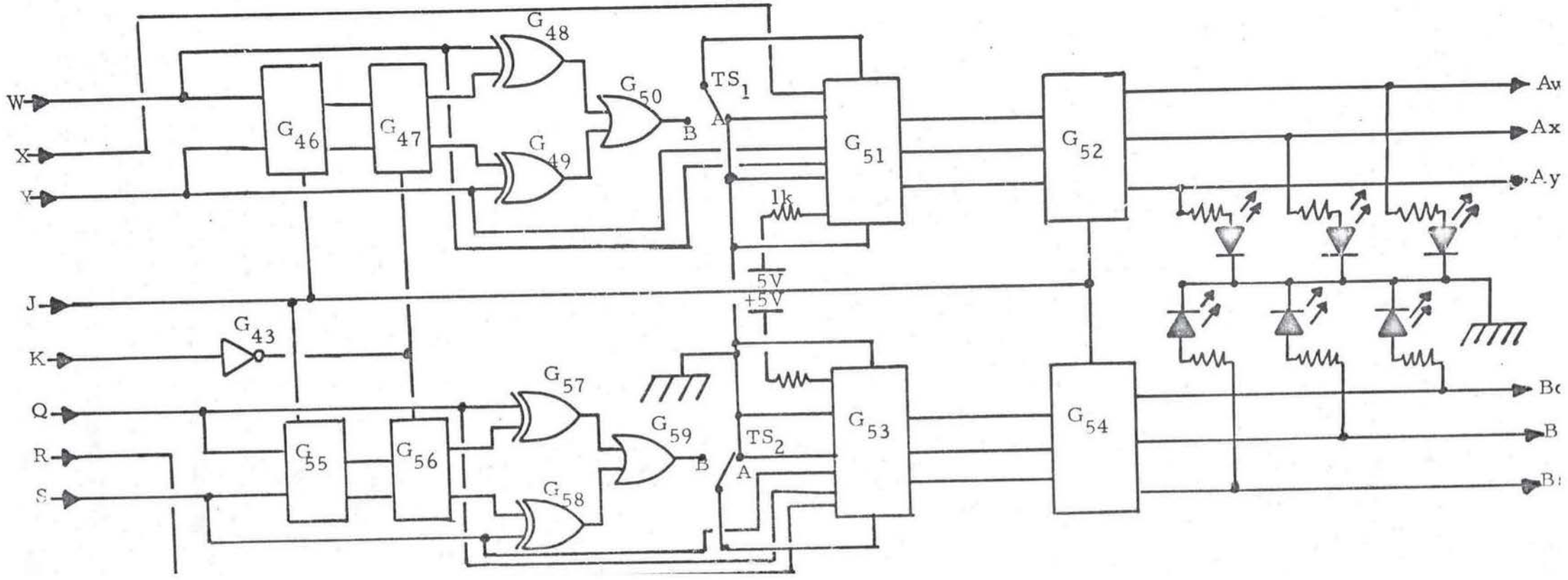
W
X
Y
J
K
Q
R
S
G48
G46
G47
G50
G49
TS1
A
B
G51
G52
1k
5V
+5V
G43
G57
G55
G56
G59
G58
TS2
G53
G54
Av
Ax
Ay
Bc
B
Bz

to produce the same steering logic in every sample, is that it is very liable to systematic counting errors and so the gate G_{44}, which performs the same function as G_{10}, is included. Until now the 'T' select input has been held low, but, if this input is now 'toggled' at a frequency equal to half the sample frequency, then T will also go high and this causes input pulses from M to be fed to scaler S_2 and input pulses from S to be fed to scaler S_1. This result produces a reversal of the unequal outputs of the comparator for the same frequency inputs at R_m and R_s. Thus the output of the comparator must be reversed in phase with the multiplexing gate G_{10}. This is done by G_{44} which reconstructs the correct information relating to the input frequency conditions. If the bits of the frequency word are considered in the order YXW (Figure 7.11), then the result (001) indicates $F_m > F_s$, (010) indicates $F_m = F_s$, and (100) indicates $F_m < F_s$. The multiplexing waveform is produced by the least significant bit of scaler S_5 which is a SN74193, binary scaler, fed from the decimal four digit of scaler S_3.

The phase measurements are made using scaler S_4 (Figure 7.10) and the steering logic is shown on the lower half of Figure 7.8. The scaler S_4 is also a 20-bit BCD scaler, basically the same as the frequency scaler but with the exception that the loading of the scaler is not gated with the overflow and underflow outputs. As with the frequency scaler, the description of the operation will assume that the T select input it low so that pulses from R_m will be fed into scaler S_1, etc. As previously stated, the results of the phase sample are not used to servo the slave rotor, unless the input frequencies are equal. Therefore the following description will assume equal input frequencies.

The zero phase position of the inputs is when $T_3 = T_4$ (Figure 7.5),

Figure 7.13

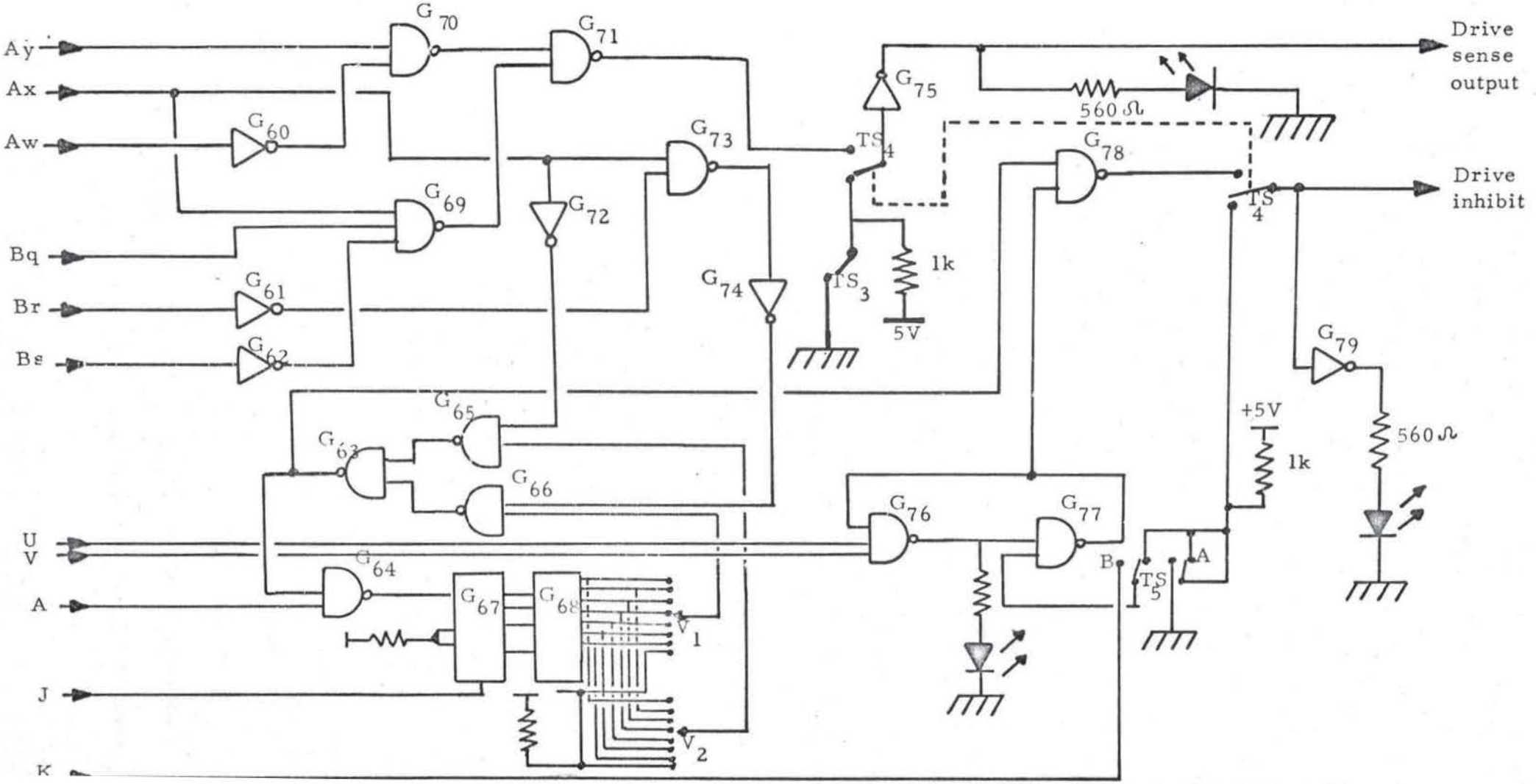
Ay
Ax
Aw
Bq
Br
Bs
U
V
A
J
K
G70
G71
G60
G73
G69
G72
G74
G61
G62
G65
G63
G66
G64
G67
G68
V1
V2
G75
TS4
TS3
1k
5V
560Ω
Drive sense output
G78
Drive inhibit
TS4
G79
+5V
1k
560Ω
G76
G77
B
A
TS5

as the phase of the input pulses before frequency division will be zero. If $T_3 > T_4$, then the phase of the slave rotor leads the phase of the master and hence, under these conditions, a retarding torque is necessary to restore the zero phase condition. If $T_3 < T_4$, then the phase of the slave rotor lags behind the phase of the master, and under these conditions, an accelerating torque is required to restore zero phase.

The steering logic produces an up or down count dependent on the state of S_1 and S_2; this is shown in the truth table Figure 7.19. The scaler will count incorrectly during the beginning of the sample cycle due to scaler S_1 or S_2 being '9' when the other is '$\bar{9}$'. This means that the phase scaler must be loaded later in the sample cycle than the frequency scaler. This is done when scaler S_1 is set on '5', which is detected by the inverter G_{20} and the three input NAND gate G_{21}.

The output from the scaler S_4 is fed to a 20-bit comparator and then to a multiplexing gate G_{45}, which performs the same function as in the frequency case.

The phase information is also set in a 3-bit word and the coding of QRS is (001) indicating that the phase of the slave rotor leads the master rotor, denoted by $\phi_m < \phi_s$, (010) indicating the in-phase condition, denoted by $\phi_m = \phi_s$, and (100) indicating the phase of the slave rotor lagging behind the master rotor, denoted by $\phi_m > \phi_s$.

The 12 MHz clock used by the scalers S_3 and S_6 is shown in Figure 7.9. It consists of two FET's used to produce the required positive voltage gain and a simple LC tuned circuit. The FET gate connected to the top of the tuned circuit produces low loading of the aforesaid and hence the Q of the circuit is limited to the resistance of the inductor and the losses

Figure 7.14.

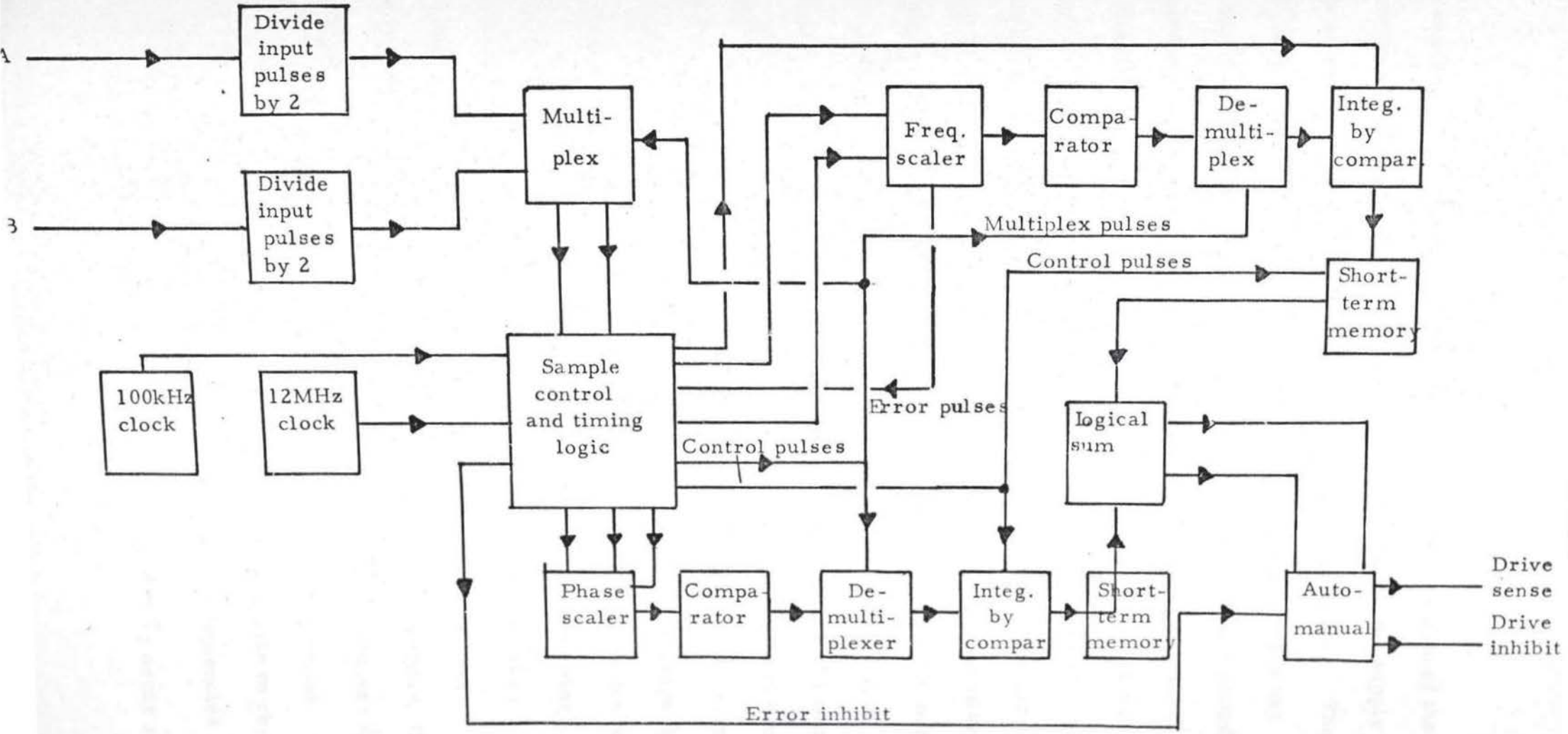
A
B
Divide input pulses by 2
Divide input pulses by 2
Multi-plex
Freq. scaler
Compa-rator
De-multi-plex
Integ. by compar.
Multiplex pulses
Control pulses
Short-term memory
100kHz clock
12MHz clock
Sample control and timing logic
Error pulses
Control pulses
Logical sum
Phase scaler
Compa-rator
De-multi-plexer
Integ. by compar
Short-term memory
Auto-manual
Drive sense
Drive inhibit
Error inhibit

in the mica capacitors. There is stray capacitance from the gate of the FET to the source and to the drain, but as the drain is held by the supply rail there is no Miller amplification of the gate-drain capacitance. The capacitor C_1 was made large enough to swamp the stray capacitance but this meant that the inductor had to be small. The 2.5μH coil was potted in epoxy resin to prevent microphonic effects producing frequency modulation. It is necessary for the oscillator to have a fairly small short term frequency drift, typically less than 1 part in 10^6 over a sample period, as the frequency of the oscillator will affect the count rates for the time periods T_1 and T_2, T_3 and T_4. Because the time measurements are comparative, the absolute frequency of the clock is not important but needs to be as high as is reasonable for the scalers to accurately count. Measurements of the frequency drift of the oscillator gave drifts of 1 part in 10^5 over one second, the drift usually being in the same sense and hence over a sample period the change in frequency was very small. A crystal-controlled oscillator could be used but would not significantly improve the counting efficiency as the multiplexing removes systematic errors due to the drifting clock. For example, if the clock were gradually slowing down, then the measurement of T_2 would give, on average, a smaller number of counts than T_1, even if the two intervals were equal; but because the multiplexing causes alternate rotors to start the samples, the average effect of a constant drift in the clock cancels out and produces no bias in the frequency measurement. It will, however, decrease the control sensitivity. A certain amount of clock drift is desirable to reduce beat effects between the clock frequency and the rotor frequencies when the rotors are locked and hence the time periods T_1 and T_2 occur at

Figure 7.15

S_1	S_2	L up input	M down input
9	9	H	H
$\overline{9}$	9	H	P
$\overline{9}$	$\overline{9}$	H	H
9	$\overline{9}$	P	H

P = clock pulses

H = no input pulses

Truth table for frequency steering logic.

Figure 7.16

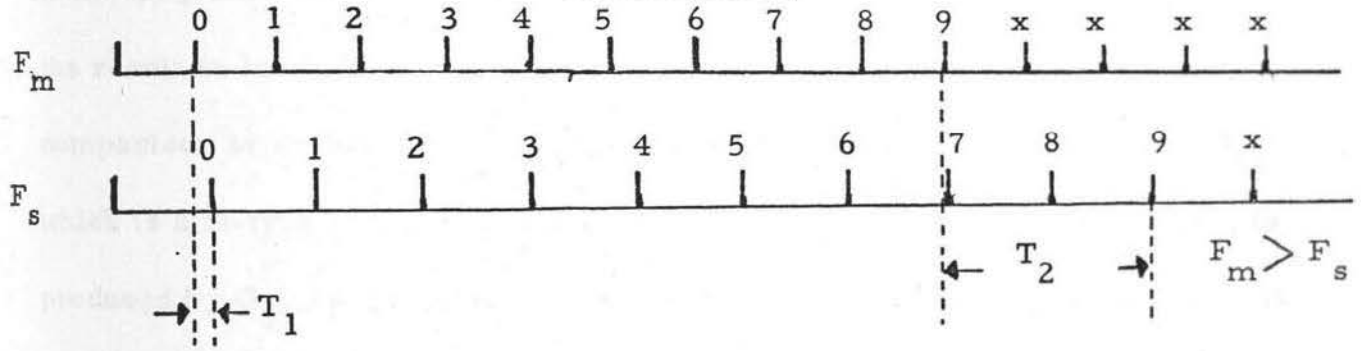

Figure 7.17

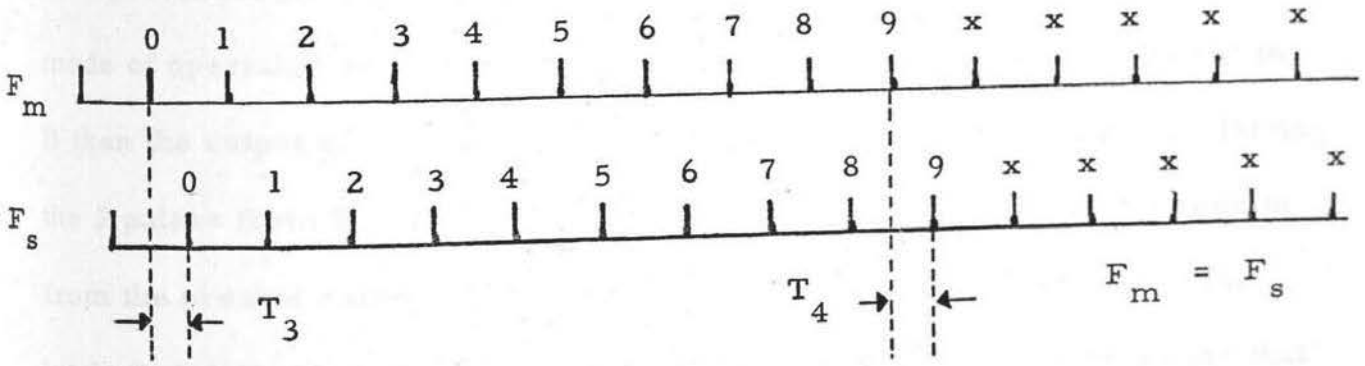

Figure 7.18

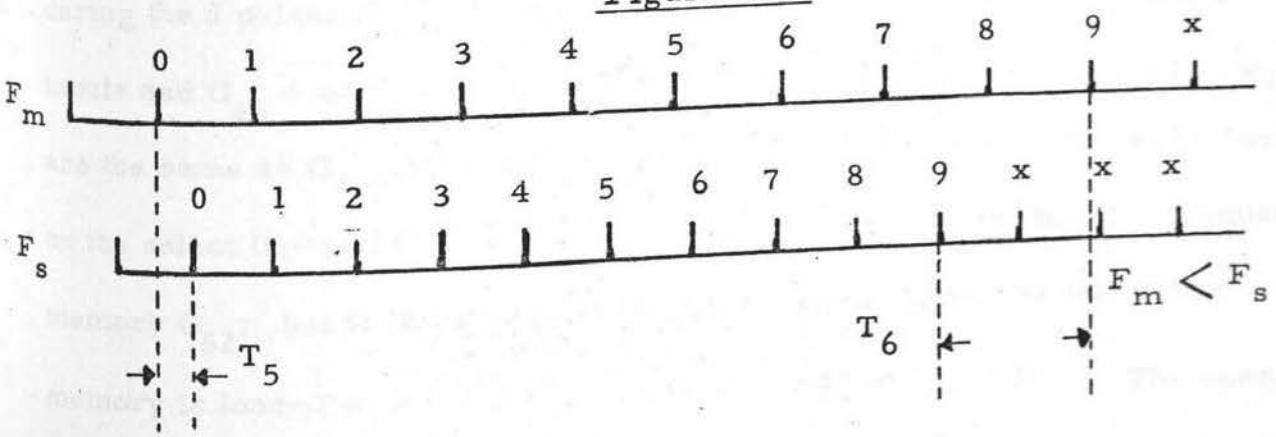

regular intervals. One fairly simple solution to these problems is the use of a random pulse generator. This would alleviate the beat effects and also ensure that the probability of producing a given count due to T_1 does not influence the probability of producing a given count due to T_2. The amount of clock drift was found to be totally satisfactory for the lock required and hence no changes were found necessary.

Both phase and frequency data are fed to a stage which compares the present sample result of frequency with the previous result (Figure 7.12). If the frequency comparison shows the two sample results to be equal, the result is loaded into the frequency memory G_{52}. The method of comparison is as follows: When scaler S_3 counts to decimal two, G_{52} which is a D-type latch, loads the output from G_{51}, but the output that is produced by G_{51} is dependent on the logical state of the select input. If switch TS_1 is set on A, the select input is held low and this means that data presented on the A input is carried through to the y outputs. This mode of operation produces no integration, but if the switch TS_1 is set to B then the output of G_{51} is defined by the state of G_{50}, an OR gate. During the J pulses from S_3, the D-type latch G_{46} is also loaded with the results from the present sample and when S_3 counts to decimal four, a K pulse loads that data into G_{47}, which is another D-type latch. This means that during the J pulse, G_{47} contains the previous sample state of W and Y inputs and G_{46} contains their present states. If the states stored in G_{47} are the same as G_{46}, then the exclusive OR gate (EXOR) will yield a low on the select input of G_{51} and hence load the present data into the frequency memory G_{52}; but if the results are not the same, then the frequency memory is loaded with (010) which corresponds to $F_m = F_s$. The operation

Figure 7.19

Scaler 1	Scaler 2	Scaler 4	
		N up	O down
7	7	H	H
8	7	H	H
8	8	H	P
9	8	P	H
9	9	H	H

P = clock pulses

H = no input pulses

Truth table for phase steering logic.

Figure 7.20

Frequency			Phase			Control	
$F_m > F_s$ Aw	$F_m = F_s$ Ax	$F_m < F_s$ Ay	$\phi_m > \phi_s$ Bq	$\phi_m \; \phi_s$ Br	$\phi_m < \phi_s$ Bs	Sense 1 = Accel. 0 = Decel.	Drive 1 = Drive 0 = Inhibit
1	0	0	x	x	x	1	1
0	0	1	x	x	x	0	1
0	1	0	1	0	0	1	1
0	1	0	0	0	1	0	1
0	1	0	0	1	0	1	0

x = irrelevant

of the phase section is the same but with different data. If W_t, X_t and Y_t correspond to the results of the previous sample and W_{t+1}, X_{t+1} Y_{t+1} correspond to the results of the present sample, then the stored word Aw Ax Ay in the frequency memory will be as follows:

$$\text{If } W_{t+1}, X_{t+1}, Y_{t+1} = W_t, X_t, Y_t$$

$$\text{then } A_w, A_x, A_y = W_t, X_t, Y_t$$

$$\text{If } W_{t+1}, X_{t+1}, Y_{t+1} \neq W_t, X_t, Y_t$$

$$\text{then } A_w, A_x, A_y = 010$$

If the input frequencies F_m and F_s are equal, then with a systematic error, the multiplexing would cause an oscillation every sample between $F_m > F_s$ and $F_s < F_m$ at the input of the integrator. This would be expressed on the output of the memory G_{52} as 010 ($F_m = F_s$). Without the integration the inertia of the rotor can provide the necessary integration of the torque, but this digital form could be useful if a very low moment of inertia rotor were used. Light emitting diodes are used to indicate the frequency and phase relationship of the master and slave rotors.

The final stage of the locking unit deals with the gating process to produce the correct drive conditions to put the slave-rotor into lock with the master rotor. Priority is given to the frequency information to drive the rotors into frequency lock, and then, when $F_m = F_s$ the phase information controls the rotor. If the phase information pushes the rotor out of frequency lock, the frequency information again dominates. The control switches V_1 and V_2 enable the drive to be applied for a discretely variable fraction of a sample period, such that a balance can be set

between the average torque produced when the phase information is dominant, and the average torque when the frequency information is dominant. The frequency torque level adjustment was made by V_2 and was found to give the best control when set on 7, while the phase adjuster V_1 was best set on 2 or 3 as the phase-lock only required small bursts of torque. The truth table for the drive outputs is shown in Figure 7.20. Switch TS_4 enables the two outputs to the drive unit to be manually controlled. The manual control for the drive sense is made by TS_3 and for drive-inhibit by TS_5. Error counts produced by the frequency scaler are fed to the S-R Flip-Flop composed of G_{76} and G_{77}. The setting of this flip-flop inhibits the drive via G_{78}. If TS_5 is set on A, then the inhibit holds until the switch is momentarily set to B, but if the switch is permanently set to B, then the drive will only be inhibited for one sample and will then clear, unless another error pulse is received. These errors can occur for one of two reasons. As previously stated, if the input frequency of the two inputs are so low that the time period T_1 or T_2 causes the frequency scaler to overflow or underflow, then a count error will be produced (T_1 or $T_2 > 5$ms). The second possible cause of error would be the loss or partial loss of input pulses from one of the inputs. When the two input frequencies are approximately equal, the number of possible torque corrections per sec. is of the order of $F_m/10$.

In the situation when the master rotor and the slave rotor are locked in phase, and both rotors are subject to a constant deceleration or acceleration, with the locked phase condition holding, then the time period T_2 sampled at some time later than T_1 will give $T_2 - T_1 \neq 0$, even though the rotors have an average difference frequency of zero. This produces

within the unit an error equivalent to a systematic error and is neutralized by the multiplexing. Provided the deceleration is not too large, i.e. less than 2.5×10^2 Hz/sec. for rotors at 5×10^3 Hz, there will be sufficient information to produce frequency control, but for the best phase lock the common deceleration rate must be kept to a minimum. This can be done by simply applying a small torque to the master rotor to reduce its time rate of change of frequency.

Adjustment for locking the slave rotor to the master rotor at any phase difference other than zero has not been built into the unit but it can easily be achieved by changing the number used by the phase comparator to produce the phase word, and the removal of the phase multiplexing gate to the input of the phase scaler S_4.

7.4 Results of Phase-Lock Tests.

The phase-lock unit was tested by locking one rotor to a simulated rotor, produced by a frequency standard, stable to 1 in 10^9. This offered the most convenient method of measuring the degree of frequency and phase-lock for various frequencies of a master rotor. The main difference between locking the slave rotor to a frequency standard, rather than a master rotor, is that there is no decrease of the frequency of the standard, which would be present to some small degree with a coasting rotor. Adjustments for this, however, can be made such that the deceleration rate is very slow, by applying a small amount of drive to the master rotor.

Measurements of frequency lock only for rotational speeds of up to 3,500 revolutions/s. showed frequency locking to better than 5×10^{-2} Hz.

Figure 7.21

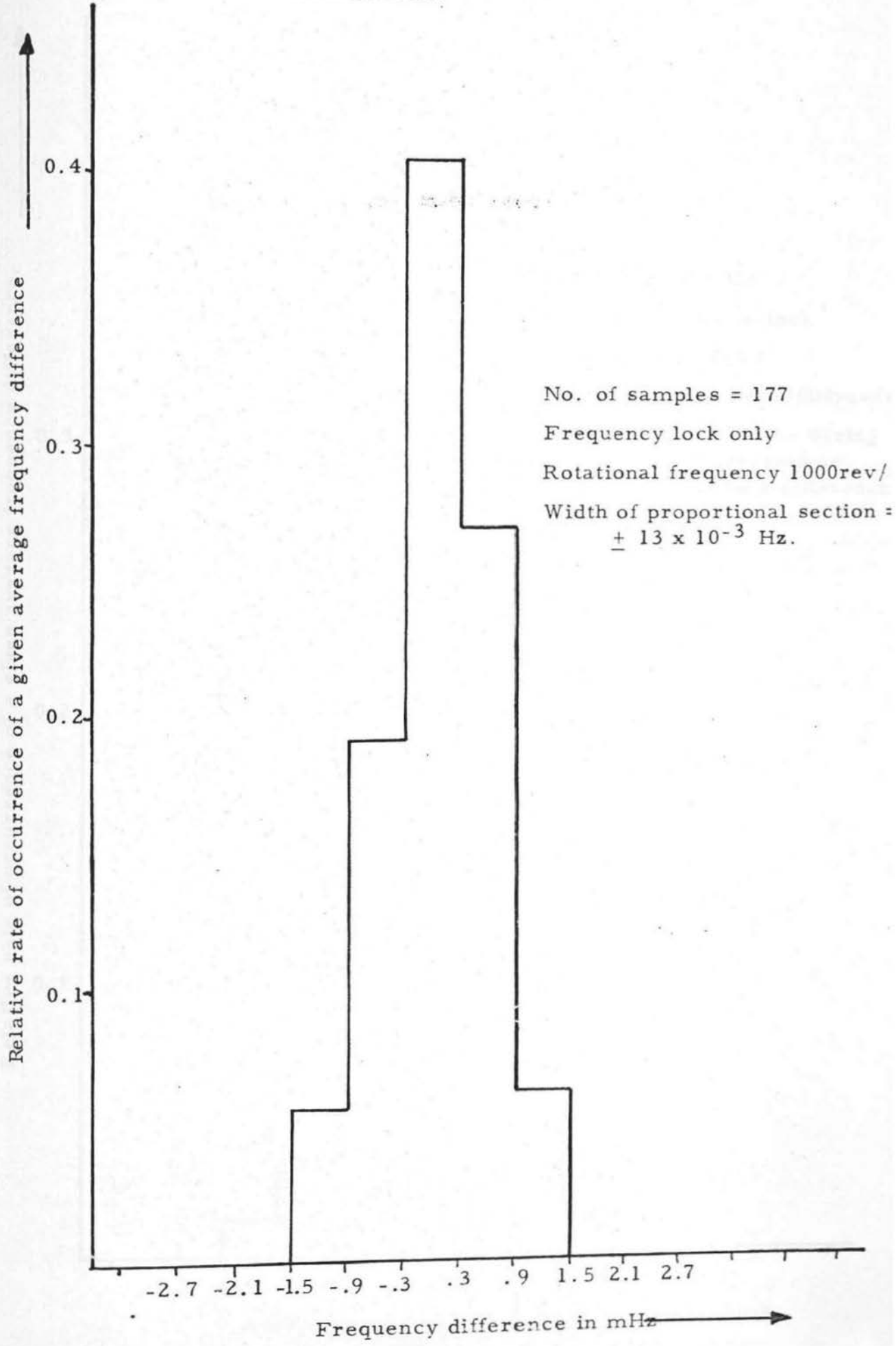
Relative rate of occurrence of a given average frequency difference
0.4
0.3
0.2
0.1
No. of samples = 177
Frequency lock only
Rotational frequency 1000rev/
Width of proportional section =
± 13 x 10^-3 Hz.
-2.7 -2.1 -1.5 -.9 -.3 .3 .9 1.5 2.1 2.7
Frequency difference in mHz

Figure 7.22

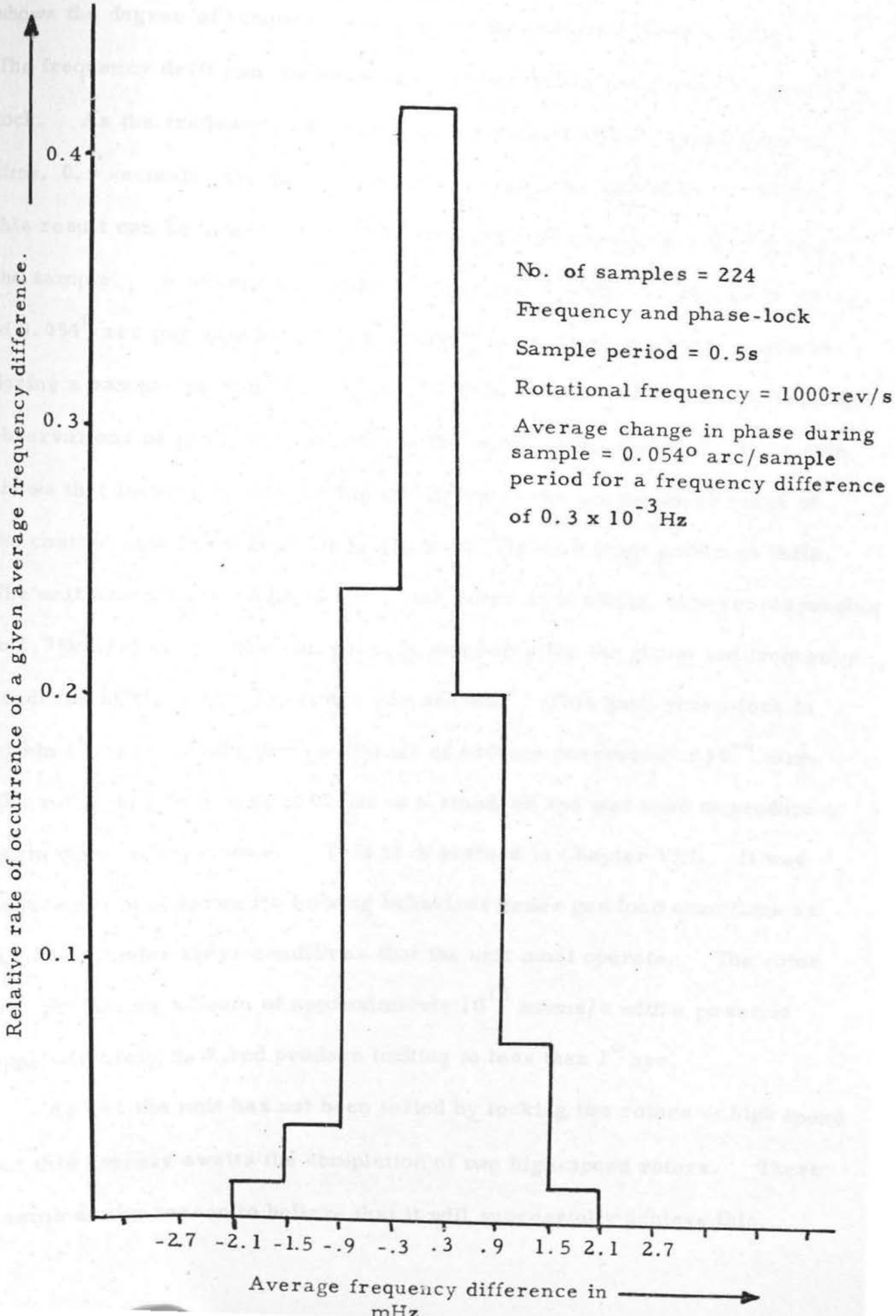
Relative rate of occurrence of a given average frequency difference.
0.4
0.3
0.2
0.1
No. of samples = 224
Frequency and phase-lock
Sample period = 0.5s
Rotational frequency = 1000rev/s
Average change in phase during sample = 0.054° arc/sample period for a frequency difference of 0.3 x 10^-3 Hz
-2.7 -2.1 -1.5 -.9 -.3 .3 .9 1.5 2.1 2.7
Average frequency difference in mHz.

Figure 7.21 shows, in histogram form, the results of many samples of frequency difference when the rotor is frequency-locked. Figure 7.22 shows the degree of frequency-lock when the rotor is phase-locked. The frequency drift can be used as an indication of the degree of phase-lock. As the frequency difference was measured over a set period of time, 0.5 seconds, the result was an average over this time. Hence this result can be used to determine the average change of phase during the sample. A change of 0.3×10^{-4}Hz corresponds to a change in phase of 0.054^{o} arc per sample period. Thus the maximum change of phase during a sample period is 0.3^{o} arc. This agrees with direct oscilloscope observations of phase difference. The width of the frequency histogram shows that locking is well within the limits of the proportional range of the control unit, as this limit is $\pm 13 \times 10^{-3}$Hz with input pulses of 1kHz. The unit was also tested by locking the rotor at 3,500Hz, this corresponding to 1.75km/s, where the control unit was sampling the phase and frequency condition of the rotor 350 times per second. This gave phase-lock to within 1^{o} arc, even under conditions of vacuum pressures of 10^{-4} torr. The rotor was locked at 3,000Hz to a standard and was used to produce a beam of mercury atoms. This is described in Chapter VIII. It was necessary to observe its locking behaviour under gas load conditions as it will be under these conditions that the unit must operate. The rotor was producing a beam of approximately 10^{13} atoms/s with a power of approximately 5μW and produce locking to less than 1^{o} arc.

As yet the unit has not been tested by locking two rotors at high speed but this merely awaits the completion of two high-speed rotors. There seems every reason to believe that it will successfully achieve this.

CHAPTER VIII

EXPERIMENTAL RESULTS AND FUTURE PROSPECTS

8.1 A Successful High Speed Rotor.

After many problems associated with the carbon fibre composite and the bonding of the composite to the rotor boss, a rotor was finally made which, when spun at 4,250 revolutions per second, attained the tip speed of 2km/s.[15] This had arms and a boss of the design described in Chapter II and a photograph of the rotor is shown in Plate 2.1. Taking into account the breaking strength of the carbon fibre composite, the theoretical breaking speed of this rotor was calculated to be 2.47km/s. This rotor was safely brought back to rest and showed no physical damage.

A second rotor was made of slightly weaker composite and run to 1.75km/s and subsequently used to produce a mercury beam, as will be described in the next section.

8.2 Using a High Speed Rotor to Produce a Beam of Mercury Molecules.

Using the 1.75km/s rotor just mentioned, a simple experiment was undertaken to produce a beam of mercury atoms and measure the velocity distribution.

The single rotor unit was employed and set up as indicated in Figure 8.1, using a beam unit, described in Chapter III, to produce the primary beam of atoms. These were arranged to strike the rotor tip and then evaporate, or possibly bounce, such that the resultant beam travelled freely within the vessel for 1.34×10^{-1} m and then entered a glass tube which served to collimate the beam. At the end of the tube was placed an ionisation gauge, type IG6, which is a vacuum measuring gauge. This

Figure 8.1

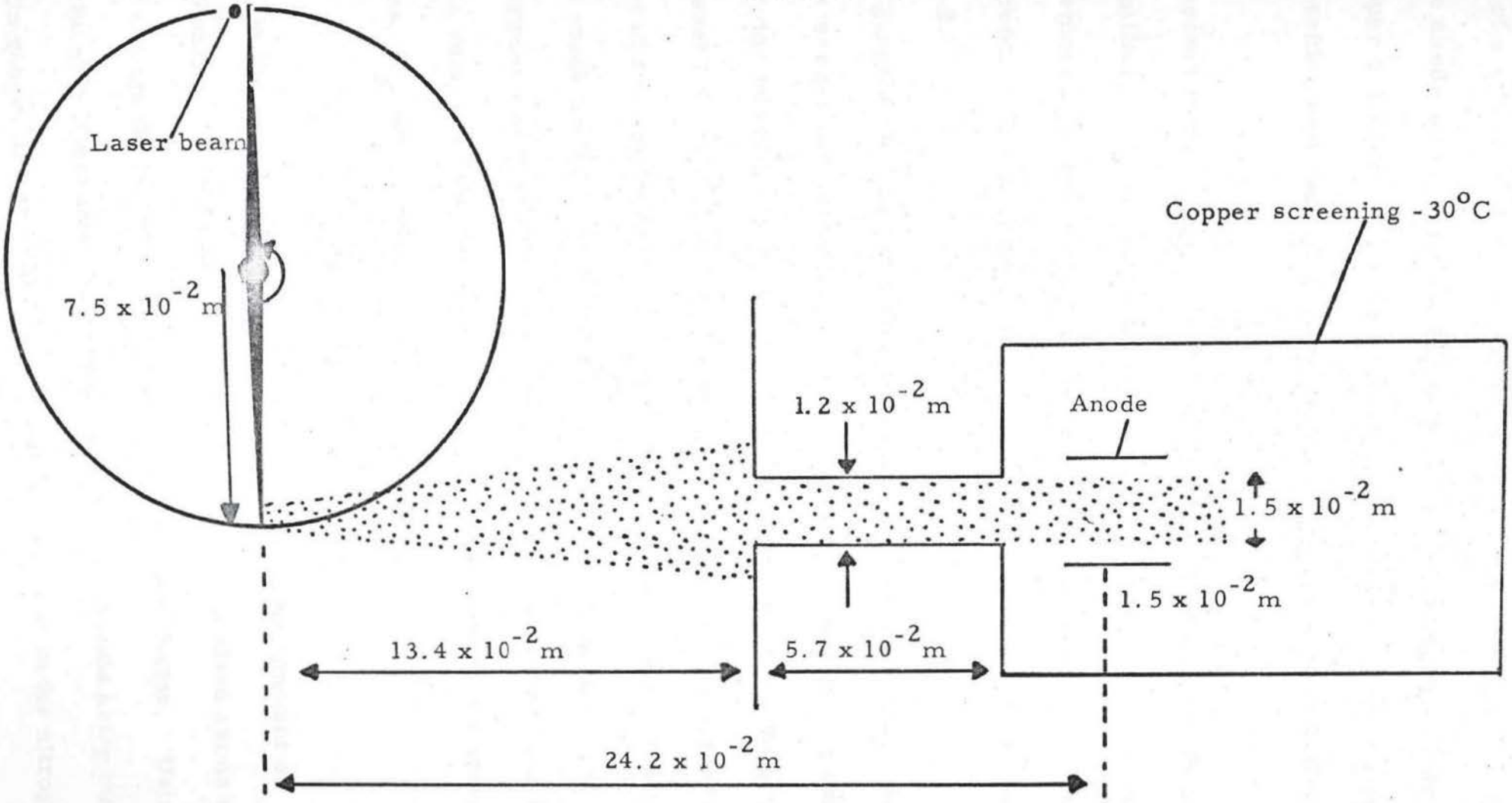
Laser beam
7.5 x 10^-2 m
Copper screening -30°C
1.2 x 10^-2 m
Anode
1.5 x 10^-2 m
1.5 x 10^-2 m
13.4 x 10^-2 m
5.7 x 10^-2 m
24.2 x 10^-2 m

consisted of a cylindrical anode and within this a thin wire grid. On the axis of the anode was a tungsten filament and surrounding the whole unit was a copper cylinder, which was cooled and earthed to provide electrostatic screening and some degree of cryogenic pumping through the glass envelope.

Connected to the gauge head was a modified version of the P.I.N. diode amplifier. The modified amplifier merely had the output voltage clamps removed so that the output voltage swing was linear for an applied input current. The circuit diagram for the ionisation gauge is shown in Figure 8.2.

The gauge was calibrated by comparison with another gauge placed within the vessel and connected to a standard vacuum measuring unit. With no rotor running and no cooling applied to the detector, the pressure in the vessel ($\backsim 10^{-6}$ Torr) was compared with the voltage appearing on the output of the amplifier. The beam detector gauge was operated in the same mode as if it were used as a normal vacuum gauge; thus the output current was directly proportional to the number of nitrogen atoms within the volume of the detector. From this statement, the number of molecules, N_d, within the detector is given by:

$$N_d = I_d \cdot m \qquad (8.1)$$

where I_d is the current from the detector and m is the constant of proportionality. This assumes that the number of ionised atoms detected does not change the density of molecules within the detector. Using the manufacturer's literature and comparative measurements using the other ionisation gauge, it was possible to produce a value of m for nitrogen of 1.29×10^{19} molecules/detector volume/A. However, it was necessary

Figure 8.2

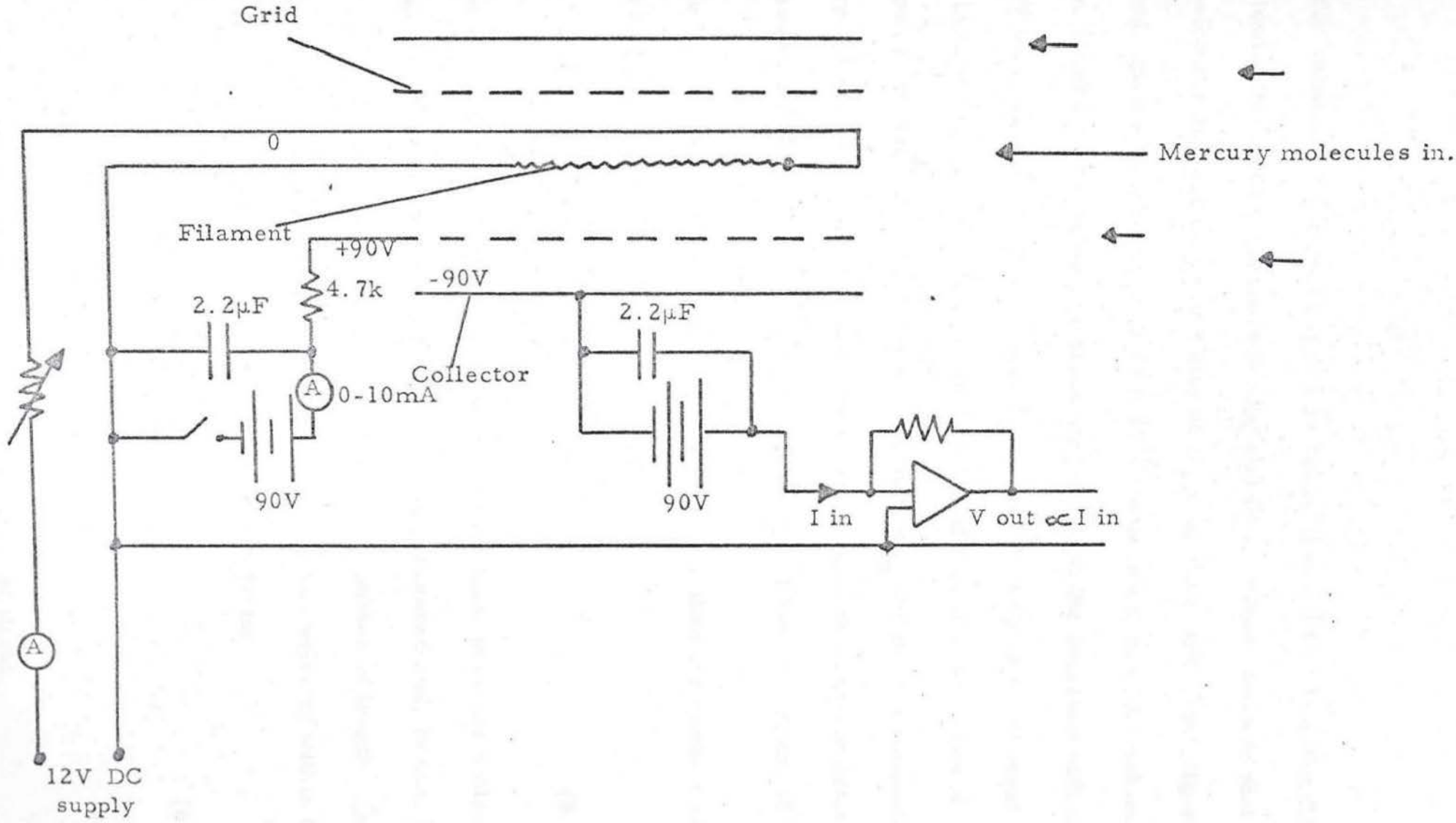
Grid
0
Mercury molecules in.
Filament
+90V
4.7k
-90V
2.2μF
2.2μF
Collector
A
0-10mA
90V
90V
I in
V out ∝ I in
A
12V DC
supply

to know the value of m for mercury, this being deduced by using handbook data for ionisation cross-sections for Hg and N_2. These showed that Hg had twice the ionisation probability of N_2 and, thus, the above figure was halved, giving m a value of 6.45×10^{18} molecules/detector volume/A.

Now, if molecules of Hg are travelling through the detector with a velocity V and, if the detector volume is defined by a cylinder of length L_d then in one second a cylinder of molecules of length V will have to pass through the detector to produce a current of I_d lasting one second. Therefore, the number of molecules which must pass through the detector in one second must be $\frac{m \cdot V \cdot I_d}{L_d}$. Thus if a pulse of current of amplitude I_d, lasting only for a period of time, T , then the number of molecules, N_p, within the pulse is given by:

$$N_p = \frac{V \cdot I_d \cdot m \cdot T}{L_d} \qquad (8.2)$$

As the laser beam is positioned such that the time when the molecular pulse began is known, the time-of-flight can be measured and, hence, by dividing any given shaped pulse into small squared pulses of length $\triangle t$ and height I, the number of molecules $\triangle A$ of a given velocity within that range of time $\triangle t$, can be approximately deduced from:

$$\triangle A = \frac{I . \triangle t \cdot k}{T_f} \qquad (8.3)$$

where

$$k = \frac{m}{L_d} \cdot S \qquad (8.4)$$

where S is the distance of flight and T_f is the time of flight.

The efficiency of the detector was low, of the order of 10^{-3}% and hence noise was a problem and will be discussed later.

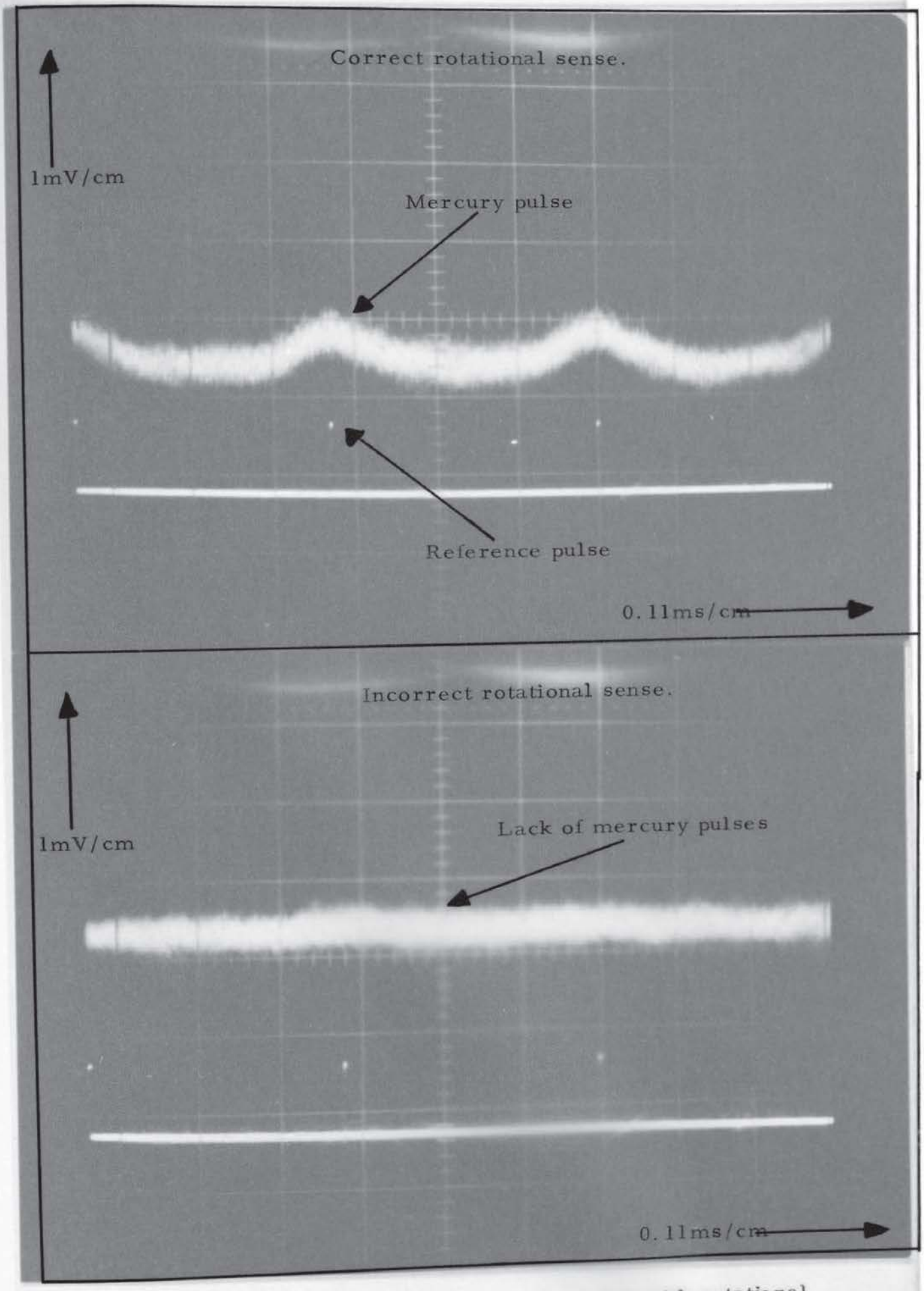

PLATE 8.1 Mercury pulses produced by rotor with rotational speed of 1,500rev/s.

The rotor was run in a vacuum of 10^{-5} Torr and the beam unit temperature set on 140°C. The laser beam was so positioned that the rotor blade intercepted the beam when in a direct line of sight with the detector. This pulse was used for measuring the frequency of rotation of the rotor and also for the time-of-flight measurements. Further to this point, it was used as a reference signal in the Boxcar detector unit discussed later. Next, the rotor was run up to 1,500 revolutions/s, producing a tip speed of 700 m/s. The output from the amplifier is shown in Plate 8.1. The upper frame shows pulses of mercury and below there is the pulse from the laser to show the 'shooting position'. The lower trace shows the output from the amplifier when the rotor is spinning in the wrong direction, but all other conditions being the same as for the upper trace. Plate 8.2 shows mercury pulses produced by the rotor at 3,000 revolutions/s, equivalent to a tip speed of 1.4 km/s. As will be seen from the photographs, the signal to noise ratio is approximately 2:1, making it very difficult to obtain useful information directly from these photographs. However, the noise can be substantially reduced by the use of a linear gate with integration, combined with a triggerable delay sweep generator, to form a Boxcar detector, a brief description of which will follow.

The Boxcar detector (26) can be used to reduce noise in any signal provided the signal is periodic and some reference signal can be produced at the same repetition rate. The reference signal needs to be fairly noise-free, but the actual shape of its waveform is not important. This reference signal is used to trigger a pulse with an adjustable width, which can be made to occur at some delayed period after the trigger point.

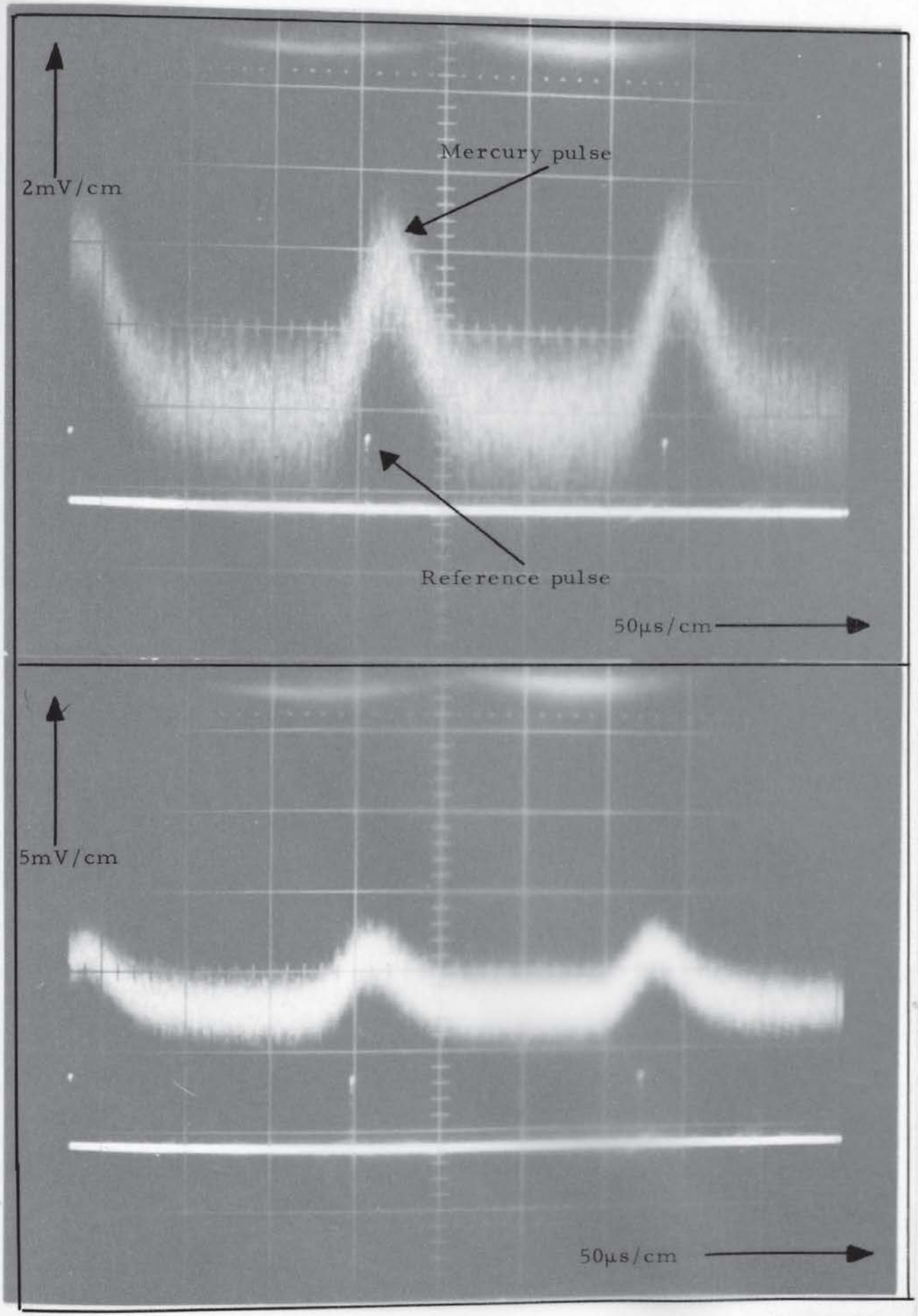

PLATE 8.2 Mercury pulses produced by rotor with rotational speed of 3,000rev/s.

Figure 8.3

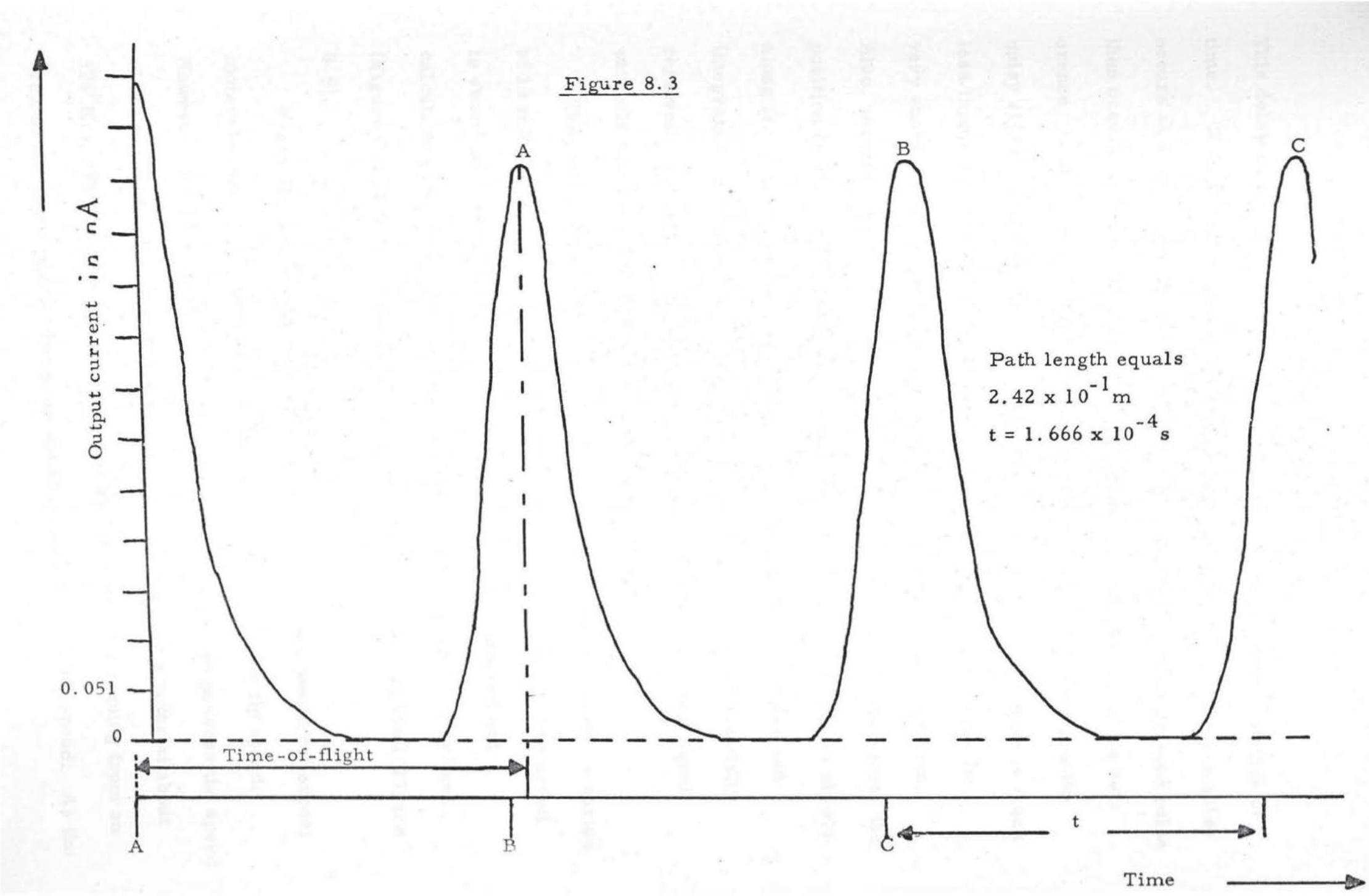
Output current in nA
A
B
C
Path length equals
2.42 x 10^-1 m
t = 1.666 x 10^-4 s
0.051
0
Time-of-flight
A
B
C
t
Time

This delay can be set as a constant or it can vary as a linear function of time. It is in this latter state that the unit is operated. Thus, a pulse occurs at some time-delay after the reference pulse and this delayed pulse then occurs at a steadily increasing time-delay with respect to the reference. This pulse is then used to open the linear gate and allow the noisy signal to be fed into an integrator. The width of the pulse is much less than the repetition of the waveform and hence the gate opens for a very short time and samples only a very small part of the waveform. Also, the period of the delay only varies slowly with time; therefore, the position on the noisy waveform, where the gate opens, only moves slowly along it. Hence, each point on the noisy waveform is sampled and integrated many thousands of times, so that the noise is substantially removed. Noise is any signal that appears with the required signal, which is not periodic with the reference signal.

The output from this unit was fed to a graph plotter and over a period of 15 minutes the waveform was scanned and 'cleaned up'. The output is shown in Figure 8.3. The waveform was then measured and calculations made of the number of atoms within a given velocity band (Figure 8.4) and the number of atoms within a given energy band (Figure 8.5).

From simple considerations given in Chapter I, one would not expect molecules within the beam to have a velocity less than the tip speed. However, it will be seen from Figure 8.4 that molecules possess the speed of the rotor tip plus and minus the thermal velocity for a rotor at about $370^{o}K$. This can be partly explained by the molecules coming from an area of the rotor blade, where the speed is less than the tip speed. As the

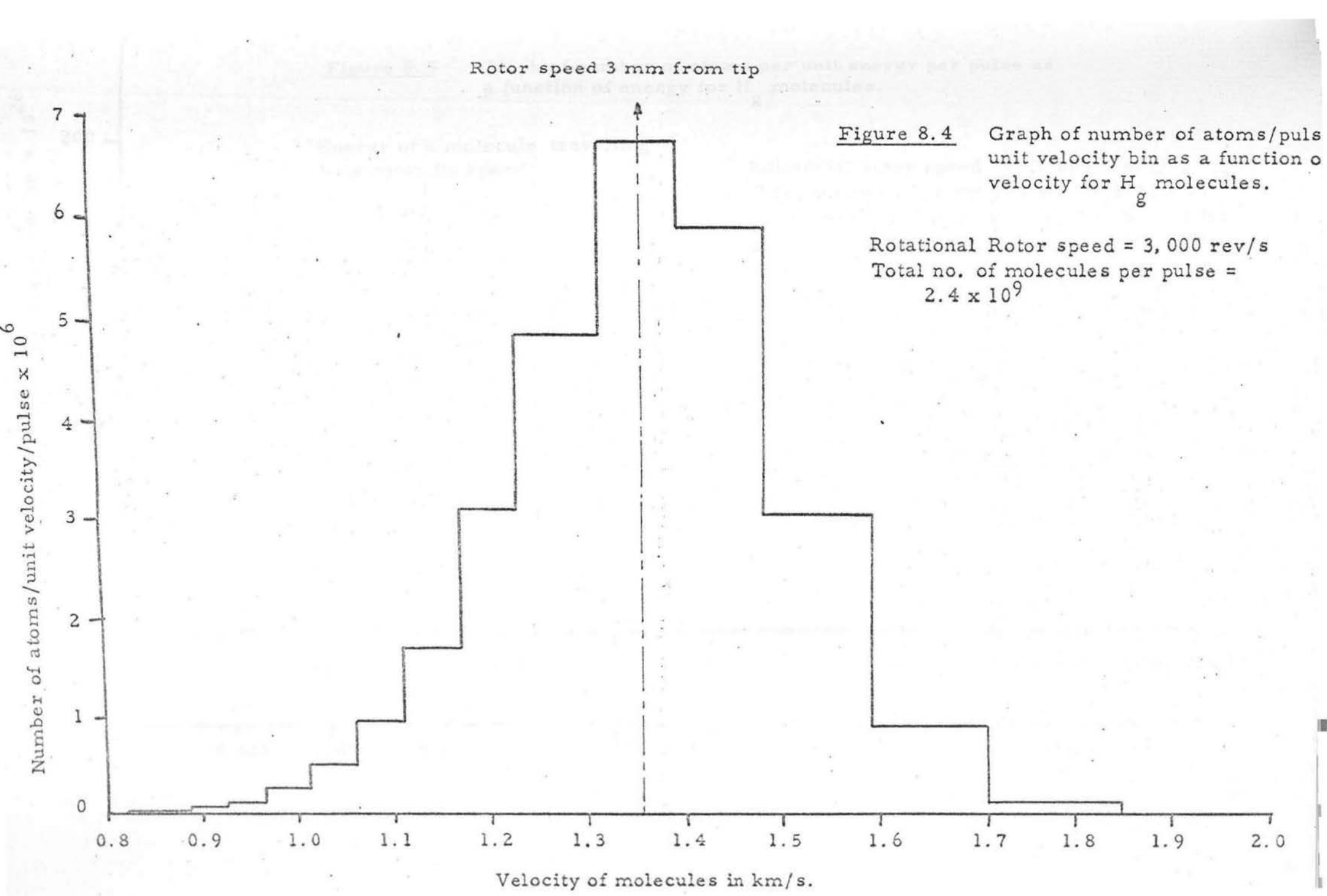

Figure 8.4 Graph of number of atoms/puls unit velocity bin as a function o velocity for H_g molecules.

Rotational Rotor speed = 3,000 rev/s
Total no. of molecules per pulse = 2.4×10^9

Figure 8.5 Graph of number of atoms per unit energy per pulse as a function of energy for H_g molecules.

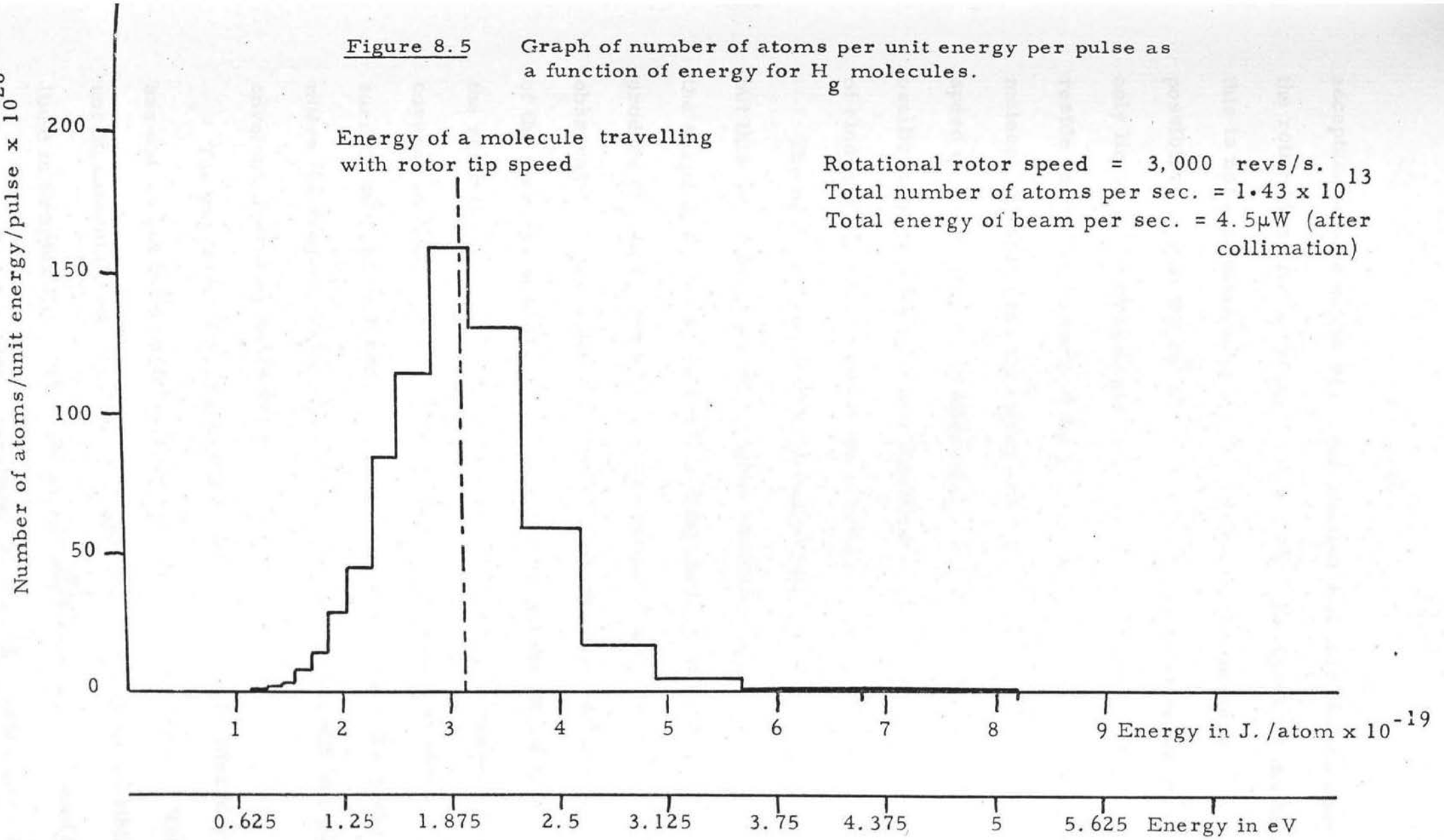

acceptance angle of the beam collimation will only allow a 6mm length of the rotor blade from the tip to be in a line-of-sight with the detector, this is not sufficient to produce an effect of this magnitude. Another possibility is that the collected mercury molecules on the rotor tip do not only lie on the leading curve of the cone but, due to surface diffusion, some reside on the flat truncated tip of the rotor blade. This means that molecules leaving the tip could have speeds of plus or minus.the thermal speed of the molecules in addition to the tip speed. Observation of the oscilloscope photographs and the Boxcar-processed signal shows no sign of elastic collisions between the rotor arm and mercury molecules.

The beam intensity was approximately $5 \times 10^{+15}$ molecules/sr/s but this would increase with higher rotational speeds and also by changing the shape of the tip as outlined in Chapter II. The rotor was used to produce this beam for a continuous period of six hours and after this observation of the rotor tip indicated that the fast molecular collisions of the mercury with the arm had not damaged the fibres or the resin at the rotor tip. The inside surface of the beam detector was found to be covered in a thin metallic layer, which appeared to be mercury. The surface was not uniformly covered but tended to have the thickest layer where the copper cooling jacket was in good contact with the glass envelope over a sizeable area.

The experiment to observe the effect of mercury-mercury collisions has not as yet been performed due to material problems. These are not fundamental and therefore the experiment should be possible as outlined in Chapter III. The optical resonance[27] which it is hoped to excite is the so-called forbidden transition $^3P_1 \rightarrow {}^1S_o$, which gives a wavelength

of 253.7nm. Thus the reaction would be of the form:

$$\overrightarrow{Hg} + \overleftarrow{Hg} \longrightarrow Hg^{*} + Hg \longrightarrow Hg + Hg + h\nu \nearrow$$

As the value for the cross-section for this resonance is not known, it is difficult to know the degree of sensitivity required for the photon-counting system. However, cooling of the photo-multiplier cathode is provided to reduce the dark current and the general light background can be reduced by using U-V transmission filters.

8.3 Conclusions.

The results which have been achieved during the last three years indicate that rotors are a practical proposition for producing molecular beams with energies between 1 and 10eV. The techniques used for making the rotors and the control electronics have proved reliable. The equipment built during this time is to be transferred to the Department of Chemistry, where modified apparatus will be built and rotors used to study the chemical properties of molecules. Also, at Heriot-Watt[19] University carbon fibre rotors are to be used to investigate molecule surface phenomena.

The principles are simple and the apparatus is less costly in man power and finance than alternative methods. However, the enormous forces created by high speed rotation require great precision in manufacture and assembly of the rotorsif they are to be used with confidence in the future. Yet it would seem that rotors,and carbon fibre-armed rotors in particular,have a future as molecular beam producers.

CHAPTER IX

SUPPLEMENT TO THE THESIS

The following work does not constitute a part of the thesis but is a supplement to conclude the work presented within it. This work was accomplished by the author in the period between the submission of the thesis and the oral examination.

M. P. Ralls.

CHAPTER IX

9.1 Introduction.

The following work was carried out mainly by the author and is divided into three sections: firstly, the testing of the rotor synchronization electronics using two high-speed rotors; secondly, the colliding mercury beam experiment, in which it was hoped to excite atoms of mercury and observe the 253.7nm intercombination line; and, thirdly, a re-examination of the velocity-intensity results produced by the single rotor experiment.

9.2 Rotor Synchronisation.

After some delay, two rotors were accelerated in the double rotor apparatus, which has already been described in Chapter III. The rotors had previously been individually tested to a rotational speed of 3,750 rev/s. The purpose of this double rotor acceleration was to ascertain the effectiveness of the phase locking electronics described in Chapter VII. The electronics had already been tested using one rotor and a frequency standard, but this could not be made to simulate two phase-locked, slightly decelerating rotors.

The mercury ovens were run at a temperature of 140^{o}C producing a vessel pressure of 10^{-5} Torr, and hence a gas load on the rotors. The rotors were first locked at 1,000 rev/s and then at 2,300 rev/s. Both attempts were completely successful and produced an approximate R.M.S. phase lock of 1.5^{o} arc. Following this successful locking, the rotors were deliberately un-locked and re-locked several times to enable observations to be made of the damping characteristics of the control system. There appeared to be no significant phase overshoot, indicating sufficient damping. The relative phase condition of the two rotors was

Figure 9.1 Arrangement of Apparatus Scale 0.5

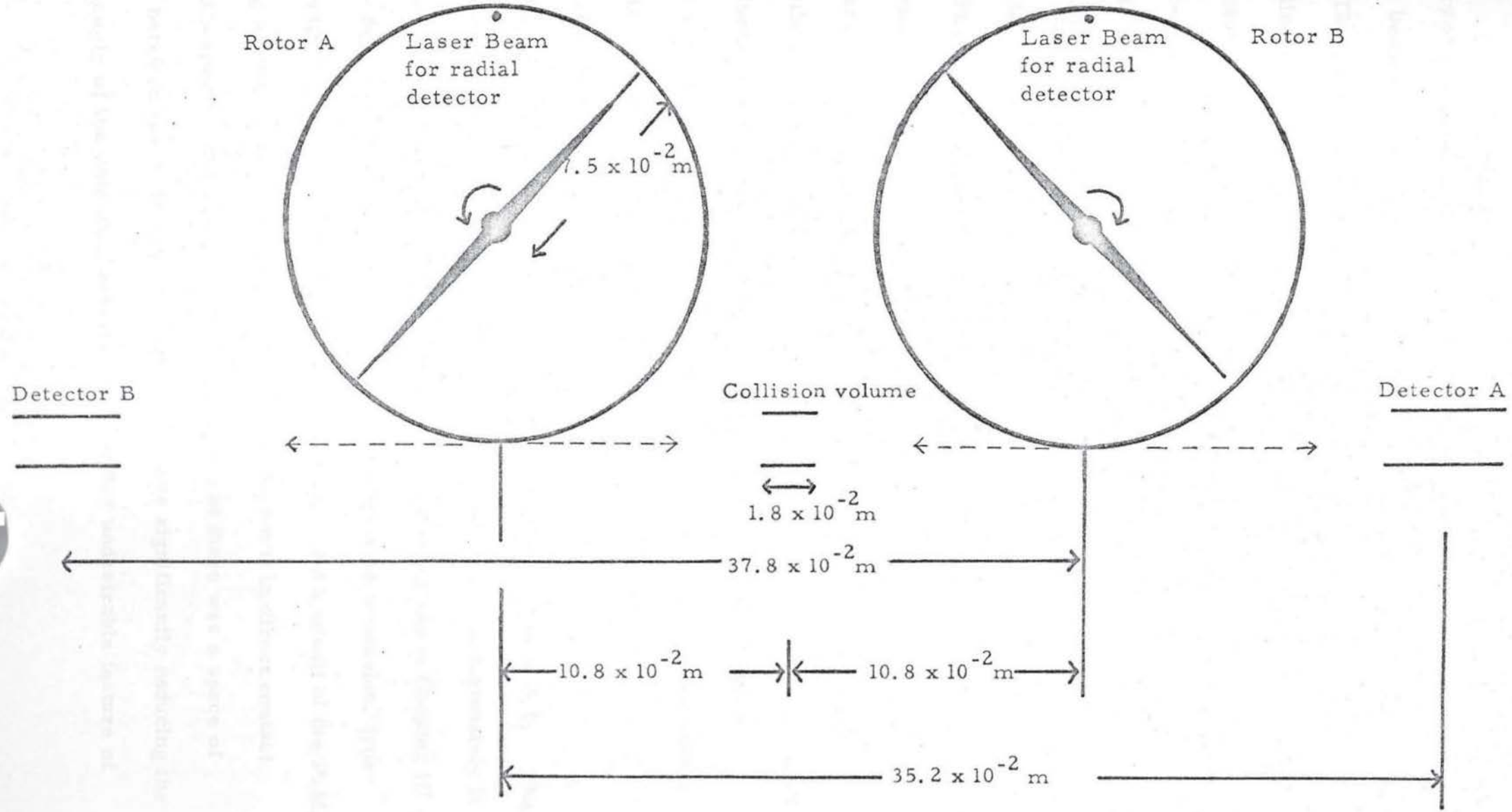

observed oscilloscopically using pulses derived from the interrupted laser beams.

The rotors were also run and phase-locked when performing the colliding beam experiment to be discussed in Section 9.3. In this case the rotors were accelerated to a rotational speed of 3,600 rev/s and were phase-locked. The phase-lock was established as easily as at the lower speeds but the phase wander was slightly smaller at the higher speed.

9.3 The Colliding Beams Experiment.

9.3A Introduction.

The colliding-beam experiment outlined in Chapter III and Chapter VIII was attempted using two conical, carbon fibre composite rotors of the same design as those used in the production of a mercury beam described in Chapter VIII. The object of the experiment was to convert the kinetic energy released in a head-on collision of two Hg atoms to excite one into the $^3P_1$ state, and hence observe the singlet-triplet inter-combination line at 253.7nm.

9.3B Apparatus.

The physical layout of the components is shown in Figure 9.1. The photomultiplier (P.M.) was mounted as in Figure 3.2. Unfortunately it was not possible to use the end-window P.M. as described in Chapter III due to its failure and so this was replaced by a side-window version, type IP28 with a quantum efficiency of 20% at 254nm. As a result of the P.M. having a side window, it was not possible to mount it in direct contact with the spectrosil light pipe. This meant that there was a space of 15cm between the P.M. and the light pipe, thus significantly reducing the solid angle of the detecting system. A further undesirable feature of

Figure 9.2 Spectral Response of Ultra-Violet Transmission Filter

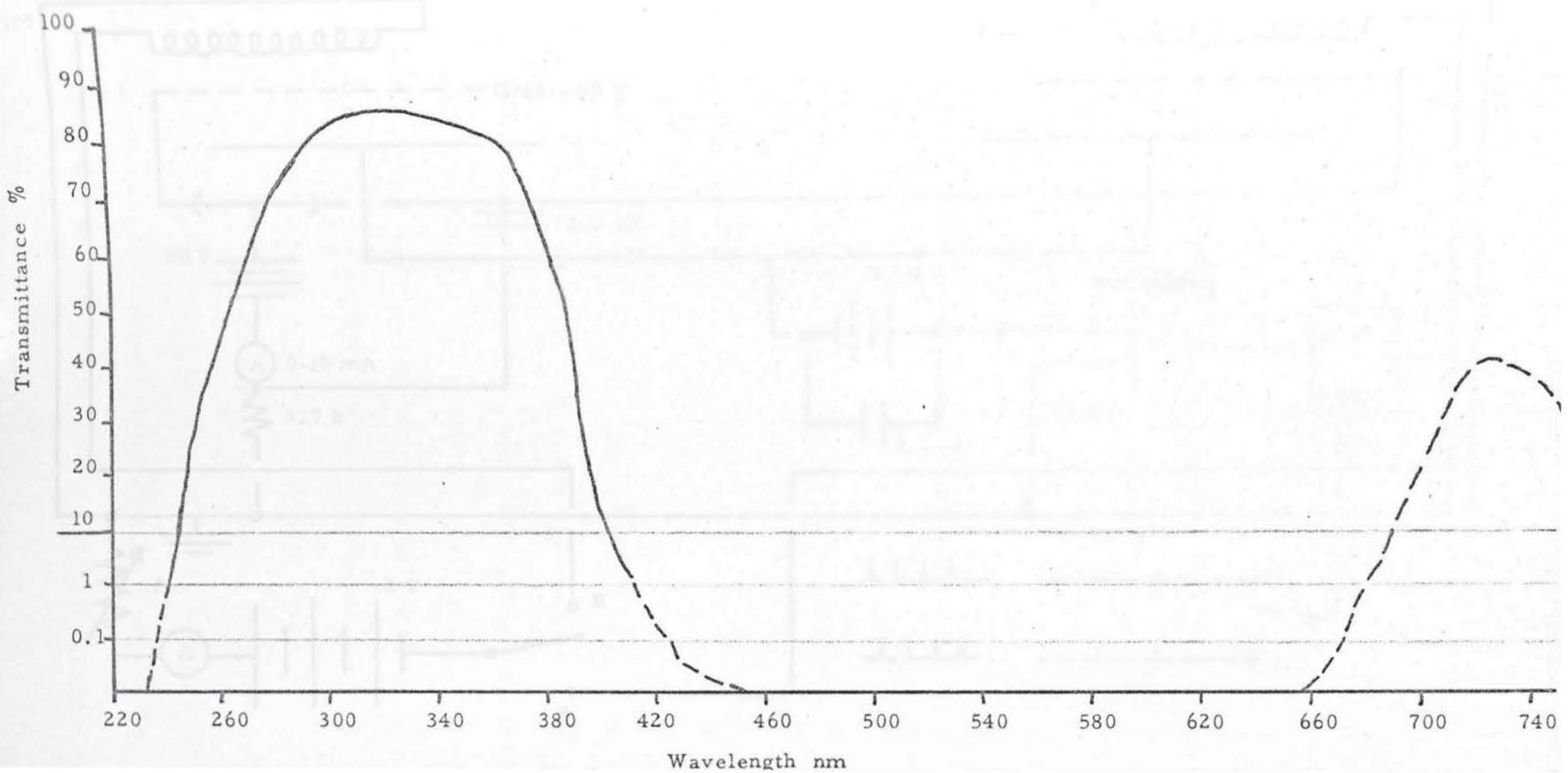

Figure 9.3

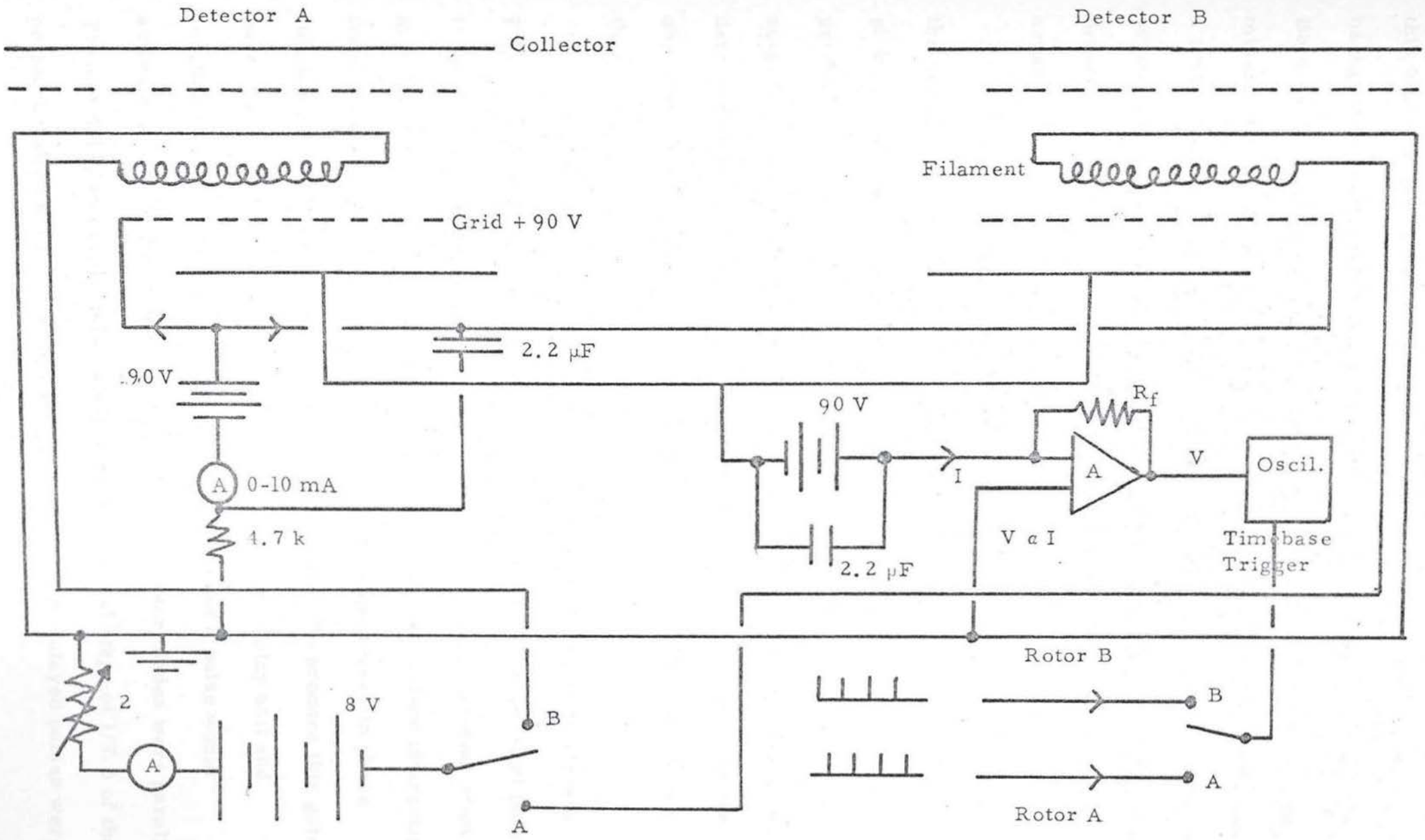
Detector A
Collector
Detector B
Filament
Grid + 90 V
2.2 μF
90 V
R_f
I
A
V
Oscil.
A 0-10 mA
4.7 k
V α I
Timebase
Trigger
2.2 μF
Rotor B
2
8 V
B
A
B
A
Rotor A

this was that the cathode of the P.M. could not be cooled and hence the background count rate from the P.M. was limited by the dark current. Between the light pipe and the P.M. was placed an ultra-violet transmission filter with a spectral response shown in Figure 9.2. This had a transmission of 35% at 254nm. Taking the geometry of the system into account, in addition to the above factors, the arrangement had an optical detection efficiency of 0.0056%, compared with 0.22% for the original arrangement.

Beam monitors were wired up as shown in Figure 9.3. Either of the beam monitors could be selected for displaying the pulses from a given rotor, by switching the relevant heater-current on and hence producing an ionising electron current. The output from the current amplifier was fed to an oscilloscope which was triggered by the radial detector of the relevant rotor. Thus it was possible to check that the observed pulses were phase-locked to the rotor which was producing them.

A schematic diagram of the photon-counting circuit is given in Figure 9.4. During a measurement period, scaler S_1 would count pulses from the P.M. continuously while scaler S_2 only counted photons when the gate input allowed. The signal for the gate input was derived indirectly from a pulse which was produced when the two rotors were in phase (blades parallel) and hence in a shooting position. To produce this gate pulse the in-phase pulse was fed to a variable time delay unit and lengthened before being fed to the gate input. Thus a pulse would activate scaler S_2 some pre-set time after the rotor blades were parallel. The set delay interval could be adjusted by integral steps of 1/7.6 of the period between successive in-phase pulses. These delayed pulses were

Figure 9.4

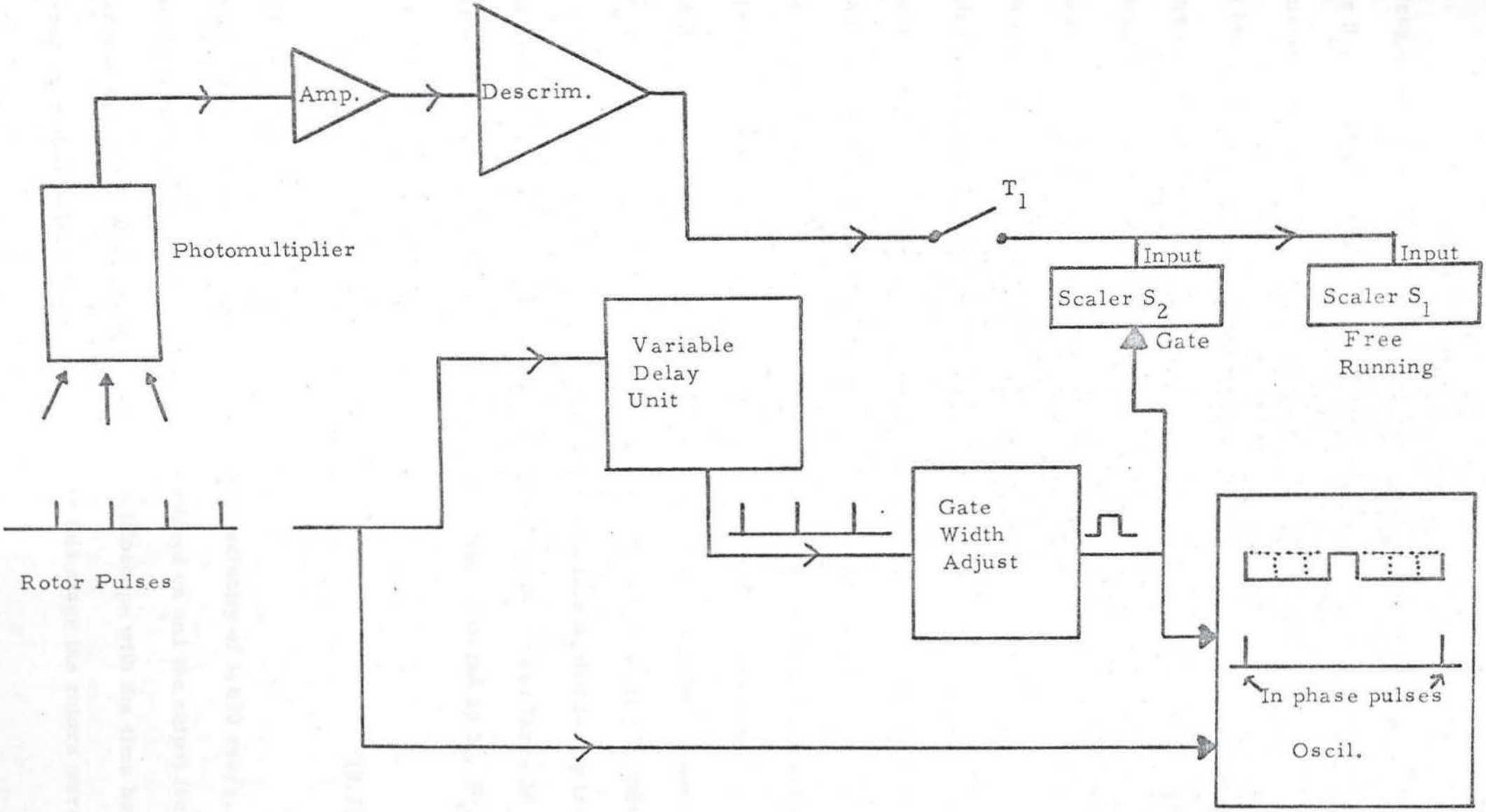
Amp.
Descrim.
Photomultiplier
T_1
Input
Input
Scaler S_2
Scaler S_1
Gate
Free
Running
Variable
Delay
Unit
Gate
Width
Adjust
Rotor Pulses
In phase pulses
Oscil.

then lengthened to 1/7.6 of this time period and fed to the gate input of scaler S_2. Thus when switch T_1 is closed, assuming the photon flux to be constant, the count/unit time produced in scaler S_1 should be 7.6 times the count in scaler S_2. However, should an increased number of photons arrive at the P.M., to coincide with the time that S_2 is counting and should this occur consistently, then the ratio of S_2/S_1 would show an increase value compared with that produced when these are not correlated. In this way it was possible to observe the photons collected from the collision volume at various times after the production of the beams. If during a period of time comparable with the gate pulse, there was an increase of $\triangle N$ counts in the number of photons detected and N was the number of non-correlated photons counted by S_1 between two successive parallel blade positions, then after (M + 1) parallel blade positions, scaler S_1 will have counted $M(N + \triangle N)$ and scaler S_2 will have counted $M(N\overline{P}_s + \triangle N)$. $\overline{P}_s$ is the average ratio of S_2/S_1, when $\triangle N = 0$, this being equal to the gate width of the pulses fed to scaler S_2 divided by the period between successive gate pulses fed to scaler S_2. For large M the ratio of counts collected by S_2 divided by counts collected by S_1, P_s, is given by:

$$P_s = \frac{N\overline{P}_s + \triangle N}{N + \triangle N} \qquad (9.1)$$

9.3C Results.

The rotors were accelerated to an angular velocity of 3,600 rev/s. The beam detector filament for rotor A was turned on and the output from the current amplifier was displayed on the oscilloscope with the time base triggered by radial pulses from rotor A. At this stage the rotors were

not synchronised. With an electron ionisation current of 5mA, small pulses could be seen above the noise locked to the timebase, but the pulses were too small to allow sensible measurements to be made. The primary beam units were at a temperature of 140°C comparable with the temperature used in the single Hg beam experiment. Observation of rotor B pulses with the timebase locked to radial pulses from rotor B yielded similar results. However, when detector pulses were displayed with the timebase triggered by the other rotor's radial pulses, there was no observable waveform locked to the timebase. This indicated that pulses of atoms were, in fact, being produced by the rotors and were travelling through the collision volume. The size of the pulses could be attributed to the distance the beams had to travel and the fact that the beam had to pass above the other rotor's mercury vent and possibly through a volume of relatively high pressure where the chances of collision were increased.

The rotors were then synchronized using the phase-locking electronics described in Chapter VII. Lock was maintained to within 1.5° arc. The beam unit filaments were turned off to prevent light entering the collision volume. For a given delay time the scalers were allowed to count for 60s and then the delay increased until 7 delay periods had been used to sample the ratio of scaler S_2/scaler S_1. The scaler counts are shown in Figure 9.5 and the ratios shown in Figure 9.6 Figure 9.7 is a histogram showing the ratios as a function of delay time. The marked bin denotes the delay time which would be expected to have a greater ratio than the others if photons were produced by the return of excited Hg atoms from the $^3P_1$ state to the ground state.

Average Delay of Bin μs	S_1	S_2
9.1	38,191	4,901
27.3	40,276	5,357
45.5	40,097	5,303
63.7	84,069	11,079
81.9	41,818	5,403
100.1	42,966	5,666
118.3	38,400	5,078

Figure 9.5

Average Delay of Bin μs	Ratio S_1/S_2
9.1	0.1283
27.3	0.1330
45.5	0.1322
63.7	0.1318
81.9	0.1292
100.1	0.1318
118.3	0.1322

Figure 9.6

The results shown in Figure 9.7 show no obvious effect, as the delay of the observation time-window is increased. The adjusted standard deviation for the ratios S_2/S_1 is 1.75×10^{-3}. This compares favourably with a standard deviation of 1.76×10^{-3} calculated using random counting fluctuations expected from counting typically 5,000. Using the criterion of a statistically significant ratio being greater than 3σ, from the mean of all the ratios, where σ is the standard deviation, there are no bins which produce a significant result. However, it is of interest to know how many photons, emitted during every beam interaction, would be needed to produce a ratio which would be greater than 3σ. If P_s is the observed ratio in one bin and $\overline{P}_s$ is the average ratio of all the bins, then the ratio will be significant if:

$$P_s > \overline{P}_s + 3\sigma \qquad (9.2)$$

Combining this with equation 9.1 to give the minimum number of detected events/beam interaction, $\triangle N$,

$$\triangle N > 3\sigma \; N/[1 - (\overline{P}_s + 3\sigma)] \qquad (9.3)$$

With the rotors rotating at 3,600 rev/s this gives 7,200 beam interactions/s. The dark current counting-rate was determined when the rotors were spinning at much slower speeds and gave a count-rate of 660 counts/s. Using this and knowing the period between successive parallel blade positions and the values of $\overline{P}_s$ and σ, a minimum count of 5.57×10^{-4} events/beam interaction would be necessary before they could be considered significant. However, the optical collection system was only 0.0056% efficient and hence the minimum number of events/beam interaction must be increased to 9.85 events/beam interaction.

Figure 9.7 Graph of delay time from parallel position against scaler Ratio S_2/S_1

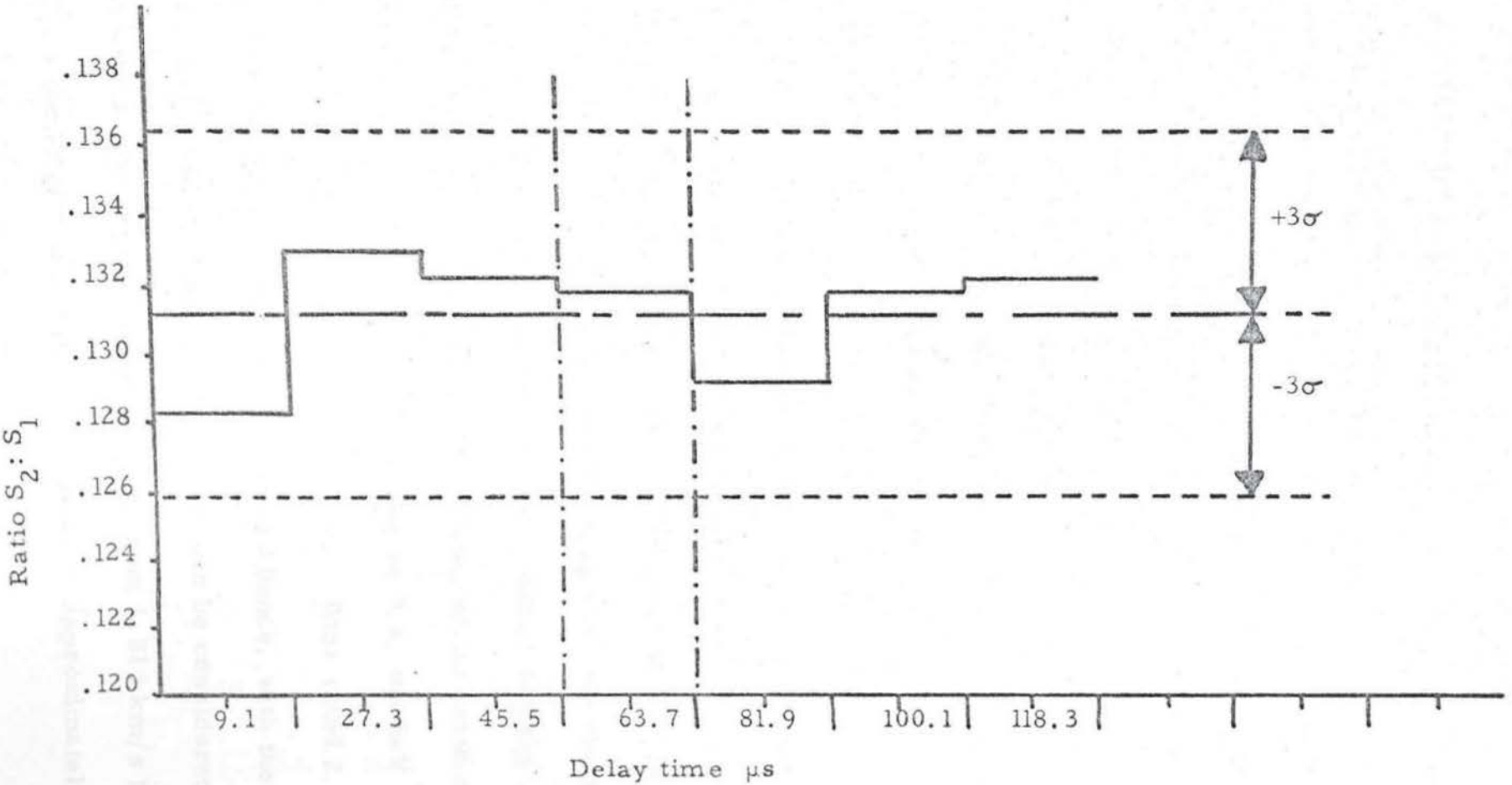

The results of this experiment can be used to arrive at an approximate upper limit for the cross-section for the excitation and decay of the 253.7nm intercombination line of Hg. Firstly it is necessary to estimate the sensitivity of the detection arrangement and this has been achieved in the previous section. Secondly, it is necessary to estimate the number of atoms in each pulse. Unfortunately the beam detectors were not sensitive enough to enable accurate measurements to be made of the beam characteristics. However, the temperature of the ovens was comparable with the temperature of the oven used in the single mercury beam experiment, as was the vessel pressure. The design of the rotors was the same and so it is reasonable to use the beam characteristics measured in the single beam experiment to estimate the characteristics of the beams in the double experiment. The data produced by the single rotor experiment does, however, require a small modification before it is reasonably compatible with the double rotor experiment. The results given in Chapter VIII were taken for a rotor rotating at 3,000 rev/s while the double rotor experiment was performed with rotational speeds of 3,600 rev/s. Thus the results of the single beam experiment shown in Figure 9.8 have to have a constant velocity added to them in order that they should be reasonably compatible with a rotor of the same radius rotating 600 rev/s faster. With reference to Figure 9.8, the 5eV threshold for the reaction is just exceeded by bin 6. Bins 1 and 2 contain only a relatively small number of atoms and hence, with the contents of bins 1 and 2 added to bin 3, each beam can be considered to be a uniform beam with a velocity spectrum ranging from 1.813 km/s to 1.55 km/s. Thus the total number of atoms/pulse is approximately

Figure 9.8 Results of Single Rotor Hg Beam exp. with rotor at 3,000 rev/s

Bin No.	Velocity Range km/s	Number of Atoms in Bin x 10^8
1	2.22 - 2.02	0
2	2.02 - 1.85	0
3	1.85 - 1.71	0.16
4	1.71 - 1.59	1.12
5	1.59 - 1.48	3.36
6	1.48 - 1.39	5.58
7	1.39 - 1.31	5.72
8	1.31 - 1.23	3.89
9	1.23 - 1.17	2.03
10	1.17 - 1.11	1.03
11	1.11 - 1.06	0.53
12	1.06 - 1.01	0.26
13	1.01 - 0.966	0.11
14	0.966 - 0.926	0.04
15	0.926 - 0.889	0.007
16	0.889 - 0.854	0
17	0.854 - 0.822	0

equal to 2×10^{9} with an average velocity of 1.68 km/s. As this beam travels from the 'shooting position' to the collision volume, a distance of 1.08×10^{-1} m, the beam will spread out along the flight path, such that the time taken by the fastest molecules to reach the centre of the collision volume will be 59.5μs and in this time the slowest molecules will have travelled 9.225×10^{-2} m. Thus the length of the pulse is approximately 1.6×10^{-2} m. Using this information it is possible to conclude that the interaction time is about 10.1μs and this interaction will occur 64μs after the parallel blade position. The total number of atoms in each pulse is approximately 2×10^{9}. This is the number of atoms detected in the single rotor experiment where the detector presented a solid angle of 0.0031 sr. However, in the double apparatus the collision volume had a solid angle of 0.0218 sr relative to the shooting position. It would be reasonable to scale up the number of atoms detected in the single rotor experiment by the ratio of these solid angles, provided the beam produced by the rotor expanded into a greater solid angle than the collision volume. The solid angle into which the atoms from the tip expand is approximately given by $\pi V_T^2 / V_R^2$ where V_T is the thermal speed and V_R is the rotor tip speed. This produces a beam solid angle of approximately 0.1 sr; thus it is valid to scale up the number of atoms/pulse entering the collision volume by the factor 7, giving 1.4×10^{10} atoms/pulse.

Considering two cylindrical volumes of atoms of length L_p with a cross-sectional area, A, travelling towards one another, as in Figure 9.9, if they both enter the collision length, X_c, at the same instant, then the pulses will begin the interaction at a point $X_c/2$ along the collision

Figure 9.9 Simplified form of the Hg pulses

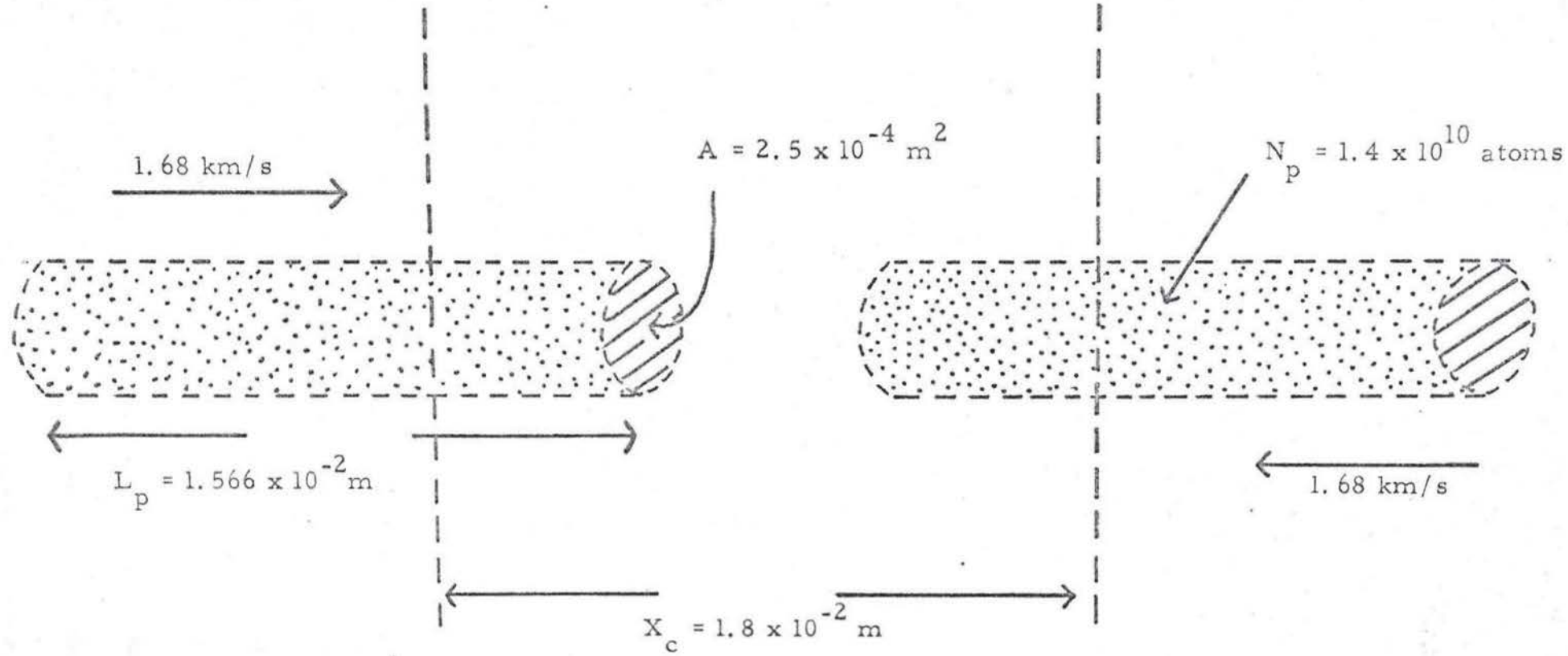

length and the two volumes will then move through one another and separate at $X_c/2$. Provided the length of the pulses, L_p, is shorter than X_c, the detection system observing all the distance X_c will observe all parts of the interaction. This was the case in the colliding beams experiment and hence the P.M. was capable of observing the whole interaction. The volume of the pulse was $L_p \times A$. and the probability of an atom from pulse A intereacting with an atom from pulse B is given by $1-e^{-[\frac{\sigma}{A} \cdot N_p]}$, where σ is the cross-section for the interaction and N_p is the number of atoms/pulse. As the probability of an intereaction is very small in this case for the excitation and emission of the intercombination line, $e^{-[\frac{\sigma}{A} \cdot N_p]}$ is very close to unity and hence the probability of interaction is given approximately by $\sigma N_p/A$. This means that, if there are less than $\triangle N$ observed interactions, then the cross-section for the interaction will be:

$$\sigma < A . \triangle N/N_p^2 \qquad (9.4)$$

The cross-section area (A) of the beam, which is equal to $2.5 \times 10^{-4} m^2$ is governed by the diameter of the collision volume. Using the minimum detectable count required to produce a statistical result of 9.35 photon events/pulse interaction and the estimate of the number of atoms/pulse of 1.4×10^{10}, an upper limit of the cross-section for the excitation by collision of the $^3P_1$ state and return to the ground state by emission of a 253.7nm photon, can be calculated, this being equal to $1.27 \times 10^{-23} m^2$. If the radius of a mercury atom in a metal or non-ionic solid is used to estimate the geometric cross-section, then the ratio of the cross-section for collisional excitation and decay mentioned above, to the geometric cross-section yields a factor of 5×10^{-5}.

9.3D Summary and Conclusions.

The experiment was hoped to give some information about the head-on impact of two Hg atoms, both being in the ground state. As the atomic collision was produced by atoms with the same speed but opposite direction, all of the kinetic energy of the pair could be used to energize some type of excitation. The characteristics of the colliding beams were that each beam pulse had an average speed of 1.68 km/s relative to the laboratory, with a result that the average available reaction energy/atom pair was 5.84eV. In the event of a two-beam collision, the first interactions would occur between the fastest members of the two pulses, giving a reaction energy of 6.88eV/Hg_2, this being equivalent to 660kJ/mole. Later collisions would involve lower available reaction energies until the lowest energy interaction of 5eV/Hg_2, equivalent to 480kJ/mole, would take place between the slowest members of the pulses.

Of the approximately 2.3×10^5 interactions that took place during one pulsed beam interaction, calculated using the geometric cross-section, less than 10 of these resulted in the emission of the 253.7nm intercombination line, even though the available energy for each interaction was above the threshold of 4.9eV. Therefore, it is necessary to consider some of the other routes of the interaction. The two ground state ($^1S_0$) Hg atoms could simply collide and form the molecular state $^1{}_0{}_g^+$ (see Figure 9.10). This would not produce a bound state, but would dissociate very shortly after the initial impact. The potential energy, built up as the two atoms became closer together, would then be re-converted to kinetic energy and hence this interaction would be purely elastic. This process is likely to be the most dominant of the

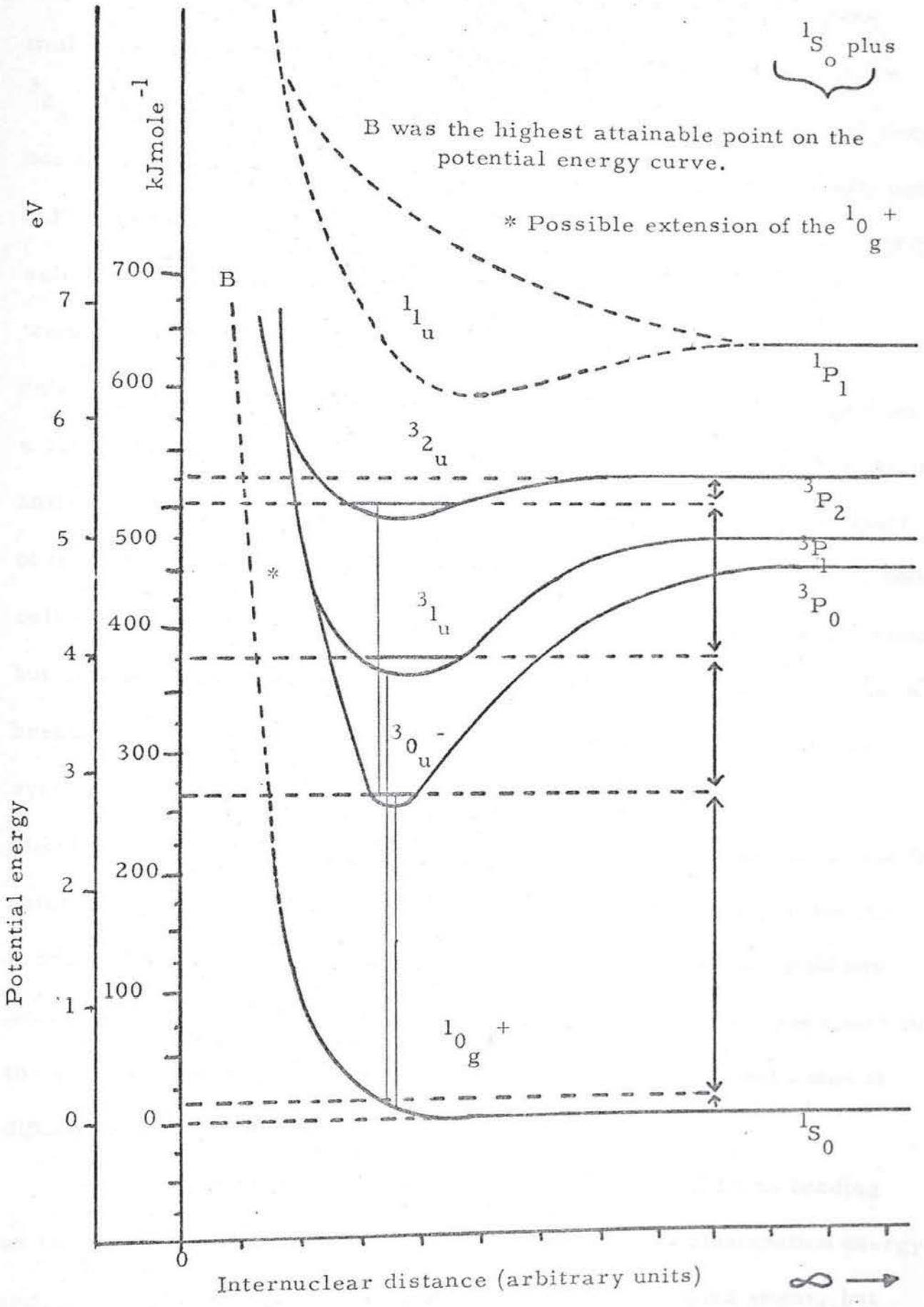

Figure 9.10 Potential energy curves for some of the lower energy states of Hg_2

interactions. However, during the formation of the $^1 0_g^+$ state, the molecular state may intersect with one of the following triplet states $^3 2_u$, $^3 1_u$ or $^3 0_u^-$. If the potential energy of the ground state pair does not quite reach the crossing points, or if the curves do not actually cross but come very close to one another, there is a possibility, restricted by selection rules, of tunnelling between the states, such that $^1 0_g^+$ transfers to $^3 2_u$, $^3 1_u$ or $^3 0_u^-$. The singlet - triplet restriction is relatively weak compared to the g - u selection rule. The change from a symmetric wave function, when the interaction is homo-nuclear, to an anti-symmetric result is very strongly forbidden unless the symmetry of the interaction can be broken. One possibility is to have a three-body collision which will allow a radiationless transition from a g to a u state, but this is a very unlikely occurrance. A second possible reason for a breakdown in this selection rule is that the collision of the two-body system is not completely homo-nuclear. The two atoms may not be identical due to isotope effects. In particular, mercury has seven stable, naturally occurring isotopes of which six have abundances greater than 6.5%. Thus, the chances of a homo-isotopic collision are small and hence the collision is not strictly homo-nuclear. However, the effect on the g - u selection rule of lowering the symmetry of the interaction is difficult to estimate.

Once in the new molecular state, there can still be no bonding as the potential energy of the pair is greater than the dissociation energy and, hence, the molecule dissociates to form two unbound atoms, but one of the atoms will not now be in the ground state. Depending on which

Figure 9.11 Possible reaction routes.

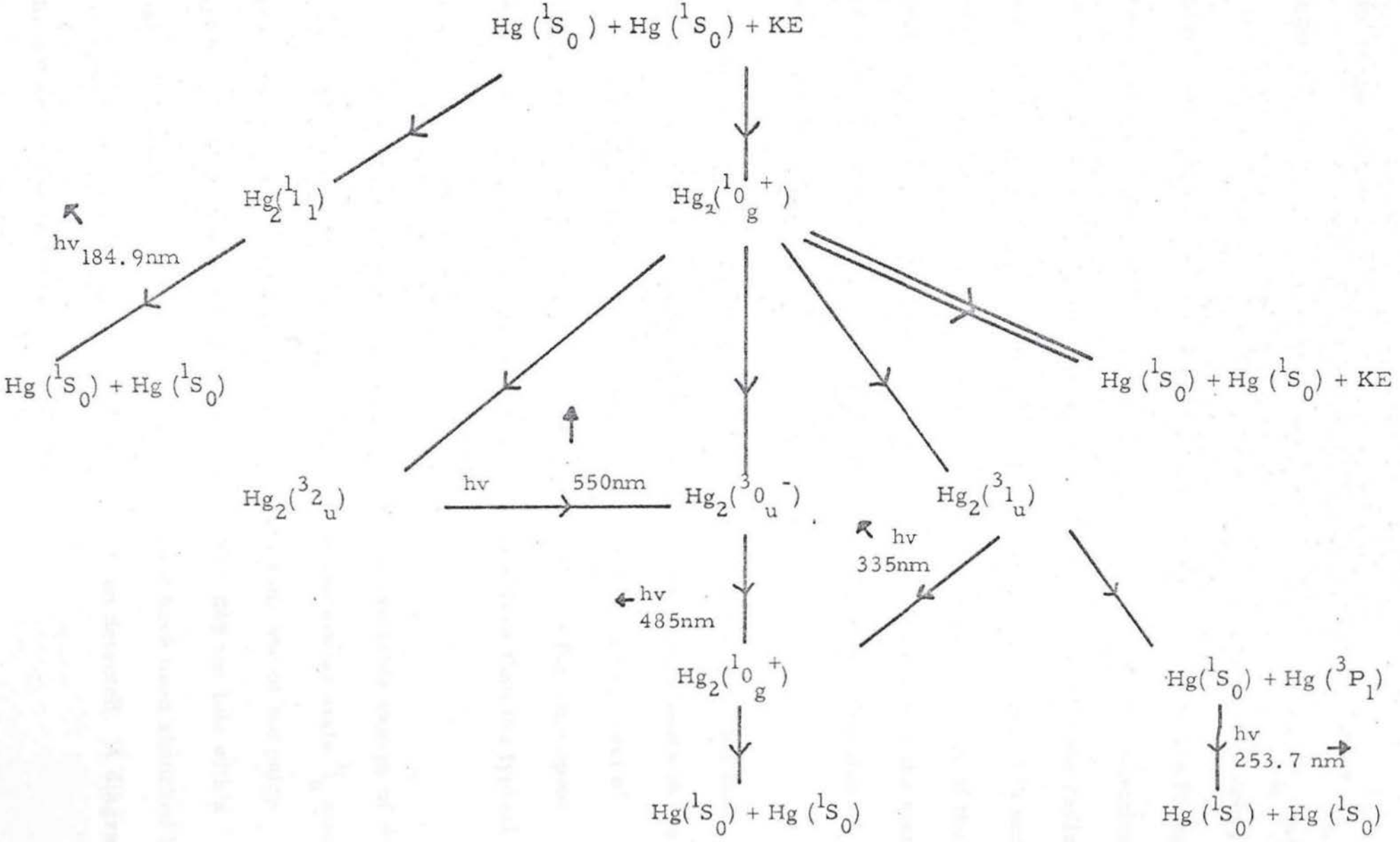

of the three molecular states, $^3 2_u$, $^3 1_u$ or $^3 0_u^-$, the molecule has changed to, one of the unbound pair will be in the $^3P_2$, $^3P_1$, or ^3P_o state respectively. The atomic states $^3P_2$ and ^3P_o are forbidden, to decay by electric dipole radiation to the ^1S_o state and these, if they are formed, would most likely be brought to the ground state by collisional deactivation. This process could also de-activate the $^3P_1$ state and prevent the radiative decay to the ^1S_o state. While it is a triplet-singlet transition, it is not as strongly forbidden as the $^3P_2$ and the ^3P_o transition and, hence, if the average time before a collision is greater than the lifetime of the state (1.06×10^{-7} s), then $6s^1, 6p^1, \quad ^3P_1 \longrightarrow 6s^2, \ ^1S_o$ by the emission of a 253.7 nm photon.

Another possible decay mode is by molecular vibrational band emission. This is a transfer from one of the vibrational levels in the $^3 2_u$, $^3 1_u$, or $^3 0_u^-$ states, to any other, energetically lower level of these three. This is a fairly unlikely decay route as the time spent in the vicinity of the potential well would be much less than the typical lifetime of the level (1 ms).

It was possible in a few cases, where the available energy of the two, colliding atoms exceeded 6.67 eV, that the molecular state $^1 1_u$ could be formed, which would mean that after separation, one of the pairs would be in the $^1P_1$ state and thereafter emit the 1.849 nm line with a radiative lifetime of 1 ns. This U-V line would have been absorbed by the oxygen in the air and hence would not have been detected. A diagram of the decay routes is given in Figure 9.11.

This was a fairly simple experiment which, while it needs to be performed with greater sophistication, highlights the possible use of double rotors to observe atomic/molecular interactions.

9.4. Simple Mercury Beam Analysis.

9.4.A. Re-Measurement of the observed data.

When the mercury pulses shown in Chapter VIII. Figure 8.3. were first analysed, the time axis was divided into equal intervals. This made it possible to determine how many atoms arrived in the detector within a flight time from t to t + Δt. These results were then converted into velocity ranges, which inevitably led to unequal width velocity intervals see Figure 8.4. and the need to normalize each bin height to take account of the varying width. This type of plotting also meant that the number of bins/unit velocity range varied as the bin velocity increased and hence, there was a loss of information concerning the shape of the pulse at the higher velocities. In view of these limitations, the author decided to re-measure the results shown in Figure 8.3. such that the time-axis was divided into twenty bins, which gave 20 velocity bins of equal width of 50 m/s. Figure 9.12 shows a histogram of the re-measured pulses. The mercury pulse shows a peak at a velocity of 1.36 km/s, which can be compared to an absolute tip velocity of 1.42 km/s. The error on the velocity-axis is approximately $\pm$ 4%, the main contribution being due to the uncertainty in the position along the flight path within the detector, where a molecule is ionised and collected. The pulse appears to have a high degree of symmetry about its maximum, which is surprising in view of the method of producing the pulse.

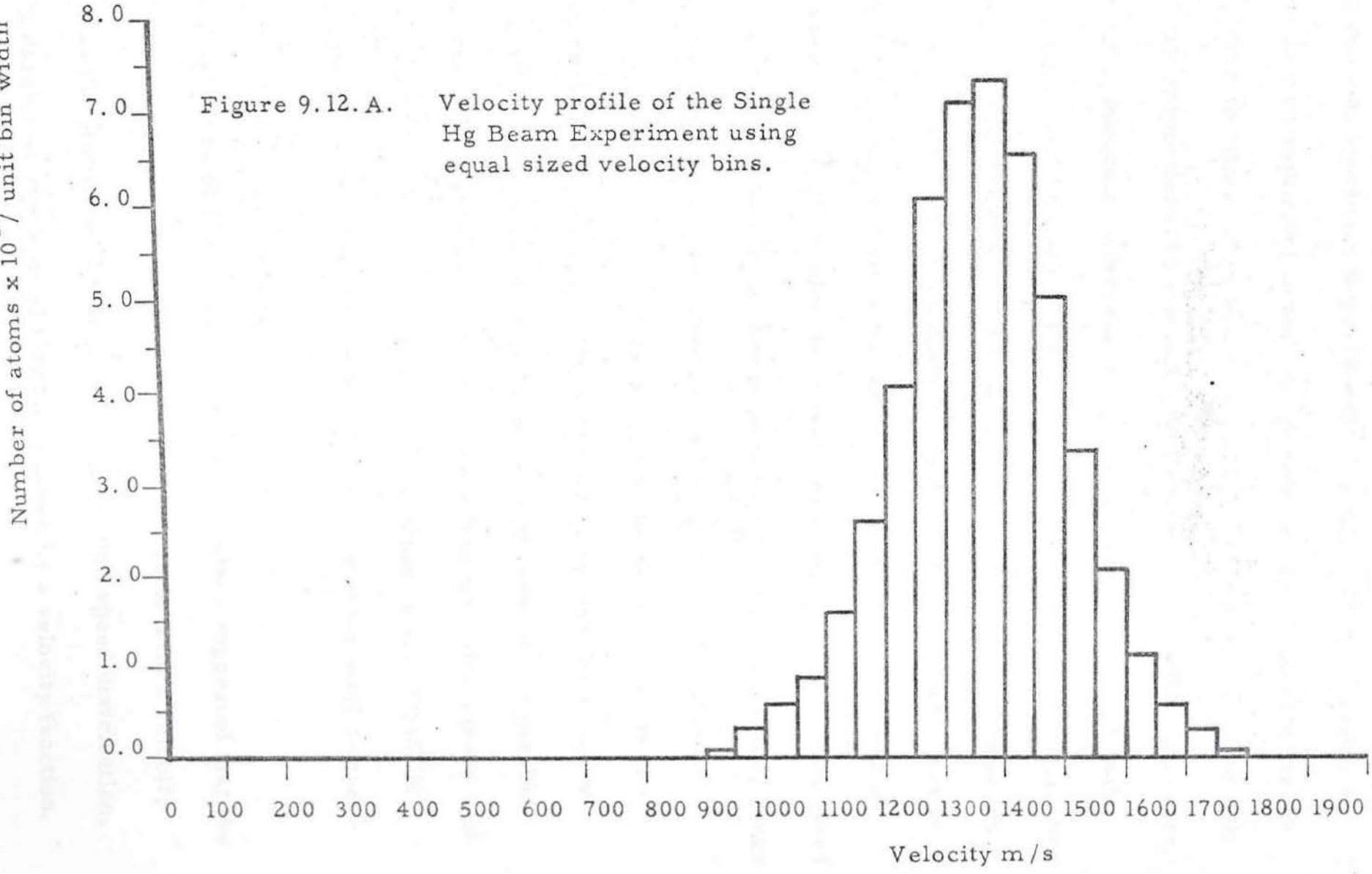

Figure 9.12.A. Velocity profile of the Single Hg Beam Experiment using equal sized velocity bins.

9.4.B. Simple Pulse Shape and Position Considerations.

If the rotor position for emission is simplified such that the rotor arm is perpendicular to the line joining the tip of the rotor to the detector, then the time taken by any molecule to reach the detector will be inversely proportional to the velocity imparted to it by the rotor arm, added to the component of thermal velocity parallel to the flight path. Taking into account the apparent symmetry of the observed pulse and this last point, the author considered a Gaussian curve as a fit to the shape of the pulse. A possible explanation for the apparent Gaussian shape is revealed if one considers the function produced by taking a volume of gas and resolving all the molecular velocities along one axis. This gives the familiar result that the number of molecules within the velocity range $V_x \rightarrow (V_x + \Delta V_x)$ is proportional to $e^{-\frac{mV_x^2}{kT}}$, which has its maximum centred on $V_x = O$. Relating this to the shape of the re-measured pulses suggested that the observed pulse was the result of displacing all the x-components of velocity by an amount comparable to the tip-speed of the rotor. Also, the width of the pulse agreed with that which would be expected from a gas at a temperature of 400° K, which is compatible with earlier measurements of rotor-body temperature.

Initial ideas on the rotor-produced gas pulses suggested that the molecules would leave the advancing face of the rotor with a velocity distribution that resembled a displaced Maxwellian speed distribution, namely a displaced exponential term multiplied by a velocity function.

However, this would have the effect of shifting the maximum of the pulse to higher speeds compared with a simple displaced Gaussian and would also destroy the symmetry of the pulse. On the other hand, emission from the back face would also produce another peak, slower than the rotor tip, thus producing an over all distribution with two peaks separated by about 360 m/s, this being twice the value calculated using the "most probable speed" for a simple Maxwellian speed distribution given by $\sqrt{\frac{2kT}{m}}$. It would be possible to fill the space between the peaks and thus make it appear as one pulse, but this requires very elevated temperatures.

In Chapter VIII is discussed the possibility of the mercury atoms moving to the very tip of the rotor arm and evaporating. Under these circumstances, one could expect a Gaussian distribution centred on the tip velocity. However, the tip speed was 1.42 km/s while the pulse peak lies at 1.36 km/s. The difference between these two velocities can barely be accounted for by the 4% measurement error. It may not be necessary to assume that the emission is from the very tip, but at some point, 2-3 mm, displaced from the tip, the emission mimmicks a gas cloud.

When the rotor tip is travelling with a speed of 1.4 km/s and is passing through a gas at a low pressure, $\sim 10^{-5}$ torr, it could be considered to be comparable with a space vehicle re-entering the upper atmosphere. At this pressure, the mean free path is many metres, but the velocity of the tip is about four times the speed of sound and

hence, it may be possible for the gas just in front of the advancing edge of the rotor to be compressed and produce an effect similar to the compression wave produced by supersonic objects in normal pressures. However, as the pressure is lower than atmospheric by several orders of magnitude, the degree of the compression will be considerably reduced. The fact that the mean free path would appear to be longer than the dimension of the apparatus does not preclude the possibility of local, relatively high pressure areas existing within the vessel, especially as the diameter of the rotor is comparable with the diameter of vacuum vessel. Therefore, the observed pulse may be a small part of a shock wave produced by the rotor blade, from the general gas within the rotor vessel.

The author attempted to refine the comparison between the displaced Gaussian and the observed pulse by producing a simple, mathematical model and least-squares-fitting it to the observed pulse. This model consisted of two parts, the first being simply a re-write of the Gaussian function, such that the Gaussian was displaced. The resultant equation then gives the number of atoms within the velocity range $V_x \rightarrow V_x + \Delta V_x$, accelerated as a result of some interaction with a very small area of the rotor arm, proportional to $e^{-\frac{m}{kT}(V_x - V_R)^2} . \Delta V_x$, where V_R is the speed of that point on the rotor arm which was responsible for the acceleration of the molecules. The second part attempts to account for the possibility that at different distances from the tip the number of molecules available for acceleration may change. The criterion which defines the form of the function of proportionality was based

on the fact that whatever the nature of the molecule/arm interaction, it is likely to be one in dynamic equilibrium and hence, the number of atoms leaving any small area of the arm per rotation is equal to, or at least proportional to the number collected per rotation. This produces a simple function of proportionality of $2\pi \Delta x(mx + c)\, x$, where x is the distance from the centre of the rotor to the element of the arm, which is of length Δx and height governed by the profile function of the rotor arm. This expression represents the volume swept out by the element Δx, during one rotation of the rotor arm. Thus, for each element of the rotor arm extending a few millimetres from the tip, there corresponds a displaced Gaussian curve. To re-create the shape of the pulse produced by the above expressions, it is necessary to perform a convolution of them. This was done using a computer to perform a numerical convolution. The result was then normalized, requiring that the number of molecules in the model pulse be equal to the number of molecules in the observed pulse. Once this had been done, the curve was compared with the observed pulse using a "least-squares" criterion. Two variables were adjusted in the convolution exercise to produce the best fit. These were the temperature of the gas , T, and the effective length of the arm that the detector would have been able to "see". The best fit is shown in Figure 9.12 C., while Figure 9.12.B, is a smooth curve drawn through the histogram. The "best fit" was produced with a value for T of 405^{o}K and an effective length of 5.9 mm. These values are quite compatible with previous expectations of temperature and of geometry of the detection system. The positions of the two centroids for the

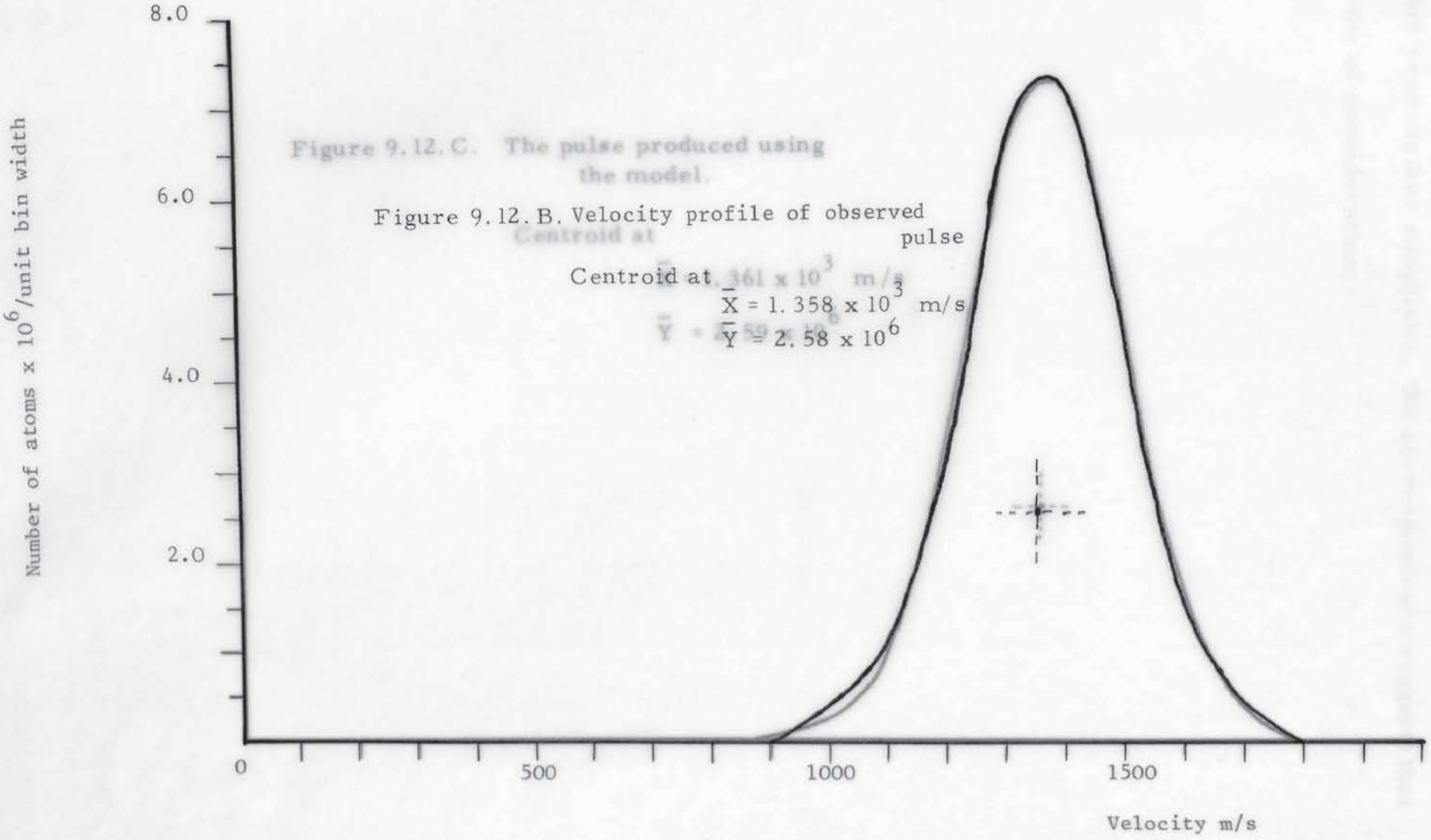

Figure 9.12.B. Velocity profile of observed pulse

Centroid at

$\bar{X} = 1.358 \times 10^3$ m/s

$\bar{Y} = 2.58 \times 10^6$

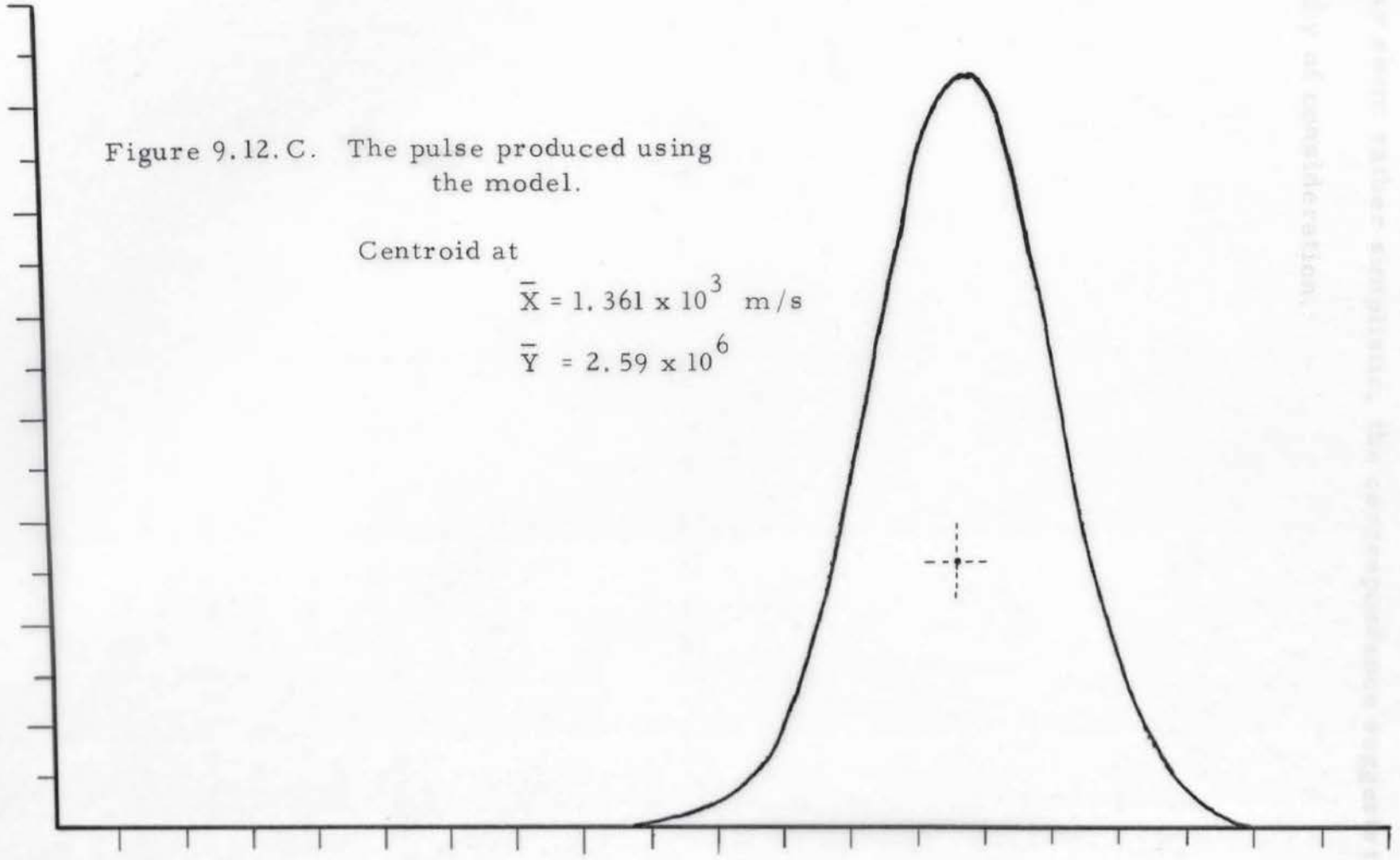

Figure 9.12.C. The pulse produced using the model.

Centroid at

$\bar{X} = 1.361 \times 10^{3}$ m/s

$\bar{Y} = 2.59 \times 10^{6}$

two curves also show a high degree of correspondance. While this model may seem rather simplistic, the correspondance suggests that it is worthy of consideration.

This is the end of the supplement to the thesis.

APPENDIX 1

Derivation of counting probability for digital drive unit

(See Chapter VII)

$$T_1 = (n-1)T_c + {}^1P_n\, T_c \qquad \text{for } nT_c > T_1 > (n-1)Tc$$

$$T_2 = nT_c + {}^2P_{(n+1)}\, Tc \qquad \text{for } (n+1)T_c > T_2 > nT_c$$

Therefore:

$$T_2 - T_1 = T_c\,[{}^2P_{(n+1)} - {}^1P_n + 1]$$

Also:

$$T_2 - T_1 = 9\left[\frac{1}{F_s} - \frac{1}{F_m}\right]$$

And if $F_s \simeq F_m$, then:

$$T_2 - T_1 = \frac{9\,\triangle F}{F^2}$$

where $\triangle F = F_m - F_s$ and $F = F_s$ or F_m

Therefore:

$$\triangle F = \frac{F^2 T_c}{9}\,[{}^2P_{(n+1)} - {}^1P_n + 1]$$

Average torque fraction $T_q = (1 - {}^2P_n \cdot {}^1P_n)$ in this case

and as $${}^2P_n = 1 - {}^2P_{(n+1)}$$

$$T_q = 1 - {}^1P_n\,[1 - {}^2P_{(n+1)}]$$

Hence:

$$T_q = {}^1P_n\left[{}^1P_n + \frac{9\,\triangle F}{F^2\,T_c} - 2\right] + 1$$

for ${}^1P_n \neq 0$ or 1

${}^2P_{(n+1)}$ range from $1 \longrightarrow 0$

Therefore:

$$\Delta F \text{ must be } \frac{F^2 T_c}{9}(2 - {}^1P_n) \rangle \Delta F \rangle \frac{F^2 T_c}{9}(1 - {}^1P_n)$$

if ${}^1P_n = 1$ then $\frac{F^2 T_c}{9} \rangle \Delta F \rangle 0$

Therefore: $$T_q = \frac{9 \Delta F}{F^2 T_c}$$

For $$nT_c \rangle T_1 \rangle (n-1)T_c$$

and $$(n-1)T_c \rangle T_2 \rangle (n-2)T_c$$

$$T_1 = (n-1)T_c + {}^1P_n T_c$$

$$T_2 = (n-2)T_c + {}^2P_{(n+1)} T_c$$

Therefore: $$T_2 - T_1 = T_c [{}^2P_{(n-1)} - {}^1P_n - 1]$$

Hence: $$\Delta F = \frac{F^2 T_c}{9} [{}^2P_{(n-1)} - {}^1P_n - 1]$$

This gives for the average torque fraction T_q

$$T_q = (1 - {}^1P_{(n-1)} \cdot {}^2P_{(n-1)})$$

$$= 1 + ({}^1P_n - 1)[\frac{9 \Delta F}{F^2 T_c} + {}^1P_n + 1]$$

for ${}^1P_n \neq 0$ or 1

For the range of ΔF

$$-\frac{F^2 T_c \, {}^1P_n}{9} \rangle \Delta F \rangle -\frac{F^2 T_c}{9}({}^1P_n + 1)$$

if ${}^1P_n = 1$ $$0 \rangle \Delta F \rangle -\frac{F^2 T_c}{9}$$

Hence $$T_q = - \frac{.9 \triangle F}{F^2 T_c}$$

For $$nT_c \rangle T_1 \rangle (n-1) T_c$$

and $$nT_c \rangle T_2 \rangle (n-1) T_c$$

$$T_1 = (n-1)T_c + {}^1P_n T_c$$

$$T_2 = (n-1)T_c + {}^2P_n T_c$$

$$T_2 - T_1 = T_c({}^2P_n - {}^1P_n)$$

$$\triangle F = \frac{F^2 T_c}{9} ({}^2P_n - {}^1P_n)$$

$$T_q = ({}^2P_n - {}^1P_n)$$

Therefore: $$T_q = \frac{9 \triangle F}{F^2 T_c} \qquad {}^1P_n \neq 0 \text{ or } 1$$

for $\triangle F$ such that $(1 - {}^1P_n) \frac{F^2 T_c}{9} \rangle F \rangle - \frac{F^2 T_c \, {}^1P_n}{9}$

Generally if ${}^1P_n \neq 0$ or 1, then width of proportional section

$$= \frac{3F^2 T_c}{9}$$

but if ${}^1P_n = 1$ or 0, the width of proportional section

$$= \frac{2F^2 T_c}{9}$$

See Figures 7.2, 7.3 and 7.4.

APPENDIX 2

Component values for circuit diagrams

Figure 4.2 The Rotor Suspension Circuit.

R_1	390 ohms	R_{11}	470k	R_{21}	390 ohms
R_2	390 ohms	R_{12}	1k	R_{22}	0.22 ohms
R_3	68 ohms	R_{13}	100k	R_{23}	10 ohms
R_4	33k	R_{14}	10k	R_{24}	0→30V FSD
R_5	33k	R_{15}	100k	R_{25}	0→10A FSD
R_6	2.2k	R_{16}	100k	R_{26}	100k
R_7	220k	R_{17}	10k	R_{27}	1Mohm
R_8	10 ohms	R_{18}	1k	R_{28}	1Mohm
R_9	10 0hms	R_{19}	10 ohms	R_{29}	10 ohms
R_{10}	470k	R_{20}	3.3k	R_{30}	1k
VR_1	100k	D_1	10V	TR_1	BC182
VR_2	10k	D_2	10V	TR_2	2N3054
VR_3	10k	D_3	IN4001	TR_3	2N3055
VR_4	10k	D_4	IN4006		
VR_5	10k				
A_1	741	C_1	10μF Tant.	C_9	1nF Disc.
A_2	741	C_2	10μF Tant.	C_{10}	22μF Tant.
A_3	741	C_3	0.1μ Disc. Cer.	C_{11}	22μF Tant.
		C_4	68pF Disc. Cer.	C_{12}	470pF Disc.
		C_5	22μF Tant.	C_{13}	22μF Tant.
		C_6	22μF Tant.	C_{14}	22μF Tant.

Figure 4.2 continued.

L_1	3 ohms	C_7	0.1μF Disc. Cer.	C_{15}	640μF
		C_8	10nF Disc.	C_{16}	640μF

Figure 4.11 P.I.N. Diode Amplifier.

R_1	1.0M	R_{10}	100 ohms	R_{19}	22k
R_2	1k	R_{11}	100 ohms	R_{20}	150 ohms
R_3	1M	R_{12}	2.2k	R_{21}	150 ohms
R_4	2.7k	R_{13}	5.6k	R_{22}	10 ohms ½ W.
R_5	1k	R_{14}	1.2k	R_{23}	10 ohms ½ W.
R_6	680 ohms	R_{15}	1k	R_{24}	2.7k
R_7	10k	R_{16}	1k	R_{25}	47 ohms
R_8	1M	R_{17}	5.6k		
R_9	100 ohms	R_{18}	5.6k		
D_1	10 VZ	D_5	IN4148	D_9	IN4148
D_2	10 VZ	D_6	IN4148	D_{10}	IN4148
D_3	6.8 VZ	D_7	IN4148	D_{11}	IN4148
D_4	4.7 VZ	D_8	3.3 VZ	D_{12}	L.E.D.
TR_1	TIS49	C_1	10nF	C_7	10μF Tant.
TR_2	BC182LA	C_2	10μF Tant.	C_8	10μF Tant.
TR_3	BC212LA	C_3	10μF Tant.	C_9	10μF Tant.
		C_4	10μF Tant.	C_{10}	10μF Tant.
		C_5	10μF Tant.	C_{11}	10μF Tant.
		C_6	470pF		

Figure 4.12 Rotor Speed Monitor

R_1	39k	C_1	0.1μF Disc.	G_5	$\frac{1}{4}$ SN7400
R_2	10k	C_2	680μF	G_7	$\frac{1}{4}$ SN7400
R_3	1k	C_3	2.2nF	G_{10}	$\frac{1}{4}$ SN7400
R_4	100 ohms	C_4	22μF Tant.		
G_1	$\frac{1}{6}$ SN7404	G_4	$\frac{1}{6}$ SN7404		
G_2	$\frac{1}{6}$ SN7404	G_8	$\frac{1}{6}$ SN7404		
G_3	$\frac{1}{6}$ SN7404	G_9	$\frac{1}{6}$ SN7404		

Figure 5.5 Pulse Length and Base Current Drive Circuit

R_1	680 ohms	R_7	27 ohms	R_{13}	68 ohms
R_2	1k	R_8	270 ohms	R_{14}	470 ohms
R_3	2.5k	R_9	470 ohms	R_{15}	27 ohms
R_4	220 ohms	R_{10}	470 ohms	R_{16}	470 ohms
R_5	33 ohms	R_{11}	12 ohms	R_{17}	0.22 ohms
R_6	1.5k	R_{12}	150 ohms	R_{18}	680 ohms
				R_{19}	680 ohms
D_1	IN4148	TR_1	V405A	TR_5	BC182
D_2	IN4148	TR_2	P346A	TR_6	BC212
		TR_3	P3468	TR_7	MJE2901
		TR_4	BC182		
C_1	0.01μF	C_2	0.1μF	C_3	470pF

Figure 5.6 Electronic Drive Output Stage

$R_5 \longrightarrow R_{14}$	68 ohms	$R_{16} \longrightarrow R_{25}$	0.22 ohms
		$TR_2 \longrightarrow TR_{11}$	MJE2801
$D_1 \longrightarrow D_{10}$	IN4148		

Figure 6.2 Rotor Analogue Phase-Lock Circuit.

R_1	10k	R_{17}	10 ohms	R_{33}	10 ohms
R_2	18k	R_{18}	1k	R_{34}	10k
R_3	820 ohms	R_{19}	100k	R_{35}	10k
R_4	1k	R_{20}	10k	R_{36}	1M
R_5	10k	R_{21}	10k	R_{37}	1k
R_6	1k	R_{22}	1k	R_{38}	10k
R_7	10 ohms	R_{23}	10k	R_{39}	100k
R_8	10k	R_{24}	100k	R_{40}	100k
R_9	10 ohms	R_{25}	100k	R_{41}	100k
R_{10}	1Mohm	R_{26}	10k	R_{42}	2.2k
R_{11}	10 ohms	R_{27}	33k	R_{43}	39k
R_{12}	10 ohms	R_{28}	10k	R_{44}	390k
R_{13}	2.2k	R_{29}	5.7k	R_{45}	68 ohms
R_{14}	1Mohm	R_{30}	50k	R_{46}	10k
R_{15}	10 ohms	R_{31}	50k	R_{47}	1k
R_{16}	1Mohm	R_{32}	10 ohms	R_{48}	100 ohms
				R_{49}	100 ohms
				R_{50}	100 ohms

Figure 6.2 continued.

C_1	22μF Tant.	C_8	22nF	C_{15}	22μF Tant.
C_2	22μF Tant.	C_9	22μF Tant.	C_{16}	1μF
C_3	1μF	C_{10}	22nF	C_{17}	22μF Tant.
C_4	22μF Tant.	C_{11}	22μF Tant.	C_{18}	22μF Tant.
C_5	22μF Tant.	C_{12}	22μF Tant.	C_{19}	10μF
C_6	1μF	C_{13}	1μF		
C_7	22μF Tant.	C_{14}	22μF Tant.		

Figure 6.3 Rotor Analogue Phase-Lock

D_1	IN4148	D_4	L.E.D.
D_2	IN4148	D_5	L.E.D.
D_3	L.E.D.		

APPENDIX 3

Logic Symbols Used in Circuit Diagrams

NOT (inverter)

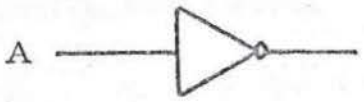

$X = \overline{A}$

BUFFER

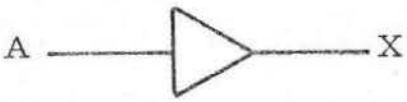

$X = A$

NAND gate

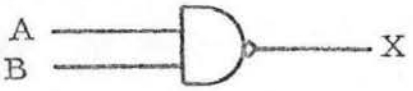

$X = \overline{A \cdot B}$

AND gate

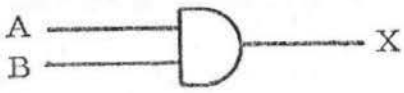

$X = A \cdot B$

OR gate

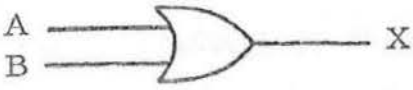

$X = A + B$

NOR gate

$X = \overline{A + B}$

Exclusive OR gate

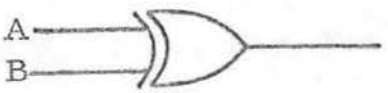

$X = A.\overline{B} + \overline{A}.B$

Exclusive NOR gate

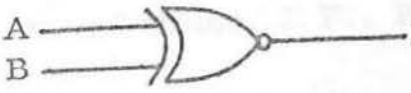

$\overline{X = A.\overline{B} + \overline{A}.B}$

REFERENCES

1. Bull, T.H., 'Applications of High Speed Rotational Speeds', Ph.D. Thesis, University of Birmingham. (1953).
2. Marshall, D.G., and Moon, P.B., 'A Technique for High Rotational Speeds', Journal of Scientific Instruments and of Physics in Industry, Vol. 25, No.10, October 1948.
3. Bull, T.H. and Moon, P.B., Disc. Far. Soc., Vol. 17, p.56 (1954).
4. CIBA-Geigy (U.K) Ltd., Publication A.22C, M37b and A17a.
5. MacHattie, L.E., Rev. Sci. Instr., Vol.12, p.429 (1941).
6. Beams, J.W., Ross, J.D. and Dillon, J.F., Rev. Sci. Instr., Vol.22, p.77 (1951).
7. Beams, J.W., Boyle, R.D. and Hexner, P.E., 'Magnetically Suspended Equilibrium Ultracentrifuge', Rev. Sci. Instr., Vol.32, p.645 (1961).
8. Stubberud, W., and Di Stefano III, 'Feedback and Control Systems'.
9. Buckley, R.V., 'Fundamentals of Servomechanisms'.
10. Fluendy and Lawley, 'Chemical Application of Molecular Beam Scattering'.
11. Abuaf, N., Anderson, J.B., Andres, R.P., Fenn, J.B. and Marsdon, D.G.H., 'Science', 155, 997 (1967).
12. Herschbach, D.R., 'Reactive Scattering', Far. Disc. Chem. Soc., No.55, p.233 (1973).
13. Marshall, D.G. and Moon, P.B., Nature, Vol.167, p.478 (1951).
14. Bull, T.H., and Moon, P.B., Disc. Far. Soc., Vol.17, p.54 (1954).
15. Moon, P.B., Ralls, M.P., Saul, J.B. and Broadhurst, J.H., 'High Speed Rotors', Physics Bulletin, Vol.25, p.511 (1974).
16. Beams, J.W., Ross, J.D. and Dillon, J.F., Rev. Sci. Instr., Vol22, p.77 (1951).

17. Marshall, D.G., 'Experiments with Fast Moving Rotors', Ph.D. Thesis, University of Birmingham (1950).

18. Moon, P.B., 'Rotors and Molecular Beams', Internal Report, University of Birmingham (1969).

19. Nutt, C.W., Bale, T.J., Cosgrove, P. and Kirby M.J., 'Production of Intermediate Energy Beams by High Speed Rotors', Proc. of 5th International Symposium on Molecular Beams, Nice (April 1975).

20. Moon, P.B., 'Some Scientific Applications of High-Speed Rotation', Brit. Journal of Applied Physics, Vol.4, pp. 97-101 (April 1953).

21. Preikschat, E., 'The Mössbauer Effect and Tests of Relativity', Ph.D. Thesis, University of Birmingham (1968).

22. Feynman, 'The Feynman Lectures on Physics', Vol.II - Addison-Wesley Publishing Co.

23. Bozorth, R.M., 'Ferromagnetism'., D. Van Nostrand Co., New York (1951).

24. 'Transistor Manual', General Electric Co.

25. Morris, N.M., 'Logic Circuits', McGraw-Hill Publishing Co.

26. Abernethy, J.D.W., 'The Boxcar Detector for Waveform Recovery', Brookland Electronics Ltd., Wireless World (December 1970).

27. Herzberg, G., 'Atomic Spectra and Atomic Structure'.

28. 'Semiconductor Circuit Design', Vol.II, Texas Instruments Ltd.

29. Barlow, B.V. and Read, R.S., 'High Speed Rotating Devices', Contemp. Phys., Vol.13, No.4, pp. 355-374 (1972).

30. 'The TTL Data Book for Design Engineers', Texas Instruments Ltd.